Integrated Reservoir-Geomechanics Upscaling Workflow

by

Bo Zhang

A thesis submitted in partial fulfillment of the requirements for the degree of

Doctor of Philosophy

in

Geotechnical Engineering

Department of Civil and Environmental Engineering
University of Alberta

ABSTRACT

The impact of geomechanical behavior in the SAGD process has received increased attention over the last decade because of its importance in assessing caprock integrity and potential influence on production performance. The deformations and potential shear failures in the reservoir lead to alterations of porosity, absolute permeability and water relative permeability due to high pressure and temperature changes induced by the SAGD process. Ignoring these geomechanical responses in the simulation of the SAGD process may lead to erroneous predictions of reservoir performance and a failure to recognize potential hazards similar to the Joslyn Creek steam release incident. To improve our understanding of these issues, coupled reservoir-geomechanics simulation on a reservoir-scale SAGD project is necessary. However, the limitation of computational power and appropriate upscaling techniques have restricted the wide application of coupled simulation in field cases.

A local deformation-based upscaling technique has been proposed for the elastic and plastic properties and integrated with the flow-based upscaling technique for permeability. To further improve the computational efficiency of upscaling process for different realizations, the local numerical upscaling technique is integrated with the analytical solution generated from the numerical investigations on the impact of heterogeneity on the stress-strain response and failure modes. The upscaling technique has the best performance when the upscaling ratio is optimized at different regions and directions guided by the level of heterogeneity parameterization in reservoir-scale SAGD processes. The field case study has shown that the proposed technique can reduce the simulation time by 20 times while retaining the accuracy in both geomechanical response and reservoir performance, e.g. steam chamber shape, cumulative oil production, subsurface volume change and surface heave.

PREFACE

Chapter 6 of this thesis has been published in Petroleum Geoscience with my colleagues Dr. Deisman and Dr. Khajeh in the Reservoir Geomechanics research group. Dr. Khajeh contributed to the preliminary study for the methodology, which is the local numerical testing regime in two-dimension (Khajeh et al. 2012). Dr. Deisman helped generate the parallel program in the coupling platform for applications in field scale. I am responsible for establishing the methodology in the three-dimension orthogonal system, coding the local testing environments, validating the global response and implementation in the SAGD process.

Zhang B., Deisman N., Khajeh M., Chalaturnyk R. and Boisvert J. 2019. Numerical Local Upscaling of Elastic Geomechanical Properties for Heterogeneous Continua. *Petroleum Geoscience*, https://doi.org/10.1144/petgeo2018-159.

The other chapters of this thesis have not yet been published elsewhere yet.

DEDICATION

To my home country, China

To my dear parents, Lingqiao Zhang and Yaling Zhong

To my beloved wife and son, Xinming and Aidan

ACKNOWLEDGEMENT

TABLE OF CONTENTS

LIST OF TABLES

LIST OF FIGURES

NOMENCLATURE

α	Thermal expansion coefficient
σ_1	Major principal stress
σ_3	Minor principal stress
σ_d	Deviator stress (σ_1-σ_3)
σ_F	Failure deviator stress
σ_p	Peak deviator strength
σ_{sand}	Failure deviator stress of sand when σ_3 is 0.1 MPa
σ_{shale}	Failure deviator stress of shale when σ_3 is 0.1 MPa
ε_a	Axial strain
ε_v	Total volumetric strain
ε_s^p	Plastic shear strain
μ	Viscosity
γ	Engineering shear strain
$\gamma\,(h)$	Semivariograms
v_{ij}	Poisson's ratio characterizing lateral contraction in j axis when stress is in i axis
$\emptyset$	Porosity
$\emptyset_o$	Initial porosity
$\emptyset_{new}$	Updated porosity
ϕ	Friction angle
ϕ_{cv}	Critical state friction angle
ϕ_p	Peak friction angle
ϕ_r	Residual friction angle
ψ	Dilation angle
ψ_p	Peak dilation angle
ψ_r	Residual dilation angle
a_h	Horizontal range
a_h^d	Dimensionless horizontal range

a_{hmax}	Maximum horizontal range
a_{hmin}	Minimum horizontal range
a_v	Vertical range
a_v^d	Dimensionless vertical range
a	Scale factor for new permeability due to deformations
C_e	Shape factor for elastic deformations on updated permeability
C_p	Shape factor for plastic deformations on updated permeability
C_Φ	Shape factor for updated permeability
E	Young's modulus
$E_{0.5}$	Tangent Young's modulus at 50% of peak stress
E_i	Young's modulus on i axis
E_{sand}	Young's modulus for sand
E_{shale}	Young's modulus for shale
E_{tan}	Tangent Young's modulus
G_{ij}	Shear modulus in plane ij parallel to the local coordinate planes
h	Lag distance
K_o	Ratio of minimum horizontal stress versus maximum horizontal stress
k	Permeability
k_o	Initial permeability
k_h	Horizontal permeability
k_v	Vertical permeability
k_{new}	New permeability due to deformations
$k_{v,fm}^{eff}$	Effective vertical permeability when considering failure mechanism
$k_{h,fm}^{eff}$	Effective horizontal permeability when considering failure mechanism
$k_{v,ave}^{eff}$	Effective horizontal permeability from average total and plastic shear strain
N	Number of pairs for lag distance
R	Range ratio
S_{ijkl}	Elastic compliance tensor

S_o	Ratio of maximum horizontal stress versus vertical stress
sph	Spherical model
T	Temperature
T_o	Original temperature
u	Flux velocity
V_b	Bulk volume
V_p	Pore volume
V_s	Solid volume
V_{sh}	Volume fraction of shale
$z(u)$	Value at location u
$z(u+h)$	Value at location $u+h$
API	American Petroleum Institute
DEM	Discrete element method
IHS	Inclined heterolithic stratification lithosomes
LAS	Log ASCII Standard
MOP	Maximum operation pressure
SAGD	Steam-assisted gravity drainage
SIS	Sequentially indicator simulation

CHAPTER 1:   INTRODUCTION

1.1   Background and Motivations

Canada has the third-largest proven oil reserves in the world, estimated at 171.0 billion barrels of which 166.3 billion barrels are found in Alberta's oil sands (Natural Resources Canada 2017). Oil sands production, including both surface mining and in-situ recovery totaled about 1 billion barrels per year in 2017. With the improvement in recovery, the ultimate potential reserves could increase to more than 300 billion barrels. Surface mining is used to produce oil reserves close to the surface (<65m), however approximately 80% of oil sands are below economical open pit mining depths. Thermal methods including steam-assisted gravity drainage (SAGD), cyclic steam stimulation (CSS) and in-situ combustion (ISC) are used for bitumen recovery in oil sands formations deeper than 65 m. Currently, the SAGD process is the most widely used technique for recovery of bitumen from the oil sands since being introduced by Butler (1981, 1985).

Chalaturnyk (1996) encompassed a series of laboratory, field instrumentation and numerical modeling results to investigate the complex interaction of geomechanics and multiphase thermal flow in oil sands reservoirs during SAGD. It is the deformation response of oil sands along the stress path that is of primary importance when the hot steam injection elevates temperature and pressure in the steam chamber. The importance of geomechanics in SAGD has received increased attention over the last decade because of attention given to caprock integrity when existing SAGD projects expand to shallower depths with thinner caprock. The deformations and potential shear failures in the reservoir lead to dramatic alterations of porosity, absolute and relative permeability according to experimental results and field observations. Ignoring the interactions of geomechanical and flow response in SAGD simulation leads to erroneous predictions of reservoir performance and fails to recognize potential hazards similar to the Joslyn Creek steam release

incident. Assessments of reservoir-geomechanics have become an AER (Alberta Energy Regulator) application requirement for SAGD projects in the shallow Athabasca oil sands area according to AER Directive 086, approved on November 30, 2016. Coupled reservoir-geomechanics modeling is essential to determine the maximum operating pressure (MOP) considering both tensile and shear failures in caprock.

The scale of this research is REV (representative element volume) scale (m) and above (km). REV scales are chosen sufficiently large to ensure a statistically relevant distribution for the microscopic heterogeneities, but small enough to be considered as a material point (local equilibrium) at the reservoir scale. Here, the difference of lithologies at the REV and reservoir scale is considered as the dominant source of heterogeneity rather than variations of pore structures.

The McMurray Formation, which is the major pay zone of the Athabasca oil sand area, is well known for its complex geological heterogeneity. High-resolution geo-cellular models are usually built around 1 m vertically and 1 to 100 m horizontally based on available log, seismic, core and production data to capture the detailed geological heterogeneity in the reservoir. Depending on the size of the SAGD project, the geo-cellular models may contain 10-100 million grids which are finer than grid resolutions that provide for computational efficiency in geomechanical simulation. Multi-variate simulations, e.g. sequential indicator/Gaussian simulation, are usually applied to generate the facies/properties model for regions without log data. Thus, uncertainty always exists for both petrophysical and geomechanical properties in the geo-cellular models. Random selection of geo-cellular realizations could lead to inaccurate or even misleading representation of flow/geomechanical response in SAGD simulations. Directly using the realizations of geocellular models to predict the upper and lower bound of production performance and geomechanical response would make computational time unacceptable. Thus, upscaling of heterogeneous

reservoir-geomechanics properties is needed to bridge the gap between the high-resolution geo-cellular model and a computational efficient reservoir-geomechanics model.

One of the outstanding issues in upscaling is to understand and quantify the impact of heterogeneity on the flow and geomechanical response. Only considering flow, various methods have been proposed to quantify the dynamic influence of reservoir heterogeneity on production performance, i.e. shale barriers on steam chamber propagation. On the geomechanics side, the understanding of the impact of heterogeneity on SAGD is not sufficient to provide a reliable method to provide upscaled geomechanical properties that can reproduce the complex deformation response along the stress path in the SAGD process.

The lack of appropriate and efficient upscaling techniques for full-field coupled reservoir-geomechanics SAGD simulation is the main motivation for this research. The proposed upscaling technique should be able to reproduce the non-linear stress-strain response caused by plastic deformations in porous media and associated permeability change due to pore structure alterations during deformations in full-field reservoir-geomechanics SAGD simulation. The use of appropriate upscaling techniques will result in significant computational time savings while maintaining the accuracy of predictions. The reduced computation time is valuable in order to consider uncertainty analyses for issues like caprock integrity for shallow SAGD projects where the amount of operating "elbow room" between operating pressure and MOP diminishes. Coupled reservoir-geomechanics simulations on upscaled geo-cellular models are able to provide efficient and accurate simulation results to help explore opportunities while quantifying the potential risk.

1.2   Problem Statement

The first challenge is that current understandings of the interactions of flow and geomechanical responses are not sophisticated enough when associated with plastic deformations in

3

heterogeneous oil sands and IHS (inclined heterolithic strata). In terms of flow response, a number of studies have achieved success on the quantification of reservoir heterogeneity, i.e. permeability. However, the research on quantifications of reservoir heterogeneities on geomechanical response and potential erroneous predictions in conventional reservoir simulations for SAGD is limited. Progress has been made by Elkateb (2006) and Khajeh (2011) on 2D elastic behavior at the lab and reservoir scale, but the transition from elastic to elasto-plastic behavior has significant challenges due to the highly non-linear stress-strain response and plastic strain localization in weaker zones. Thus, the quantitative estimations of geomechanical response for highly heterogeneous oil sands considering elasto-plastic behavior and 3D models are crucial to providing insights for upscaling of reservoir-geomechanics simulations.

The second challenge is the lack of numerical investigations into the impact of elastic and plastic deformations on the permeability of heterogeneous oil sands. The permeability evolution of oil sands caused by deformations in SAGD simulations is usually directly estimated by correlations based on temperature and pressure rather than analyzing the change of failure modes for local regions with different shale configurations. Current conventional reservoir simulations usually use over-simplified geomechanical assumptions, resulting in limitations associated with massive plastic deformations in the reservoir or even caprock. Thus, an efficient and accurate modeling method for flow and geomechanical response is required for full-field SAGD simulations.

The last is the upscaling for macroscopic elasto-plastic and plastic behavior of complex heterogeneous media in reservoir-geomechanics modeling. The ideal upscaling technique for reservoir-geomechanics simulation should correctly model the anisotropic elastic and plastic deformations and induced permeability changes caused by sub-grid scale heterogeneities. The

4

optimum upscaling ratio and its influence on simulation results in different directions of the reservoir in coupled reservoir-geomechanics SAGD simulation require further investigation.

1.3   Research Objectives

The ultimate objective of this research is to develop an efficient integrated numerical upscaling workflow for reservoir-geomechanics properties to address the complex interactions of flow and geomechanical response in SAGD. The research objectives are summarized into five aspects corresponding to Chapters 3, 4, 5, 6 and 7.

The first objective is the parameterization and fast estimation of the shear strength of heterogeneous oil sands with various geostatistical parameters (volume fractions, ranges and azimuth/dip of shales). The nonlinear stress-strain behavior and failure modes for a series of heterogeneous oil sands realizations under numerical compression tests are investigated here to provide a systematic relationship between the shear strength parameters and the geostatistical parameters to parameterize the level of heterogeneity.

The second objective is to investigate permeability evolutions of oil sands during shear failures at both REV (represent element volume) scale. The plastic deformations change the pore structures in the heterogeneous porous media, which leads to alterations of oil recovery and/or serious steam/oil leak in caprock. The quantification of permeability changes needs to include different modes of failure for oil sands with different levels of heterogeneity.

Moving from the REV scale to field scale, the third objective is the investigation of heterogeneity on the flow and geomechanical response in the SAGD process. Coupled reservoir-geomechanics simulations of a selected well pad from the fine-scale mechanical earth model will demonstrate

the discrepancy between the uncoupled and sequentially coupled reservoir-geomechanics simulation of SAGD.

The fourth objective is to extend the local numerical upscaling approach for elastic properties proposed by Khajeh et al. (2012) to orthotropic 3D heterogeneous models to deal with complex IHS leading to anisotropic deformations at sub-grid scale. The proposed deformation-based upscaling technique should be appropriately integrated with a reliable permeability upscaling technique to deal with the interactions of flow and geomechanical response in the SAGD process.

The fifth objective is the generation of a local numerical upscaling methodology to reproduce the sub-grid scale elasto-plastic behavior of complex heterogeneous media. The proposed plastic upscaling technique should be able to capture the anisotropic failure criteria due to sub-grid scale heterogeneity and apply in field-scale coupled SAGD simulations.

1.4   Thesis Outline

This thesis contains 8 chapters that report on my research work completed in meeting the thesis objectives. Following the general introduction in Chapter 1, Chapter 2 provides the necessary background knowledge and previous research outcomes in the literature. Previous experimental results, field observations and numerical investigations of heterogeneous oil sands are summarized with a focus on the deformation response and induced changes of flow properties following the stress path of SAGD. The available heterogeneity quantification, proxy models and upscaling techniques for reservoir-geomechanics properties are discussed to provide insights and show the necessity of this research.

Chapter 3 focuses on the heterogeneity parameterization of the stress-strain behavior and failure modes in a series of sand-shale realizations mimicking the highly heterogeneous oil sands and IHS.

The macroscopic geomechanical responses and failure modes are quantified by the key geostatistical parameters, providing meaningful insights into the proposed integrated upscaling workflow.

Chapter 4 investigates the permeability change associated with deformations and proposes a permeability updating function which separates the influence by pore expansions and pore structure changes on permeability at the REV scale (m).

The research focus moves to the reservoir scale (km) in Chapter 5. A geo-cellular model for the MacKay River oil sand area is generated based on public data. Sequentially coupled reservoir-geomechanics simulations are conducted on a selected well pad of the MEM model to demonstrate the importance of appropriate modeling of deformations in SAGD.

Chapter 6 modifies Khajeh's (2012) elastic upscaling method and extends the upscaling capability to 3D with the anisotropic geomechanical response with changes of in-situ stress directions and shale inclinations. The new elastic upscaling method is incorporated in the coupled reservoir-geomechanics simulation platform (Deisman and Juncal 2018). The upscaling module offers a customized upscaling ratio for different regions of the reservoir in a parallel upscaling scheme which improves the efficiency of the upscaling process.

Chapter 7 presents the proposed upscaling technique which incorporates the anisotropic failure criteria caused by sub-grid heterogeneity. The case study on the selected well pad demonstrates the successful application of the integrated upscaling workflow and the importance of selecting the optimum upscaling ratio in different directions and regions of the reservoir.

Chapter 8 summarizes and provides the conclusions, contributions of the thesis and topics for future research suggested.

CHAPTER 2:   LITERATURE REVIEW

2.1   Background Knowledge of Oil Sands

Oil sands are naturally occurring mixtures of sand, clay, water and bitumen. The bitumen in Alberta oil sands has extremely high viscosity (>10,000 cp) under reservoir conditions before heated or diluted. Therefore, surface mining is used to produce oil sand reserves close to surface (<65m), however approximately 80% of oil sands are below economical open pit mining depths (Canada's Oil & Nature Gas Producers 2018). Thermal methods including steam-assisted gravity drainage, cyclic steam stimulation and in-situ combustion are used for bitumen recovery in oil sands formations deeper than 65 m. The geology of Alberta oil sands, geomechanical response and induced flow behavior change due to deformations are essential background knowledge which helps to inform the numerical investigations of SAGD.

2.1.1   Geology and Lithology

The location of oil sands in Canada is illustrated in Figure 2-1. The Athabasca deposit is the largest among the three major oil sand deposits located in northeastern Alberta, along with the nearby Peace River deposits in the west and Cold Lake deposits in the east stretching into Saskatchewan. The stratigraphic units and lithology of Athabasca oil sands near Fort McMurray are shown in Figure 2-2.
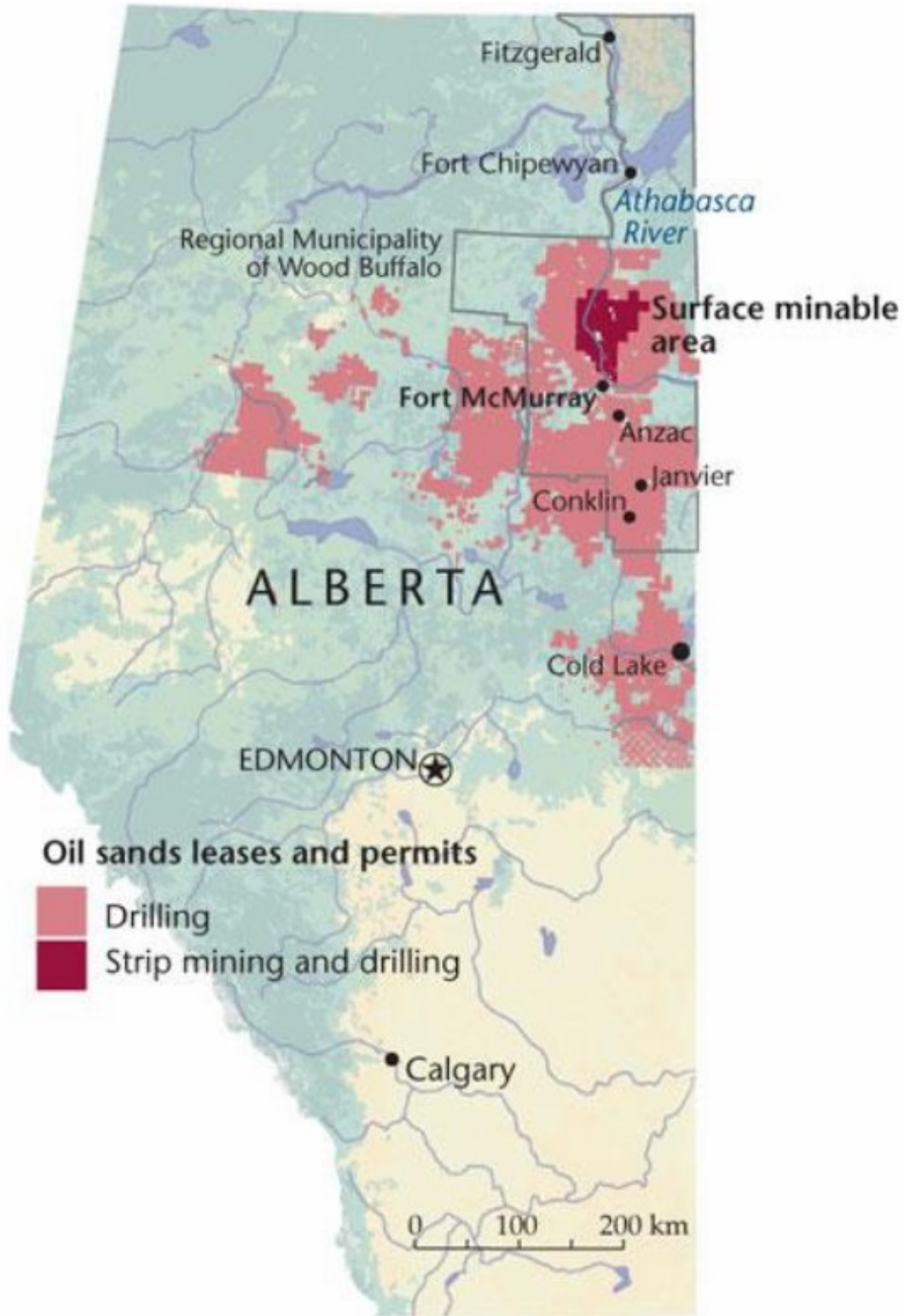
Figure 2-1.   Oil sands map in Alberta (Retrieved from Canadian Geographic 2008).

PERIOD	STRATIGRAPHIC UNITS		LITHOLOGY	HYDROSTRATIGRAPHY
HOLOCENE	recent sediments			
QUATERNARY	Quaternary sediments			Quaternary Aquifer/Aquitard
CRETACEOUS	Mannville Group	Viking Fm.		Viking Aquifer
		Joli Fou Fm.		Joli Fou Aquitard
		Grand Rapids Fm.		Grand Rapids-Clearwater Aquifer
		Clearwater Fm.		
				Clearwater Aquitard
		Wabiskaw Mbr.		McMurray-Wabiskaw Aquifer/Aquitard System
		McMurray Fm.		
DEVONIAN	Wood-bend Gp.	Beaverhill Lake Group	Elk Point Group		Wood-bend	Beaverhill Lake Aquifer System	Elk Point Aquitard

Legend: Till · Sand and gravel · Shale · Sandstone · Oil sand · Limestone · Evaporite

Figure 2-2.   Period, stratigraphic units, lithology and hydro-stratigraphy for typical Athabasca oil sands (Retrieved from Alberta Energy Regulator 2014).

The McMurray Formation is the major pay zone of oil sands and overlays the Devonian Formation. It is the basal unit of the Lower Cretaceous Manville Group and consists of fluvio-estuarine clastic deposits which are usually bitumen saturated. The stacked channels provide a wide range of lithofacies, including blocky channel sands, interbedded sandstone and shale in the form of inclined heterolithic strata (IHS), channel abandonment mud plugs, breccia horizons and intervals deposited on muddy flood plains and tidal flats. The regional McMurray-Wabiskaw resources have been widely characterized and details can be found in Phillips (2011). The Clearwater Formation overlies the McMurray Formation with the Wabiskaw Member at its base. The Wabiskaw Formation may include wavy interbeds of bitumen rich sand and thin layers of mud, but the rest

of the Clearwater Formation is a laterally continuous unit mainly consisting of silty shale which serves as the caprock of oil sands deposit.

The lithology of the Athabasca oil sands in McMurray Formation is of great importance because it directly controls net pay, flow and geomechanical characteristics. The core image (Figure 2-3) shows the complex lithologies in the McMurray Formation. The oil sands are heterogeneous with significant quantities of shale bedding planes because the McMurray Formation is a tidally influenced estuarine depositional environment, where abandoned channel-fill facies dominated by mud may embed in the cross-stratified bitumen saturated coarse sand. Thomas et al. (1987) reviewed the terminology, description, interpretation and significance of inclined heterolithic stratification (IHS) lithosomes in Alberta, Canada. The presence of steeply dipping clay seams can also be identified and has drawn increasing interest in studies on IHS due to their significant impact on the interactions between flow and geomechanical response.

The specific geological history of the McMurray Formation determines the grain-scale characteristics, sedimentation and stress history in the reservoir, which makes the structure and fabric of oil sands unique from other sands. Oil sands are primarily bitumen-saturated sand and mixed with fine clay/slit layers saturated with water. Figure 2-4 shows the schematic of the in-situ structure of undisturbed oil sands composed of sand and silt (Dusseault 1977). The quartz grains have extensive contacts with bitumen occupying the void. Most of the quartz grains are water-wet, so a water sheath can be found around the mineral grains containing fines in the sand layers. This makes bitumen extraction feasible using hot water/steam in SAGD (Dusseault 1977). The clay seams in oil sands are expressed as a water-saturated silty layer surrounded by micaceous partings.
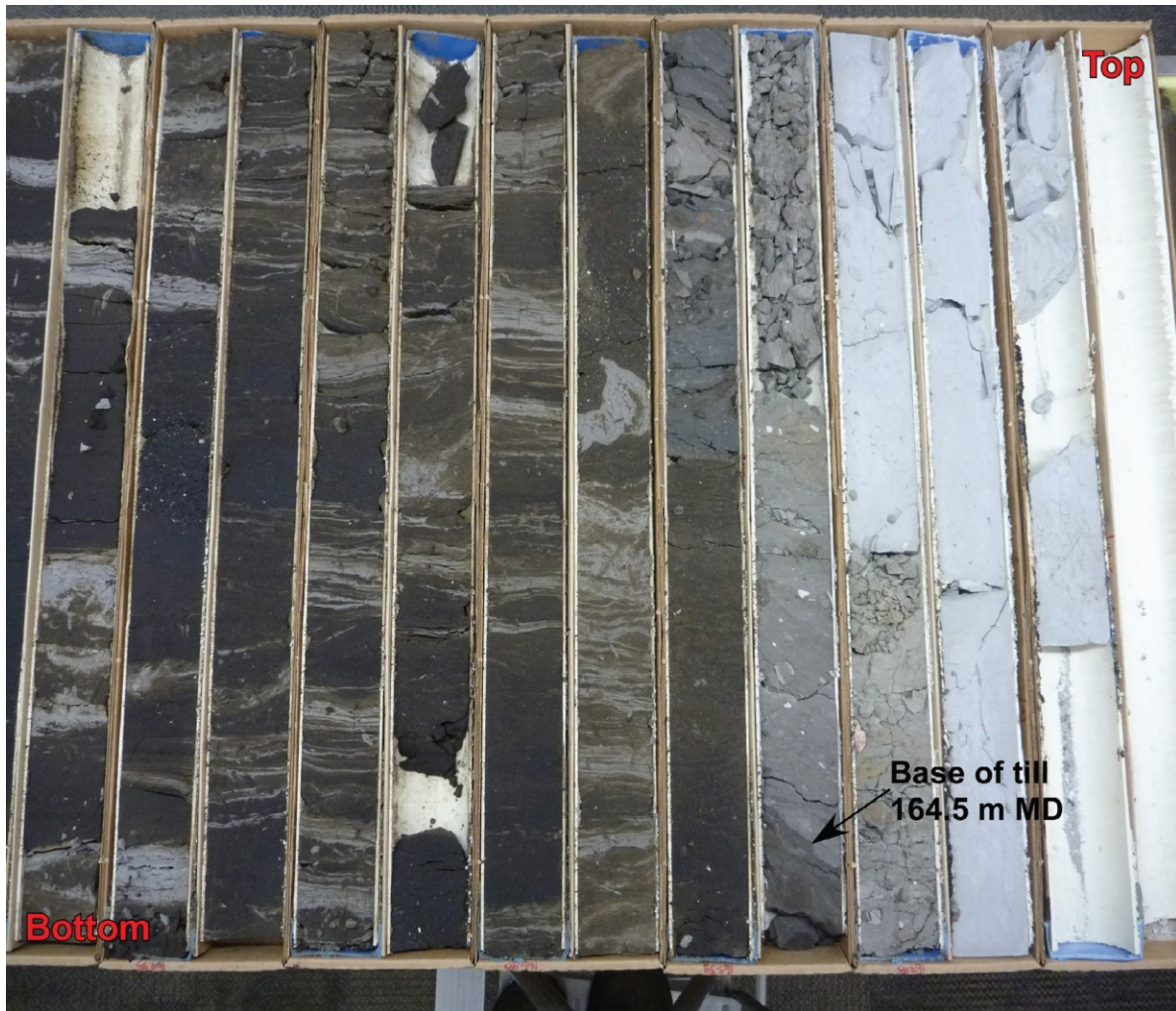
Figure 2-3.   Core image of bitumen-bearing McMurray Formation and overlying sediments in the Well AA/10-25-095-04W4/0; depth from 162.9-169.8 m. (Retrieved from Alberta Energy Regulator 2014).
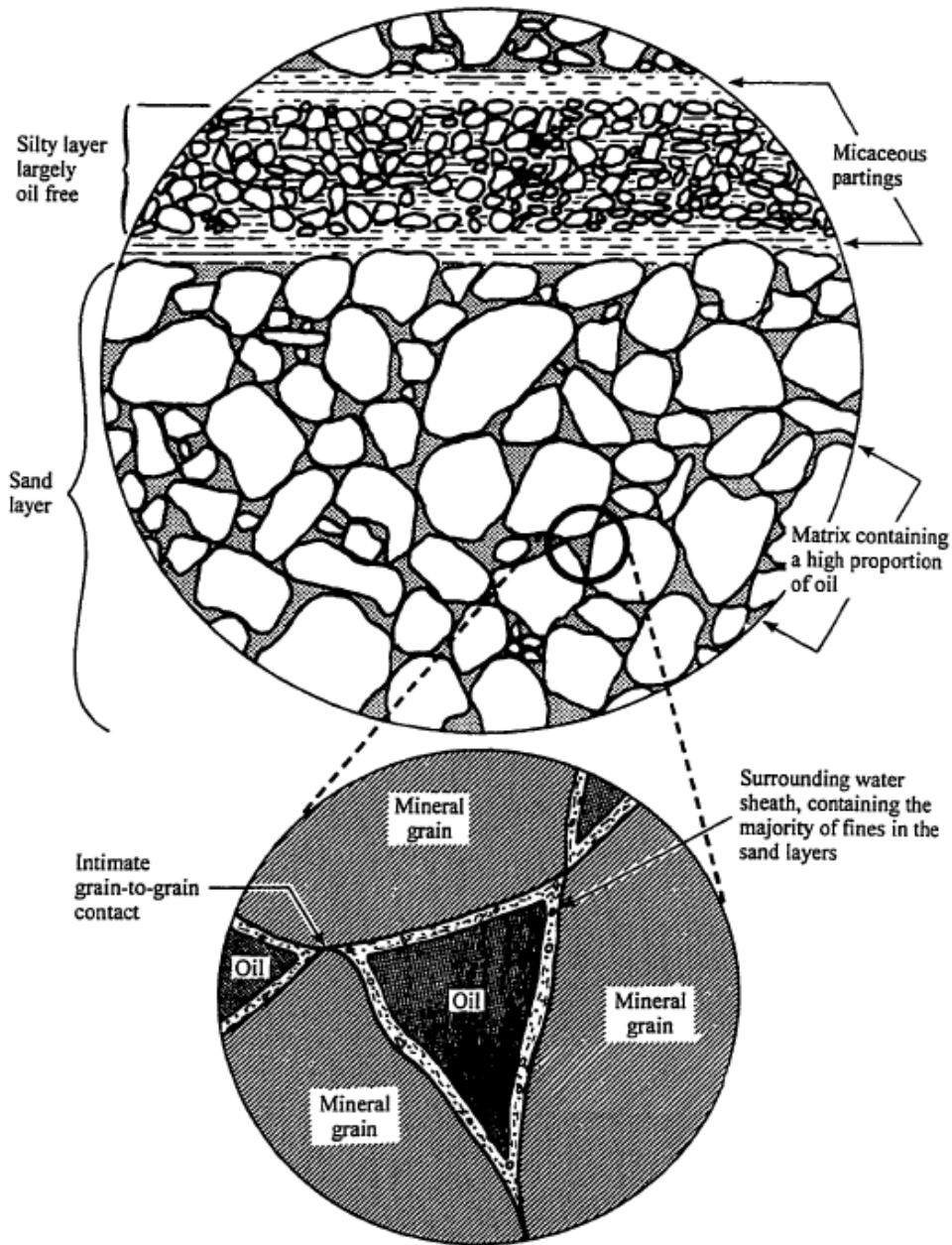
Figure 2-4.   In situ structure of oil sands (Retrieved from Dusseault 1977). Bitumen saturated sand layer and oil-free silty layer occupy the main portion of oil sands in the microscopic scale

Dusseault (1977) showed that the Athabasca oil sands have a stiff structure if undisturbed, usually accompanied by a large degree of dilation when loaded to failure and therefore has higher frictional strengths compared to dense sand. The geological history and quartzose mineralogy are believed to be the main reason for the unique fabric of oil sands. Dusseault (1977) used optical and scanning

13

electron microscopy to observe the intergranular fabric of oil sands and found an interlocked texture characterized by a relatively high incidence of long and interpenetrative grain contacts. For the McMurray oil sands, tangential, straight and interpenetrative contacts are three main types of intergranular contacts (Dusseault and Morgenstern 1978). Figure 2-5 illustrates the environmental scanning electron microscopy (SEM) images of original and solvent extracted oil sands, where the interlocked structure of oil sands are clearly visible. The reservoir-geomechanics properties of oil sand, such as deformation-failure behavior and permeability, are not only determined by density and void ratio but also strongly dependent on the structure and fabric of oil sands.

In most numerical reservoir engineering investigations on oil sands, sand and shale facies are widely used in the models as they have distinct flow response due to their large discrepancy in permeability. The simple bi-model assumption (sand and shale facies) has been confirmed to be efficient for decision making in reservoir engineering. In this study, sand and shale facies are adopted in our spatial variated models for oil sands. The volume fraction, spatial ranges and inclination of shale beddings are used to characterize the level of heterogeneity for oil sands. The modes of failure of oil sands are found to be sensitive to volume fraction and spatial variability of shale in Chapter 3. The shear failures in the oil sands break the interlocked structure and create high-permeability flow channels which significantly increase the permeability as demonstrated in Chapter 4.

a) Original oil sands (250 micros)
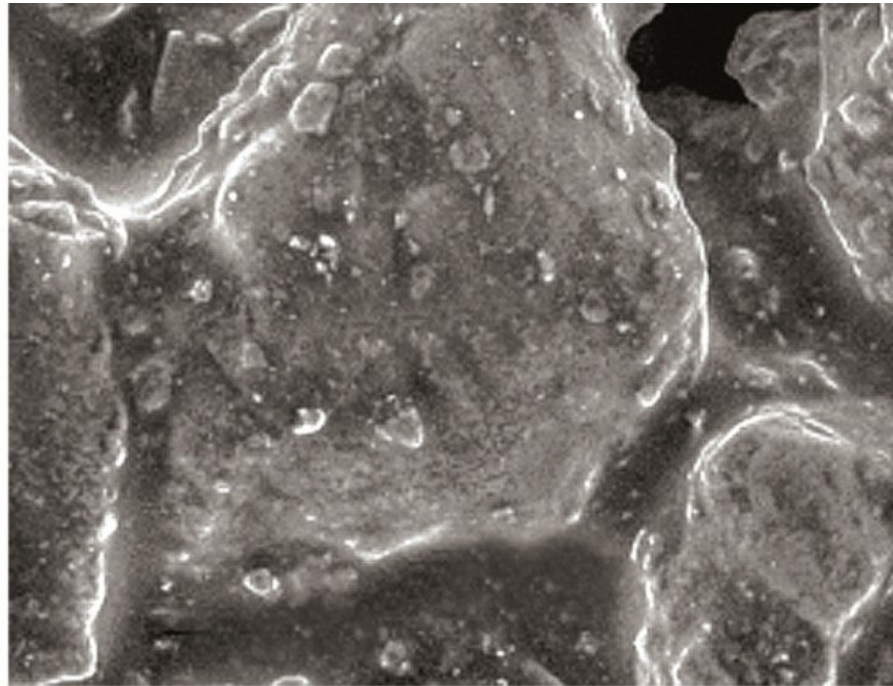
b) Solvent extracted oil sands (250 micros)
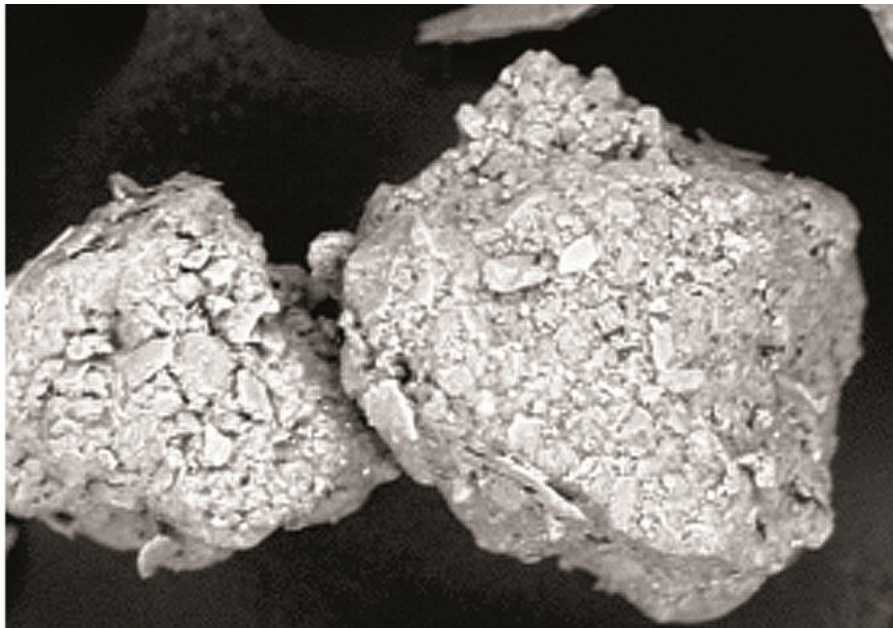
Figure 2-5.   Environmental scanning electron microscopy image of a) original and b) solvent extracted oil sands by the Institute for oil sands innovation at the University of Alberta (Retrieved from Natural Resources Canada 2018).

2.1.2 Stress-paths in SAGD

For oil sands below economical open pit mining depths (65 m), in-situ methods are used, including SAGD, CSS, ISC and vapor extraction process (VAPEX). The key to in-situ methods is to decrease the viscosity hence increase the mobility of bitumen. CSS is the second most applied thermal method in Alberta oil sands providing quick payout in first few cycles. The impact of reservoir-geomechanics on CSS may be even more important than SAGD as: 1) Higher injection pressure (>1 MPa) and temperature; 2) Dramatic effective stress changes during the transition of huff and puff periods.

Currently, SAGD is the most widely used technique for bitumen recovery. During SAGD, hot steam (200 °C) is continuously injected into the reservoir at a higher pressure than the initial reservoir pore pressure. The latent heat of the steam warms up the cold oil sands and reduces bitumen viscosity. When the connectivity between the horizontal injection and production wells is established, the mobile bitumen gradually flows to the production well due to gravity drainage.

Due to the high pressure and temperature in the reservoir, deformations occur and change the permeability of oil sands. The geomechanical behavior of oil sands in the Athabasca McMurray Formation and Cold Lake Clearwater Formation were studied thoroughly since the 1970s, and it has been confirmed that the stress-strain responses of oil sands are stress-path dependent. Chalaturnyk (1996) concluded that two predominant stress paths control the geomechanical response in the initialization and production stage based on investigations in the UTF (Underground Testing Facility) project (Figure 2-6).
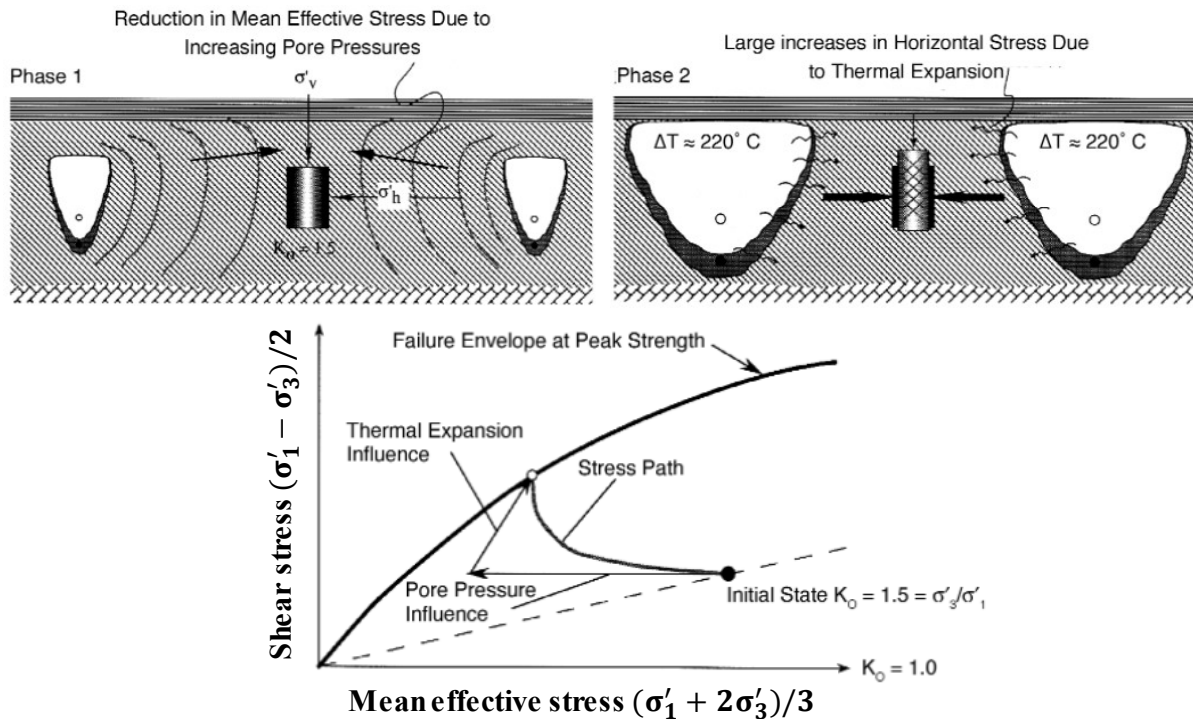
Figure 2-6. Two predominant stress paths during SAGD (Retrieved from Chalaturnyk 1996). Phase 1 is the initial stage when a reduction in mean effective stress dominates. Thermal expansion plays a key role in phase 2 when the steam chamber has built up.

The first predominant stress path is the reduction in mean effective stress due to the increasing pore pressure. Thus, there is a horizontal stress path in p-q space because pore pressure increases result in equal reductions of σ_1' and σ_3'. Unloading of the sand grains and reservoir matrix occurs because the effective stress is decreased by the same amount in all directions within the steam chamber. The oil sand grains become less packed; however, the relative position of grains does change compared to the state before unloading. The isotropic unloading process in SAGD is usually elastic and reversible when steam injection stops and effective stress returns to its original value.

The second stress path is a large increase in horizontal stress following the injection stage. The thermal expansion of sand grains, reservoir matrix and pore fluid within the developing steam

chamber initiate a stress path where the shear stress and mean effective stress increase simultaneously.

The volumetric thermal expansion coefficient α is defined in Equation 2-1.

$$\alpha = \frac{1}{V}\left(\frac{\partial V}{\partial T}\right),$$

Equation 2-1

Thermal expansion in the high-temperature steam chamber front creates a large thermal stress normal to the chamber edge, e.g. horizontal thermal stress for a vertical chamber edge. The thermal stress due to volumetric thermal expansion can be calculated by Equation 2-2.

$$\sigma_T = -E\,\alpha\,\Delta T$$

Equation 2-2

where E is Young's modulus for in-situ oil sands, ΔT is the change of temperature after the steam front passes.

The shearing process causes plastic deformation where the interlocked structure of oil sands changes and causes large changes in reservoir properties. For shallow-depth reservoirs, vertical total stress change is usually negligible but the impact of vertical total stress changes in deep reservoirs needs to be considered carefully. Chalaturnyk and Li (2006) investigated the role of geomechanics in SAGD operations at different depths and found it is difficult to be conclusive about specific geomechanical processes relative to the multiphase characteristics of SAGD. The evolutions of shear-induced volume changes are sensitive to the initial stress state and injection pressure.

For the SAGD process, the deformation response along this stress path is of primary interest because of the impact on porosity, absolute permeability and relative water permeability. If only thermal expansion is considered, the stress-path follows path 1 (Figure 2-7), which is similar to a conventional drained triaxial compression test. For deep reservoirs, the thermal stress is larger due

to higher in-situ Young's modulus (Equation 2-2), so the stress path is close to path 2. For shallow reservoirs, the influence of pore pressure change becomes more significant due to the decrease in thermal stress. To analyze the deformation response and permeability change during SAGD, the experimental regime ideally should include following all possible stress paths.
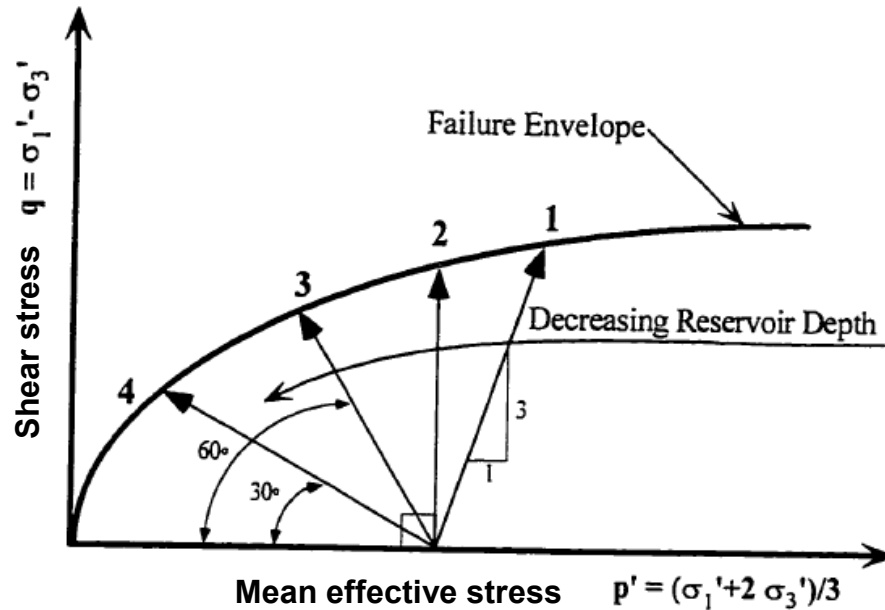
Figure 2-7.   Possible stress paths at different reservoir depth during the SAGD process (Retrieved from Touhidi-Baghini 1998).

2.1.3   Geomechanical Response of Oil Sands in Lab Experiments

The geomechanical response of oil sands has been of interest since the early work conducted by Dusseault (Dusseault 1977; Dusseault and Morgenstern 1978, 1979). The observed geomechanical characteristics of locked sands can be summarized as zero to low cohesion, a large degree of dilation when loaded to failure, high peak strength, steeply curved failure envelopes and small strain to failure in shear tests.

With an increasing interest in thermal recovery for oil sands in the early 1980s, Agar (1984, 1985)

investigated the influence of elevated temperature and pressure on geomechanical properties and

observed a proportional decrease of shear strength of oil sands with an increase in pore pressure

and temperature. The peak friction angle of oil sands is systematically higher compared to Ottawa

dense sand due to the enhanced frictional strength of the interlocked fabric of oil sands illustrated

(Figure 2-8).
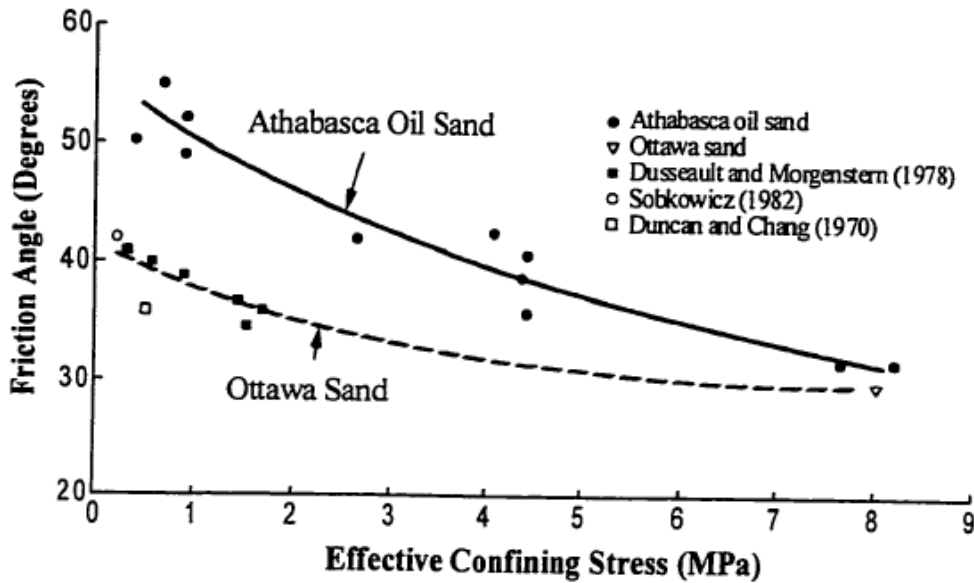
Figure 2-8.   Comparison of shear strengths of Athabasca oil sand and dense Ottawa sand
(Retrieved from Agar 1985).

Plewes (1987) studied the undrained strength of Athabasca oil and determined a critical confining

stress above which the volume contracts at 7.3 MPa. The undrained deformation modulus was

observed to be less than one-third of the drained modulus, which indicates larger strains due to

pore pressure increase in SAGD.

Kosar (1989) examined the influence of stress paths and observed that interbedded shale had a significant impact on the stress-strain behavior and shear strength of the Athabasca and Cold Lake oil sands. The thermal stresses of rich oil sands usually increase during drained heating due to a positive thermal expansion coefficient, while the stresses and strains of oil sands mixed with shale may increase or decrease due to the impact of interbedded shale seams. The presence of shale bedding planes in oil sands results in a significant decrease in shear strength compared to rich and low fines oil sands.

Chalaturnyk (1996) combined consolidated drained compression test results with previous experimental results to develop the most suitable peak failure envelope for rich and low fines Athabasca oil sands. Linear and nonlinear Mohr-Coulomb failure envelopes are fit to the experimental data (Figure 2-9). For the linear failure envelope, the peak friction angle is 60° and cohesion is 0. The residual friction angle is estimated at 34° from the lowest data points in p'-q space. Chalaturnyk also proposes an exponential correlation of Young's modulus based on the confining stress to characterize the stiffness of rich oil sands at various confining stress (Figure 2-10).

To summarize, rich oil sands have a relatively high friction angle (60°) and zero cohesion. Shear dilatancy is widely observed when oil sands are loaded to failure. The interbedded shale planes tend to have a significant impact on the strength and stress-strain behavior of oil sands at elevated temperature and pressure. Thus, the in-situ stress path and appropriate confining stress should be considered carefully to select the appropriate geomechanical models of oil sands.
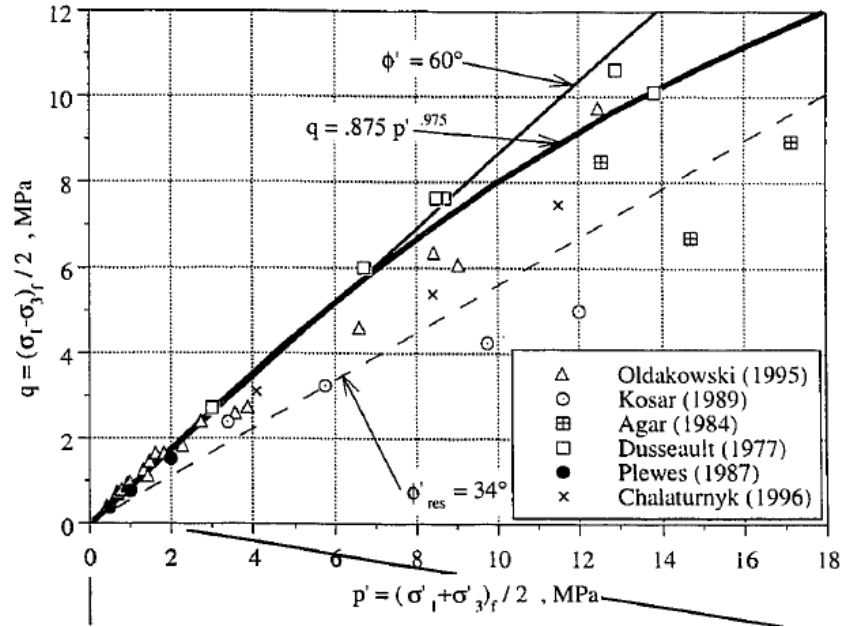
Figure 2-9.　Peak failure envelope of Athabasca oil sands fit by Chalaturnyk (1996).
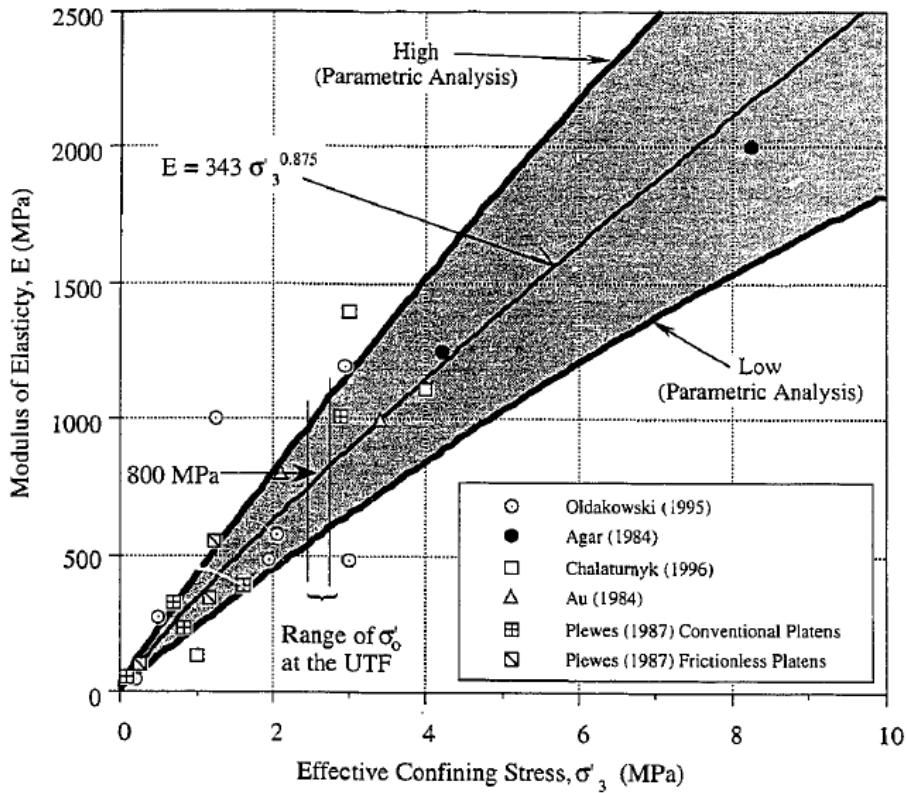
Figure 2-10.　Variation of Young's modulus with effective confining stress for McMurray Formation oil sands characterized by Chalaturnyk (1996).

22

2.1.4 Permeability Change Due to Deformation

Elastic deformation results in pore volume changes which change porosity and permeability. When plastic deformations occur, the pore structure changes as sand grains rotate and break down generating new preferred flow paths which increases permeability.

Mori and Tamura (1986) investigated the relationship between permeability and dilatancy of oil sands in triaxial compression tests of medium-dense sand stabilized by silicate and acrylamide grout. When the specimen is in contraction at the beginning of the triaxial shear, the measured permeability does not change which indicates the effect of pore structure change and volume contraction balance. When the axial strain increases to more than 2% at the beginning of dilation, the permeability increases because of the development of new flow channels. For silicate grouted sand with the same stiffness as oil sands, a two order of magnitude increase in permeability is measured at peak strength (Figure 2-11). For acrylamide grouted sand which is similar to soft rubber and more easily restored its original shape, no significant permeability change is observed. This is another indication that plastic deformation tends to alter permeability more significantly than elastic deformations.
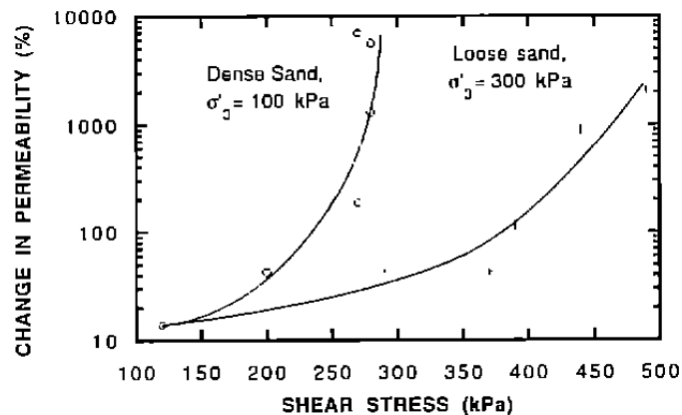
Figure 2-11   Permeability variations during drained triaxial shear of silicate grouted sand. (Retrieved from Mori and Tamura 1986).

23

A series of triaxial tests have been conducted by researchers in Alberta to investigate the impact of deformation on permeability. To mimic the stress paths in SAGD, two different boundary conditions, isotropic unloading and triaxial shear tests, are applied by Oldakowski (1994) for Athabasca McMurray Formation oil sands and Scott (1994) for Cold Lake oil sands. It is observed that absolute permeability change is a strong function of pore volume change under both isotropic and shear loading conditions.

For isotropic unloading of intact and reconstituted specimens of Athabasca McMurray Formation, Oldakowski (1994) observed that the absolute permeability increase varies from 13% to 70% for an average increase of 1.4% volume change in isotropic unloading; while there is a 46% decrease for a specimen contracting by 2%. Scott et al. (1994) found that the permeability change of Cold Lake oil sands during isotropic unloading is not as significant as high porosity sand because it is a strong function of the degree of unloading, initial porosity and stress path. Li and Chalaturnyk (2006) summarized Oldakowski and Scott's experimental results on permeability increase with increasing volumetric strain in isotropic unloading (Figure 2-12). For the same volumetric strain, a lower initial permeability (< 1 μm^2) results in a larger permeability increase. The maximum increase in permeability is 70% for Sn-5 at 1.2% volumetric strain. The permeability ratio is always within 1.2 for cores with initial permeability larger than 1 μm^2.
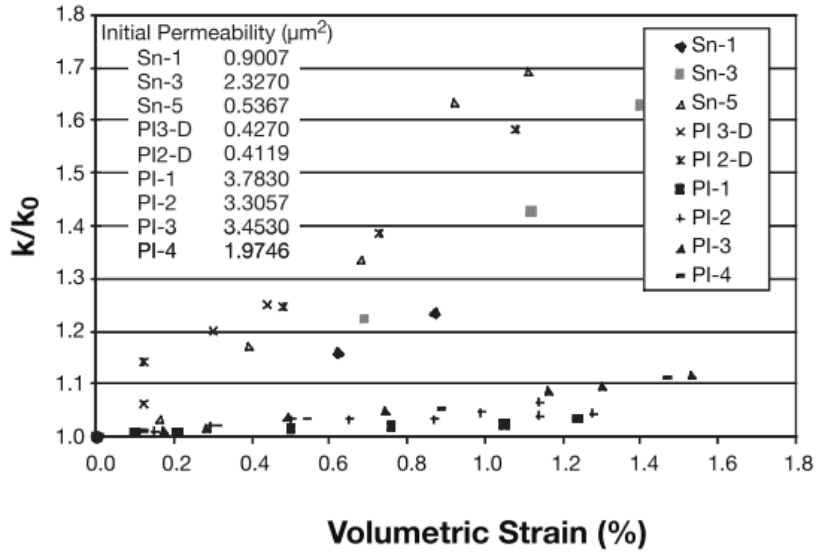
Figure 2-12. Absolute permeability ratio versus volumetric strain (Retrieved from Li and Chalaturnyk 2006a).

Scott et al. (1994) found that the volume and permeability in oil sands during triaxial compression or anisotropic unloading are strong functions of the average mean effective stresses. At low isotropic effective stress (<1 MPa), the permeability of Cold Lake oil sands increases during shear. However, it can be observed that most of the triaxial tests of oil sands were conducted at relatively high confining stress (>1.0 MPa) in Figure 2-9. The permeability change of Athabasca oil sands due to shearing at low confining stress remained unknown until Touhidi-Baghini (1998). Bitumen-free outcrop specimens from the McMurray Formation were used to avoid the potential sample disturbance during coring and the influence of bitumen extraction on oil sands structure. During triaxial shear tests (σ_3'=250kPa) following stress path 4 (Figure 2-7), the volumetric strain decreases due to contraction until peak and then increases because of shear dilatancy (Figure 2-13). The absolute permeability ratio is almost constant during the contraction but increases dramatically (up to 6 times) during dilation. This experiment clearly demonstrates that plastic deformation is

the dominant source of permeability enhancement compared to elastic deformation which is consistent with Mori and Tamura's (1996) triaxial compression tests on medium-dense sand.

According to Oldakowski (1994), effective permeability to water in bitumen saturated specimens shows a dramatic response. During the isotropic unloading process, effective permeability to water increased by 500% after an increase in a sample volume of 1.6%. The effective permeability to water caused by shear dilation could be more than 1000 times with only 6% volume change. The shearing process induces significant enhancement of absolute permeability and effective permeability to water compared to isotropic unloading. During the isotropic unloading process, the relative position and contacts of grains remain the same due to elastic deformation. The permeability increase is a result of the expanded pore volume. However, plastic shear failures during shearing completely change the original interlocked structure and create flow channels, which significantly change the pore space and tortuosity of oil sands.

When the scale increase from lab scale to field scale, the permeability change due to deformation and failure plays an important role in SAGD. Isotropic unloading occurs near the chamber front where effective mean stresses drop dramatically due to pore pressure change. The shear failures can be predominantly found around the interface between the drained and partially drained zone in SAGD (Li 2006).

Evidence of shear failures in oil sands can be found in both laboratory shear tests and field observations. Samieh and Wong (1997) investigated deformations of Athabasca oil sands at low effective stresses (50 kPa to 750 kPa) in triaxial compression tests. Lower-density shear planes with higher porosity and absolute permeability were observed in a sequence of computer-aided tomography (CAT) scan slices through the core. According to the field observations of heat transfer during SAGD by Birrell (2001) and Ito et al. (2000), high permeability shear planes

formed ahead of steam chambers allowing hot fluids to enter the cold oil sands. The sudden increase of temperatures profile for thermocouples away from injector and producer wells indicates that existing shear planes are being reactivated or new shear planes are being created. Collins (2007) proposed that the optimum injection pressure during well-pair start-up should be sufficiently high to trigger shear failures in oil sands between the injector and producer wells to accelerate interval heating by convective heat flux. However, as the steam chamber approaches the caprock, the injection pressure should be gradually reduced and kept within 500 kPa of the fracture pressure to avoid caprock failure. For the cold regions of the reservoir ahead of the growing chamber, an increase in absolute permeability of 30% to 50% may occur due to shear failures (Chalaturnyk 1996).
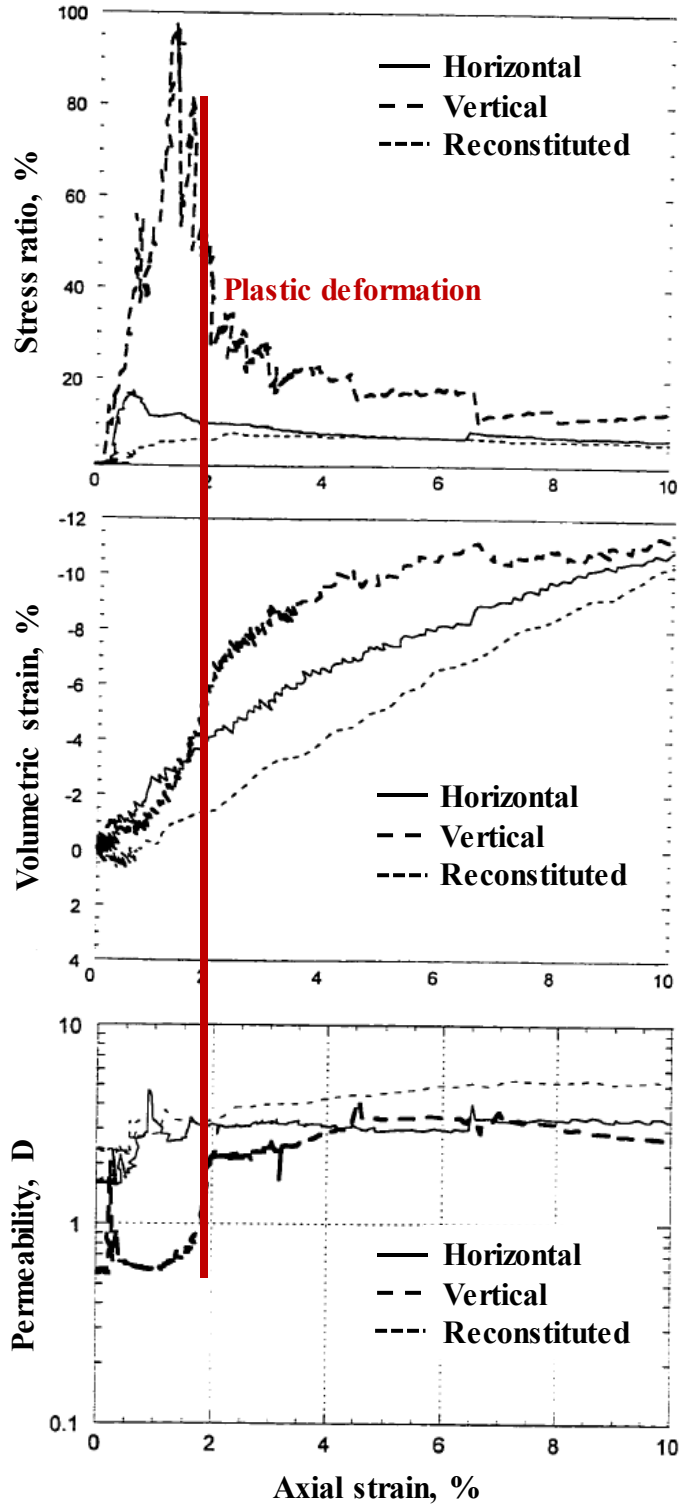
Figure 2-13.   Stress-strain behavior and permeability change during triaxial compression tests when confining stress is 250 kPa (Modified from Touhidi-Baghini 1998). The red line labels the dramatical changes of permeability after peak in stress-strain response.

2.1.5 Importance of Geomechanics in SAGD

The first impact of geomechanics on SAGD is the change in porosity because many reservoir properties, such as pressure, saturation and permeability, are directly related to porosity. During the injection stage of SAGD, the increase in pore pressure causes effective stress to decrease in the reservoir leading to the movement of sand grains. The porosity increases as the void ratio of oil sands become larger. When steam chamber grows, thermal expansion leads to shearing of oil sands, which significantly changes the pore geometry with sand grains rotating or even breaking down. The Alberta oil sand reservoirs are shallow, so the porosity is expected to increase with shear dilation of oil sands during the production period of SAGD process.

Absolute permeability of oil sands increases during shearing because the pore volume expands, and the tortuosity of flow decreases. A series of lab experiments by Touhidi-Baghini (1998) have been conducted to characterize the impact of deformations on absolute permeability and demonstrate that more attention should be focused on the plastics failures in the reservoir during SAGD.

The increase in effective water permeability creates a larger mobility contrast between water and bitumen, which also affects the saturation distribution of oil sands in or close to the steam chamber. When deformations occur, water quickly occupies the extra pore space and water saturation increases. Thus, the oil saturation in situ reduces although the volume of oil remains constant, leading to a further increase of effective permeability to water.

Given the importance of geomechanical response on both the production performance and caprock integrity, coupled reservoir-geomechanics simulation is recommended to provide a more comprehensive understanding of SAGD (Chalaturnyk and Li 2004 and Collins 2007).

29

2.2 Coupled Thermal-Flow-Geomechanics Simulation

2.2.1 Classifications and Comparisons of Coupling Techniques

Most reservoir parameters, e.g. porosity, absolute/relative permeability, saturation, capillary pressure, are influenced by deformations during SAGD as explained in Section 2.1.5. Conventional reservoir simulations focus on multiphase flow response in porous media but often ignores the impact of deformation on flow response. Elastic rock compressibility is widely used and kept constant in simulations to characterize the volume change caused by pressure variations, which is not appropriate for oil sands (Li et al. 2004). To fully consider the interactions between flow and geomechanical response, coupled thermal-flow-geomechanics simulation has been developed for thermal recovery on bitumen.

There are four approaches for coupling flow and geomechanics: fully coupling; sequentially coupling; explicit coupling and pseudo coupling approach. The characteristics of coupling methods are summarized by Tran et al. (2004, 2005) and Kim et al. (2011). These four types of coupling are explained and compared based on the robustness of results, convergence difficulty and simulation efficiency.

In fully coupling, the entire system is discretized on one grid, and the governing equations of flow and geomechanics are solved simultaneously at each timestep. The development of a fully coupled 3D thermal-flow-geomechanics full-field simulator is complex and requires extensive validation of the self-developed code. In terms of convergence, fully coupling is unconditionally stable but can be very computationally expensive for the SAGD process in oil sand reservoir following nonlinear geomechanical models (Kim et al. 2011).

Sequentially coupling, sometimes termed as iterative coupling, solves the equations of flow and geomechanics separately. The main difference compared to fully coupling is that the key parameters (pressure, temperature, strain) are passed back and forth between the reservoir and geomechanics simulators. Usually, the mechanical models are solved first until equilibrium at an initial temperature and pressure. Then the output strain or displacement information is used to update the flow parameters (porosity, permeability and capillary function). The updated flow parameters are used as the input for the next time step in flow simulation. This sequential coupling loop is repeated for each coupling step, where iterations are required for the flow and geomechanical solutions to converge to an acceptable tolerance. For each time step, the sequentially coupling method is expected to have identical solutions compared to the fully coupled method if discretization schemes are the same for the reservoir and geomechanical model. The main advantage of sequential coupling is the flexibility and convenience because users can pick any separate well-established reservoir and geomechanical simulators with its own advanced functionality.

Taking the RGRG coupling platform as an example, CMG and Itasca software packages are sequentially coupled. For SAGD, the two finite-difference codes are coupled together: STARS (© CMG) is used from thermal simulation while FLAC3D (© Itasca) is chosen for geomechanical simulation. When phase behavior in flow response becomes crucial, GEM (© CMG) is selected as it has been tested and confirmed to be efficient in compositional simulation. For reservoir models built with discrete fracture networks (DFN), 3DEC (© Itasca) is used for the geomechanical module as this discrete element code has been designed to solve mechanical problems with DFN. Another advantage brought by sequential coupling is the flexibility of model size in the reservoir and geomechanical model. For SAGD, the reservoir model is often limited to the McMurray

Formation for Alberta oil sands. The geomechanical models are larger, as they include overburden (Clearwater Formation) and underburden (Devonian Formation) to provide realistic stress and strain boundary conditions.

The converge efficiency of sequentially coupling methods is debatable. Kim et al. (2011) considered sequentially coupling (e.g. Newton-Raphson) to be more efficient in nonlinear problems; while Tran et al. (2004) demonstrated that the main disadvantage of sequential coupling is that the solution may not be accurate and have poor converge when the compressibility varies significantly with pressure or temperature change. Tran et al. (2004, 2005) propose a new porosity function based on pressure, temperature and mean total stress to improve accuracy and reduce the number of iterations in sequentially coupling, which enables the application of sequentially coupling model to full-field studies. Garipov et al. (2018) presented a coupled thermal-compositional-mechanics framework which includes a fully implicit and sequentially implicit approach. In the application in waterflooding process, the sequentially implicit approach usually performs well for stiffer reservoirs with a higher Young's modulus multiplier. With a decrease in Young's modulus multiplier, the sequentially implicit approach is more sensitive, which may increase simulation time substantially for single-phase flow models or non-linear plastic geomechanical models.

Explicit coupling, sometimes refers to one-way coupling, is a special case of sequential coupling. The information obtained by the flow simulator is only transferred to the geomechanics module but not sent back to the reservoir simulation. Changes in the pressure and temperature induce changes in stresses and strains, but the changes in the stress and strain fields do not influence porosity and permeability. Explicit coupling is usually applied to gas reservoirs where the mass balance is mainly controlled by the gas pressure rather than the stress of solids.

In pseudo coupling, the reservoir simulator updates porosity and absolute permeability through an empirical model as a function of pressure. The CPU time is usually smaller since geomechanical simulations are not conducted during coupling. This provides an estimate of reservoir compaction where rigorous geomechanical simulations are not necessary.

2.2.2 Development of Thermal-Flow-Geomechanics Simulation

The advantages and disadvantages of the previous thermal-flow-geomechanics simulation are discussed here for the reader's reference. With the improvements in the coupling logistic and understanding of reservoir-geomechanics, the RGRG coupling platform is considered as the best option available for this research.

Tortike and Farouq (1993) proposed the first fully coupled reservoir-geomechanics model of CSS in an elasto-plastic formation. Assuming incompressible solid grains, the porosity change of oil sands can be calculated based on the volumetric strain:

$$\Phi = (\Phi_o + \varepsilon_v - (1 - \Phi_o)\alpha(T - T_o))/(1 + \varepsilon_v) \, , \qquad \text{Equation 2-3}$$

where Φ_o is the original porosity, ε_v is the volumetric strain, α is the volumetric thermal expansion coefficient of the solids, T and T_o are the current and original temperature under reservoir condition. The porosity updating function in Equation 2-3 and the Kozeny-Carman equation are combined to obtain the permeability updating function which is based on porosity and volume change. This may cause erroneous predictions when shear failures create massive new flow paths in the reservoir.

Fung et al. (1994) proposed a numerical model coupled with CMG STARS for the solution of elasto-plastic deformation and multiphase, thermal flow in unconsolidated oil sand reservoirs. A finite element incremental plasticity model with Mohr-Coulomb and Drucker-Prager as the yield

criteria are used to determine the state (elastic/plastic) of the grid. The volume change is calculated by the plasticity model, whereas the permeability increase is related to the volume change via tabular data. Because plastic deformation can produce substantial permeability changes to the shear dilated grid block, an additional set of relative permeability curves are used to represent the enhanced flow paths generated by shear failures. The flow across the grid with plastic deformation is calculated as the combined flow through the shear planes and the undisturbed original rock matrix. The implementation of the coupling technique in a CSS case study demonstrated the importance of elastic and plastic deformations on production performance.

Adopted from the early work of Settari (1988), Settari and Mourits (1998) proposed coupling of a commercial reservoir simulator with a 3D finite element stress code and a fracture-propagation model. The widely used porosity updating function in petroleum society is used and will be updated during the coupled simulation.

$$\Phi^* = \Phi_o[1 + c_p(p - p_o) - c_T(T - T_o)] \,, \hspace{3cm} \text{Equation 2-4}$$

where c_p and c_T are rock compressibility based on pressure and temperature. The updating function for c_p and c_T based on rock deformations are:

$$c_p = \frac{\Phi_n(c_b - c_s) + c_\phi(1 - \varepsilon_v)]}{\Phi_o} \,, \hspace{3cm} \text{Equation 2-5}$$

$$c_T = -\frac{\Phi_n}{\Phi_o}\alpha \,, \hspace{3cm} \text{Equation 2-6}$$

where c_b and c_s are bulk and solid compressibility. α is the volumetric thermal expansion coefficient. Updated permeability is calculated from the hysteresis curve as a function of minimum or mean effective stress. The proposed sequentially coupling method could handle poroelastic

geomechanical models with up to 20,000 to 30,000 grids by 1998; however it still provides insights on the reservoir-geomechanics simulation.

Settari and Walters (2001) extended the coupling technique for modeling pressure-induced compactions in full-field studies with complex, realistic descriptions of the geomechanical behavior of the reservoir. Settari et al. (2001) showed the potential of their coupled modeling becoming a comprehensive tool for integrated reservoir analysis and management in several field applications to provide a better understanding of recovery mechanisms or even significantly change the economic evaluation of the project.

For the SAGD process, Chalaturnyk (1996) conducted a 2D uncoupled reservoir-geomechanics simulation to demonstrate the geomechanical response of SAGD for the UTF Phase A project. Chalaturnyk and Li (2004) investigate the importance of geomechanics on SAGD for reservoirs at different depths with one-way coupled simulation. Two well-established simulators, EXOTHERM for reservoir simulation and FLAC for geomechanical simulation, are sequentially coupled to characterize the fluid flow and geomechanical response in SAGD by Li et al. (2006). Li and Chalaturnyk (2009) successfully applied the proposed 2D coupled reservoir-geomechanics simulation to history matching the UTF Phase A project. They recommended developing comprehensive 3D coupled reservoir-geomechanics simulation to history match especially when heterogeneity leads to a non-uniform steam chamber.

Du and Wong (2007) develop a coupled finite element model that incorporates the full strain-induced permeability tensor to gain insight into the reservoir response to temperature and pore pressure changes. The coupled finite element code solves the governing equations in a consistent manner so that the full permeability tensor can be used in a simulator. However, challenges remain for most reservoir simulators as diagonal tensors (orthotropic) are usually assumed. A coupled

geomechanics-thermal reservoir simulation for the UTF Phase A SAGD project is conducted and shows that the anisotropic deformations lead to a 22.5% increase in major principal permeability and a 9.0% increase in the minor principal permeability. The predicted horizontal displacements have an unacceptable error compared to measured field data because the impact of heterogeneity on the geomechanical simulation is not considered correctly.

Wang et al. (2009) developed a fully coupled approach for thermal reservoir modeling with large volume changes and induced stresses. A finite element method is adopted for the reservoir and the surrounding thermally affected zone together with a displacement discontinuity method used for the surrounding elastic and non-thermal zone. It can provide stress and displacements around the reservoir without introducing extra grids outside the FEM zone which reduces the simulation time for the over, under and side burden. The application in full-field reservoir-geomechanics model still requires further investigation.

Azad and Chalaturnyk (2011) developed a 2D sequentially coupling code integrating the widely used finite-difference flow simulator for thermal methods (CMG, STARS) and the geomechanical finite-difference module for continuity (Itasca, FLAC). Three 2D homogeneous models with different depth, in-situ stress regime and injection pressures, classified as a shallow, medium and deep reservoir, are tested in the coupled reservoir-geomechanics simulation to demonstrate the importance of geomechanics for different reservoir conditions. For simplicity, an elastic perfectly plastic model was selected as the constitutive model for the reservoir layer. The simulation results show that reservoir performance improvement of SAGD is more pronounced for shallow reservoirs. The horizontal stress arrangements have negligible influence on oil production and steam injection, but the reservoir deformation and surface heave depend on the direction of maximum horizontal stress. For the homogeneous models applied, more plastic deformations are

36

observed in zones near the bottom and top of the reservoir due to the distinct flow, geomechanical and thermal properties of the overburden, reservoir and underburden. Although limited to 2D, this sequential coupling technique can be easily applied with existing reservoir and geomechanical simulators.

Garipov et al. (2015) employed a fully implicit approach solving the mass, energy and momentum conservation equations simultaneously on an unstructured grid. Elasto-plastic behavior is assumed for the skeleton with a thermal-compositional formulation used to describe the multi-component multiphase flow of mass and heat. A mixed finite-volume approximation for flow and a Galerkin finite-element approximation for geomechanics are used for the quasi-static Drucker-Prager plasticity model. The computational framework is implemented in the Automatic-Differentiation General Purpose Research Simulator. Garipov et al. (2016) extended the discrete fracture model in the proposed fully coupled method and applied it to a shale-gas synthetic reservoir with 100 natural fractures.

However, the common practice of coupled reservoir-geomechanics simulation has limitations: 1) capability to be applied in 3D full-field model with the heterogeneous flow and geomechanical properties; 2) updating porosity and absolute permeability tensors based on elasto-plastic deformations; 3) the complex interactions between multiphase flow and non-linear geomechanical response with different appropriate constitutive models. To address these issues, Deisman and Juncal (2018) developed a sequential coupling platform combining the widely used CMG and Itasca software.

For the SAGD process, STARS and FLAC3D are sequentially coupled to deal with the deformation response and induced permeability change caused by pore pressure changes and thermal expansions. STARS is a finite-difference reservoir simulator developed for modeling of

the thermal recovery processes; while FLAC3D is a finite-difference geomechanical simulator developed by Itasca for fast simulation of nonlinear mechanical behavior in continua. Combing these two well-established finite-difference simulators, the non-linear geomechanical response caused by shear failures of oil sands can be accurately modeled by FLAC3D and linked with reservoir simulation in CMG by updating porosity and permeability in each coupling step.

Figure 2-14 presents the schematic for the coupled reservoir-geomechanics simulation for SAGD processes. For each coupled step, the outputs of pore pressure and temperature from STARS are passed to FLAC3D to compute the corresponding stress and strain response. Because the geomechanical properties are a function of confining stress and plastic shear strain (Chalaturnyk 1996; Li and Chalaturnyk 2005), they are updated and input back to FLAC3D to obtain the updated stress-strain behavior until the new geomechanical model reaches equilibrium (unbalanced force becomes negligible). The updated total and plastic shear strain are input to the porosity and permeability function to calculate the new porosity and permeability for flow simulations in STARS. This sequentially coupled routine is applied only for user-defined coupling steps. If each time step is selected as a coupling step, the results are identical to fully coupled simulations. However, it will be overly computational expensive to couple every time step. Depending on the size of the model and accuracy requirement, the user should balance between the simulation speed and accuracy. Generally, for a reservoir scale case of a well pad in the SAGD pilot (1000 by 1000 by 200 m), it is suggested to set the coupling step every 100 days during the production period.
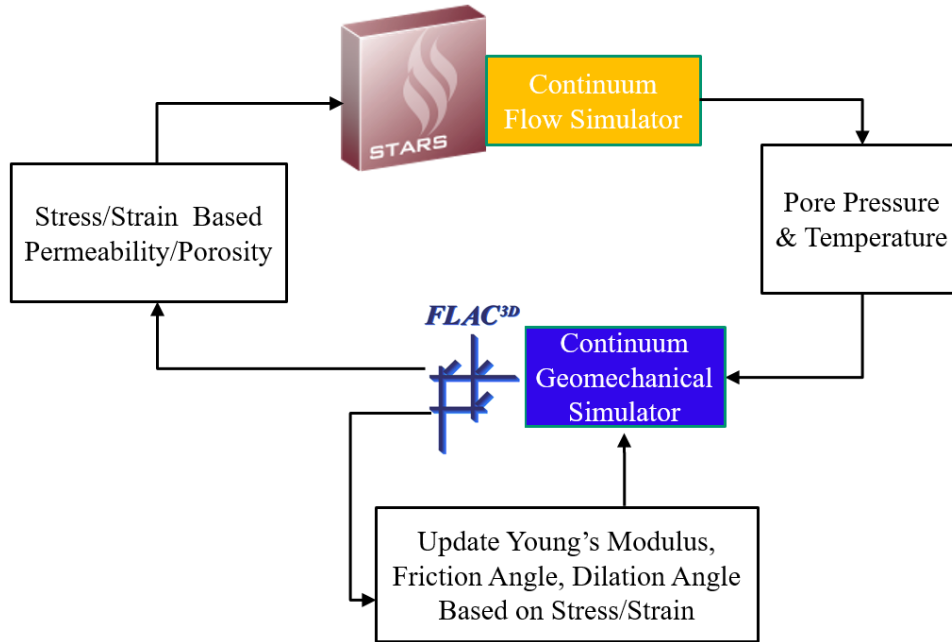
Figure 2-14.   Schematic for sequentially coupled reservoir-geomechanics simulation of the SAGD process.

2.3   Impact of Heterogeneity on Reservoir-Geomechanics

Heterogeneity includes flow and geomechanical heterogeneity in this research. Extensive field observations and numerical investigations demonstrate the importance of understanding and honoring reservoir heterogeneity in SAGD to explain and history match the measured field data. The existence of low permeability shale barriers obstructs the communication between the injected hot steam and cold viscous bitumen which hinders the propagation of the steam chamber. If the injection pressure is high enough to trigger plastic deformations across the shale barriers, the hot steam and mobile bitumen still can channel through the created flow path as observed by Birrell (2001) and Ito et al. (2000) in the UTF SAGD project.

2.3.1 Flow Heterogeneity

Butler's model (1981) is the origin of analytical models for SAGD and is modified for different conditions. Reis (1992) proposed a linear geometry for the steam chamber to account for heat loss to the surroundings. Sharma and Gates (2010) modified Reis's linear model to include the effects of relative permeability, and Cokar et al. (2013) further extended the theory to consider thermal expansion on drainage at the chamber edge and production rates. Yang and Butler (1992) conducted steam injection experiments on a mini steam chamber, which demonstrates that long shale barriers have a significant impact on chamber shape and oil recovery. Field observations of SAGD also show that massive continuous shale barriers with low permeability have a negative effect on SAGD performance (Birrell et al. 2000, 2001 and Ito et al. 2000). The over-simplified chamber shape in analytical models leads to errors in the prediction of SAGD performance because flow heterogeneities have not been properly considered.

Numerical simulation has its advantages when investigating the impact of heterogeneity on SAGD, showing SAGD performance is closely related to the configurations of the shale barriers. The initial hydraulic conductivity near the wellbore is highly sensitive to the shale barriers, while the propagation of the steam chamber away is compromised by long and continuous shale layers. Flow heterogeneity is not the focus of this research, only a few recent studies quantifying the impact on flow are briefly mentioned here. Shale/lean zone indicator, defined by the distance between a shale barrier and the well pair divided by the shale volume, is used to quantify the flow response in the SAGD process. With the decreasing distance from shale barrier to the horizontal well pair or increase volume and continuity of shale barriers, the efficiency for SAGD is expected to decrease (Amirian et al. 2015; Wang and Leung 2015).

2.3.2 Geomechanical Heterogeneity

Research on the impact of geomechanical heterogeneities on SAGD is limited and homogeneous geomechanical properties are typically assumed. The source of geomechanical heterogeneity of oil sands is classified as lithological heterogeneity and inherent spatial variability (Elkateb et al. 2003). Lithological heterogeneity exists in the thin shale layers embedded in a stiffer sand cell or the inclusion of mud/limestone within a more uniform sand mass. Inherent spatial variability is the variation of geomechanical properties from one point to another due to different deposition conditions and stress histories within a single lithology.

In traditional geotechnical design problems such as seepage flow, liquefaction risk, foundation settlement, footing bearing-capacity prediction, block compression and slope stability problems, the research focuses on the inherent spatial variability of soil properties to improve the geotechnical design at a smaller scale. In reservoir geomechanics, lithological heterogeneity draws more attention due to the large variations of lithologies for subsurface resources. In geological modeling, facies are usually determined based on well logging data, e.g. Garma ray, Neutron porosity, density porosity, spontaneous potential. Cut-offs or clustering are used to determine the facies or lithology for each geological cell. Different facies are classified by distinct interpretations of log data and are assigned to various flow/geomechanical properties.

Geomechanical analyses have been applied in hydraulic fracturing in coal-seam and tight oil/gas reservoirs. Yang et al. (2004) studied the influence of heterogeneity of mechanical properties on hydraulic fracturing in permeable rocks using the flow coupled Rock Failure Process Analyses code (F-RFPA^{2D}). The variabilities of geomechanical parameters and permeabilities are randomly assigned according to Weibull's function representing various heterogeneity levels. The fracture

initiation and propagation, roughness of rocks and breakdown pressure near-wellbore are significantly influenced by the heterogeneity of rocks.

Frias et al. (2004) investigated stochastic computational modeling of highly heterogeneous poroelastic reservoirs with long-range correlations displaying a fractal character. The COV of the log hydraulic conductivity shows that permeability variation leads to perturbations in the flow velocity resulting in the spreading of the pore pressure and rock consolidation around mean values. The growth of the plastic region is significantly higher for fractal media compared to non-correlated and homogeneous porous media, however, the extension of the model to a non-linear inelastic range of the rock matrix still requires further study.

Deisman et al. (2013) linked the Geological Strength Index (GSI) with initial reservoir geomechanical properties and permeability of coal-seam reservoirs. Reservoir heterogeneity is modeled by sequential Gaussian simulations for distributions of GSI, Young's modulus and permeability. The dynamic permeability and Young's modulus are observed to have a significant impact on the production of methane as well as the injection of CO_2.

Lin et al. (2018) presented an integrated reservoir-geomechanics case study on heterogeneous unconventional tight pay in the Montney formation in Canada. The simulation results provide some insights of geomechanical impact on the recovery of a heterogeneous tight oil/gas reservoir with a simplified geomechanics module (pressure-dependent permeability from a table for normalized permeability and pressure).

Khajeh et al. (2011) investigated the impact of lithological heterogeneity on SAGD coupled simulation. A larger range of uncertainties are observed for cumulative oil production (COP), cumulative steam oil ratios (CSOR) and vertical displacement profiles (VDP) for 100 realizations with and without heterogeneous geomechanical properties.

Heterogeneous geomechanical properties significantly increase the ranges of uncertainties in the flow and geomechanical response. Khajeh et al. (2011) recommended that the geomechanical heterogeneities should be considered carefully when assessing SAGD performance, e.g. COP and CSOR.

2.3.3   Proxy Models for SAGD Considering Deformations

Two routines can be followed to improve the efficiency of considering interactions between flow and geomechanical response: (1) fast and reliable proxy models to coupled simulations capturing the interactions of flow and geomechanical heterogeneities; (2) efficient and reliably upscaling workflow able to deal with the non-uniform flow and deformations caused by reservoir heterogeneity. Proxy models discussed here mainly discussed the analytical and semi-analytical models that are used to capture the deformation response on the production performance in the SAGD process.

Cokar et al. (2013) and Sharma and Gates (2010) uses the volumetric expansion coefficient to consider the deformation response in SAGD. Azad et al. (2012) proposed a proxy model considering deformations in SAGD for closed-loop reservoir optimization. Proxy models are efficient in terms of computational time but strongly dependent on the model complexity, dimension of the model of interest and quality of the input dataset. For the highly heterogeneous McMurray Formation, there is no universally applicable proxy model. To improve prediction, different proxies have been applied to different SAGD processes in a field case study conducted by Azad et al. (2015). In terms of the accuracy of outputs, especially steam chamber shape and surface heave profiles, proxy models are not comparable with coupled reservoir-geomechanics simulation for project design and amendment. This is the main driving force for the upscaling of coupled reservoir-geomechanics simulations rather than developing any proxy models for SAGD.

2.4 Upscaling of Reservoir-geomechanics Properties

In reservoir and geomechanical simulations, researchers want to include as many realistic geology details as possible to have a closer representation of reservoir and geomechanical response. Ideally, high-resolution geo-cellular models should be used for coupled flow and geomechanical simulation. However, most full-field geological models are finer than models applied in geomechanical simulation. Parallelizing the reservoir/geomechanical simulators can achieve faster computation but the memory required still limit the number of cells in the parallel simulation (White et al. 2006; Yang et al. 2013). Furthermore, the number of PCs and licenses available for parallel simulation is also constrained the computational power of field-scale simulations.

Upscaling is required to bridge the gap between the high-resolution geologic model and a computational efficient reservoir-geomechanics model. The most important step in upscaling is to assign accurate equivalent properties to the coarsened cells and reproduce the complex physics of the fine-scale model. The upscaling methods for reservoir properties (porosity, permeability and saturation) and geomechanical properties are discussed in the following subsections.

2.4.1 Upscaling of Petrophysical Properties

A volume-weighted average is correct for upscaling of porosity and fluid saturation, but non-linear reservoir properties such as permeability require more sophisticated techniques. At reservoir scale, permeability upscaling techniques are generally divided into two groups: analytical and numerical upscaling methods.

2.4.1.1 Analytical Methods

An arithmetic average provides a reliable prediction of effective permeability parallel to the homogeneous parallel beddings with different permeabilities. The harmonic average is sensitive

to low permeability and useful for assessing the effective permeability perpendicular to the bedding planes. The geometric average is normally used to estimate the effective permeability of porous media with low spatial correlation and log-normal histogram (Deutsch 1989). Power averaging is a viable approach combining the traditional averages (Deutsch 1989):

$$k_{eff} = [V_{sh}k_{sh}^{\omega} + (1 - V_{sh})k_{s}^{\omega}]^{1/\omega} \hspace{3cm} \text{Equation 2-7}$$

Where k_{sh} and k_{s} are the permeabilities for shale and sand, V_{sh} is the volume fraction of shale and ω is the power calibrated to experimental data. The arithmetic average is the upper bound of power averaging with $\omega = 1$. The harmonic average is the lower bound with $\omega = -1$. The spatial correlation of the porous media determines the value of ω in Equation 2-7. Analytical methods are computationally efficient but inaccurate for problems with strong permeability contrast.

However, analytical methods cannot provide accurate predictions of effective permeability in a highly heterogeneous reservoir. To improve the prediction of recovery performance in heterogeneous reservoirs, Leung and Srinivasan (2012) modified the conventional volume averaging approach with some fine-scale and coarse-scale simulations over a small sub-volume of the reservoir.

For SAGD or expanding-solvent (ES)-SAGD, phase behavior among the three distinct fluid phases (steam, water and oil) at different temperatures and pressures complex the fluid dynamics in the oil sand reservoirs. Morte and Hascakir (2016) proposed a new fractional flow theory with the modified capillary number and mobility ratio to estimate the pseudo relative permeability curves in SAGD and ES-SAGD. The pseudo relative permeability curves are claimed to be able to upscale the results to real field dimensions by explicitly matching the oil recovery history. The other

analytical techniques used to improve the model efficiency of SAGD can be classified as the proxy models in section 2.3.3.

2.4.1.2 Numerical Methods

Numerical techniques for permeability upscaling, also known as the flow-based numerical upscaling method, can capture complex flow response and use a pressure solver under different boundary conditions. The flow-based upscaling technique can be classified into three groups: 1) local, 2) global and 3) local-global methods. Local flow-based techniques solve the pressure equation for each coarse grid with various boundary conditions, e.g. no flow, steady-state flow and periodic boundary, to obtain the corresponding permeability tensors. Warren and Price (1961) determine the permeability for a heterogeneous porous media from a pressure build-up curve with a reasonable prediction of the effective permeability of the drainage area. Durlofsky (1991) presented a local upscaling method that solves the pressure equation for effective permeability tensor in the representative elementary volume (REV). The method is validated through applications to fractally generated permeability fields. For high permeability streaks, this technique cannot capture the channeling effects. Thus, detailed heterogeneities in these regions should be explicitly included, and upscaling should be done for less heterogeneous domains. Pickup et al. (1994) calculated effective tensor permeabilities with a periodic boundary condition method for sedimentary structures with a high bedding angle, high permeability contrast and various thickness of laminations. The effective tensors have been successfully applied in deterministic, stochastic and hybrid permeability fields.

In global upscaling techniques for permeability, the fine-scale pressure equations are not solved for each coarse grid. Nielsen and Tveito (1998) proposed a weighted output least square (WOLS) approach to upscale the one-phase flow in heterogeneous reservoirs. The effective permeability is

computed as the solution of an optimization problem, where the difference between the fine-scale and coarse-scale velocity field is minimized. Holden and Nielsen (2000) extended the WOLS approach to the L2 norm which predicts injection and production rates more accurately. Global upscaling is more accurate in the upscaling of blocks close to wells because the flow depends more heavily on the global flow pattern, but it is less computational efficient compared to the local upscaling technique.

Local-global techniques can be classified into two groups, e.g. extended-local and quasi-global methods, depending on whether the global flow is solved. The extended local method uses border regions surrounding the coarse block in the calculations to provides a more accurate effective permeability tensor. It is widely applied as it captures more of the flow pattern around the coarse grid (Gomez-Hernandez and Journel 1994; Holden and Lia, 1992 and Wu et al. 2002). Wen et al. (2003) presented a general procedure for the calculation of full-tensor permeabilities on the fine and coarse scales by applying a border region of fine-scale cells. The use of border regions leads to improved coarse-scale results by better resolving the effects of connectivity of permeability. In the grid refinement studies, a significant portion of the inaccuracy in the coarse models is found caused by the numerical error rather than introduced by the upscaled model. The extra computation time is not a concern compared to the computational expensive fine-scale reservoir simulation, but application in 3D cases still requires further studies to accelerate the calculations. For highly heterogeneous formations, the local and extended-local techniques still meet difficulties because the boundary conditions cannot be updated to mimic the flow pattern during fine-scale simulations. The local-global upscaling technique is proposed to deal with this issue by an iteration procedure assures consistency of boundary conditions between the local and global calculations (Gautier et al. 1999 and Chen et al. 2003). The nested gridding method proposed by Gautier et al. (1999)

retains the explicit representation of the fine-scale saturation by use of streamline simulation which is demonstrated to be much faster compared to finite-difference methods. Chen et al. (2003) extended the nested gridding method with a sub-grid velocity reconstruction procedure for transmissibility and permeability upscaling. Although the local-global upscaling technique is more time-consuming compared to the other flow-based method, it has demonstrated its capability in improving the accuracy in highly heterogeneous formations and near-well upscaling issues.

Pickup et al. (2005) investigated the feasibility of multi-stage upscaling, which is consisted of different selections of upscaling techniques depending on the types of flow systems. It is suggested to examine the large-scale structure to determine the flow regime first and then check the importance of the small-scale pore structure. Zhang et al. (2008) compared local upscaling, well drive (global) and pore volume-weighted (two-phase) upscaling method in the SPE 10 problem with a state-state flow boundary. Local upscaling is the fastest and adequate when the level of heterogeneity is low. Pore-volume-weighted is the most accurate method in highly heterogeneous porous media but not efficient enough to be applied in multi-million-cell models. Global upscaling is recommended to be carried out first before two-phase local upscaling to reduce the potential error.

Adaptive numerical upscaling and generalized multiscale basis functions started to get a wider application for highly heterogeneous porous media. Fine-scale grids are used along the saturation front while local numerical upscaling is performed away from the front in adaptive numerical upscaling methods. Gurpreet et al. (2019) applied a residual-based grid indicator to locate the fine grid where saturation front is modeled directly. Multiscale methods construct coarse-grid basis functions for oil pressure, water/gas saturation and velocity to approximate the response at the fine-scale (Aarnes 2004, Kozlova et al. 2016). Gurpreet et al. (2019) solves a local spectral

problem for each local domain and compare with the adaptivity criterion as an offline step to minimize the computational time of the multiscale simulation.

The flow-based upscaling techniques discussed above are developed for a black-oil simulator. For compositional simulation, the upscaling technique is more important because the algorithm speed is slower than black-oil simulators. Barker and Fayer (1994) proposed to use the transport coefficient (alpha-factor) to adjust the component's flux in compositional simulation. Christie and Clifford (1997) extended the alpha-factor method in the streamline simulation to obtain the upscaled alpha factors for the upscaling block surrounded by the extended fine cells. Zhang and Okuno (2015) developed a two-step method to model bypassed oil recovery in multiphase compositional simulation for gas flooding processes. The oil bypassing is first quantified by the dual-porosity method and then reproduced by the flow-based fluid characterization method for part of the heavy oil components. The proposed method has been successfully applied in the highly heterogeneous layers.

2.4.2   Upscaling of Elastic Geomechanical Properties

The geomechanical response is controlled by elastic and plastic geomechanical properties together. For elastic behavior, the relationship between stress and strain is linear and upscaled elastic properties can be directly computed from Hooke's law. Upscaling of elastic properties has been successfully applied at different scales and can be classified into three different categories based on the distribution of facies: randomly distributed, layering and spatially correlated (Figure 2-15). Periodic structures, e.g. honeycomb structure, sometimes are classified as a fourth group, which is not discussed here as periodicity is not common in reservoir geology.
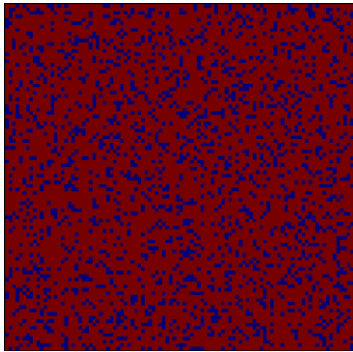
Figure 2-15. Three different types of facies distributions: (a) Randomly distributed system; (b) Layered system; (c) Spatially correlated system.

2.4.2.1 Randomly Distributed System

The upscaling of randomly distributed lithology in multi-phase heterogeneous material (Figure 2-15-a) is the first group to be investigated. Mackenzie (1950) used a self-consistent method to estimate the effective bulk and shear modulus for solids with spherical holes. Hashin (1962) solved the equivalent elastic modulus for heterogeneous materials with spherical assumption. Variational principles of elasticity are used to obtain the upper and lower bounds for Young's modulus of heterogeneous material because it is not trivial to find an exact analytical solution for the elastic modulus of heterogeneous solids fit with experimental results (Paul 1960 and Hashin et al. 1962, 1963). Budiansky (1965) extended the model proposed by Hill (1963) for reinforced solids to multiphase materials but still assumed isotropic deformations. Huet (1990) adopted Hill's condition to predict the upper and lower bound of apparent elastic modulus for elastic heterogeneous bodies with different sizes where the concept of a representative element volume does not apply. Despite the popularity of analytical homogenization for randomly distributed heterogeneous materials, the elastic modulus for each solid phase is assumed to be isotropic. The

consideration of a simplified configuration of facies is not appropriate for complex facies configurations found in the McMurray Formation.

2.4.2.2 Layered Systems

The second group of analytical upscaling methods is developed for layered systems (Figure 2-15-b). The studies of Voigt (1907) and Reuss (1929) are still of considerable interest for homogenization in layered porous media. Their models provided approximations of the upper and lower bounds for the effective elastic properties of a mixture composed of different constituents. The Backus averaging method (1962) is an analytical upscaling method used to interpret seismic wave propagation through a perfectly layered medium with linear elastic properties and no source of intrinsic energy dissipation between layers. The five linearly independent upscaled parameters are calculated based on the symmetry of the compliance matrix for transverse isotropic layered structure in the long-wave equivalent homogeneous medium. Salamon (1968) extended the Backus technique and derived the elastic coefficients of a homogeneous transverse isotropic medium based on equity of strain energies in a perfectly horizontal stratified rock mass assuming that all layers are homogenous, isotropic, continuous and there are no relative displacements at the interface between different layers. Gerrard (1982) extended Salamon's analytical solution to parallel layers with orthotropic elastic properties in a system with two horizontal layers. Chalon et al. (2004) compared Salamon's (1968) analytical method with numerical upscaling using a finite element code (Code_Aster) to generate a lower and upper bound for effective elastic properties on a simplistic layered reservoir structure. The homogenized model generated by Salamon's method matches the horizontal and vertical displacements under normal and shear loads, however the applicability of Salamon's method to a more complex heterogeneous reservoir under in-situ stress condition remains uncertain.

Rijpsma and Zijl (2000) established an upscaling technique based on Hooke's law for imperfectly layered rocks by introducing a dimensionless parameter measuring the magnitude of deviations from perfect layering. They managed to validate the upscaling method in finite element models with different boundary conditions and the equivalent elastic modulus resulted in reasonable results for vertical displacement except when shear stress is applied to the side boundary of the layers. The major difference for imperfectly layered rocks is that the upscaled compliance matrix is not symmetric compared to a perfectly layered system. Guo and Stolle (2018) develop a physically meaningful homogenization approach to determine the equivalent elastic properties of layered soil based on Reuss and Voigt approximations without employing auxiliary stresses and strains. Experimental studies of elastic modulus for varved silt and homogenous soil via different strain paths have shown that the elastic modulus for varved silt parallel to the layer is 40% higher than that in the vertical direction, which indicates that boundary conditions must be defined carefully when determining the effective elastic modulus.

2.4.2.3 Spatially Correlated Systems

Analytical solutions for homogenized elastic properties are popular for randomly distributed and layered systems, but it is not applicable for the spatially correlated systems due to the complexity in geomechanical behavior. Thus, an increasing number of numerical techniques have been conducted to help establish a numerical upscaling technique for spatially correlated elastic properties.

Zijl et al. (2002) extended his homogenization method to complex spatially correlated reservoir models for several synthetic and field tests to obtain the upper boundary for the coarse-scale rigidity matrix. Elkateb (2003) investigated the effect of intercalated clay seams on the

macroscopic behavior of sand in plane strain conditions. The equivalent elastic modulus is calculated with isotropic elastic deformation for this heterogeneous soil below a strip footing.

The boundary condition is oversimplified to compression from the top while assuming isotropic deformation, which may result in a significant error in the effective elastic modulus with complex stress paths. Due to the difficulties associated with experimental characterizations of highly heterogeneous materials, a comparative evaluation of the macroscopic elastic response of clayey rocks with different pore structures using different homogenization schemes and numerical simulations has been carried out by Goodarzi et al. (2016). The simulation and experimental data show that a self-consistent scheme is the most appropriate model to homogenize elastic properties of a porous clay matrix; however, the Mori-Tanaka model (1973) reproduces the macroscopic response more accurately for a system with isolated pores. Hill et al. (2015) presented a method that applies a rectangular tessellation to the wavelet transform and resembles the spatial information of the geological log. The tessellation can be filtered to remove unwanted variation and noise from the results and provides a high-level summary of the geochemical information, which provides a less problematic basis for classification of lithochemical units than classifications by considering individual samples without spatial context.

Willis (2013) combined Backus's method (1962) with cluster analysis for the 3D mechanical earth model of Vaca Muerta Formation to assist hydraulic fracturing design. The cluster analysis was conducted to identify the cluster group based on logging data. Backus method was used to upscale the elastic stiffness tensor for each cluster group determined from electrofacies. However, for problems where zones in the reservoir may yield or fail and exhibit non-elastic behavior, little is known about how geomechanical heterogeneity effects should be quantified and it is one of our research focuses in Chapter 3.

Berryman (2011) extended Backus's method (1962) to a poroelastic and anisotropic layered media containing fluids if one of the axes is aligned with the layering direction in drained and undrained conditions. Ita and Malekzadeh (2015) extended Berryman's method to multi-porosity layered poroelastic medium combined with both drained and undrained layers by introducing a simple indicator and obtained good results for pressure in Mandel's problem. This provides a way to consistently up and downscale in a layered poroelastic medium which may be used in multi-scale, coupled flow-geomechanical simulation. However, the application of Backus's method is restricted to layered systems due to the transverse isotropic assumption.

The importance of boundary conditions assigned to compute effective elastic modulus attracted growing attention when numerical upscaling is applied to complex reservoir systems in the coupled reservoir and geomechanical simulations. Couples et al. (2003) developed a coupled simulation approach called HYDRO-DDA (Discontinuous Deformation Analysis) and found that the upscaled fluid-flow and geomechanical properties in the matrix+fractures+fluids system are highly non-linear with strong dependencies on each parameter. The concern is that simple boundary conditions may result in erroneous upscaled properties and suggested building libraries with realistic boundary conditions considering changes in the adjacent coarse cells. Adopted from permeability upscaling, oversampling was applied by Zhang and Fu (2010) to calculate effective elastic modulus tensors based on a broader region than the upscaled grid with various external loading conditions. The upscaling technique for fluid and solid phase gave reasonable results of displacement and pressure in a 2D numerical heterogeneous ground subsidence problem based on homogenized elastic modulus tensors. Settari et al. (2013) developed an upscaling method to determine a dynamic equivalent stiffness tensor for sub-grid interbedded shales in coupled geomechanical simulation applied to a larger offshore reservoir. The equivalent elastic modulus

was calculated by an analytical method which is a function of volume fraction of sand, ratio of Young's modulus and ratio of pressure depletion based on uniaxial deformation history. Yang et al. (2013) introduced a numerical upscaling technique in a full-field simulation of a highly heterogeneous 2D reservoir model. For the elastic stiffness tensor upscaling, the strain energy-based homogenization method provided reasonable results for pressure and displacement compared to fine-scale simulation with an upscaling ratio of 16. Khajeh et al. (2012) proposed a numerical local upscaling method for elastic properties to describe macroscopic elastic behavior in a 2D synthetic reservoir realization and compared it with three traditional averaging methods and Budiansky's upscaling technique. However, the proposed workflow requires further modification to be applied in 3D reservoir.

2.4.3 Upscaling of Plastic Geomechanical Properties

After passing the elastic limit, the stress-strain behavior becomes highly nonlinear. Compared to elastic properties, the upscaling of plastic properties has additional challenges, especially in the macroscopic (m-km) scale. The Mori-Tanaka micromechanical model (Mori and Tanaka 1973) is often used to provide quick estimates of the geomechanical response of random composites with a matrix-inclusion system at the microscopic scale. Hill (1965) proposed an incremental approach to model the micro-mechanics of the arbitrarily deformed aggregate of elasto-plastic crystals, which has the advantage of being directly linked to existing linear homogenization schemes.

Desrumaux et al. (2001) developed a two-step homogenization process for three-phase fibre composites (fibre, matrix and microcracks) by use of the Mori-Tanaka scheme. The tensile strength is generated following the two-parameter Weibull distribution and is in good agreement with the experimental data. The local damage mechanism is well predicted compared to the acoustic emission amplitude analysis. Berbenni and Capolungo (2015) extended the Mori-Tanaka

homogenization scheme based on the translation fields approach to elasto-viscoplastic composites (matrix and inclusion) with non-linear viscoplastic strain rates. Zhu et al. (2018) developed a micro-mechanical model considering damage-friction coupling for quasi-brittle materials like granite and sandstone. The model combines a linear homogenization procedure with the Mori-Tanaka scheme and the irreversible thermodynamics framework, which relates the macroscopic plastic strain and frictional sliding along closed micro-cracks.

Guetry et al. (2008) extend Hill's (1965) incremental method to a nonlinear homogenization approach of the mechanical behavior of argillites composed of an elasto-plastic clay matrix and linear elastic/plastic damage inclusions. The localization of strain is considered in the Mori-Tanaka scheme because of the matrix/inclusion structure. Shen et al. (2012) proposed a two-step homogenization procedure (micro-meso and meso-macro) to estimate the macroscopic elastoplastic behavior of clayey rock. The Mori-Tanaka scheme is adopted with the iterative inverse approach proposed by Guetry et al. (2008) for the elastic properties of the clay matrix mixed with calcite and quartz. The meso-macro upscaling is performed considering the incremental approach initially proposed by Hill (1965) which accounts for the effects of mineral inclusions. For the micro-meso transition, the pressure-sensitive behavior of the solid phase of clay matrix is described using the Drucker-Prager yield criterion and the associated or non-associate flow rule for the solid phase. The non-associate flow rule has better prediction results compared to experimental volumetric strains and the transition from compressibility to dilatancy. Shen et al. (2013) proposed a closed-form macroscopic criterion for the effective plastic behavior of the argillite because it is difficult to obtain an explicit form of the support function for a porous matrix by Drucker-Prager or other realistic criteria. Zeng et al. (2015) extended Hill's self-consistent approach for homogenization of the interactions between grains and pores in sandstone, where the

plastic deformations of each grain are related to the frictional sliding along a number of planes of weakness. To simulate the anisotropic mechanical behavior of shale, a micro-mechanical framework based on the Lattice Discrete Particle Model is formulated and calibrated with UCS and Brazilian test data by Li et al. (2017). The model is upscaled by a homogenization approach based on the asymptotic expansion of field variables.

The homogenization technique described above focuses on the microscopic response of heterogeneous material. The transition from the microscopic scale to reservoir scale remains a problem especially when the geological settings are more complex than the assumptions by Hill or Mori-Tanaka scheme. The applications in coupled geomechanical-flow simulations remain uncertain for both undrained and partial drained conditions. The accuracy of reproducing failure modes also needs to be investigated because of its importance in predicting induced changes in permeability.

CHAPTER 3:   GEOMECHANICAL RESPONSE OF HETEROGENEOUS OIL SANDS

The impact of geomechanical behavior on the SAGD process has received increased attention over the last decade because of its importance in assessing caprock integrity and potential influence on reservoir production performance. The deformations and potential shear failures in the reservoir lead to alterations of porosity, absolute and relative permeability due to high pressure and temperature changes induced by the SAGD process. Ignoring these geomechanical responses in the SAGD simulation may lead to an erroneous prediction of reservoir performance and a failure to recognize potential hazards similar to the Joslyn Creek steam release incident (Total E&P Canada Ltd 2010).

To improve the understanding of these issues, numerical investigations are conducted for a range of spatially correlated oil sand models mixed with shale bedding planes to analyze the impact of heterogeneity on modes of failure and macroscopic geomechanical response. The failure mechanisms are strongly affected by the volume fraction and relative positions of the shale seams in oil sands, which causes highly non-linear stress-strain behavior before failure. The simulation results demonstrate the importance of appropriate consideration of failure modes to obtain an accurate estimation of the effective elastic and plastic properties of heterogeneous oil sands at the sub-grid scale in upscaling. The relationship between the effective plastic geomechanical properties and the key geostatistical parameters (V_{sh}, range ratios and inclinations of shale) provides insights on the proposed plastic upscaling technique in Chapter 7.

3.1 Geostatistical Characterization of Heterogeneous Oil Sands

Oil sand reservoirs in the McMurray Formation are heterogeneous due to the variety of depositional environments that occurred during formation (Phillips 2011). The two dominant physical characteristics of clean oil sands are the quartz minerals with interlocked structures and large quantities of bitumen occupying the pore space. Micaceous partings and silty seams are widely observed in cores of oil sands (Dusseault and Morgenstern 1977). Figure 3-1 shows core images from the McMurray Formation provided in the AER performance report of the MacKay River Project (Alberta Energy Regulator 2017). The core images clearly show the lithological heterogeneities of oil-rich sand (black) and laminations of shale (white). The facies in the McMurray Formation (F1-F10) are classified by the visual mud index (VMI), which is determined by V_{sh}. The term "oil sands" here is not only restricted to the clean oil sands but also includes the shaly bitumen-rich sand, e.g. inclined heterolithic stratification lithosomes (IHS), in the Athabasca McMurray Formation and Cold Lake Clearwater Formation.
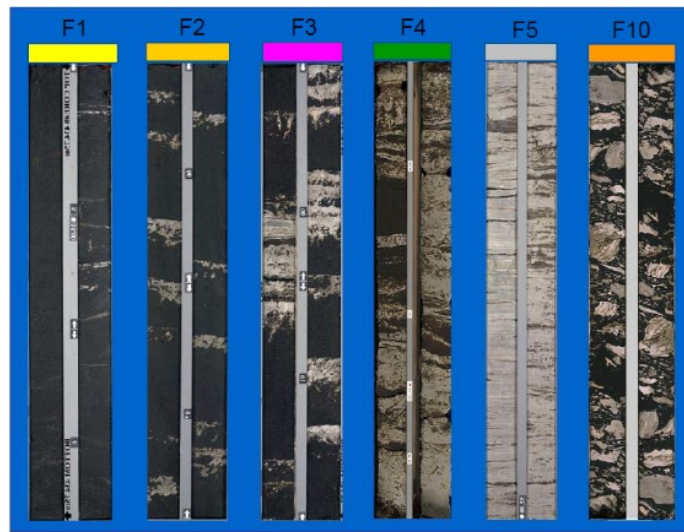
Figure 3-1.   McMurray Formation core images (Retrieved from Alberta Energy Regulator 2017).

3.1.1 Variogram Interpretation

Sequential indicator simulation (SIS) is widely used for categorical variable modeling when no clear genetic shapes are known for object-based modeling (Deutsch 2006). Numerous sand-shale sequence facies models are generated using SIS to cover the wide range of spatial variabilities in the McMurray Formation. Figure 3-2 shows a 100 by 100 vertical cross-section sand-shale sequence spatially correlated oil sand realization generated using GSLIB (Deutsch and Journel 1998).

100 (5 m)
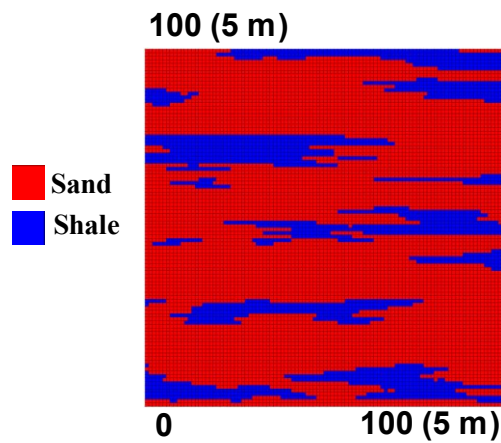
Figure 3-2.   A vertical cross-section of a sand-shale sequence oil sand SIS realization. The blue zones represent the weak and low permeability shale while the red zones represent sands.

Semivariograms are used to quantify the spatial variability of the model, defined as half of the average squared difference of local values separated by lag distance (h) (Pyrcz and Deutsch 2014):

$$\gamma(h) = \frac{1}{2N(h)} \sum_{N(h)} [z(u) - z(u+h)]^2 \ , \hspace{3cm} \text{Equation 3-1}$$

where $N(h)$ is the number of pairs for lag distance (h), $z(u)$ is the data at location u. The corresponding horizontal and vertical experimental variograms of the realization (Figure 3-2) are

illustrated in Figure 3-3. Three key parameters (sill, range and nugget effect) are used to interpret experimental variograms. The sill is the variance of the data used for variogram calculation. The range is the distance at which the variogram reaches the sill, which varies in different directions due to anisotropy in the reservoir. The horizontal range is usually larger than the vertical range because facies continuity is larger horizontally during the sedimentation process. The nugget effect is the apparent discontinuity at the origin of the variogram, which represents measurement error and geological variability at scales smaller than the smallest experimental lag distance. A low nugget effect is usually observed in a sedimentary environment because most variables are locally continuous.
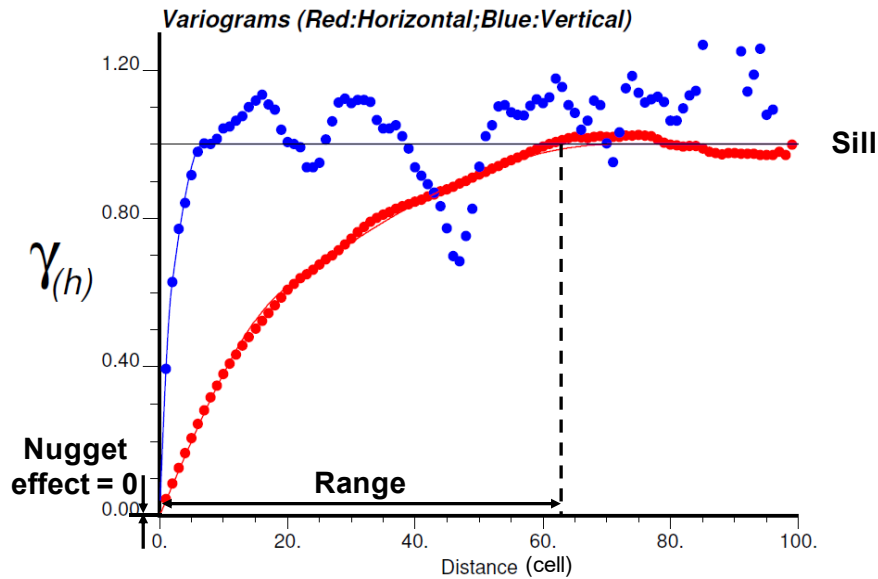
Figure 3-3.   The corresponding horizontal (red) and vertical (blue) experimental variograms and fit variogram models for the heterogeneous oil sands (Figure 3-2).

3.1.2 Variogram Model

The experimental variogram points need to be fit by a parametric variogram model like spherical, exponential, Gaussian and hole effect variograms models to be applied in geostatistical modeling. The experimental variograms can be fit by a variogram model with zero nugget effect and two spherical variogram structures (Figure 3-3):

$$\gamma(h) = 0.35sph_{\substack{a_v=1.9 \\ a_h=19.5}} + 0.65sph_{\substack{a_v=6.8 \\ a_h=71.3}} , \qquad\qquad \text{Equation 3-2}$$

where a_v and a_h are the vertical and horizontal ranges.

Variograms have three principal directions for ranges: a_v, a_{hmax} and a_{hmin}. a_{hmax} represents the range of the direction of greatest continuity in the horizontal direction while a_{hmin} represents the range of least continuity in the horizontal direction. In 3D models, a_{hmax} and a_{hmin} are determined by fitting the experimental variogram in different directions. For the 2D vertical cross-section in Figure 3-2, a_{hmax} and a_{hmin} are considered the same and merged into a_h because no information on horizontal anisotropy is available. As the size of the upscaled cells varies for different regions, a dimensionless range ratio is defined as the ranges versus the size of the upscaled cell in a corresponding direction to quantify the impact of continuity on upscaled geomechanical properties:

$$a_v^d = a_v/H , \qquad\qquad \text{Equation 3-3}$$

$$a_h^d = a_h/L , \qquad\qquad \text{Equation 3-4}$$

where H is the thickness and L is the length of the upscaled block.

3.1.3 Spatially Correlated Realizations

Using the variogram model, spatially correlated realizations are generated with user-defined volume fraction, azimuth and dip of sand and shale. In the McMurray Formation, the horizontal range is usually many times larger compared to the vertical range due to the thin and long shale bedding planes.

A series of 2D sand-shale realizations with horizontal shale bedding planes are created in Figure 3-4 when fixing V_{sh} to 20%. For example, case 50-5 represents realizations with a horizontal range of 50 and a vertical range of 5. The input a_h^d increases from 0.1 to 1 while a_v^d is kept as 0.01 (Figure 3-4a to 3-4e). In Figure 3-4f to 3-4j, a_v^d increases from 0.02 to 0.2 while a_h^d is fixed at 0.5.
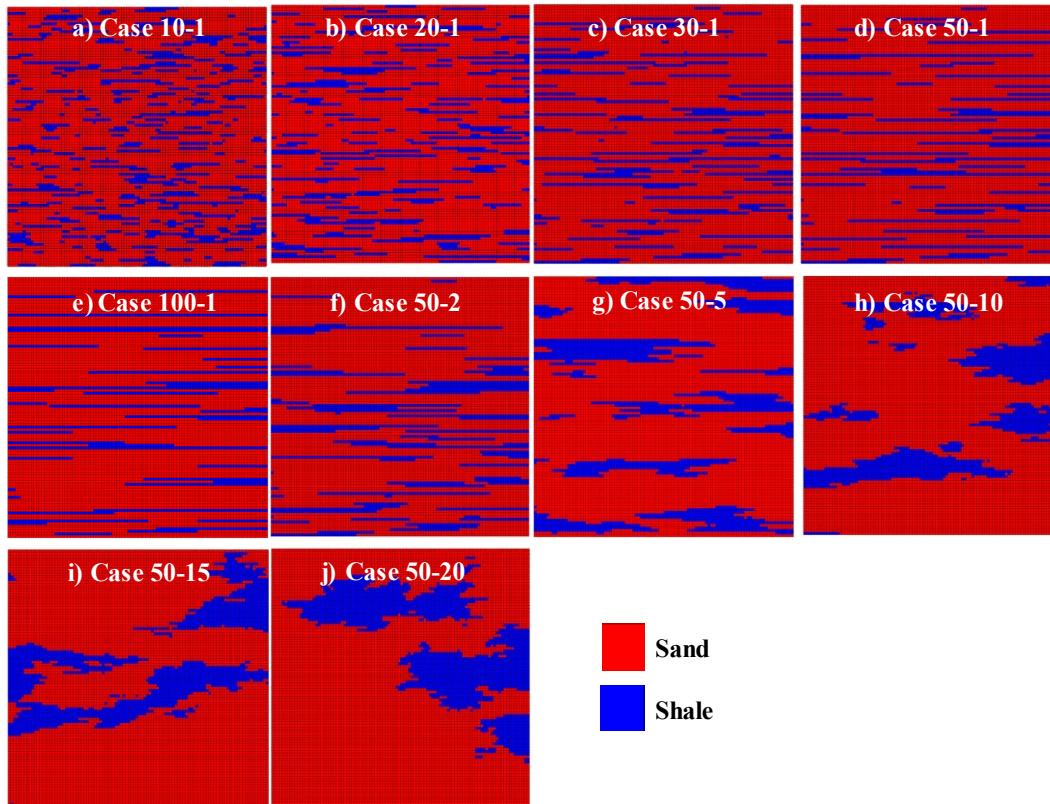
Figure 3-4.   2D spatially correlated sand-shale realizations with various ranges in the horizontal and vertical direction with $V_{sh} = 20\%$.

When investigating the impact of range on failure modes and macroscopic geomechanical response, the volume fraction of shale is fixed to 0.2 while the shale bedding planes are kept horizontal to restrict the influence by V_{sh} and inclinations of shale. For studies on the anisotropic effect of IHS, the inclination angle between the shale bedding plane and major principal stress direction has a wide range from 0° to 90°, e.g. 90° represents the major principal stress perpendicular to the shale bedding plane.

3.2   Geomechanical Properties for Sand and Shale Facies

The constitutive behavior of oil sands has been studied in comprehensive laboratory tests (Chalaturnyk 1996). Li and Chalaturnyk (2005) performed a series of numerical tests in FLAC with a strain-softening Mohr-Coulomb model to match the lab results of oil sands by Oldakowski (1994), Samieh and Wong (1997) and Touhidi-Baghini (1998). To reproduce the strain-softening behavior and shear dilatancy after failure, the strain-softening Mohr-Coulomb model in FLAC3D (© Itasca) is used here to represent the constitutive behavior of oil sands.

The Young's modulus of oil sands is strongly related to effective confining stress and correlations have been generated to represent the variation of Young's modulus for oil sands based on previous lab results (Chalaturnyk 1996). Constant Young's modulus is used here as the confining stress is fixed for each local numerical analysis. The impact of variations of Poisson's ratios of sand and shale is 0.3. The variations of Poisson's ratio on geomechanical response are investigated in Chapter 6. The bulk and shear modulus for sand and shale facies are taken from Khajeh et. al. (2011) and listed in Table 3-1. The Young's modulus is 833 MPa for sand, which is close to Young's modulus at the project area (Chalaturnyk 1996). The computed Young's modulus for

shale is 363 MPa, which is within the range of upper and lower McMurray shale (Chalaturnyk 1996) in drained triaxial compression tests.

The peak friction (55°) and dilation angle (22°) are from Li and Chalaturnyk (2005) calibrated for clean oil sand. The post-peak behavior of sand is characterized by a function of plastic strain (Table 3-2) in Li and Chalaturnyk (2005). The geomechanical properties and softening tables for shale are fit to the experimental results for the Clearwater shale by Zadeh and Chalaturnyk (2015). The upper McMurray Formation shale contains 30%-40% lean oil sands and has non-zero cohesion (556 kPa) measured by Chalaturnyk (1996). Non-zero cohesion is used for sand as the V_{sh} cut-off varies at the microscopic scale. The geomechanical properties and strain-softening tables for sand and shale are summarized in Tables 3-1 and 3-2.

Table 3-1 Geomechanical properties for the sand and shale facies.

	Sand	Shale
Bulk Modulus, MPa	700	300
Shear Modulus, MPa	320	140
Peak Friction Angle, °	55	30
Peak Dilation Angle, °	22	7
Peak Cohesion, MPa	1.2	0.55
Peak Tension, kPa	100	80

Table 3-2 Strain-softening table for sand and shale facies.

Plastic shear strain	0	0.01	0.02	0.03	0.04	0.05	0.06	0.07	0.08	0.09
Friction angle (sand), °	55	53	51	49	47	45	43	41	39	37
Dilation angle (sand), °	22	20.5	19.0	17.6	16.1	14.6	13.1	11.6	10.2	8.7
Cohesion (sand), MPa	1.2	1.15	1.1	1.05	1	0.95	0.9	0.85	0.8	0.75
Friction angle (shale), °	30	28	26	24	22	20	18	16	14	12
Dilation angle (shale), °	7	6.75	6.5	6.25	6	5.75	5.5	5.25	5	4.75
Cohesion (shale), MPa	0.55	0.53	0.5	0.48	0.45	0.43	0.4	0.38	0.35	0.33

3.3 Boundary Conditions for Numerical Tests

The increase of horizontal stress (Chalaturnyk and Li 2004) has found to be the predominant stress path after the steam injection in SAGD due to thermal expansion, while vertical total stress remains fairly constant in shallow reservoirs as in the Dover UTF Project. The increase in shear stress leads to shear deformations and includes changes in pore structure and permeability near the chamber edge. To mimic this stress path, constant horizontal displacement rates are applied horizontally on the 5 m by 5 m 2D realization as illustrated by Figure 3-5. With a strain boundary, the stress-strain behavior is highly sensitive to the displacement rate when associated with plastic behavior. Here, the displacement rate is chosen as 5×10^{-7} m/s as it will give a negligible error while considering the efficiency of the simulation according to the sensitivity studies. Zero friction is assumed between the strain boundary and the realization. A constant confining stress σ_3 is applied at the top and bottom boundary to mimic the relative constant vertical total stress during SAGD. Plane-strain condition is assumed so that no displacement is allowed perpendicular to the 2D plane in FLAC3D. For 3D realizations, triaxial tests are conducted with confining stress σ_3 and constant displacement rate. For this research, no interface slip is assumed between sand and shale elements.
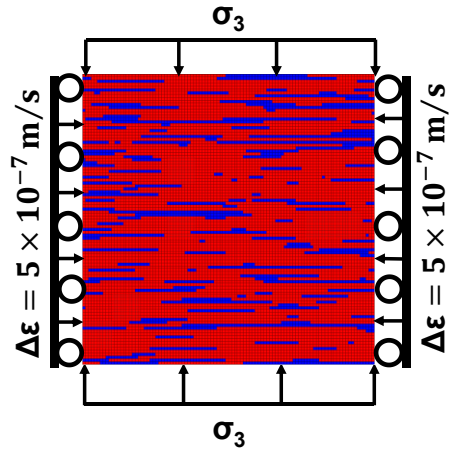
Figure 3-5.   Schematic of the boundary conditions for 2D numerical tests under plane strain condition.

3.4   Stress-Strain Behavior for Homogeneous Sand and Shale Realization

Following the boundary conditions shown in Figure 3-5, numerical tests are conducted on the homogeneous sand and shale realizations with σ_3 of 0.1, 0.5 and 1 MPa to illustrate the constitutive behavior for sand and shale. Figure 3-6a and 3-6d show that the homogeneous sand and shale realizations exhibit a linear elastic response before failure. The linear slopes for the stress-strain curve before failure representing constant Young's modulus with different σ_3. The identical slopes for the change of volumetric strain during contraction (Figures 3-6b and 3-6e) reflect the constant Poisson's ratio under different σ_3.

After the peak of stress, strain-softening behavior is observed with variations of residual strength at different confining stresses. The shear dilatancy of sand is significantly higher than shale. Figures 3-6c and 3-6f provide the Mohr-Coulomb failure envelopes for sand and shale. The friction angle and cohesion start to decrease with the increase in plastic strain leading to the mobilization of strength towards the residual failure envelope (blue line).

67
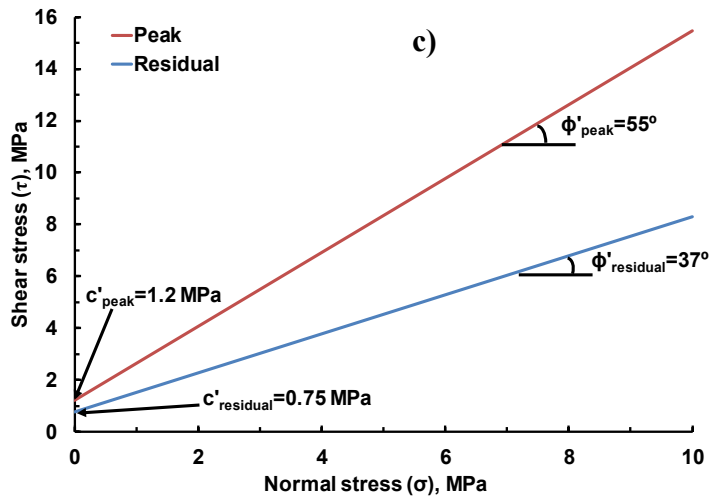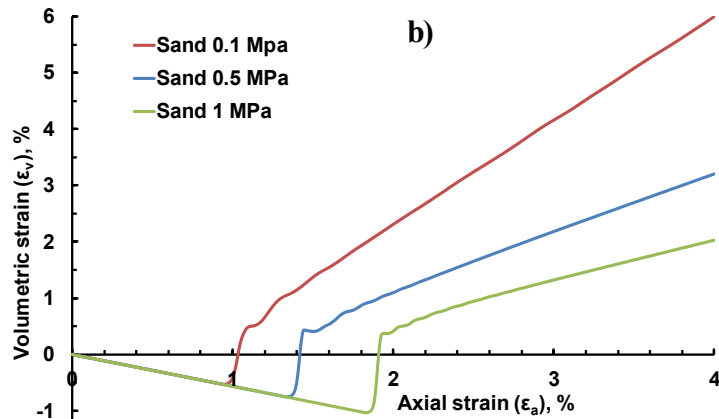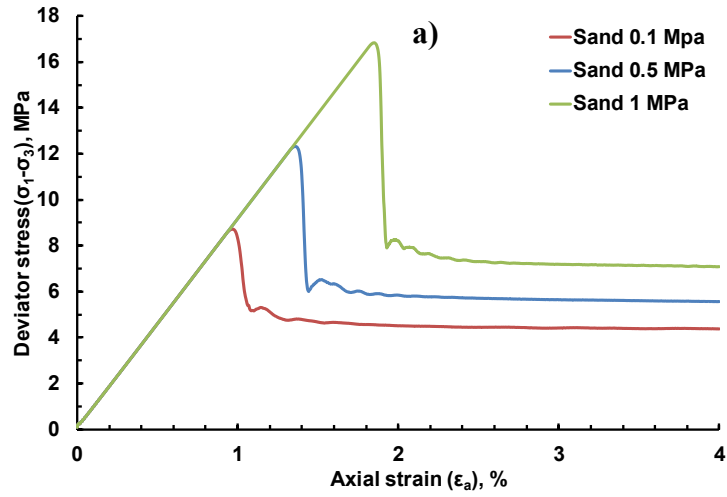
Sand:

Continued next page
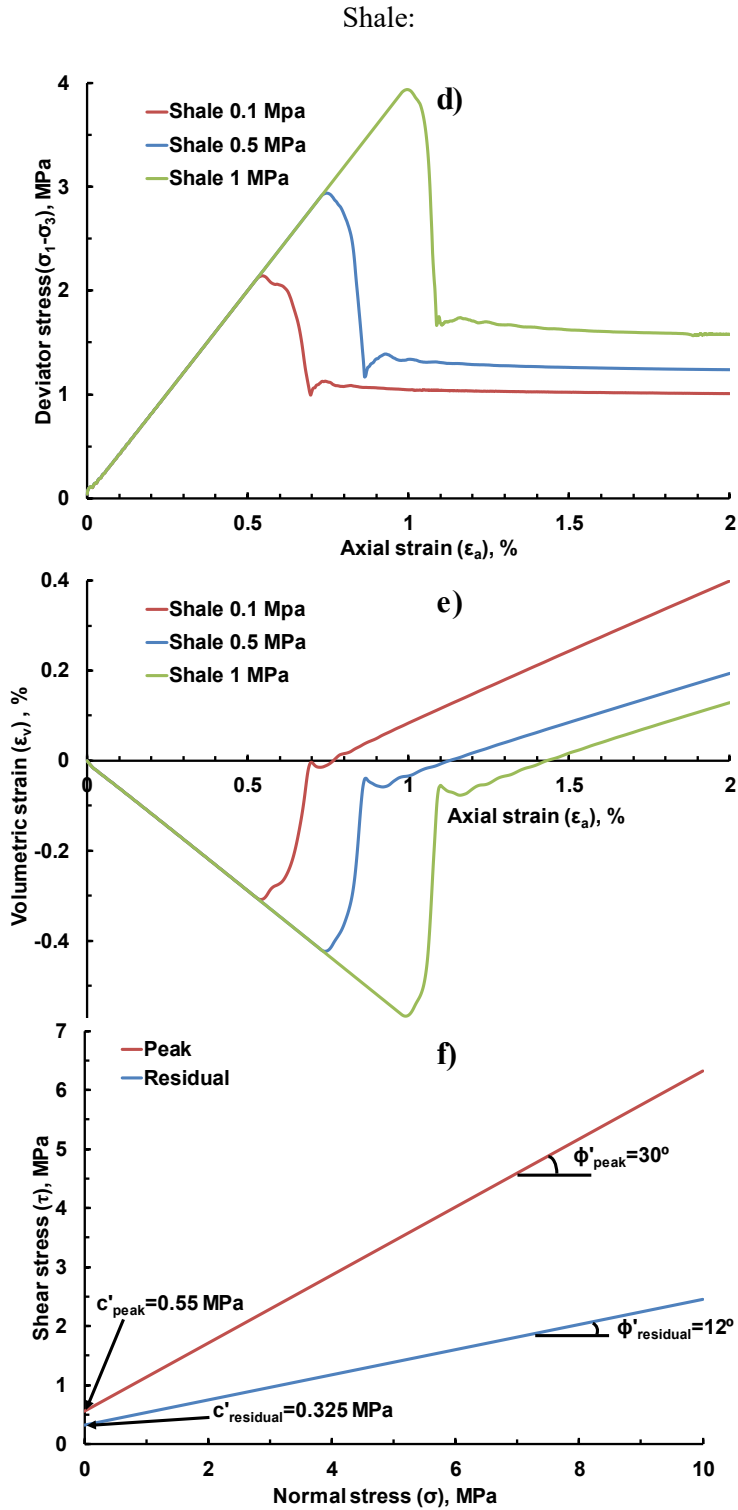
Shale:

Figure 3-6.   Constitutive behavior for homogeneous sand and shale realizations in the numerical bi-axial tests.

3.5   Volume Fraction of Shale

V_{sh} can be calculated from spectral gamma-ray data and is widely used for reservoir description. Previous experimental and numerical investigations have shown the significant impact of volume fraction of weaker material on the stiffness, strength and failure modes of the heterogeneous composite.

The experiments by Tziallas et al. (2013) demonstrated that the compressive strength and Young's modulus of the flysch consisting of sandstone and siltstone have an exponential relationship with the increase of siltstone percentage until it displays the strength of the siltstone material. The relation between uniaxial compressive strength (UCS) and siltstone percentage may differ according to the ratio of compressive strength of the two main facies in the composite heterogeneous rock mass. Liakas et al. (2017) revisited Tziallas's experimental study and used a 3D discrete element method (DEM) model with a parallel bond model to reproduce the failure patterns and variations of strength with different portions of weaker material.

Elkateb (2003) investigated the effect of intercalated clay seams on the macroscopic behavior of sand under plane strain conditions in FLAC (© Itasca). It showed that even a small fraction of shale (5%) has a non-negligible effect on both peak stress and failure mode. Models with different shale thickness have been classified into three zones based on their impact on peak stress and failure mode. Tang et al. (2000) conducted numerical parameter-sensitivity analyses to evaluate the effect of heterogeneities on the fracture processes and strength characterization of brittle materials under uniaxial compressive loadings using the Rock Failure Process Analyses code (RFPA2D). More diffused acoustic emission events and microfractures appear in the early stage of loading, which results in lower strength and nonlinear deformation behavior compared to a homogeneous specimen. The failure modes are more sensitive to local variations of mechanical

70

properties rather than the strength of the specimen. The impact of V_{sh} on the stiffness, strength and failure mode of the spatially correlated materials with shale bedding planes are quantitively investigated.

3.5.1 Failure Modes and Nonlinear Stress-Strain Response

Ten examples of the 2D spatially correlated sand-shale realizations for V_{sh} of 2%, 10%, 20%, 30%, 40%, 50%, 60%, 70% 80% and 90% are illustrated in Figure 3-7. When V_{sh} is 0, the realization is a pure sand realization. When V_{sh} equals to 1, the realization represents a pure shale realization. With the increase of V_{sh}, more horizontal shale bedding planes are embedded with fixed vertical (0.01) and horizontal (0.02) dimensionless ranges.

Following the boundary conditions in Figure 3-5, numerical tests are conducted for the sand-shale sequence oil sands realizations. The macroscopic stress-strain behavior is significantly impacted by V_{sh} (Figure 3-8a) when σ_3 is 0.1 MPa. The deviator stress used here is:

$$\sigma_d = \sigma_1 - \sigma_3 .$$
<div align="right">Equation 3-5</div>

The deviator stress is normalized by the peak deviator stress for homogeneous sand (8.7 MPa). The peak deviator stress for shale is 2.2 MPa, which is 25% of σ_{sand}. With the increase of V_{sh} from 2% to 30%, the normalized peak deviator stress decreases from 90% to 65% as shale has lower shear strength than sand. Before the macroscopic peak, plastic deformations occur in the weaker shale cells leading to nonlinear stress-strain behavior. The nonlinearity becomes more notable for realizations with V_{sh} larger than 20%, which is the further evidence that plastic deformations in the shale cells leading to elasto-plastic behavior. After the macroscopic peak, shear dilation is observed for oil sand realizations with various V_{sh} in Figure 3-8b. The volumetric strain does not

have a monotonic relationship with V_{sh} like the peak deviator stress; it is case dependent due to the strain localization affected by the configurations of weaker shale cells.
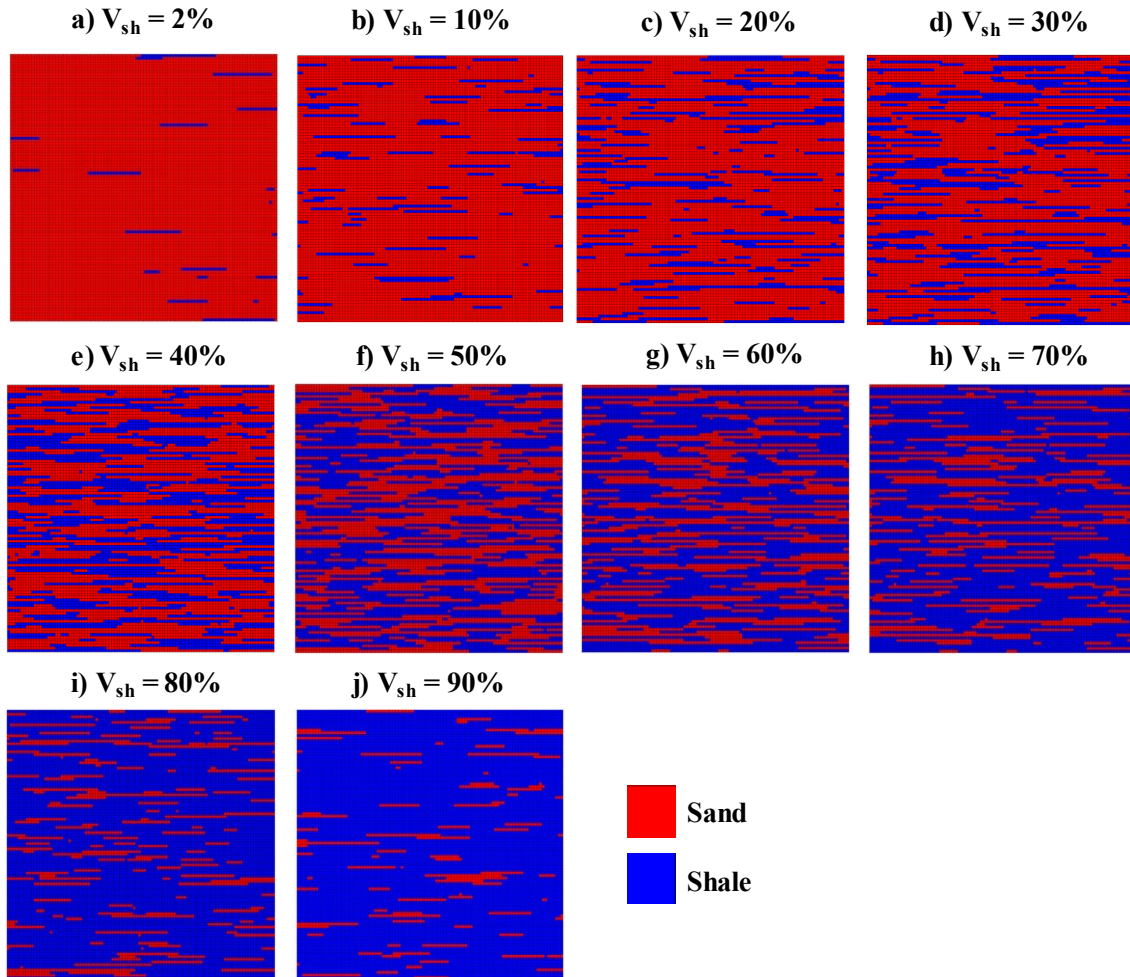
Figure 3-7.   2D spatially correlated sand-shale sequence realizations with V_{sh} from 0 to 1. Each realization has 100 by 100 cells. The size of each cell is 5 cm by 5 cm.
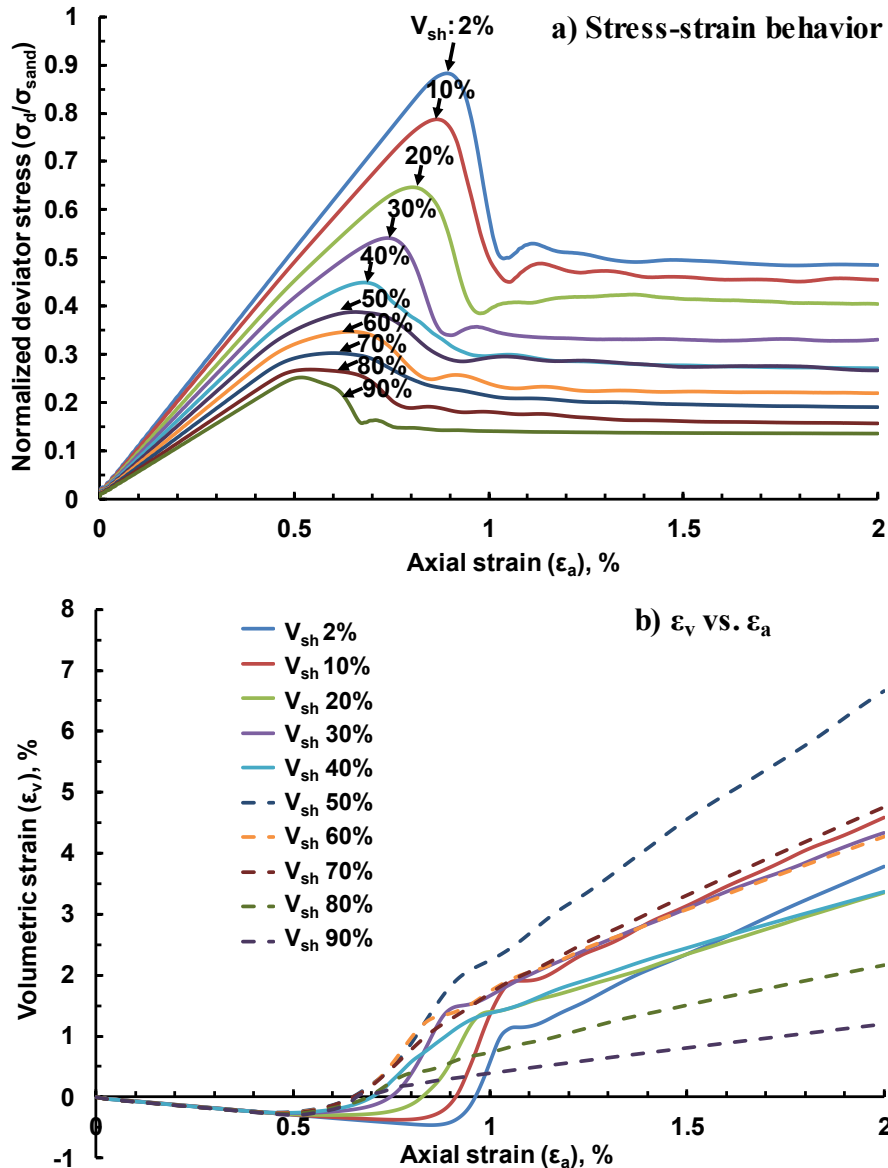
Figure 3-8.   Stress-strain behavior and ε_v vs. ε_a for 2D sand-shale sequence realizations with V_{sh} of 2%, 10%, 20%, 30%, 40%, 50%, 60%, 70%, 80% and 90% when σ_3 is 0.1 MPa.

The modes of failure control the strength and non-linear pre-peak stress-strain behavior for heterogeneous oil sands. Figure 3-9 illustrates the evolution of failure modes caused by strain localization for V_{sh} of 20%. Elastic deformations dominate before 0.4% axial strain. At 0.4% axial strain, plastic strain starts to localize in the shale cells with lower strength. As σ_d increases during the horizontal compression, shear failures (red) continue to build up in the shale cells (0.5% ε_a). It

73

is interesting to observe that tensile failures (green) are triggered vertically for the sand cells close to the failed shale cell. With the increase of σ_d, shear failures occur in the shale cells which have not failed (0.6% ε_a). Tensile failures start to extend and connect most of the separate failed shale layers. Some tensile failures gradually transfer to shear failures in the sand cells (the black circles @ 0.6% and 0.7% ε_a). When σ_d reaches the macroscopic peak stress (0.8% ε_a), the shear band starts to form across the entire realization before it gradually takes shape during the progressive failure period from ε_a of 0.8% to 1.0%. No further changes in modes of failure occur after σ_d drops to the residual state (1.0% ε_a).

The simulation result is consistent with the experimental results by Basu et al. (2013) for rock failure modes under different testing regimes. The coalesced wing cracks slowly build up in the zones with higher shear strength surrounding the pre-existing cracks of weak zones. In order to release the strain energy, the coalesced adjacent wing cracks propagate until the major shear band takes shape across the sample.

The plastic shear strain changes (Figure 3-10) are the consequence of complex failure modes. The location and magnitude of the plastic shear strain clearly demonstrate the initiation, propagation and formation of the shear band before reaching the macroscopic peak stress. The shear band quickly takes shape during the progressive failure period from 0.8% to 1.0% axial strain. When σ_d decreases to the residual value, the plastic strain continues to accumulate in the shear band without changing the shape of it.
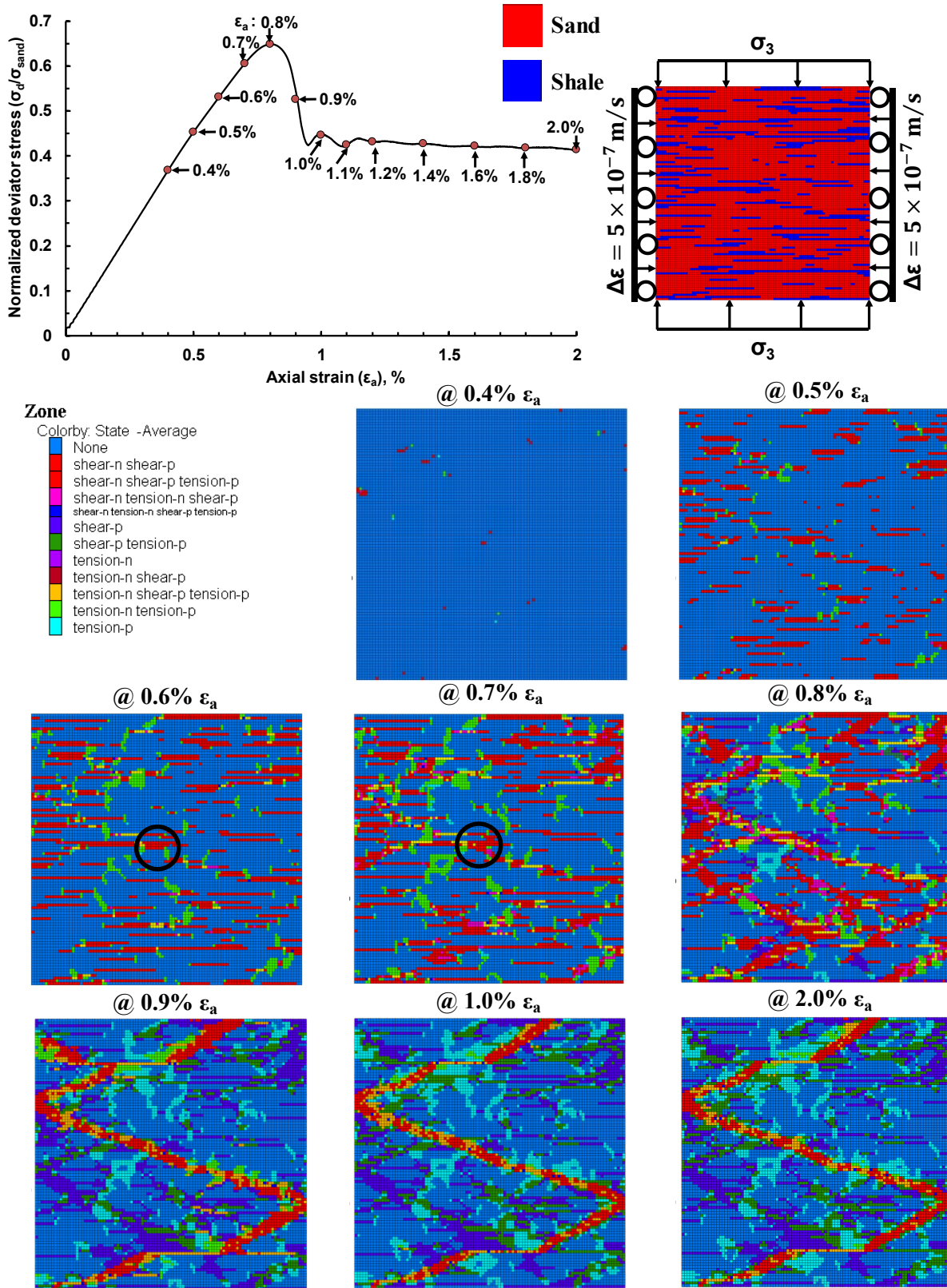
Figure 3-9.   Failure modes evolution under bi-axial tests for the realization with V_{sh} of 0.2.
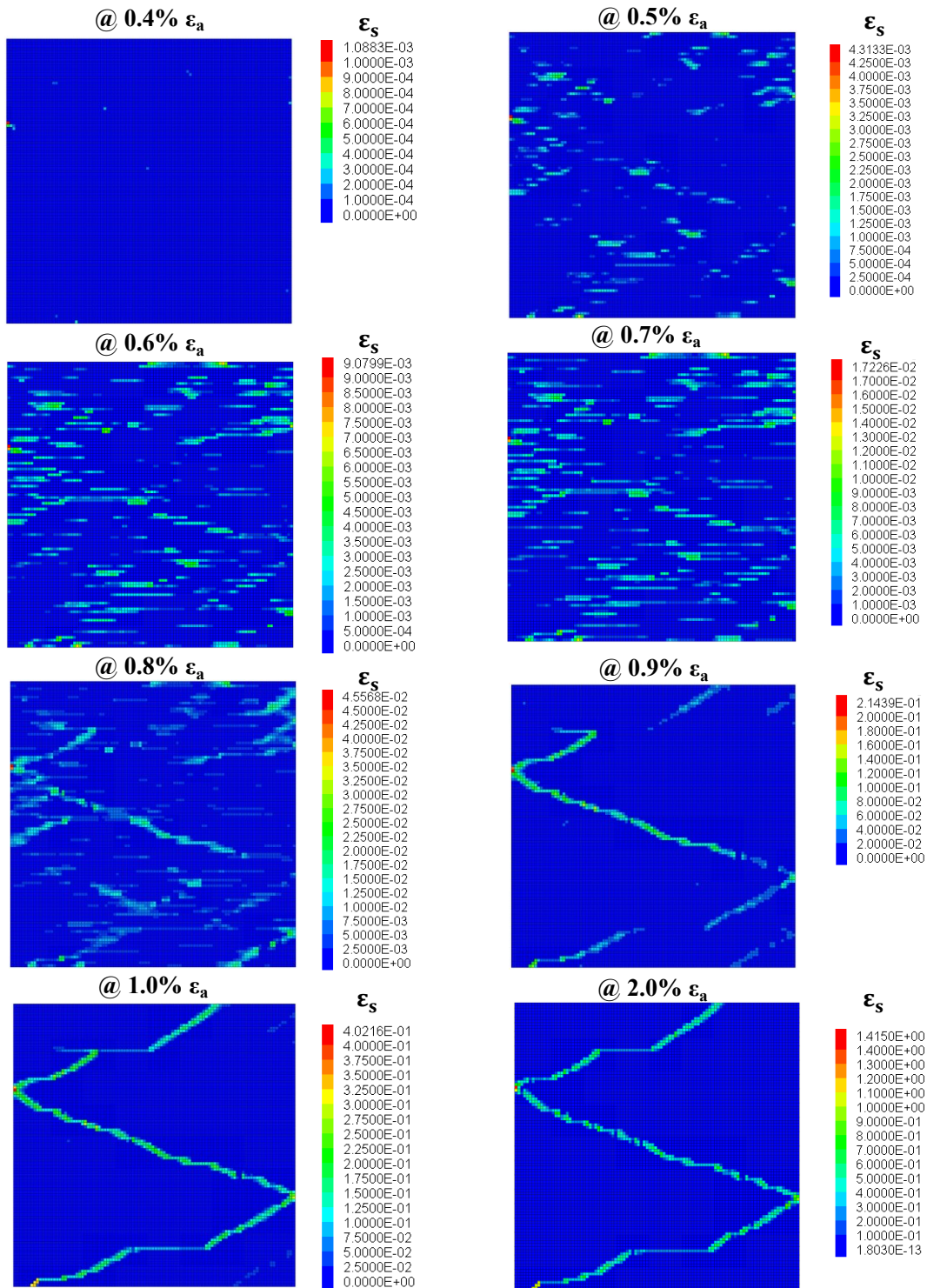
Figure 3-10   Localization of plastic shear strain during the bi-axial test for the realization with V_{sh} of 0.2.

Figure 3-11 shows the plastic shear strain at 2% axial strain when shear bands have developed for realizations with various V_{sh} (Figure 3-7). The failure modes are unique for each realization due to strain localization in weaker shale cells. The friction angles at 2% axial strain are illustrated in Figure 3-11k to 3-11t showing the influence of heterogeneity on the modes of failure. It can be observed that the locations and V_{sh} have a strong impact on the propagation of the shear band. For realization with V_{sh} of 2%, the shear failures start from the shale cells on the edge and propagate through the sand cells across the realization. This explains the higher effective peak deviator stress because creating shear failures in the stronger sand cells is more difficult than connecting the sheared shale cells to form the final shear band. With the increase in V_{sh}, plastic deformations in the nearby sand cells are easier to be triggered by the strain localization in the shale cells. The volume fraction of failed shale cells along the shear bands increases with V_{sh} until they dominate the shear band, which explains why the residual strength for cases with higher V_{sh} is systematically lower (Figure 3-8a). The axial strain transferring from contraction to dilation decreases with the increase of V_{sh}. For sandy realizations, a clear transition can be found between the peak and residual dilation period as observed in triaxial tests (Oldakowski 1994); while the transition becomes more smeared for higher V_{sh}.
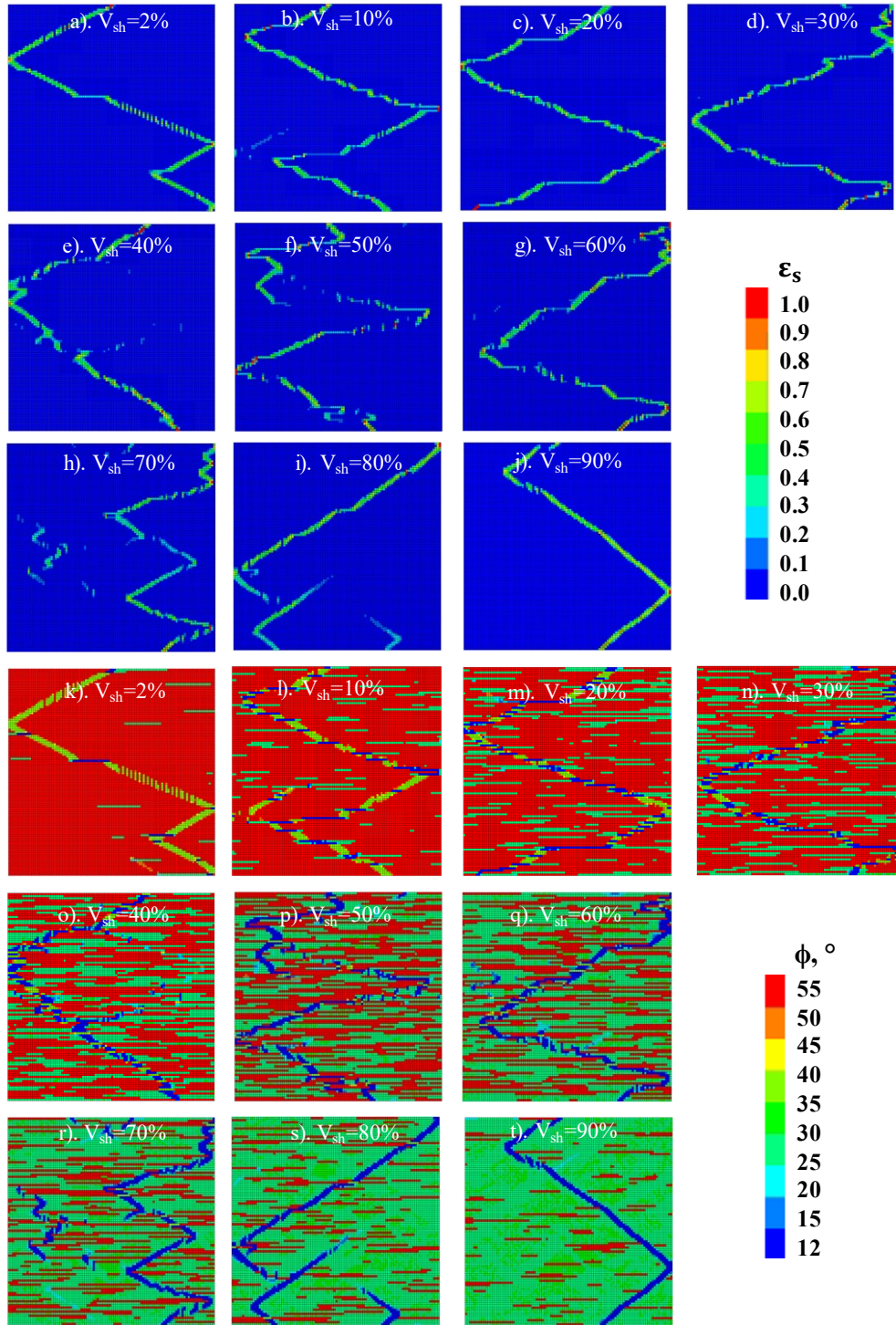
Figure 3-11.   Shear strain (a-j) and friction angles (k-t) at 2% axial strain for cases with V_{sh} from 0 to 1. The red zones represent the sand cells without plastic deformation. The green zones along the shear band are the sheared sand cells. The blue zones represent the sheared shale cells in the shear band.

Lade (1982) classified the failure modes of the dense sand into zone and line failures. Touhidi-Baghini (1998) summarized three major influential parameters for modes of failure: uniformity of density, tendency to dilate/compress and boundary conditions. The failure modes for heterogeneous oil sands in the numerical tests with low and high V_{sh} (0-20% & 80-90%) are mainly line (shear band) failures (Figure 3-11). The non-uniform distribution of weaker shale cells leads to strain localization and induces failures of nearby sand cells until the failure planes completely transecting the sample. The second reason is the tendency of shear dilation to aggravate the initial nonuniformity. Due to shear dilations, the strain localized areas become looser and weaker leading to the final line failure. For samples with medium V_{sh} (30%-70%), the failure mode is mixed with zone and line failures. Zone failures first occur in the widely spread shale cells and gradually transfer into line failure with the increase of loading stress by the smooth and uniform displacement boundary.

3.5.2   Impact of Failure Modes on the Peak Stress

To quantitatively study the impact of V_{sh} on the effective geomechanical properties of heterogeneous oil sand realizations, 85 spatially correlated realizations with V_{sh} ranging from 0 to 1 are generated and tested numerically. The macroscopic peak deviator stress (σ_p) of the oil sands realization is normalized by the peak stress of sand for systematic comparison. The normalized peak stress (σ_p/σ_{sand}) is observed to decrease monotonically from 1 to 0.25 when V_{sh} increases from 0 to 1 (Figure 3-12). It can be observed that σ_p/σ_{sand} is sensitive to V_{sh} when it is smaller than 40%. For V_{sh} larger than 40%, the slope becomes shallower and gradually reaches an asymptotic value (σ_{shale}). The normalized peak stress can be fitted with a polynomial:

$$\sigma_p/\sigma_{sand} = 0.8573V_{sh}^2 - 1.5225V_{sh} + 0.9356 \,, \qquad \text{Equation 3-6}$$

The R^2 for this model is 0.996 providing some confidence that the peak stress of heterogeneous oil sand realizations is well characterized by a polynomial relationship with V_{sh}.

Tziallas et al. (2013) and DEM simulations by Liakas et al. (2017) found a similar relationship between the strength of the sandstone with a siltstone layer versus the volume fraction of the siltstone. The peak stress of the flysch composite rock decreases rapidly with the siltstone percentage (<40%) due to a decrease in brittleness and became more ductile as the behavior of the siltstone gradually dominates the response of the composite rock.
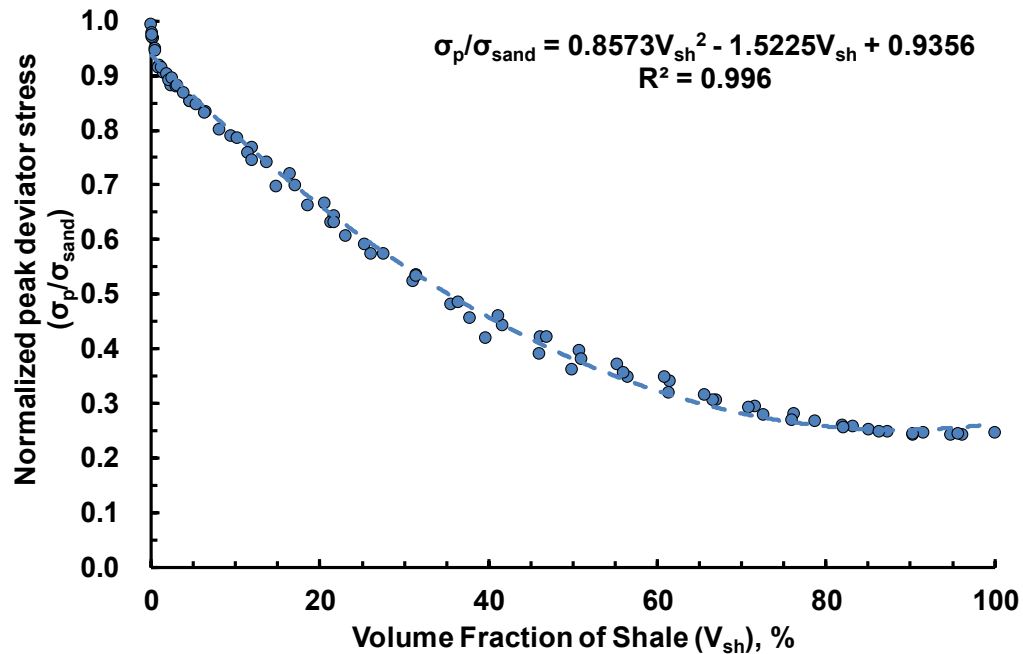
Figure 3-12. Normalized failure deviator stress for heterogeneous sand-shale realizations with V_{sh} from 0 to 1.

The geomechanical response of sand with intercalated clay seams under plane strain has been investigated in FLAC by Elkateb (2003). Although the simulation results are based on a layered model, the trend is found to be qualitatively consistent with the simulation results for spatially

correlated models. Three heterogeneity zones are classified based on the relationship between normalized peak stress and V_{sh} (Figure 3-13). In zone 1, the peak stress decreases 20% with only 10% V_{sh} change, which is significantly larger than Elkateb's simulation results. The significant change in peak stress is caused by the change of failure modes. Shear band (line) failure across the sand cells is the major mode of failure when V_{sh} is smaller than 10%. However, it is strongly dependent on the shale configurations as illustrated by Figure 3-14, showing that the location of the shale bedding planes controls the path of the failure plane. Therefore, the increase of the shale bedding planes in the reservoir provides more failed shale cells to trigger the failure in the nearby sand cell, which lowers the macroscopic shear strength of the oil sand realization.

In zone 2 ($0.1 < V_{sh} < 0.75$), the peak stress is almost logged linear with V_{sh}. The failure modes are very sensitive to the location and connectivity of the shale cells (Figure 3-11m to Figure 3-11r). Zone failures at the weaker shale cells dominate the modes of failure, mixed with coalesced failures in the sand cells nearby. The IHS in Alberta oil sands belongs to zone 2 where the interactions of sand and shale govern the geomechanical response including the modes of failure. In zone 3, the macroscopic peak stresses of the sand-shale sequence realizations are governed by the shear strength of shale because the shear failures concentrate in the weaker shale cells (blue path in Figure 3-11s and t).

The V_{sh} to distinguish zones 1, 2 and 3 are found to have a close relationship with the ratio of peak stress for the strong and weak components ($\sigma_F^{weak}/\sigma_F^{Strong}$) according to Elkateb (2003). The boundary V_{sh} is expected to be smaller for samples with weaker clay contents. For oil sands with different $\sigma_F^{weak}/\sigma_F^{Strong}$, sensitivity analyses are recommended before determining the boundary of zone 1, 2 and 3.
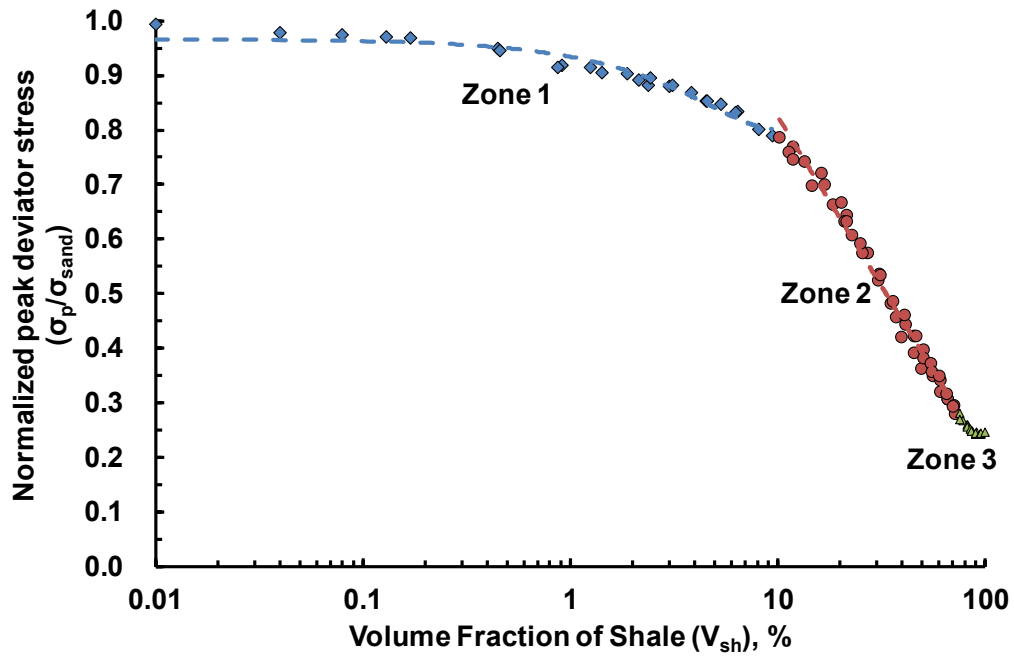
Figure 3-13. Decrease in normalized failure deviator stress of heterogeneous sand-shale realizations with increase V_{sh} from 0 to 1 in log scale.
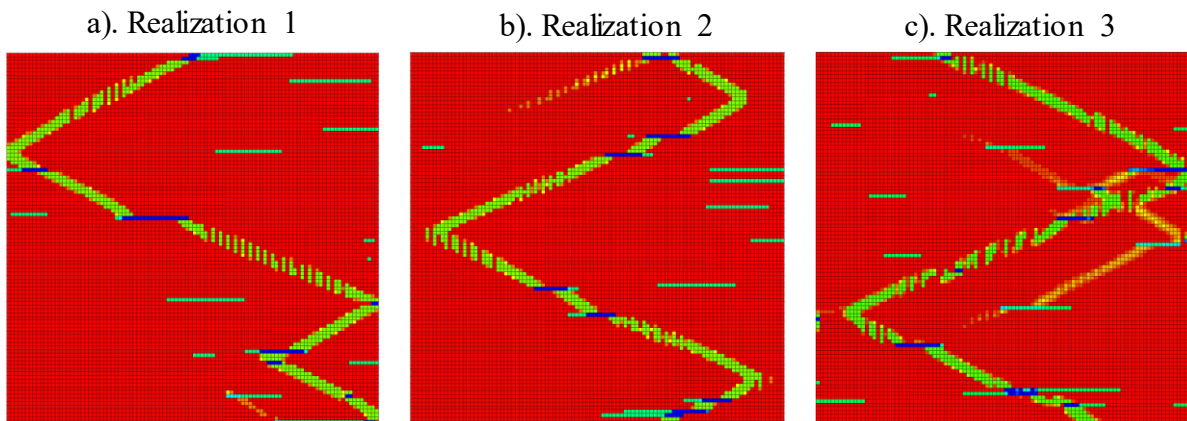
Figure 3-14. Friction angles at 2% axial strain for cases with V_{sh} of 0.2 showing the difference of failure planes caused by the shale configurations.

3.5.3   Dynamic Young's Modulus

Effective stiffness (Young's modulus) of the heterogeneous oil sands can be estimated by the ratio of stress and strain. Figure 3-8a shows that Young's modulus decreases with the increase of V_{sh}. When $V_{sh} > 20\%$, elasto-plastic behavior is observed as shale fails before the macroscopic peak. The tangent modulus (E_{tan}) is used to quantify the dynamic stress-strain response at different stages before the peak point, e.g. $E_{0.5}$ represents the tangent modulus at 50% of the peak deviator stress. Figure 3-15 illustrates the normalized tangent modulus by sand modulus (E_{tan}/ E_{sand}) for heterogeneous oil sand realizations of different V_{sh}. In zone 1 ($V_{sh} < 10\%$) and 2 ($V_{sh} > 75\%$), E_{tan} is close to sand and only decreases slightly when approaching the peak deviator stress because strains are localized in the sand cells for zone 1 and shale cells for zone 3. The change in E_{tan} becomes more complex in zone 2 ($10\% < V_{sh} < 80\%$). Figure 3-15b shows nearly constant E_{tan}/E_{sand} when $\sigma_d < 0.5\ \sigma_d$ before the failure of shale. With the increase of σ_d, the failures of shale lead to rapid decrease of E_{tan}.
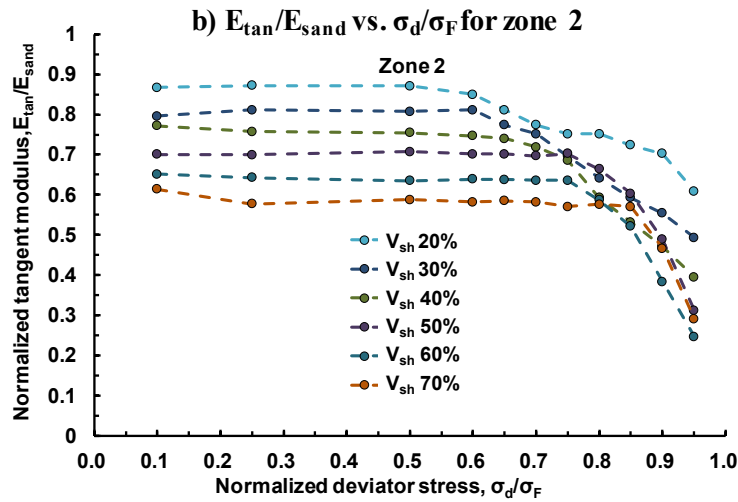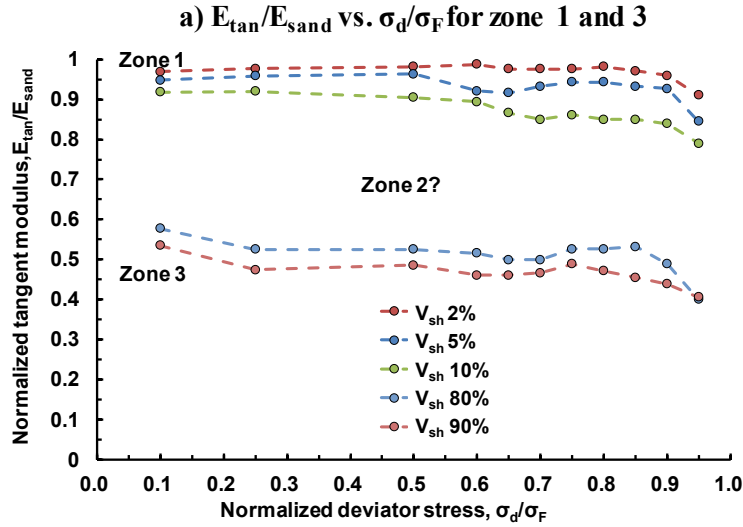
Figure 3-15.   A decrease in E_{tan}/E_{sand} at different percentages of σ_d. Realizations in zone 1 and 3 have nearly constant E_{tan} indicating linear stress-strain behavior before macroscopic peak stress. The tangent modulus of zone 2 decreases when approaching peak showing an elasto-plastic behavior for realizations with V_{sh} from 0.2 to 0.7.

To analyze the complex non-linear stress-strain behavior in zone 2, E_{tan}/E_{sand} at different levels of σ_d is plotted for realizations with V_{sh} from 0 to 1. $E_{0.5}$ is found linear with V_{sh} as elastic deformation dominates. E_{tan}/E_{sand} monotonically decreases with the increase of σ_d, e.g. $E_{0.9} > E_{0.8}$, for a given heterogeneous oil sand realization. Due to the change of failure modes, the relationship between E_{tan}/E_{sand} and V_{sh} is highly nonlinear. From $E_{0.75}$ to $E_{0.95}$, it first decreases and then increases with

V_{sh}. When approaching the macroscopic peak stress, e.g. $E_{0.95}$, E_{tan} for shaly realization ($V_{sh}>40\%$) can be even smaller than E_{shale}. This indicates that the transition from zone to linear failures in IHS may lead to softer stiffness than its shale component. For heterogeneous oil sands in zone 2, estimating the effective Young's modulus should consider the elasto-plastic behavior at different magnitudes of stress.
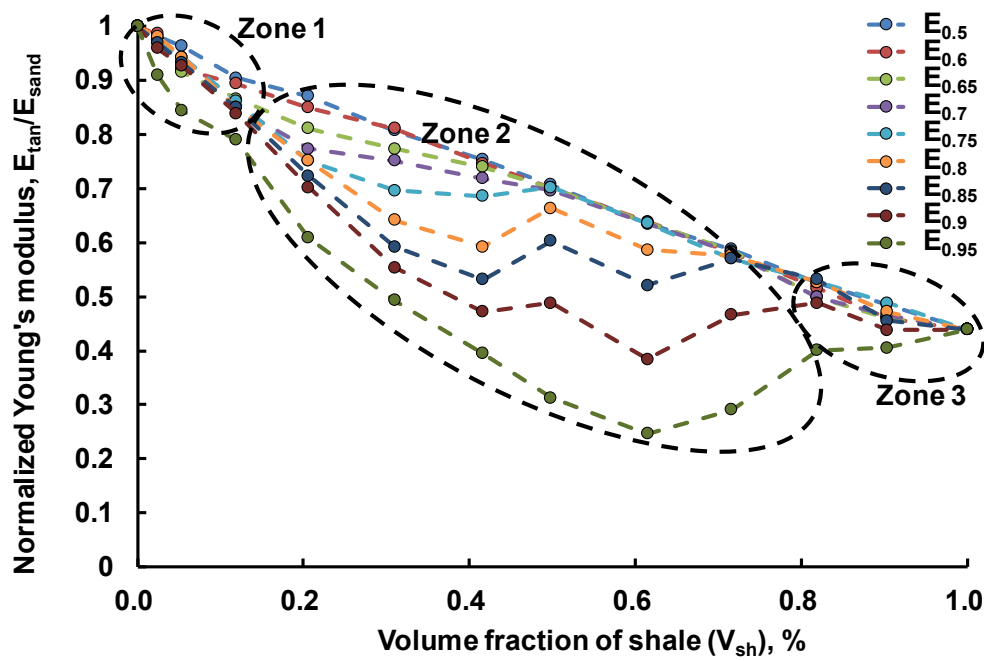
Figure 3-16.   The normalized tangent modulus at different percentages of peak deviator stress for cases with V_{sh} from 0 to 1.

3.5.4 Shear Strength

3.5.4.1 Mohr-Coulomb Failure Envelope

The Mohr-Coulomb failure criterion represents the envelope obtained from shear strength at different normal stress σ as a function of friction angle ϕ and cohesion c:

$$\tau = \sigma \tan \phi + c \qquad \text{Equation 3-7}$$

In p-q space, the M-C failure criterion is:

$$q = p \sin \phi + c \cos \phi , \qquad \text{Equation 3-8}$$

where $q = (\sigma_1 - \sigma_3)/2$ and $p = (\sigma_1 + \sigma_3)/2$ in plane strain condition.

Numerical bi-axial compression tests are conducted in three confining stresses 0.1, 0.5 and 1.0 MPa for oil sands realizations of various V_{sh}. For the case with V_{sh} of 20% (Figure 3-7c), the stress-strain response is illustrated in Figure 3-17a. The peak and residual deviator stress are higher for cases with higher confining stress. The volume change is highly dependent on the confining stresses (Figure 3-17b).
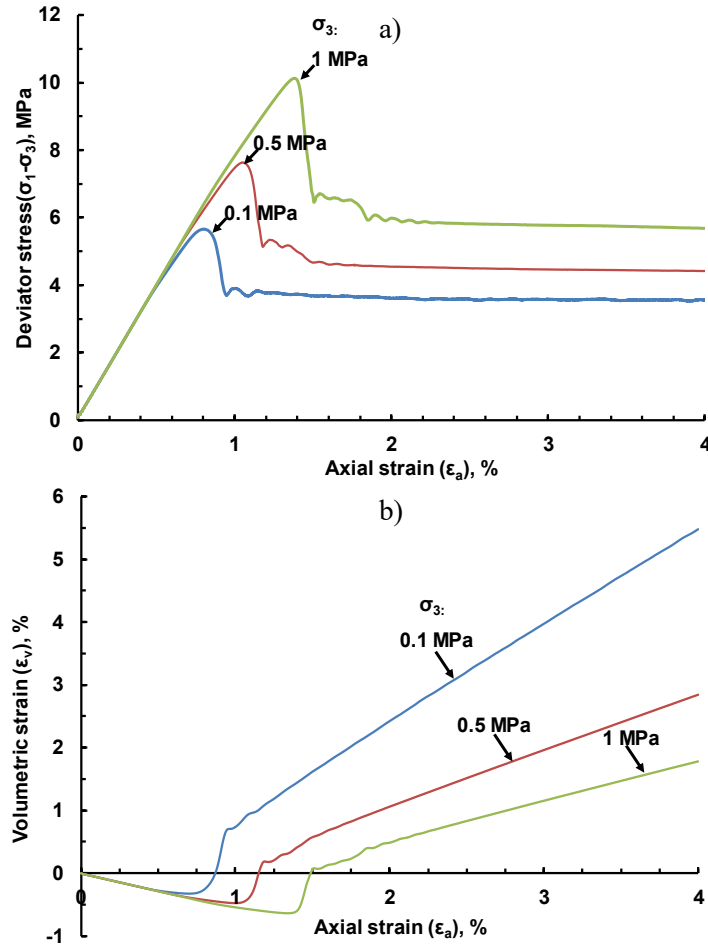
Figure 3-17. The deviator stress and volumetric versus axial strain for case $V_{sh}=0.2$ with confining stress of 0.1, 0.5 and 1.0 MPa.

The peak failure envelopes are illustrated in Figure 3-18, where sand and shale are the upper and lower boundaries for oil sand realizations with V_{sh} from 0 to 1. With the increase of V_{sh}, the peak failure envelopes drop in p-q space especially for oil sands realizations in zone 2, which explains the sensitivity of shear strength for realizations with V_{sh} from 0.2 to 0.8. To be noted, the failure envelopes in Figure 3-18 is the peak M-C failure envelopes. When associated with plastic deformation, the friction angle is mobilized leading non-linear failure envelopes. The quantification of post-peak softening response for heterogeneous oil sands is discussed in Section 3.5.5.
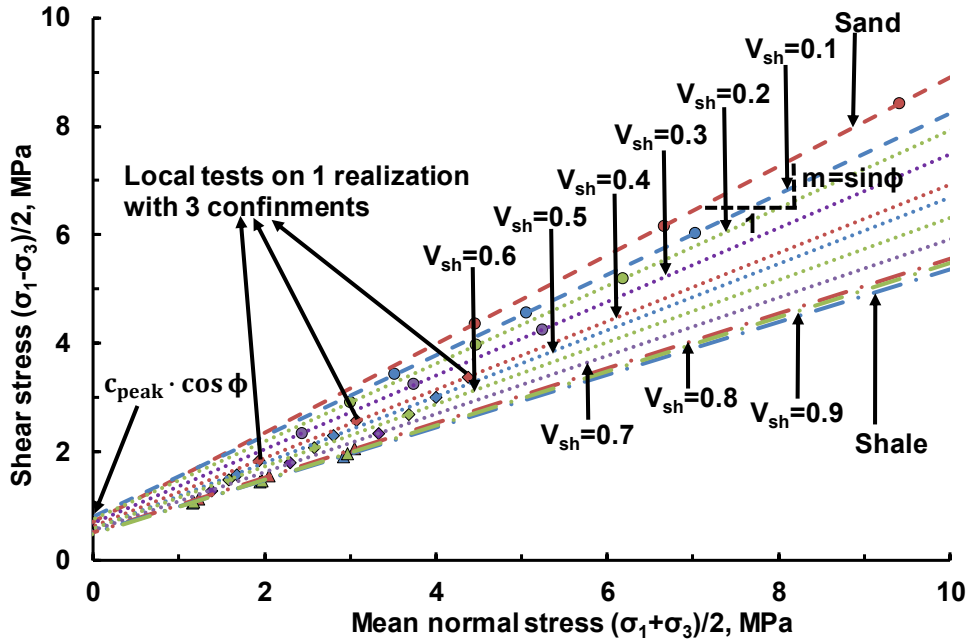
Figure 3-18. Peak Mohr-Coulomb failure envelopes for heterogeneous realizations as a function of V_{sh}.

3.5.4.2 Friction Angle

The peak friction angles determine the slope of the failure envelope. Figure 3-19 shows that it monotonically decreases with the increase of V_{sh} and fit by a polynomial with V_{sh}:

$$\phi_p = 15.667 V_{sh}^2 - 39.801 V_{sh} + 52.974 \ .$$

Equation 3-8

Among the weighted arithmetic, geometric and harmonic averages which are widely used as a quick estimation for homogenization, the harmonic average provides the best estimate of peak friction angle. The reason is that shear failures concentrate in the weak shale bedding planes so that the shear strength of shale weights more in the estimation of the macroscopic shear strength. Therefore, the harmonic average is recommended to be the initial estimate of the upscaled peak friction angle when V_{sh} is from 0.15 to 0.95 according to Figure 3-19.
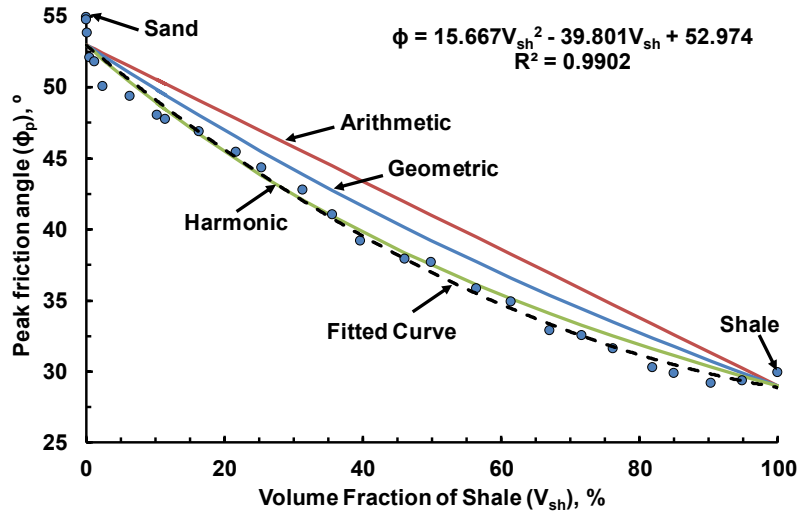
Figure 3-19.   Decrease of peak friction angle as a function of V_{sh}. The fitted curve is close to the weighted harmonic average of sand and shale friction angle.

The decrease in peak friction angle with the increase of V_{sh} is illustrated in Figure 3-20, where three heterogeneous zones can be classified. The peak friction angle is very sensitive to V_{sh} in zone 2 because of the large variations of failure envelopes.
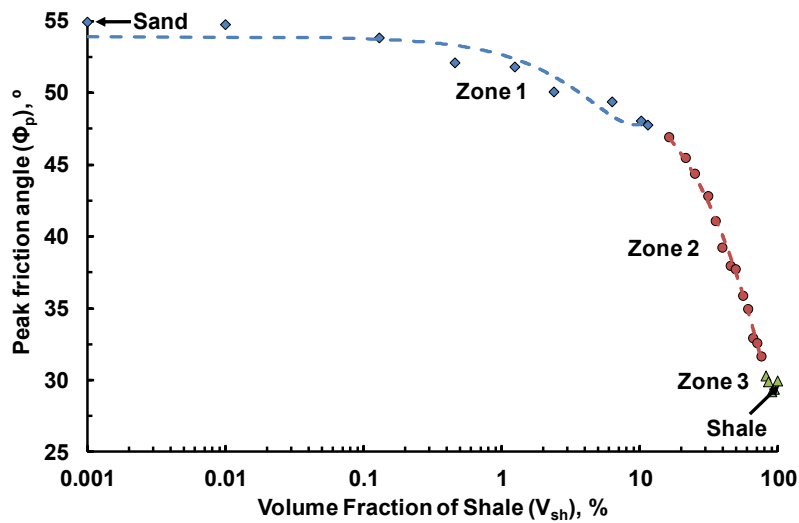
Figure 3-20.   The peak relationship between peak friction angle and V_{sh} in log scale.

3.5.4.3 Cohesion

The cohesion of the realizations can be calculated by intersections of the failure envelope and y-axis. Figure 3-21 illustrates the decrease in peak cohesion as a function of V_{sh}. The monotonic decrease of peak cohesion can be fit by a polynomial as:

$$c = 0.6512V_{sh}^2 - 1.3818V_{sh} + 1.2847 \ . \hspace{3cm} \text{Equation 3-9}$$

Similar to the friction angle, the weighted harmonic average gives the best estimate of effective cohesion among the three traditional averages. For Alberta oil sands, the cohesion of oil sands can be as low as zero, while the cohesion of the McMurray Formation shale is usually below 1 MPa. Therefore, the shear strength of the Alberta oil sands is more dominated by the friction angle in reservoir conditions.
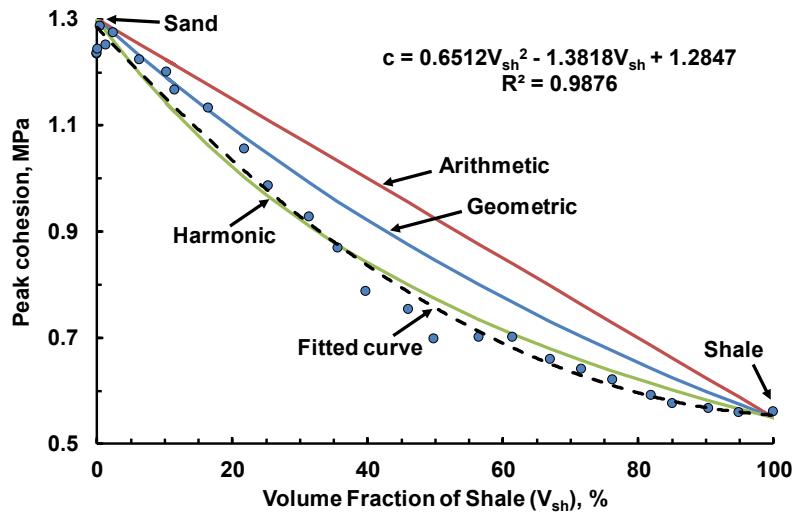
Figure 3-21.   Decrease of peak cohesion as a function of V_{sh} showing that harmonic average is a good approximate for effective peak cohesion for realizations with various V_{sh}.

The peak friction angle and cohesion determine the macroscopic peak failure envelope for heterogeneous oil sands. However, shear failures in shale and induced plastic deformations in the sand still occur before the Mohr-Coulomb circle reaches the macroscopic peak failure envelope. The lithological heterogeneity in oil sands leads to plastic deformations before the peak point of the stress-strain curve, which is the driving force for the parameterization and upscaling of macroscopic plastic properties at sub-grid scale.

3.5.5 Post-Peak Softening Response

Post-peak softening is widely observed in triaxial tests for oil sands. The post-peak strength decreases with the cumulation of plastic deformations until reaching the critical state. The mobilized strength of oil sands is bounded by the peak friction angle ϕ_p and the critical state friction angle ϕ_{cv}. The effective peak friction angle has a polynomial relationship with V_{sh} as demonstrated in Figure 3-19. The residual peak friction angle can be calculated at large axial strain (>5% for oil sand) as Figure 3-22 shows. Due to progressive failure, the failure envelope of the oil sands moves from the peak to residual failure envelope. The residual friction angles for realizations with V_{sh} from 0 to 1 are illustrated in Figure 3-23. The residual friction angle can be fitted with a linear relationship (arithmetic average):

$$\phi_{res} = -23.323 V_{sh} + 37.875 \qquad \text{Equation 3-10}$$
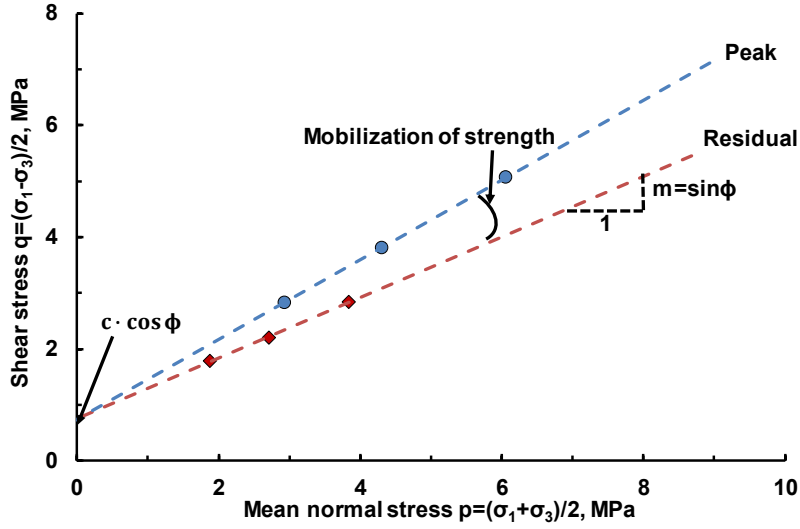
Figure 3-22.   Mobilization of strength in p-q space for realization with V_{sh} of 0.2.
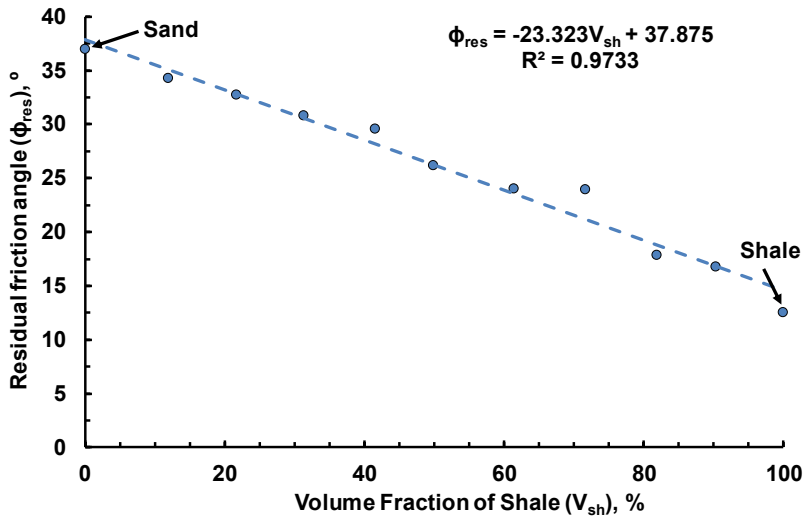
Figure 3-23.   Residual friction angle versus V_{sh} for heterogeneous oil sands realizations.

Shear dilatancy is widely observed after the peak point for oil sands and strongly related to the

confining stress. The dilation angle of oil sand is first examined in a plane strain condition and

defined by the shear dilatancy rate ($\Delta\varepsilon_v^p/\Delta\varepsilon_a^p$) (Wong 1999):

$$sin\,\psi = \frac{\Delta\varepsilon_v^p}{\Delta\varepsilon_v^p - 2\Delta\varepsilon_a^p} = \frac{\Delta\varepsilon_v^p/\Delta\varepsilon_a^p}{\Delta\varepsilon_v^p/\Delta\varepsilon_a^p - 2}\,,$$

Equation 3-11

where $\Delta\varepsilon_v^p$ and $\Delta\varepsilon_a^p$ are the increment of volumetric plastic strain and axial plastic strain. For oil sands, the shear dilatancy rate is highly non-linear and can be classified as the peak and residual dilatation rate (Figure 3-17b). The dilation angle decreases with the increase of plastic strain until it approaches the critical state. Rowe's dilatancy theory (Rowe 1962; Vermeer and Borst 1984) is used to calculate the dilation angle for dense sand from the friction angle at current and critical states:

$$sin\,\psi = \frac{sin\,\phi - sin\,\phi_r}{1 - sin\,\phi\,sin\phi_r}$$

Equation 3-12

Because the heterogeneous oil sands are defined as a mixture of sand and shale, it is safer to compute the peak dilation angle based on Equation 3-11. The relationship between peak dilation angle and V_{sh} is shown in Figure 3-24. The simulation results are scattered as the shear dilation is affected by the relative positions of shale layers due to strain localization. The peak dilation angle tends to decrease when the fine contents (shale) increases. The peak dilation angle is fit with V_{sh} by a linear relationship as:

$$\psi_p = -14.325V_{sh} + 22$$

Equation 3-13
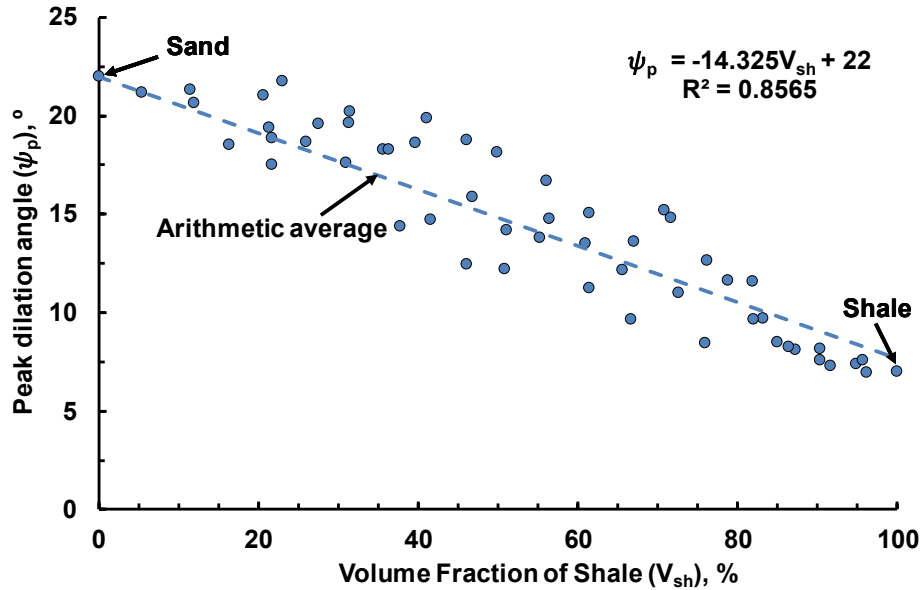
Figure 3-24.   Decrease of peak dilation angle for realizations with V_{sh} from 0 to 1.

The linear correlation obtained for residual friction angle and peak dilation angle based on V_{sh} helps to characterize the mobilized strength of heterogeneous oil sands after the peak. According to Figure 3-24, the arithmetic average is a reasonable initial estimate for the dilation angle in plastic upscaling.

3.6   Spatial Variability

The impact of spatial variability of geomechanical properties has been extensively studied as demonstrated in Section 2.3.2, but investigations on the effect of lithological heterogeneity on the reservoir-geomechanics response are still limited. The level of lithological heterogeneity is not only determined by V_{sh} but also influenced by the ranges of shale. Section 3.5 investigates the impact of V_{sh} on failure modes, stress-strain response and effective geomechanical properties. Here, the failure modes and stress-strain response are investigated for heterogeneous oil sands with various ranges.

3.6.1 Realizations with Various Ranges

The generation of the spatially correlated oil sands realizations is explained in Section 3.1. The dimensionless horizontal (a_h^d) and vertical ranges (a_v^d) are the key parameters to characterize the connectivity of shale in the sand-shale sequence heterogeneous oil sands. Respecting the geology of the McMurray Formation, vertical ranges are usually smaller than horizontal ranges. a_h^d is set from 0.05 to 1, while a_v^d is from 0.01 to 0.2 here. Figure 3-25 presents a series of 2D sand-shale realizations with various horizontal and vertical ranges, where horizontal shale bedding planes are assumed with V_{sh} of 0.2.
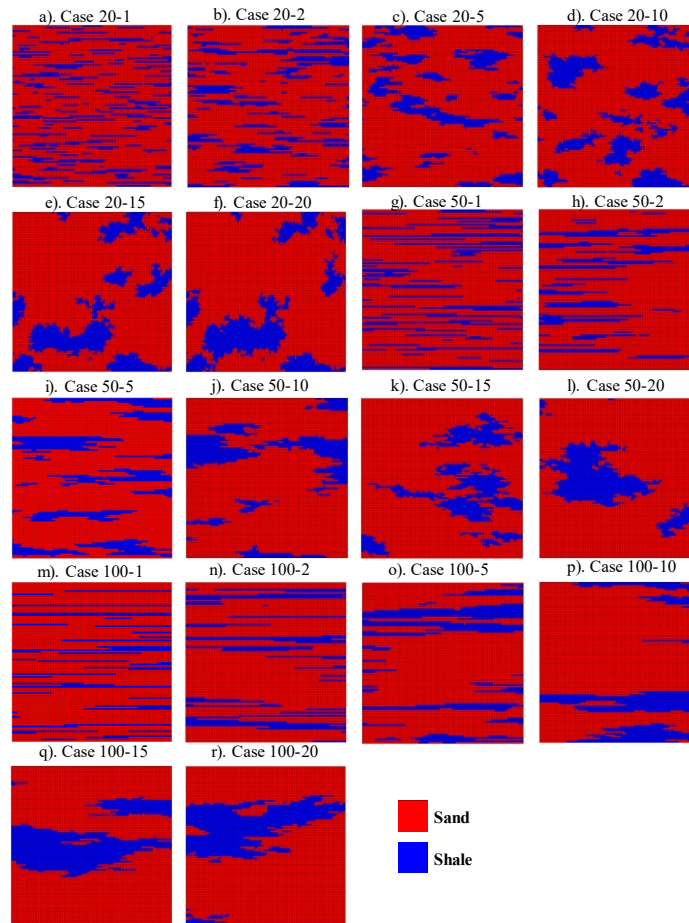
Figure 3-25.   Realizations (V_{sh} = 0.2) with various vertical and horizontal ranges. Case 100-20 represents a 100 by 100 2D realization with 100 as α_H and 20 as α_V.

3.6.2 Stress-Strain Behavior

Following the bi-axial testing regime, numerical horizontal compression tests are conducted for realizations in Figure 3-25. The stress-strain responses for case 50-1, 50-5 and 50-20 (Figure 3-26a) show the influence of vertical ranges (perpendicular to major principal stress direction) on the macroscopic geomechanical response. When a_v^d increases from 0.01 to 0.2, the peak deviator stress decreases from 6.3 MPa to 4.2 MPa. The tangent modulus is constant before 0.4% axial strain (yield point). When close to peak, the tangent modulus for case 50-5 and 50-20 decreases rapidly due to plastic deformations of shale. This is consistent with Tang et al. (2000) that a heterogeneous rock sample has more acoustic emissions and failures than homogeneous samples. Figure 3-26b presents the change of volumetric strain with the increase in axial strain. The transition point from contraction to dilation has a lower axial strain for cases with thicker shale layers when under compression horizontally. The shear dilations of the thick shale layers further decrease the strength of the sand cells leading to a smoother transition in terms of dilatancy rate.

The stress-strain responses for case 20-5, 50-5 and 100-5 are plotted in Figure 3-27a showing that the shear strength in bi-axial tests increase from 4.2 MPa to 6.0 MPa when a_h^d increases from 0.2 to 1.0. The elasto-plastic behavior is more obvious for realizations with shorter (case 20-5) and thicker (case 50-20) shale layers. Figure 3-27b illustrates that cases with short shale layers tend to transfer from contraction to dilation at a smaller axial strain. The difference between the peak and residual shear dilatancy rate is smaller for realizations with shorter shale bedding planes (case 20-5) compared to longer shale layers (cases 100-5 and 50-5).
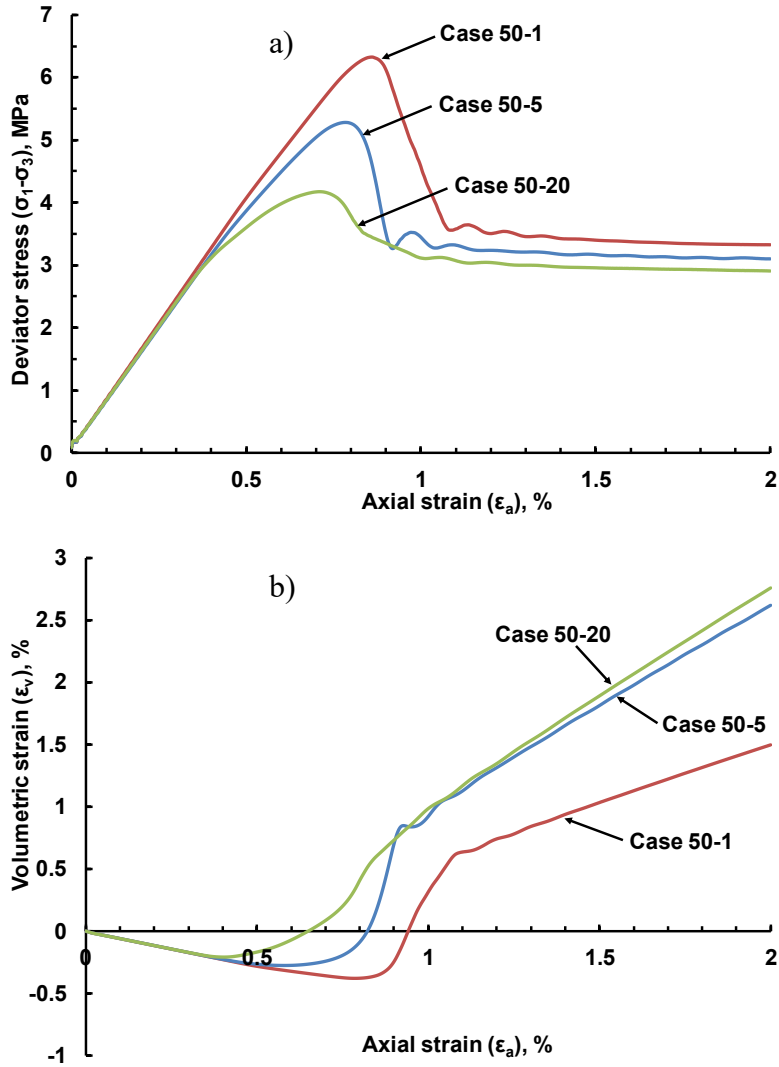
Figure 3-26.   Stress-strain behavior and ε_v vs. ε_a for case 50-1, 50-5 and 50-20. Horizontal ranges are fixed while vertical ranges increase from 1 to 20.

97
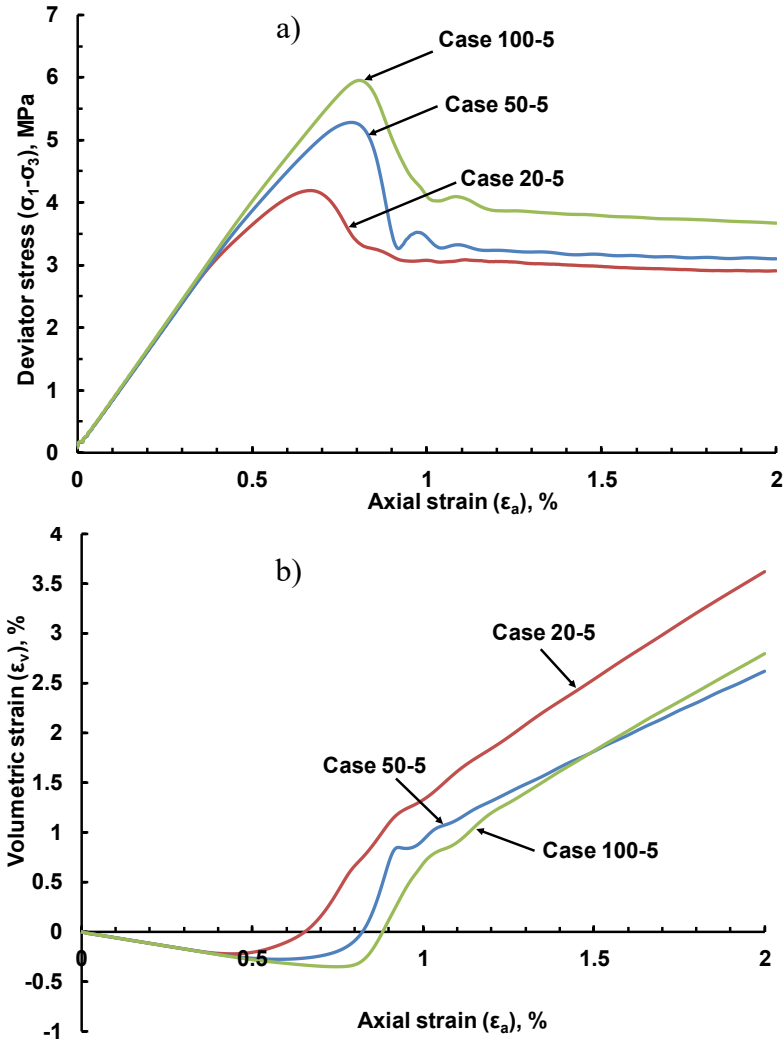
Figure 3-27.   Stress-strain behavior and ε_v vs. ε_a for Case 20-1, 50-5 and 100-5. Vertical ranges are fixed while horizontal ranges increase from 20 to 100.

3.6.3   Failure Modes

The failure modes of heterogeneous oil sands are significantly affected by V_{sh} as demonstrated in Section 3.5. Three heterogeneous zones are classified based on the failure modes and induced changes in stress-strain response for heterogeneous oil sands and IHS. The evolution of failures during the bi-axial numerical tests are illustrated in Figure 3-9 and 3-10. Plastic deformations first

appear in the weaker shale cells and then trigger the coalesced failures in the nearby sand cells, which explains the non-linear stress-strain response before the peak.

Figure 3-28 illustrates the friction angle at 2% axial strain and shows the failure modes for cases with various spatial ranges in bi-axial compression tests with a confining stress of 0.1 MPa. Similar to V_{sh}, the spatial variability of shale bedding planes causes considerable changes in failure modes. At the residual state, when the shear bands have established at 2% of ε_a, the failure plane is unique for each realization. From Figure 3-28a to 3-28f, the failure planes gradually transfers from line failure to zone failures with the increase of thickness of shales. The strain localization in the thicker shale layers leads to the formations of cracks from the tips of the oriented failure planes in the surrounding sand in order to release the strain energy in the form of shear failures. Therefore, the realizations with thicker shale layers have lower stiffness and shear strength because of elasto-plastic behavior before peak (Figure 3-26a). The observed volume change is significantly larger for cases with larger vertical ranges.

With an increase in horizontal range of shale layers, the shear band becomes more regular in shape because the intact failures (line failure) are more dominant compared to local failures in the weaker shale cells (zone failure). As a consequence, the shear strength and stiffness are larger for realizations with continuous shale layers.

a). Case 20-1 b). Case 20-2 c). Case 20-5 d). Case 20-10
e). Case 20-15 f). Case 20-20 g). Case 50-1 h). Case 50-2
i). Case 50-5 j). Case 50-10 k). Case 50-10 l). Case 50-10
m). Case 100-1 n). Case 100-2 o). Case 100-5
p). Case 100-10 q). Case 100-15 r). Case 100-20
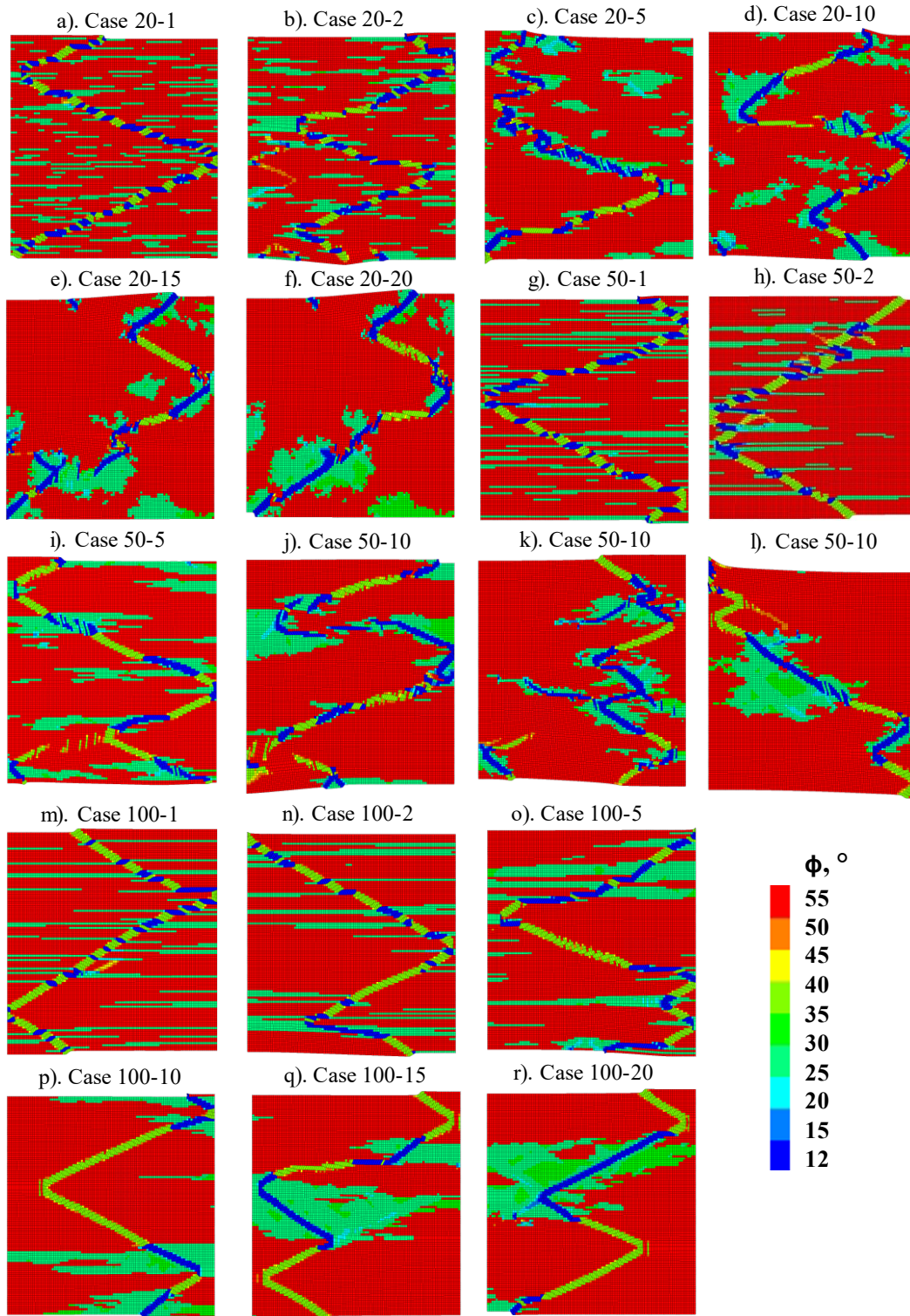
Figure 3-28. Friction angle at 2% ε_a showing the failure modes impacted by shale configurations. The shear bands in blue represent the plastic deformations in shale cells while shear bands in green are the failed sand cells surrounded by non-failed sand cells (red).

The variety of failure modes is the most important reason for the difference in macroscopic stress-strain response and it is closely related to spatial continuity. The parameterization of the macroscopic geomechanical response when considering the complex failure modes with various spatial ranges of shale will allow for quick estimations of the upscaled geomechanical properties.

3.6.4 Parameterization of Geomechanical Response Due to Various Ranges

Three sets of spatially correlated sand-shale sequence realizations, classified by horizontal ranges (20, 50 and 100), are tested by in the same boundary conditions (Figure 3-5) to study the effect of ranges on macroscopic geomechanical response. Figure 3-29 summarizes the relationship between shear strength and ranges. For each group of realizations with a fixed horizontal range, the shear strength becomes lower with the increase of dimensionless vertical ranges. Given a fixed vertical range, the shear strengths of realizations with larger horizontal ranges, e.g. 100-(1~20), are systematically higher.

The range ratio, defined as the ratio of dimensionless horizontal range against dimensionless vertical range, is introduced to characterize the interactions of vertical and horizontal ranges on σ_F:

$$R_a = a_h^d / a_v^d .$$

Equation 3-14

Figure 3-30 shows that σ_p monotonically increases with the range ratio. An exponential relationship can be fit between σ_p and R_a:

$$\sigma_F = m_{\sigma_F} \ln R_a + n_{\sigma_F} ,$$

Equation 3-15

where m_{σ_F} represents the change of σ_p as a function of range ratio. n_{σ_F} is the peak deviator stress of the weaker material for the binary mixture. For the selected sand and shale geomechanical properties (Table 3-1), m_{σ_F} is 0.72 MPa and n_{σ_F} is 3 MPa.
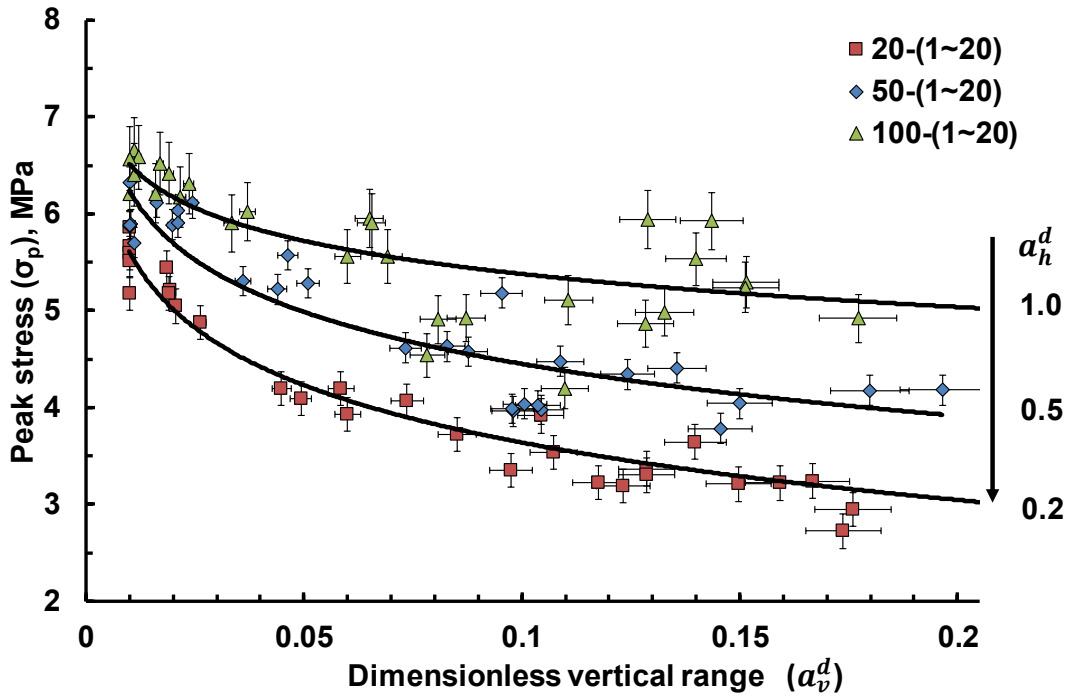
Figure 3-29. The change of σ_p due to variations of a_v^d and a_h^d. The error bars show the plus and minus 5% error.
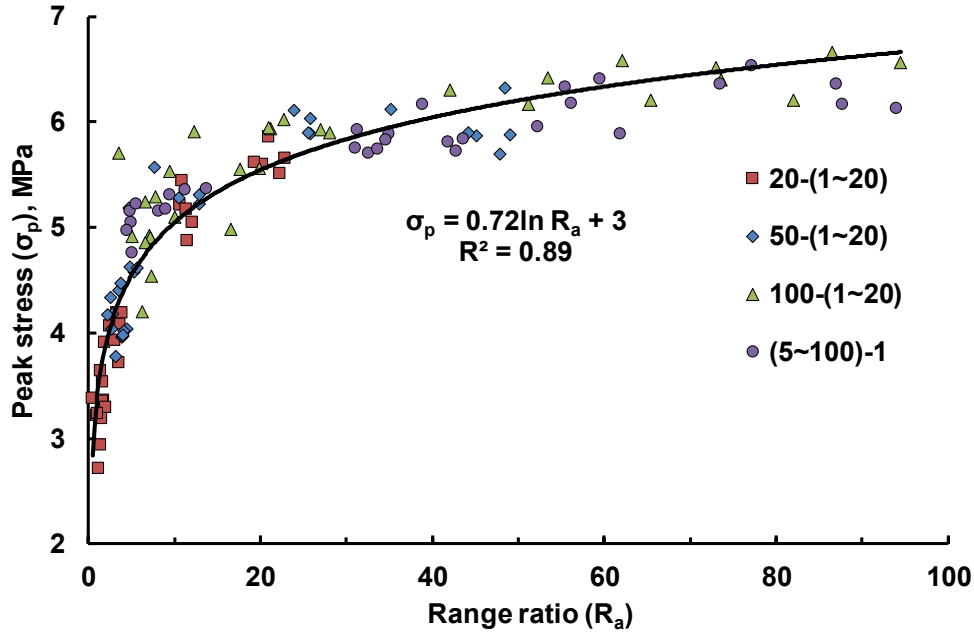
Figure 3-30. The change of σ_p versus range ratio for realizations with various ranges.

To obtain the Mohr-Coulomb failure envelopes in p-q space, numerical tests are conducted with three confining stress of 0.1, 0.5 and 1 MPa following the bi-axial testing regime. The stress paths are illustrated by the straight line across the failure points on the corresponding failure envelopes for case 50-1, 50-5 and 20-5 (Figure 3-31) showing that the case with the largest range ratio has the highest failure envelope. This is due to the failure modes transferring from the zone failures in the thick and short shale cells to line failure across the strong sand cells for realizations with the increase of range ratio.
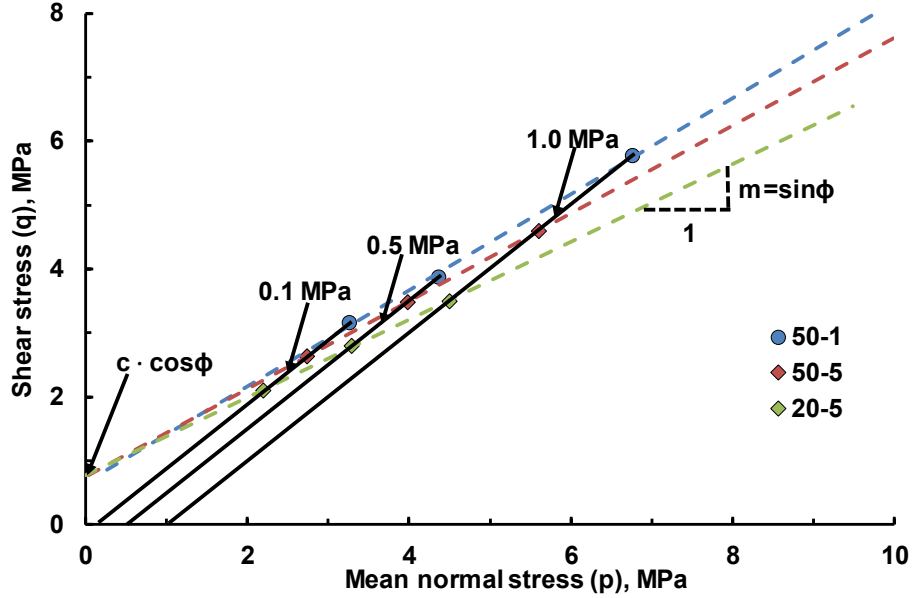
Figure 3-31.　Mohr-Columb failure envelopes and stress paths for Case 50-1, 50-5 and 20-5.

From the M-C failure criterion, the calculated ϕ_p monotonically increase with range ratio (Figure 3-32) for case 20-(1~20), 50-(1~20) and 100-(1~20), e.g. 1~20 represents that the vertical ranges increase from 1 to 20. The relationship between ϕ_p and R_a can be fit with a logarithm:

$$\phi_p = m_{\phi_p} \ln R_a + n_{\phi_p} .$$ Equation 3-16

Here m_{ϕ_p} is 3.25° and n_{ϕ_p} is 34.2° for the selected geomechanical properties for sand and shale (Table 3-1). It is hypothesized that the peak friction angle has a logarithmic relationship with R_a for the sand-shale sequence oil sands. The fitting parameter m_{ϕ_p} and n_{ϕ_p} should be characterized based on experimental and numerical tests at the target scale.
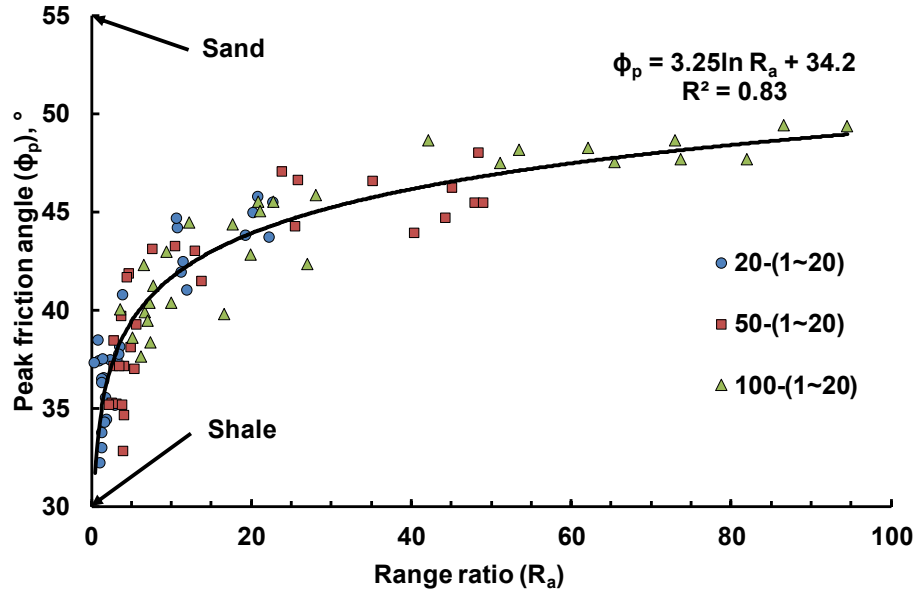
Figure 3-32.   Peak friction angle versus range ratio of heterogeneous oil sands.

The calculated c_p are plotted versus the corresponding range ratio in Figure 3-33. The relationship between c_p and R_a can be classified into two zones: 1) Very sensitive when $R_a < 10$; 2) Constant when $R_a \geq 10$. For the first zone, a logarithm can be fit:

$$c_p = 0.16 \ln R_a + 0.76, \ Ra < 10 .$$
<div style="text-align: right">Equation 3-17</div>

For the second zone when $R_a \geq 10$, the cohesion reaches an asymptotic value ($c_{sand} = 1.1$ MPa). It can be concluded that the cohesion for the heterogeneous binary mixtures can be approximated as the cohesion of the cohesive material when the plane of weakness is long and thin ($R_a \geq 10$).
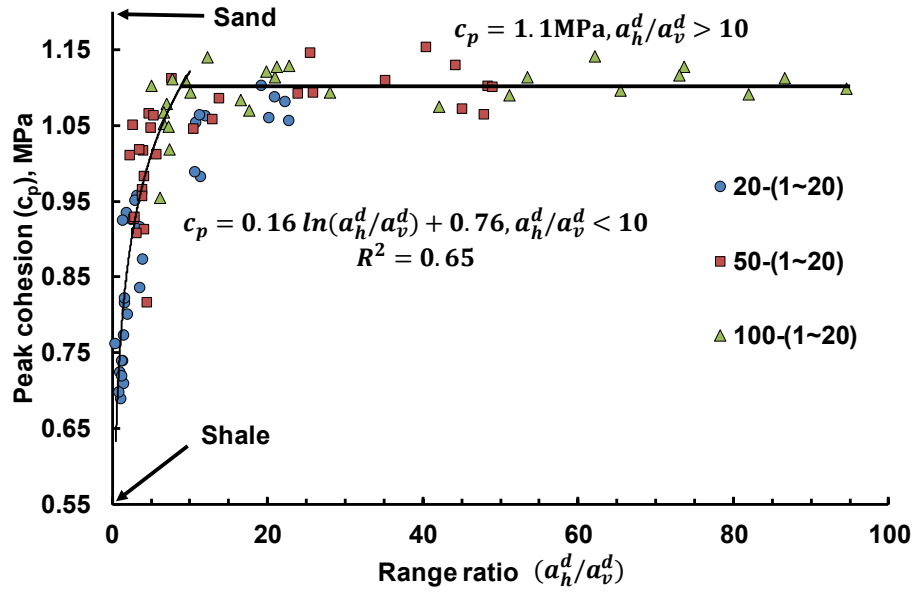
Figure 3-33.   Peak cohesion versus range ratio of heterogeneous oil sands realizations.

In Section 3.5.5, the dilation angle was found to have a linear relationship with V_{sh}. However, the calculated dilation angles for realizations with various range ratios are scattered and do not have a clear correlation with R_a. Thus, the spatial ranges can be neglected when considering the shear dilatancy of heterogeneous oil sands and IHS.

The macroscopic failure envelope is determined by the peak friction angle and cohesion. σ_F, ϕ_p and c_p of the heterogeneous oil sands have logarithmic relationships with the range ratio. Due to the variations of the depositional environment, the range ratios could vary a lot at different regions of the reservoir. Therefore, the range ratio is another key element beside V_{sh} as a geostatistical parameter to quantify the geomechanical response of heterogeneous material.

3.7 Anisotropy Caused by Inclined Shale Beddings

Anisotropy in geological media exists at all length scales from nanometer for pores to centimeters for facies in cores to kilometers for lithologies imaged in seismic data. The major principal planes of weakness have a significant impact on failure modes and shear strength of the anisotropic sedimentary material according to various experimental (Saeidi et al. 2014; Islam and Skalle 2013; Basu et al. 2013; Vergara et al. 2015; Liang et al. 2007) and simulation studies (Lin et al. 2013). The failure modes of anisotropic material are complex combinations of tensile failure, shear failures and visco-plastic dilatant distortion (Liang et al. 2007). In uniaxial or triaxial compression tests, anisotropic rocks may fail or deform along or across the plane of weakness depending on the orientations of weaker bedding planes and confining stress, which results in a large discrepancy in strength (McLamore and Gray 1967; Tien et al. 2006). Various failure criteria are proposed to give a systematic prediction of compressive strength and failure modes, e.g. single plane of weakness (Jaeger 1960), modified variable cohesive strength (McLamore and Gray 1967), Tien-Kuo's criterion (Tien et al. 2006) and patchy weakness model (Fjaer and Nes 2014). In this section, the impact of shale inclination angle and major principal stress direction are investigated to explain the link between failure modes and macroscopic geomechanical response for IHS at the macroscopic scale.

3.7.1 Angle between Shale Bedding Planes and Major Principal Stress (α)

Two series of IHS realizations (case 20-1 and 20-5) are generated with dips of shale bedding planes from 0 to 90° (Figure 3-34) to cover the anisotropy at different regions of reservoirs. Case 20-1 and 20-5 are selected to show the anisotropic effect for realizations with different range ratios. The in-situ major principal stress direction changes from vertical in the initial injection period to horizontal in the production stage during SAGD. Therefore, the inclination angle between the

major principal stress direction and shale bedding plane (α) is defined to quantify the anisotropic effect caused by inclined shale bedding planes and rotation of major principal stress at different stages of SAGD.
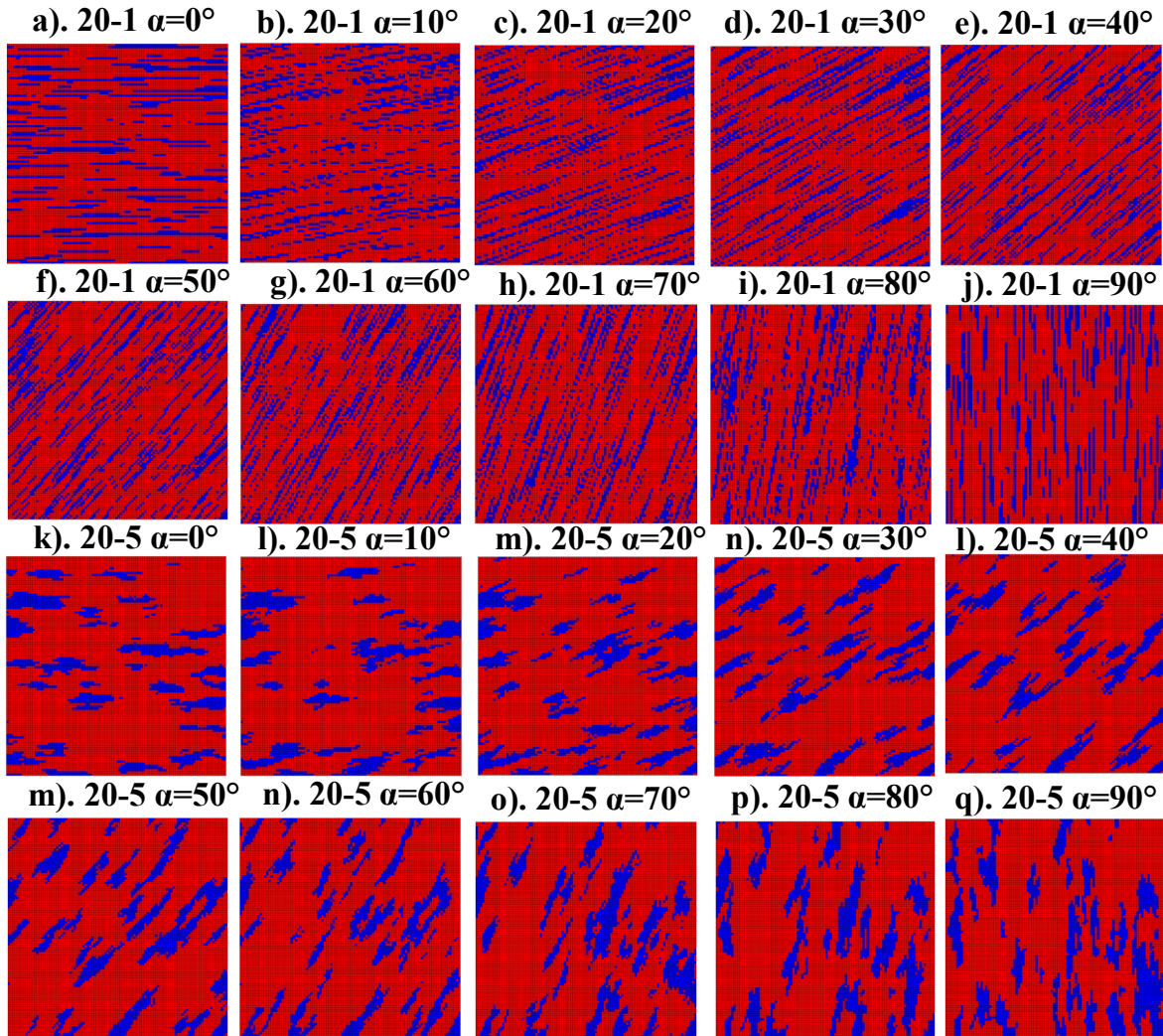
Figure 3-34.   Case 20-1 and 20-5 with shale inclination angles from 0 to 90°. Blue: shale; red: sand.

The numerical tests on these realizations follow the boundary condition in Figure 3-5. The principal stress direction is kept unchanged to investigate the potential influence of shale bedding planes on the failure modes and shear strength. For the impact of stress rotation in anisotropic material, Lade et al. (2006) conducted torsion shear tests along various stress paths and compared with true triaxial tests where material tends to behave isotropically. The target of the simulation is to provide insights into the failure modes and macroscopic geomechanical response for IHS when the angle between shale bedding planes and major principal stress direction changes during SAGD.

3.7.2 Effect of Confining Stress on Failure Modes of IHS

Three different confining stresses (0.1, 0.5 and 1.0 MPa) are applied to obtain the failure envelopes in p-q space. The stress-strain behaviors for bi-axial compression tests on case 20-1 and 20-5 with dip 0, 30°, 60° and 90° are illustrated in Figure 3-35 and 3-36. The shear strength increases with confining stress; while the stiffness is constant until shear failures happen in the weaker shale cells ($\varepsilon_a > 0.4\%$) when approaching the peak point. The elasto-plastic behavior is more obvious for case 20-5 than case 20-1 which indicates that shear failures in shale are more dominant for realizations with thicker shale bedding planes. The shear strength is significantly lower for cases with α of 30°, compared to 0, 60° and 90°. The elastic-plastic behavior (black circles in Figure 3-35 and 3-36) for case α=30° is more pronounced, indicating the longest history of plastic deformations of shale before peak due to the difference of failure modes.
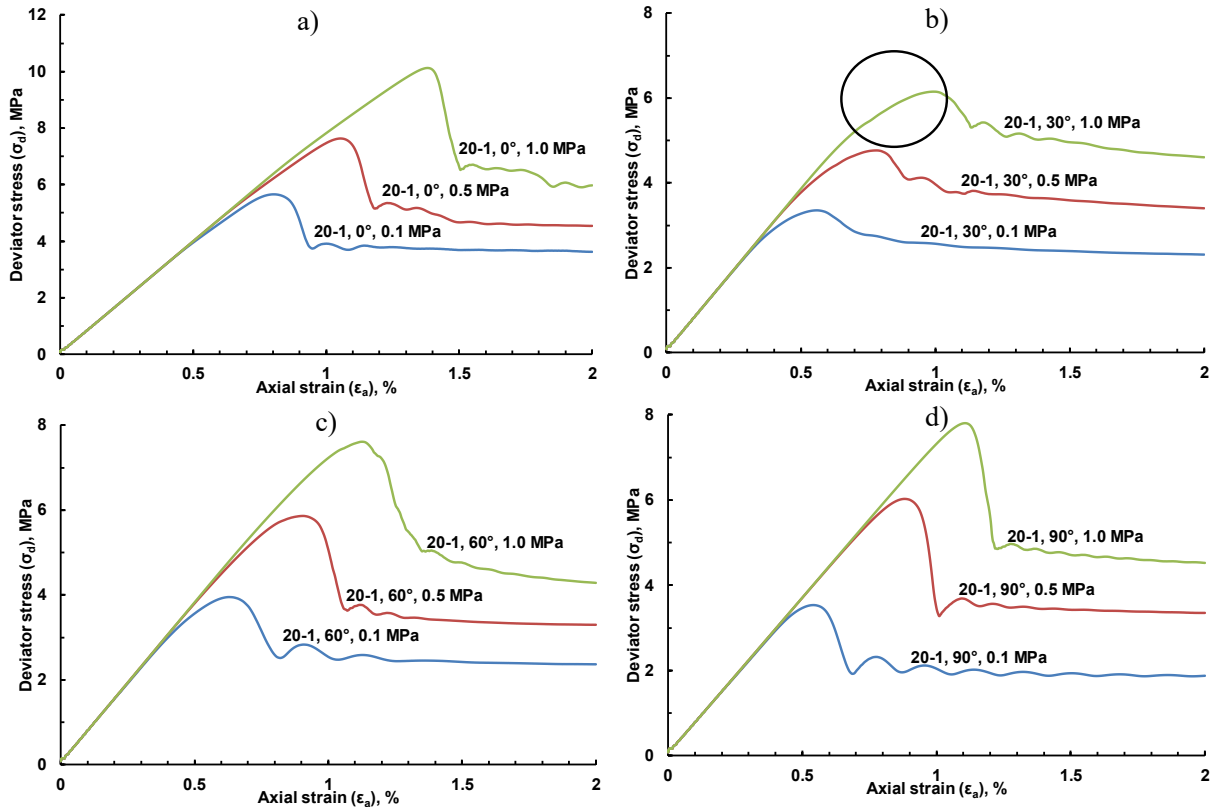
Figure 3-35.   Stress-strain behavior for case 20-1 with α of 0, 30°, 60° and 90° when σ$_3$ is 0.1, 0.5 and 1.0 MPa.

The failure modes for case 20-1 (0, 30°, 60° and 90°) are illustrated by the profiles of friction angle and plastic shear strain (Figure 3-37) at residual state. For case 20-1 α=0°, line failure is the dominate mode where a single shear band transverses the horizontal shale bedding planes continuously. When confining stress increases from 0.1 to 0.5 MPa, the failure plane is split into two connected failure planes. For case 20-1 α=30°, the failure mode is a zone failure where shear planes are parallel with the weaker shale cells. Increasing confining stress creates more shear failures in the horizontal direction but the plastic shear strain still concentrates in shale. When α=60° and 90°, the failure modes migrate from zone failures to line failures with increasing confining stress. The plastic shear strain concentrates in shale when confining stress is 0.1 MPa and moves to the nearby sand cell with increasing confining stress. Figure 3-38 shows the failure

modes for case 20-5 (0, 30°, 60° and 90°) and presents similar changes when confining stress increases from 0.1 to 1.0 MPa. The increase in confining stress creates more horizontal shear planes in the sand cells which enhances the connectivity of failure planes in the principal stress direction (horizontal). Therefore, the chances of line failures are higher with increasing confining stress.
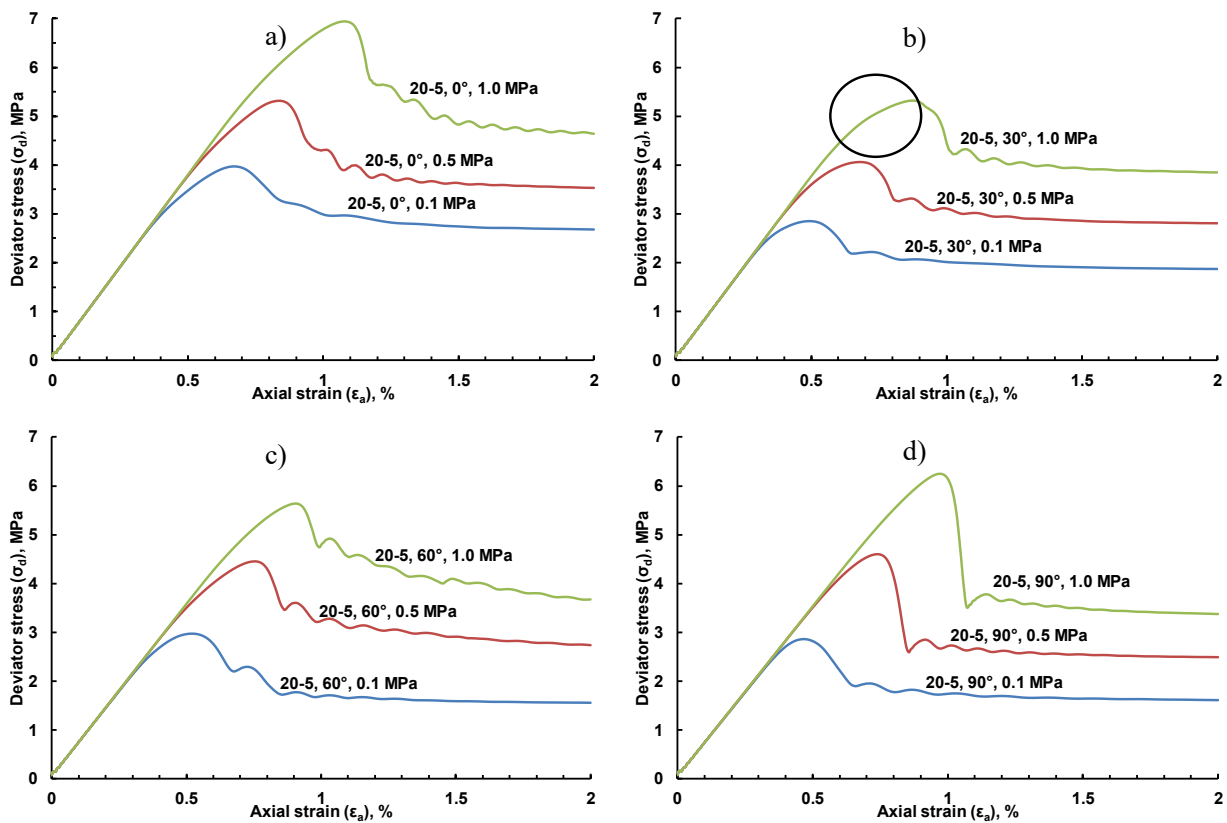
Figure 3-36.   Stress-strain behavior for case 20-5 with α of 0, 30°, 60° and 90° when σ_3 is 0.1, 0.5 and 1.0 MPa.
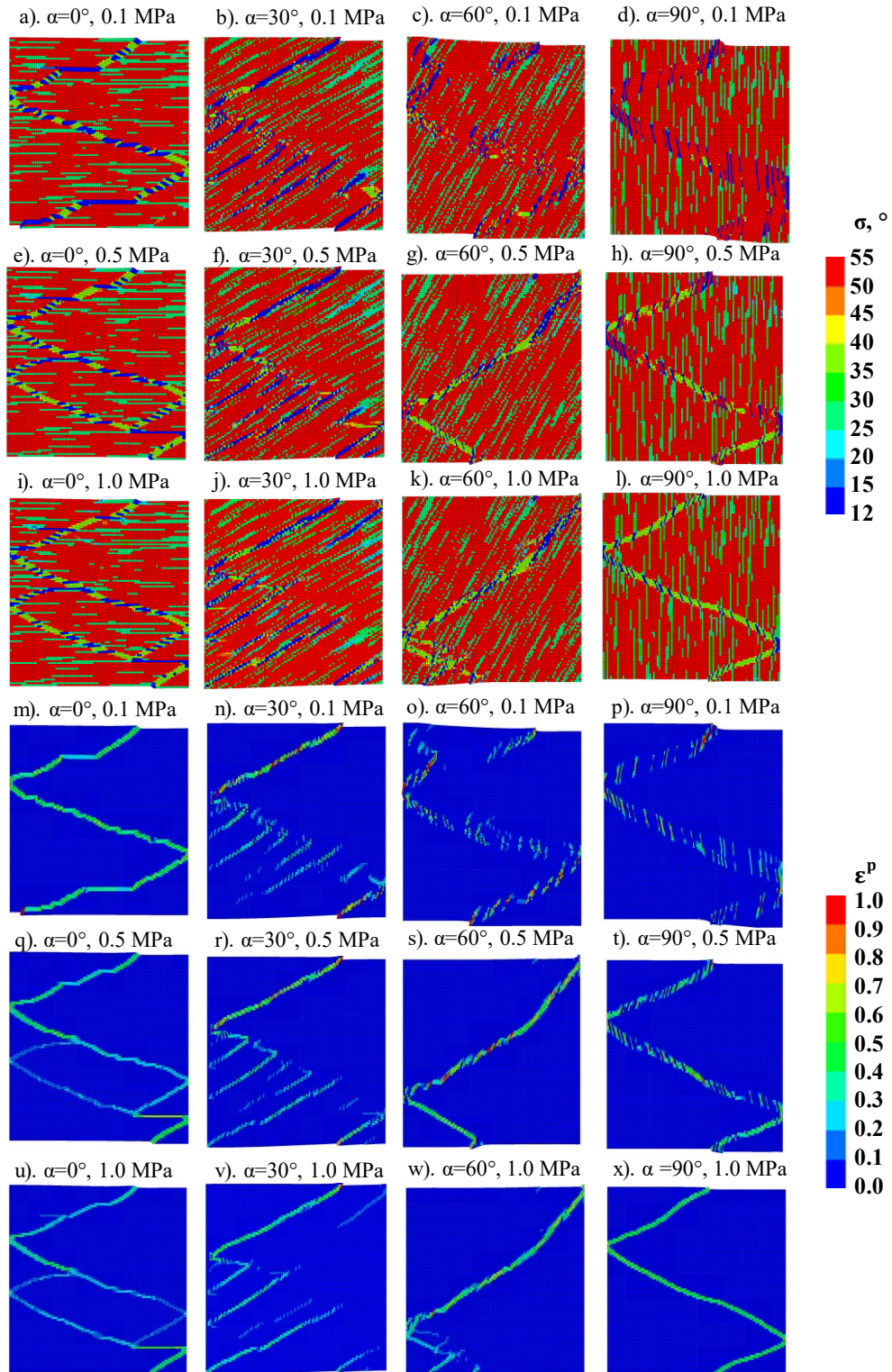
Figure 3-37   Impact of confining stress on the failure modes for case 20-1 with α of 0, 30°, 60° and 90°. Friction angle and shear strain at 2% axial strain are illustrated.
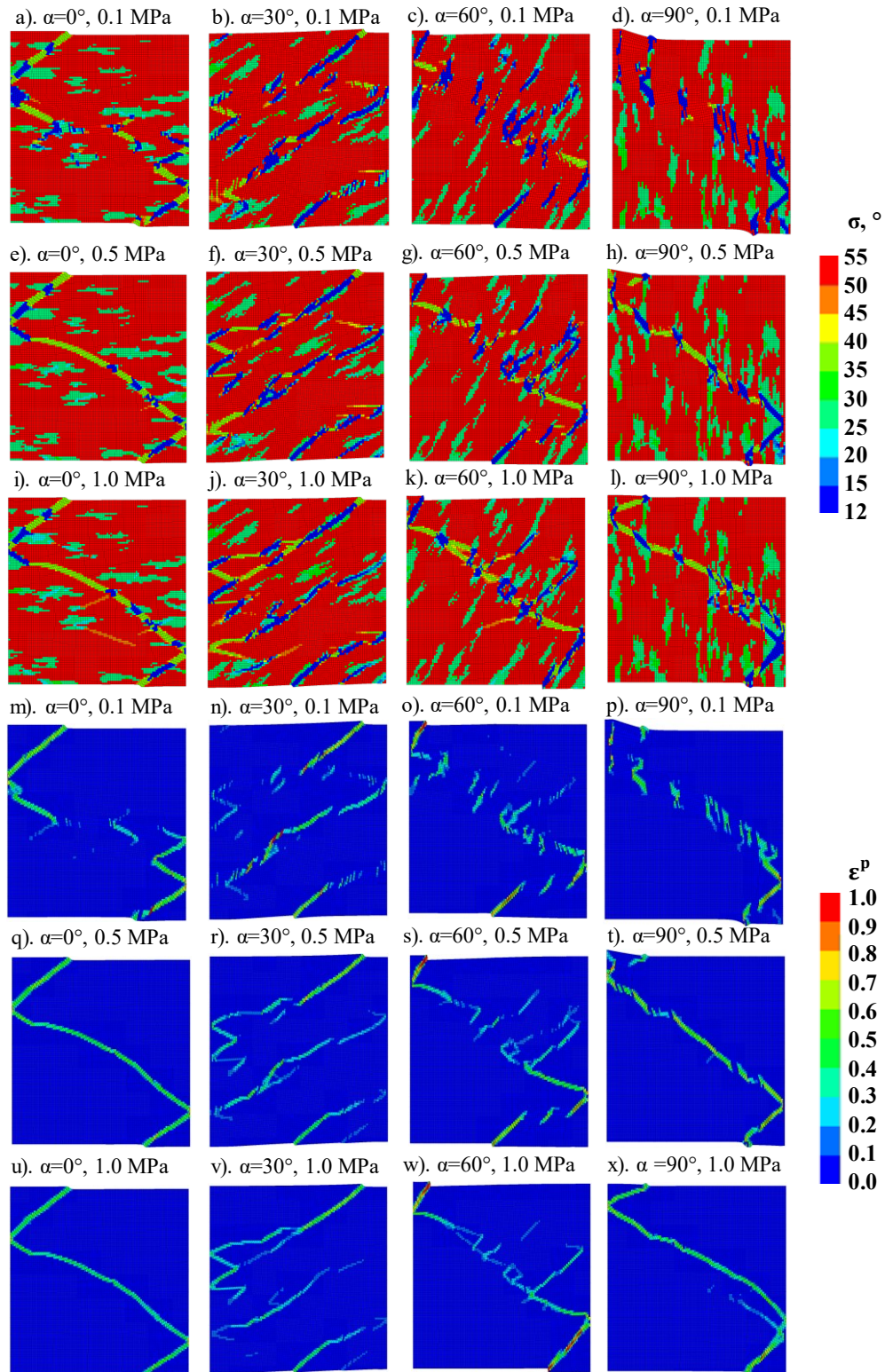
Figure 3-38. Impact of confining stress on the failure modes for case 20-5 with α of 0, 30°, 60° and 90°. Friction angle and plastic shear strain at 2% axial strain are illustrated.

3.7.3   Impact of Shale Orientation

In Section 3.7.2, the influence of α on the stress-strain behavior and failure modes is demonstrated for case 20-1 and 20-5 (0, 30°, 60° and 90°). The Mohr-Coulomb failure envelopes in p-q space (Figure 3-39) show the significant impact of α on the failure criteria of IHS. For bi-axial tests on realizations with different α, the stress paths are the same under fixed confining stress until reaching the designated failure envelope. The shear strength for case α=30° is the lowest while case α=0° leads to the highest shear strength for both cases 20-1 and 20-5.
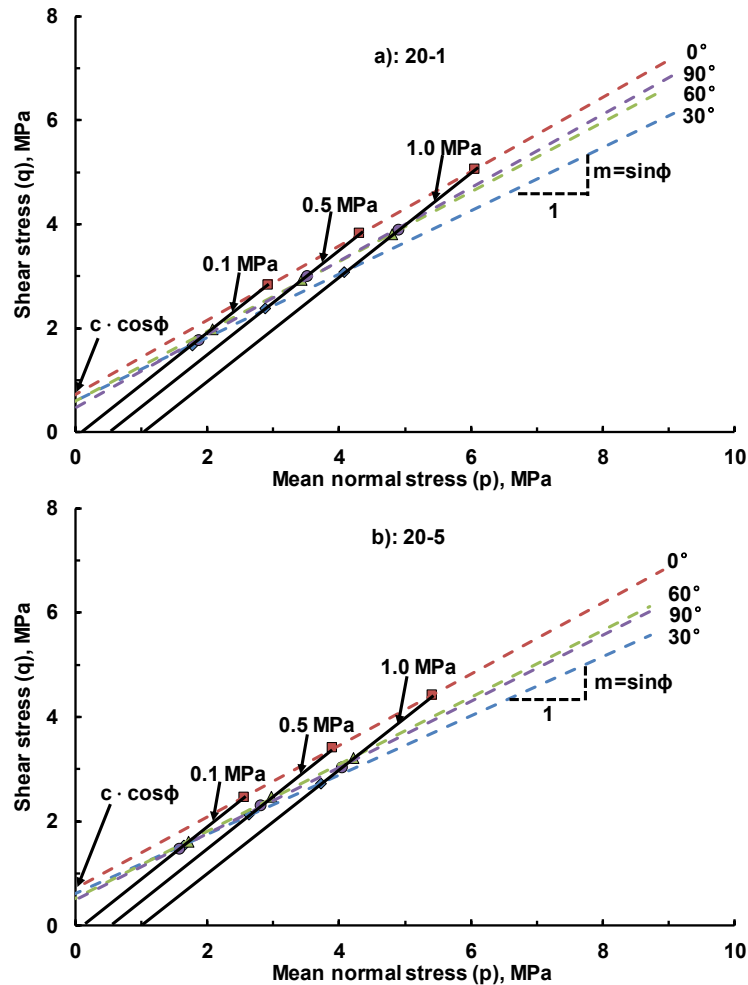
Figure 3-39.   Failure envelopes and stress paths for case 20-1 and 20-5 (0, 30°, 60° and 90°).

For α from 0 to 90° with an increment of 10°, 60 realizations are created and tested under 0.1, 0.5 and 1.0 MPa for case 20-1 and 20-5, where three realizations are tested for each α. Averaging the peak stress with fixed α, the relationship between σ_F and α (Figure 3-40) indicates that the peak stress increases with confining stress. The failure deviator stress for case 20-1 is systematically higher for case 20-5 which is consistent with the results that σ_F monotonically increase with R_a. The difference between the maximum and minimum σ_F caused by the rotation of major principal stress decreases from 3.9 MPa (20-1) to 2.3 MPa (20-5) when the confining stress is 1.0 MPa. It indicates that the change of major principal stress direction during SAGD tends to lead to more significant changes in shear strength for IHS with a larger range ratio.
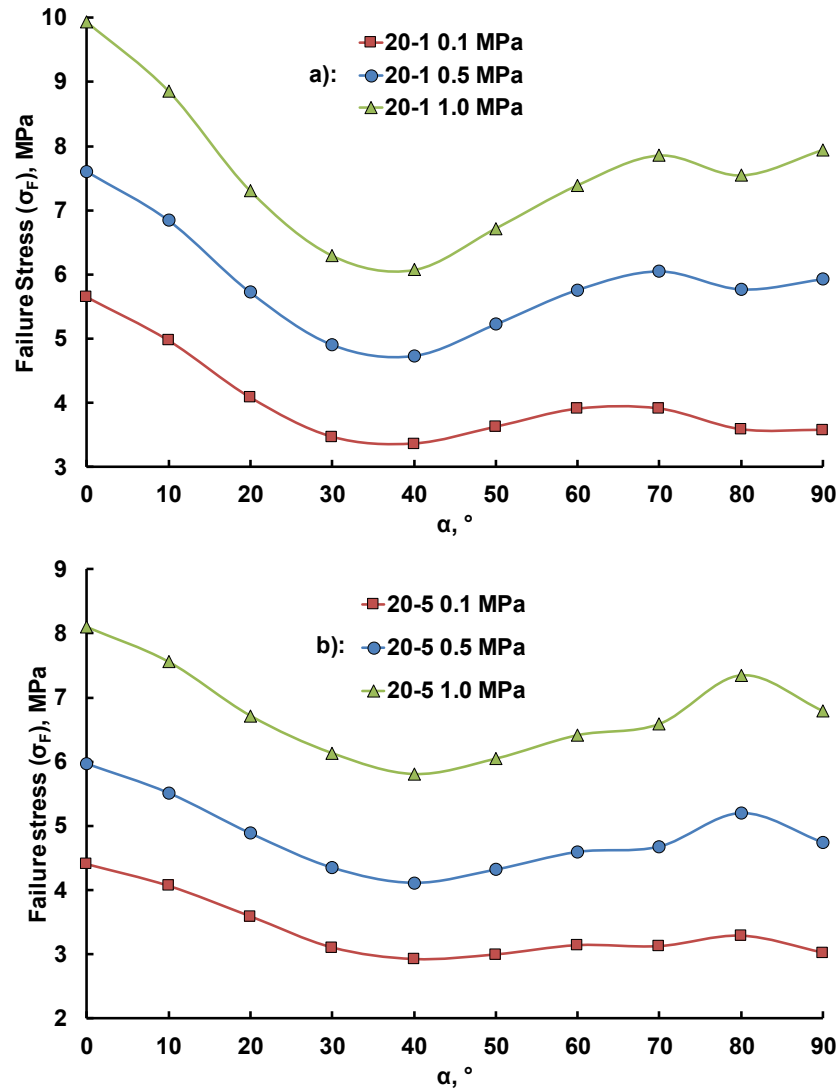
Figure 3-40.   Peak stress versus α for Case 20-1 and 20-5 with σ₃ of 0.1, 0.5 and 1.0 MPa. Each data point is the average of three different realizations with fixed volume fraction, spatial ranges and inclination angle of shale.

The trend of σ_p versus α for spatially correlated IHS realizations is similar to the experimental results on anisotropic materials that contain a single plane or a system of parallel planes of weakness (McLamore and Gray 1967; Saeidi et al. 2014; Tien et al. 2006). The peak stress in compression tests is closely related to the failure modes (Figure 3-40). When α is below 20°, line failure across the entire sample is observed leading to the peak stress close to the shear strength of

the sand. With the increase of α, more shear failures along the shale bedding planes (weak plane failure) are triggered and mitigate to zone failure mode when α is close to 40°. When α > 40°, σ_F gradually increases until the plane of weakness is normal to the major principle stress. Although shear failures along the plane of weakness still dominate the plastic deformations, the shear failure planes in sand cells start to be connected and form a shear band with an increase of α from 40° to 90°, leading to higher peak stress. For the plane of weakness model proposed by Jaeger (1960), this failure mode is also defined as intrinsic failure which is the same as the line failure when α is below 20°. Tien et al. (2006) classified the mode of failures into sliding (30°-80°) and non-sliding failures (0-30° & 80°-90°) along discontinuities and developed a failure criterion to predict the shear strength of transversely isotropic rock.

Figure 3-41 shows the calculated ϕ_p and c_p from the M-C failure theory. The relationship between ϕ_p and α is analogous to Jaeger's (1960) single plane of weakness theory assuming fixed cohesion. The peak cohesion decreases from sand (1.2 MPa) to shale (0.55 MPa) with increasing α. Therefore, the peak cohesion of a spatially correlated IHS realization has a monotonic relationship with range ratios. The orientation of the major principal stress rotates with the propagation of the steam chamber, so it is not appropriate to ignore the impact of α on the shear strength of IHS when considering issues of caprock integrity and well stability. It is recommended to consider both the upper and lower boundary of the equivalent strength parameter (ϕ_p and c_p) for heterogeneous oil sands and IHS in SAGD.
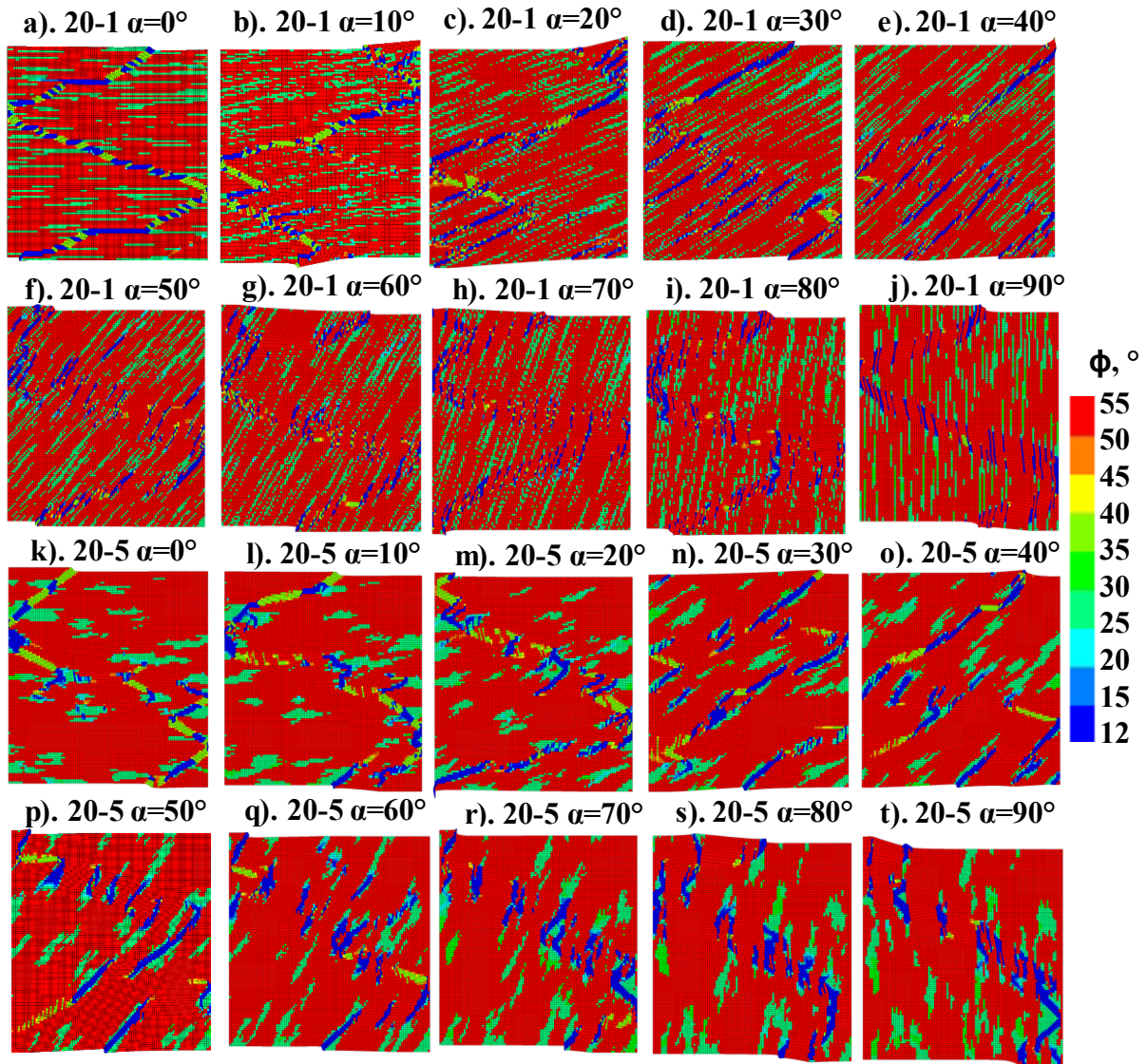
Figure 3-41. Friction angle at 2% axial strain showing the failure modes affected by inclinations of shale for case 20-1 and 20-5.
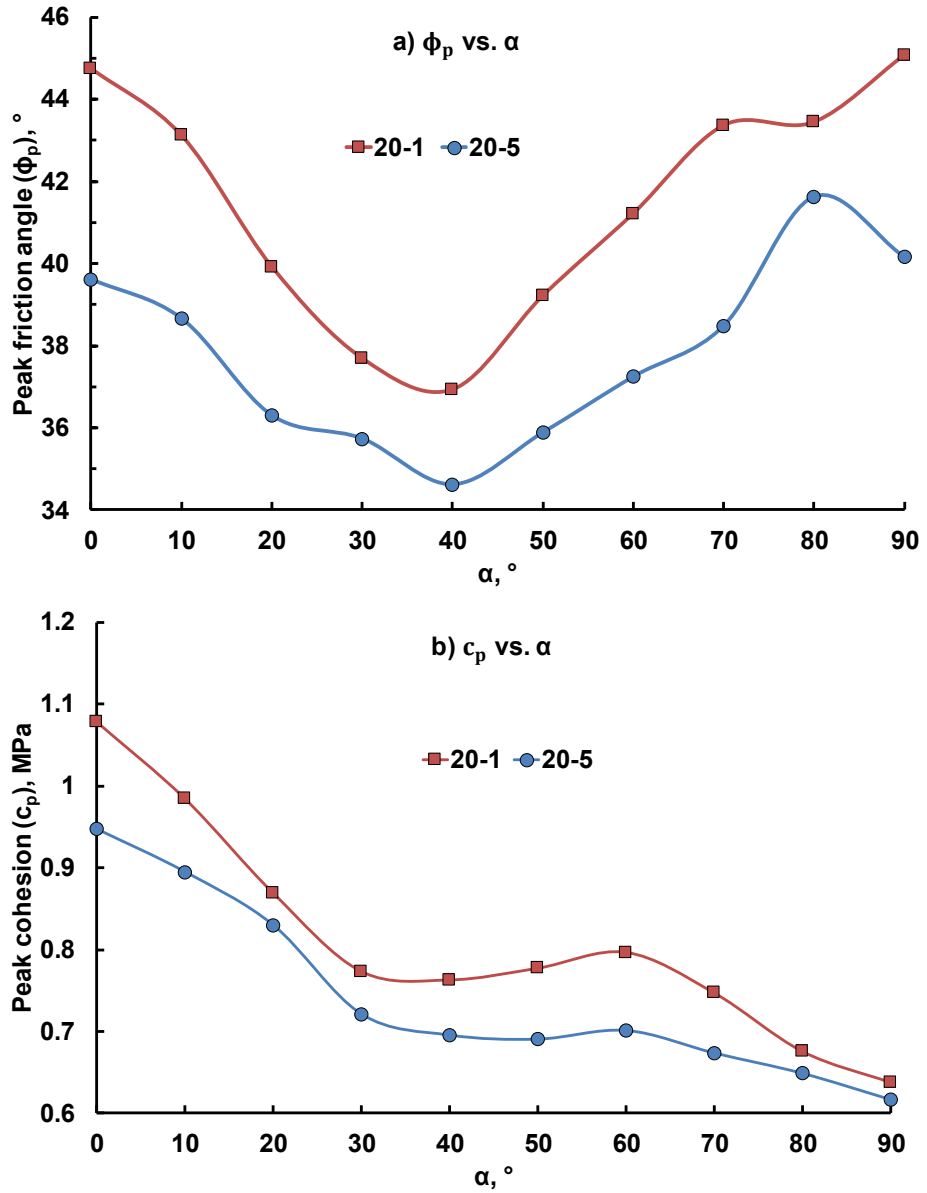
Figure 3-42.   Peak friction angle (ϕ_p) and cohesion (c_p) versus α for case 20-1 and 20-5.

3.8   Summary

Chapter 3 quantifies the impact of heterogeneity caused by spatially correlated shale bedding planes on the geomechanical response. The failure modes are highly sensitive to the volume fraction, spatial ranges and inclination angles between shale bedding planes and the major principal stress direction. Strain localization plays an important role in the development of modes of failures. Shear failures first occur in the weaker shale cells and then trigger the coalesced failures in nearby sand cells before the peak. The local shear failures before macroscopic peak lead to a highly elasto-plastic stress-strain response for heterogeneous oil sands mixed with spatially correlated shale seams (IHS). The tangent modulus for oil sands with more than 40% shale is found to be even lower than the shale stiffness when approaching the peak. The effective geomechanical properties for the heterogeneous mass, such as stiffness, cohesion, friction angle and dilation angle, are found to be well correlated with V_{sh}.

The spatial ranges quantify the length and thickness of shale bedding planes which both have significant influences on geomechanical responses. Large horizontal ranges lead to a shear band failure. The shear strength and tangent modulus are larger than realizations with sparse and short shale bedding planes where zone failures are dominant. Massive shear failures in thicker shale layers trigger coalesced failures in surrounded sand cells resulting in lower stiffness and shear strength. The range ratio is introduced to parameterize the impact of spatial variability on the macroscopic geomechanical response and shear strength parameters (friction angle and cohesion) of heterogeneous oil sands.

The inclined shale bedding planes and rotation of major principal stress direction during SAGD cause non-negligible changes on the geomechanical response. The failure modes migrate from line failure to zone failures along the plane of weakness when the inclination angle increases from 0 to

30°, which causes a nearly 50% reduction in peak strength. Thus, the impact of shale bedding planes dip and rotation of major principal stress should be considered when evaluating the issues of caprock integrity and well stability.

To be noted, the relationship between shear strength and geostatistical parameters (V_{sh}, R_a and α) is based on the sand-shale sequence realizations with input geomechanical properties fitted to the McMurray Formation. For other reservoirs that are not Alberta oil sands, simulations need to be re-conducted with the characterized geomechanical properties for the investigated region. The workflow and boundary conditions remain the same, but the generated correlations are significantly affected by depositional environments.

CHAPTER 4: EFFECTIVE PERMEABILITY CHANGE DUE TO DEFORMATIONS

The change in porosity and absolute permeability of oil sands due to deformations is important when considering thermal methods in the Alberta oil sands. Previous research has shown that shear failures (Touhidi-Baghini 1998) cause more significant changes in absolute permeability compared to isotropic unloading (Scott et al. 1991; Oldakowski 1994) due to pore structure changes. Shear failures in uncemented sands (Desrues and Viggiani 2004) and stiff clays (Manica et al. 2018) are strain localized in a narrow path providing flow shortcuts to enhance the effective absolute permeability. The contraction of oil sands causes negligible changes in permeability because the permeability reduction due to volume decrease is neutralized by the permeability enhancement caused by the development of flow channels (Touhidi-Baghini 1998). The permeability enhancements due to shear dilatancy are significant because of pore space expansion and flow channels created by shear failures. Here, the evolution of permeability associated with deformations in heterogeneous porous media is investigated to provide insights on the impact of heterogeneity on permeability changes.

4.1 Permeability Updating Due to Deformation

When elastic deformations dominate geomechanical behavior, the change of permeability comes from a change in the pore space. The equation used for porosity ($\emptyset$) change is derived based on the pore volume change reflected by total volumetric strain. Porosity is defined as the volume of pores (V_p) divided by bulk volume (V_b). The bulk volume consists of pore and solid volume in porous media.

$$\emptyset = \frac{V_p}{V_b} = \frac{V_b - V_s}{V_b}.$$

<div align="right">Equation 4-1</div>

The volumetric strain (ε_v) is defined as the change of bulk volume (ΔV_b) divided by original bulk volume (V_b).

$$\Delta V_b = \varepsilon_v V_b \ . \hspace{4cm} \text{Equation 4-2}$$

The new porosity led by deformations of porous media is written as:

$$\emptyset_{new} = \frac{(V_b + \Delta V_b) - (V_s + \Delta V_s)}{(V_b + \Delta V_b)} = \frac{(V_b + \varepsilon_v V_b) - (V_s + \Delta V_s)}{(V_b + \varepsilon_v V_b)} = \frac{V_p + V_b \varepsilon_v - \Delta V_s}{(1 + \varepsilon_v) V_b} \ . \hspace{1cm} \text{Equation 4-3}$$

Divide bulk volume in both denominator and nominator in Equation 4-3:

$$\emptyset_{new} = \frac{\emptyset_o + \varepsilon_v - \Delta V_s / V_b}{1 + \varepsilon_v} \ . \hspace{4cm} \text{Equation 4-4}$$

The change of solid volume is correlated with temperature changes and the thermal expansion coefficient in reservoir-geomechanics simulation (Tortike 1991). Tortike and Farouq Ali (1993) proposed the change of solid volume as a function of temperature changes:

$$\frac{\Delta V_s}{V_b} = (1 - \emptyset_o)\alpha(T - T_o) \ , \hspace{4cm} \text{Equation 4-5}$$

where α is the solid thermal expansion coefficient. The final form of the new porosity is:

$$\emptyset_{new} = \frac{\emptyset_o + \varepsilon_v - (1 - \emptyset_o)\alpha(T - T_o)}{1 + \varepsilon_v} \ . \hspace{3cm} \text{Equation 4-6}$$

If there is no temperature change, α becomes zero and the new porosity depends only on original porosity and volumetric strain:

$$\emptyset_{new} = \frac{\emptyset_o + \varepsilon_v}{1 + \varepsilon_v} \ . \hspace{4cm} \text{Equation 4-7}$$

The permeability change due to deformation can be classified into two categories: 1) expansions of pore space and 2) new flow channels created by plastic deformations. For the permeability change due to porosity change, a linear relationship between the porosity and logarithm of

hydraulic conductivity is applied, e.g. Kozeny-Carman Equation (Carman 1939), Oldakowski (1994). However, a sudden jump in permeability can be observed in the triaxial tests of oil sands when massive shear failures occur after peak (Touhidi-Baghini 1998). To include the increase in permeability due to plastic deformations, the equation considering both porosity change and plastic shear strain is:

$$k_{new}/k_o = a \, exp[C_e(\emptyset_{new} - \emptyset_o)] \, exp[C_p \varepsilon^p] \, , \qquad \text{Equation 4-8}$$

where a is a scale factor to consider scale effects of permeability change, C_e and C_p are the shape factors for elastic and plastic deformations to match the experimental results.

This equation is generated upon the investigation by Li and Chalaturnyk (2006) on the permeability variation associated with shearing and isotropic unloading. At the sub-grid scale, a is assumed to be 1. At the reservoir scale, a should be fitted to match the field data. Matching the experimental results of Touhidi-Baghini (1998) for vertical cores at low confining stress, C_e is 1 to quantify the slight changes of permeability by pore expansion and C_p is 40 to reproduce the increase in permeability caused by plastic deformations. When applied in other porous media, both C_e and C_p should be re-calibrated to the experimental and field data as they are closely related to the confining stress, stress path, grain size distribution and pore structures. The permeability of oil sands usually ranges between 0.5 and 15 Darcy (Olson et al. 2009). Thus, the upper boundary for the updated permeability should be set to 15 Darcy to prevent over-estimation of permeability change in the localized shear band.

4.2   Permeability Evolution Associated with Deformation

Case $V_{sh} = 0.2$ (Figure 3-7-c) in Section 3.5 is selected to show the permeability evolution during the shearing process. Isotropic permeabilities are assumed for each cell (5 cm by 5 cm). The

permeability is assumed 3000 mD for sand and 10 mD for shale. Equation 4-8 is used to calculate

the normalized permeability when deformations occur during the numerical compression tests.

The permeability evolutions associated with deformations at different ε_a are illustrated in Figure

4-1.
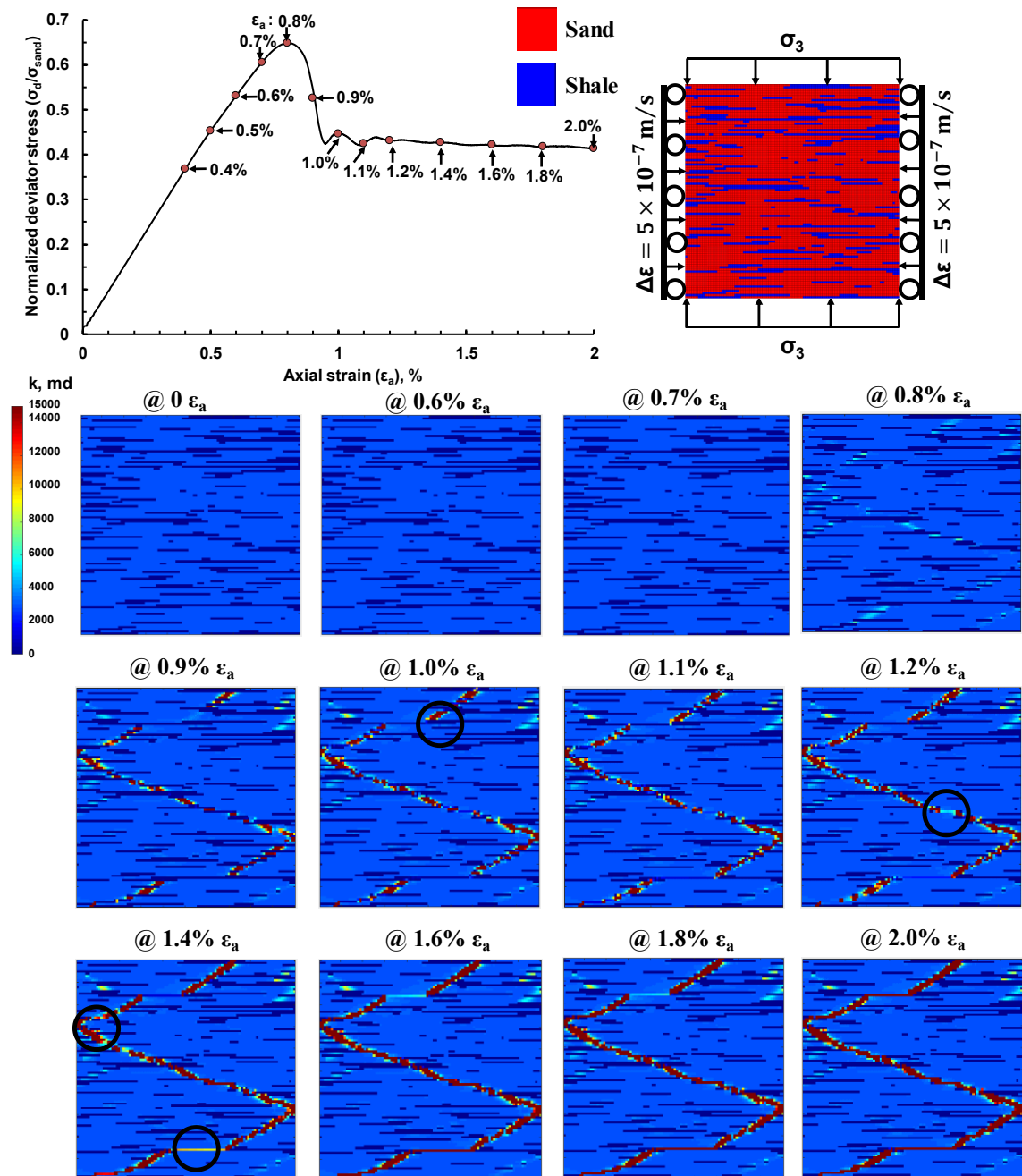
Figure 4-1.   Permeability evolution due to deformations with V_{sh} of 0.2 under bi-axial test.

When ε_a<0.6%, no significant changes are observed on the permeability because the shear failures are concentrated in shale cells and the plastic shear strain is not large enough to cause any notable change in shale permeability. This is consistent with the experimental results of the triaxial tests by Touhidi-Baghini (1998). When ε_a approaches peak (0.8%), permeability enhancement can be observed in the failed sand cells close to the shale bedding planes. When ε_a is 0.9%, the permeability in the failure planes reaches the upper limit. However, these high permeability channels are separated by the low permeability shale. During the progressive failure period, the high permeability flow paths become wider and slowly extend to shale after 1.1% axial strain. The high permeability flow path finally becomes connected across the realization at 1.8% axial strain.

To quantitively study the impact of shear failures on permeability change, the effective vertical and horizontal permeabilities are estimated at different axial strains by flow-based upscaling. The program "flowsim" (Deutsch 1999) is used to compute the effective permeability by solving the steady-state single-phase flow equations. At initial conditions, the computed effective vertical permeability (196.4 mD) is much smaller than the horizontal permeability (2162.4 mD) due to the low permeability (10 mD) horizontal shale bedding planes. The effective permeabilities in the vertical and horizontal directions are normalized by the corresponding initial permeabilities (Figure 4-2).

The updated effective permeability is close to the initial permeability before the stress-strain curve reaches its peak (0.8% ε_a), which is consistent with the observation that no clear high permeability channels are observed when ε_a is smaller than 0.8%. When $0.8 < \varepsilon_a < 1.0$, the vertical effective permeability increases significantly due to the formation of flow channels. During the progressive failure period, the effective permeability increases because the shear band grows and plastic

126

deformations in shale connect high permeability channels. The enhancement of the vertical permeability (2.6 times) is more pronounced than horizontal permeability (1.3 times) when the major principal stress is horizontal. The vertical effective permeability is 515.4 mD (2.6 times) and the horizontal effective permeability is 2817.3 mD (1.3 times) of the initial permeability at an axial strain of 2%, which is consistent with Touhidi-Baghini's (1998) experimental results that the enhancement of permeability for vertical cores are twice that of vertical cores. This phenomenon explains the hypothesis by Olsen et. al. (2009) that the change of permeability normal to the load direction could be more significant especially if discrete shear failure planes are formed. The most important reason for this is the permeability shortcuts created by shear bands piecing the low permeability continuous shale layers. The vertical permeability is usually much lower because the horizontal shale bedding planes hinder vertical flow. Thus, localized vertical shear bands create highly permeable vertical channels. Vertical flow in the shear failures is much easier comparing to flow across the horizontal shale layers or channel through the permeable sand cells at the initial condition. However, the horizontal shear bands only offer an alternative higher permeability flow path while the horizontal flow can still go through the existing high permeability sand cells without any shear failures. As a consequence, the horizontal permeability changes are smaller than vertical.
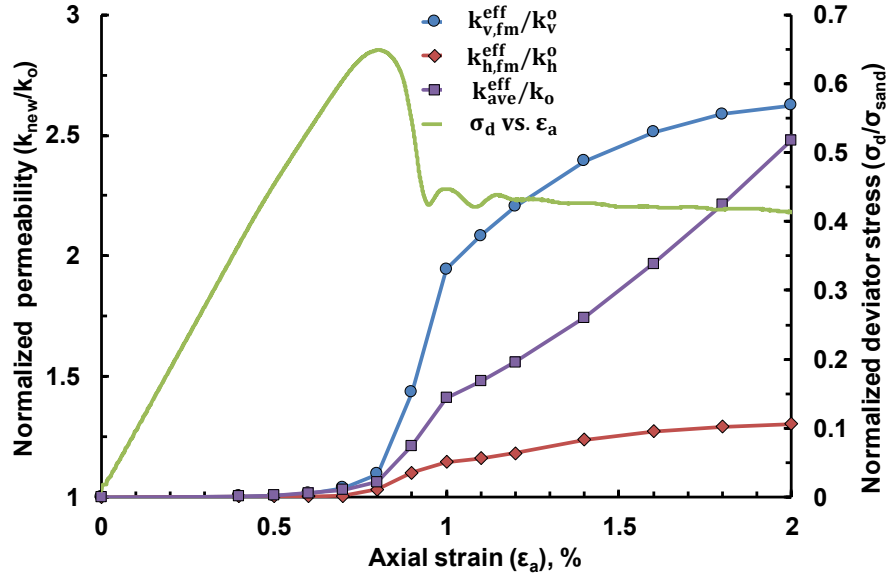
Figure 4-2.   Effective normalized permeability at different ε_a during the horizontal compression test. Blue: normalized effective vertical permeability; Red: normalized effective horizontal permeability. Purple: normalized permeability when using volume average total and plastic shear strain.

The propagation of shear failure planes has shown a significant impact on the vertical and horizontal effective permeability. Potential error is expected without considering the configurations of shear failures. If assuming uniform deformations for all of the 100 by 100 cells, total volumetric and shear strains of the entire realization are used to compute the normalized updated permeability. The purple curve in Figure 4-2 shows the change of permeability during the failure process without considering modes of failure, which sits between the horizontal and vertical normalized permeability. Enhancement of permeability is expected with increasing strains until the effective permeability reaches the upper limit for the entire realization. If fine-scale simulations considering the modes of failure in all local upscaled regions are not computationally feasible, it is recommended to select a few representative local upscaled regions to find the appropriate scale factor "a" in Equation 4-8 because their changes may vary for different pore structures of the heterogeneous porous media. The upper limit for vertical and horizontal updated permeability

should be selected carefully based on the local fine-scale simulation results to prevent exaggerated predictions of effective permeabilities caused by plastic deformations.

4.3   Impact of Heterogeneity on Permeability

The permeability changes for realizations with V_{sh} from 2% to 90% are investigated to quantify the impact of heterogeneity. The permeability distributions at critical state of the bi-axial compression test are illustrated for cases with various V_{sh} in Figure 4-3. The high permeability flow channel is created by the localized shear band but is more continuous for cases in zone 1 (0 < V_{sh} < 10%) and zone 3 (80% < V_{sh} < 100%) when line failures dominate. In zone 2, the high permeability path travels from failed sand and shale cells because shear failures first initiate in shale cells and gradually extend to the nearby sand cells in the zone failure regime.
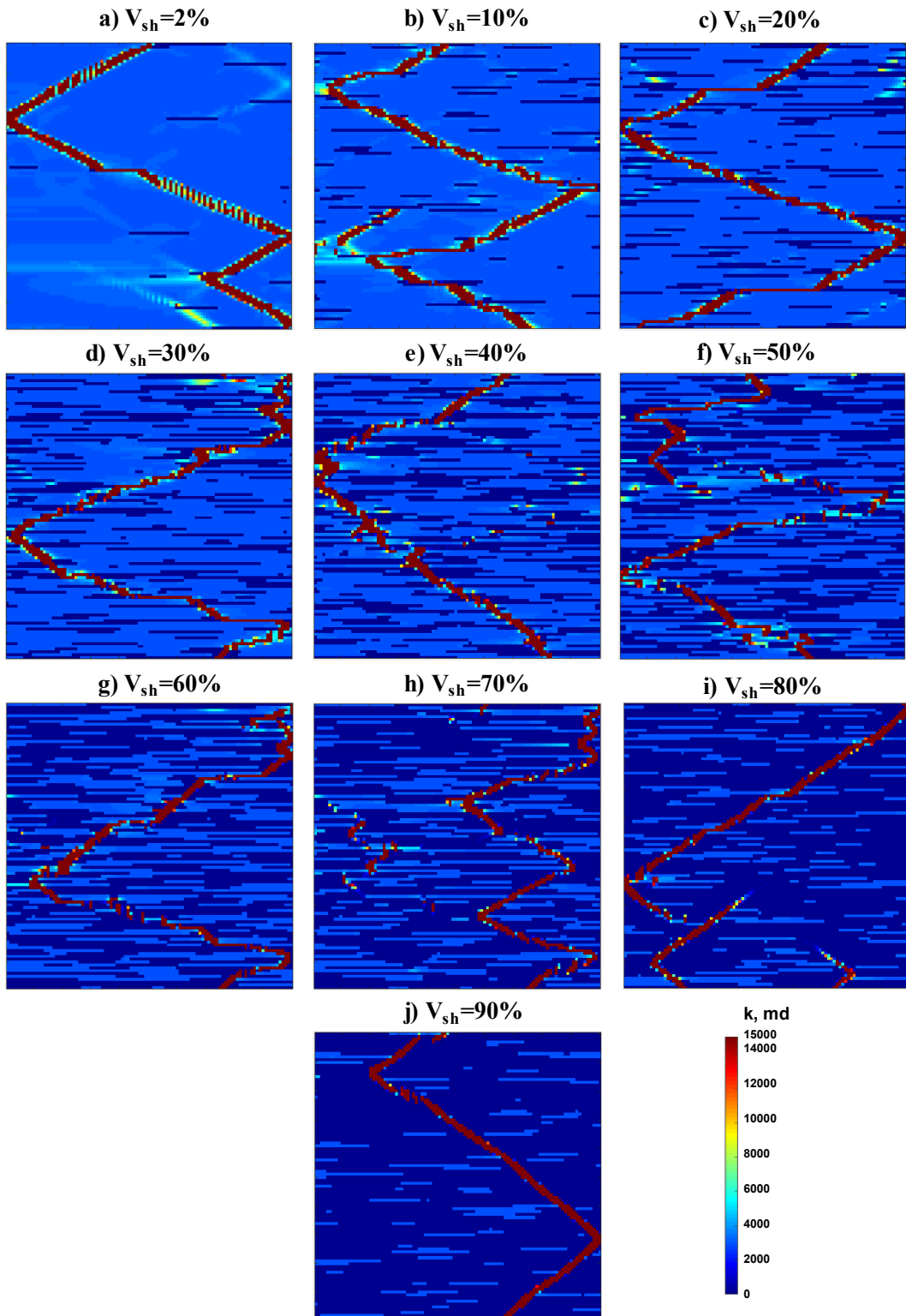
Figure 4-3. Permeability distribution at residual state (2% axial strain) for cases with various V_{sh}.

The computed effective vertical and horizontal permeability for the realizations at 0 and 2% axial strain are in Table 4-1. The vertical effective permeability is more sensitive to V_{sh} than horizontal permeability at the initial condition. The horizontal effective permeability is systematically higher than vertical due to the low permeability horizontal shale layers. After 2% ε_a, the effective horizontal and vertical permeabilities are both enhanced by shear failures. The upscaled permeabilities at 2% ε_a are normalized by the permeability at initial condition and plotted in Figure 4-4, showing that the normalized vertical effective permeability is systematically higher than horizontal. For cases with $V_{sh}>80\%$, the normalized vertical permeability is more than 7 times at 2% ε_a because flow can channel through the high permeability flow paths (Figure 4-3i and 4-3j).

Table 4-1 Effective k_v and k_H with/without considering failure modes at 0 & 2% ε_a.

V_{sh}	$k_{v,fm}^{eff}$ @ 0	$k_{v,fm}^{eff}$ @ 2% ε_a	$k_{v,ave}^{eff}$ @ 2% ε_a	$k_{h,fm}^{eff}$ @ 0	$k_{h,fm}^{eff}$ @ 2% ε_a	$k_{h,ave}^{eff}$ @ 2% ε_a
0.02	2128	2702	4897	2916	3565	6709
0.10	853	1467	2116.	2624	3349	6508
0.22	196	515	487	2162	2817	5365
0.31	86.1	265	219	1749	2298	4441
0.42	45.3	226	108	1251	1748	2983
0.51	32.9	131	89.2	831	1308	2251
0.62	20.5	85.3	52.2	532	910	1351
0.72	15.3	57.1	37.9	252	506	624
0.82	12.5	111.3	28.3	108	360	244
0.90	11.1	78.5	24.4	31.0	101	68.3
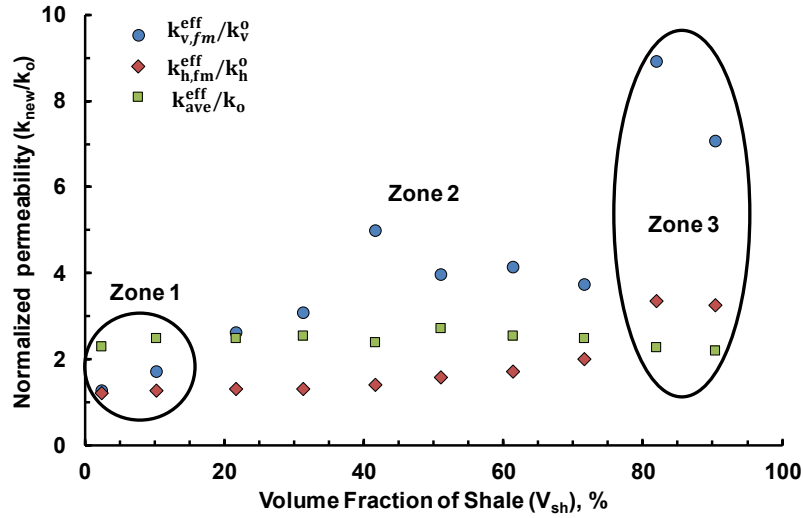
Figure 4-4.   Effective permeability changes at 2% ε_a for cases with different V_{sh} in horizontal bi-axial compression. Blue: normalized effective vertical permeability; Red: normalized effective horizontal permeability. Green: normalized permeability when using volume average total volumetric and plastic shear strain

The effective permeability using the volume average total and plastic strain in Equation 4-8 are also listed in Table 4-1 and plotted in Figure 4-4. In zone 1, the effective permeability which does not consider the modes of failure overestimates the enhancement of permeability, while underestimates the changes of permeability in zone 3. The reason is that the volume average of plastic shear strain (Figure 4-5a) does not consider the localized shear band (Figure 3-11). Therefore, it cannot capture the flow response after deformation. Therefore, the scale factor "a" in Equation 4-8 should be characterized for the realizations with various V_{sh} to compensate the error caused by the ignorance of failure modes.
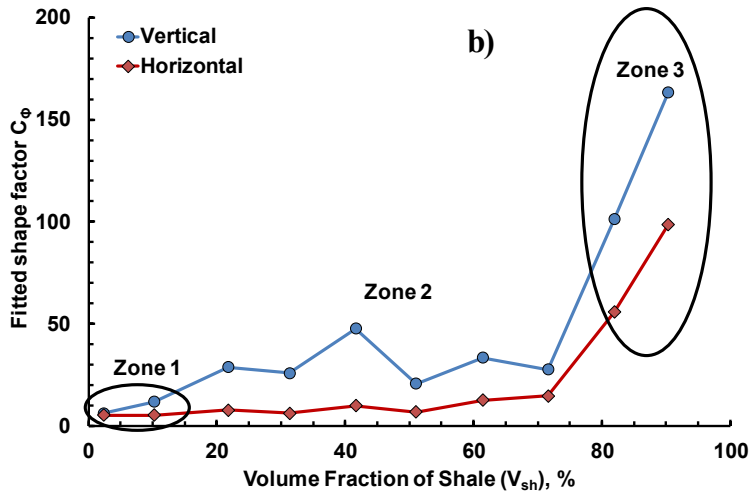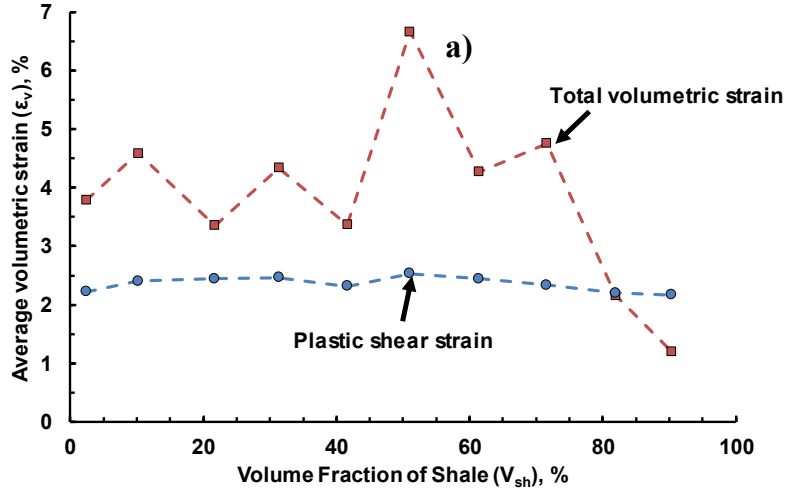
Figure 4-5.   a) Volume average total and plastic shear strain for cases with different V_{sh}. b). Vertical and horizontal tuning parameters C_Φ if applying Equation 30.

Touhidi-Baghini (1998) proposed Equation 4-9 to estimate updated permeability based on the total volumetric strain:

$$k_{new}/k_o = exp[C_\emptyset \varepsilon_v],$$ Equation 4-9

where $C_\emptyset$ is a shape factor calibrated to experimental results. Li and Chalaturnyk (2006) matched the absolute permeability due to shearing for both horizontal and vertical samples with $C_\emptyset$ of 5.9 for the horizontal sample and 14.76 for the vertical sample. The total volumetric strain for cases

with different V_{sh} is plotted in Figure 4-5-a. Using a constant $C_\emptyset$ can hardly match the effective permeability for realizations with different V_{sh} shown in Figure 4-4. By matching the vertical and horizontal effective permeability when considering modes of failure, $C_\emptyset$ are plotted versus V_{sh} in Figure 4-5b, which is highly sensitive to V_{sh} from 6.3 to 163.3 in vertical direction and 5.3 to 98.7 in horizontal direction. The $C_\emptyset$ obtained by Li and Chalaturnyk (2006) lies between the V_{sh} from 10% to 20% for the horizontal and vertical directions. The high sensitivity of $C_\emptyset$ for cases with different V_{sh} indicate that absolute permeability increase is strongly dependent on the fines content in the oil sands. As a consequence, the modes of failure in the upscaled block should be treated carefully in order to accurately reproduce the permeability change caused by shear failures.

4.4   Summary

Modes of failure are found extremely important in the prediction of permeability changes during the shearing process because it determines the tortuosity of the localized high permeability flow channels. If the impact of heterogeneity on the failure modes is not considered correctly, the widely used global average total volumetric or plastic shear strain will lead to erroneous estimations of the effective permeability change due to deformations. Ideally, the scaling and shale factor should be characterized based on the failure modes of each upscaled block, which may significantly increase the computational effort in the upscaling process. As an alternative, the fit shape factor $C_\emptyset$ in Equation 4-9 is a better option with current computational power to be used to limit the potential error in estimation of permeability changes due to deformations. The same concepts apply for fractured reservoir with pre-existing and extended fractures during hydraulic fractures that the orientation and apertures of fractures should be carefully considered to have an accurate estimation of the effective permeability.

CHAPTER 5:   ASSESSING SAGD RESPONSE DUE TO DEFORMATIONS

In Chapter 3, the impact of heterogeneity on the geomechanical response of heterogeneous oil sands is parameterized in numerical investigations of spatially correlated sand-shale realizations. The shear failures of oil sand realizations lead to significant changes in effective permeability which can be quantified by total volumetric and plastic shear strain as explained in Chapter 4. The geomechanical response and induced change on flow properties are expected to have an impact on SAGD because of the significant changes in the pressure and temperature in the reservoir. With the coupled reservoir-geomechanics simulations, the complex interactions of flow and geomechanical response can be better analyzed and understood. The main objective of this chapter is to develop the geological modeling workflow and apply the coupled reservoir-geomechanics SAGD simulation to the heterogeneous oil sand reservoir to assess the stress-paths and reservoir performance affected by deformations and failures.

5.1   MacKay River Geological Model

The workflow for the mechanical earth model (MEM) is developed and applied to the MacKay River oil sand area. The geo-cellular model can be directly used or upscaled as input for the reservoir-geomechanics coupling platform.

5.1.1   Overview of Geological Modeling Work Flow

The geological modeling workflow with calibrations of reservoir-geomechanics simulation is illustrated in Figure 5-1, with the following four steps:

a) Data audit and framework model generation: the geologic, seismic, log and core data are collected and sorted from all possible sources. The framework model includes the formation tops, location of fractures and fine grids. It serves as the foundation of the fine-scale geological model.

Seismic data or well markers at different formation tops are often used to determine the stratigraphic information and appropriate cell size.

b) Analyze seismic, well log and core laboratory test data to obtain initial estimates of the reservoir (facies, density, porosity, permeability and saturation), geomechanical (elastic and plastic properties) and in-situ conditions (stress state, pore pressure and temperature). The measurements of porosity and saturation are widely used to calibrate the available log data. The appropriate relations between permeability and porosity, dynamic elastic and plastic geomechanical properties and compression and shear wave velocities are generated from the experimental geomechanical tests.

c) Generate stratigraphic full-field geocellular models with heterogeneous petrophysical and geomechanical properties. The variograms for reservoir and geomechanical properties are modeled to generate the distributions of heterogeneous properties by Sequential Gaussian simulation (SGS).

d) Input the full-field geocellular model into the coupling platform and post-process the geo-cellular model. The geocellular model is calibrated with the production and monitoring data, e.g. oil rate, steam oil ratio, surface heave, interferometric synthetic aperture radar (InSAR), by comparing with the coupled reservoir-geomechanics simulation results.
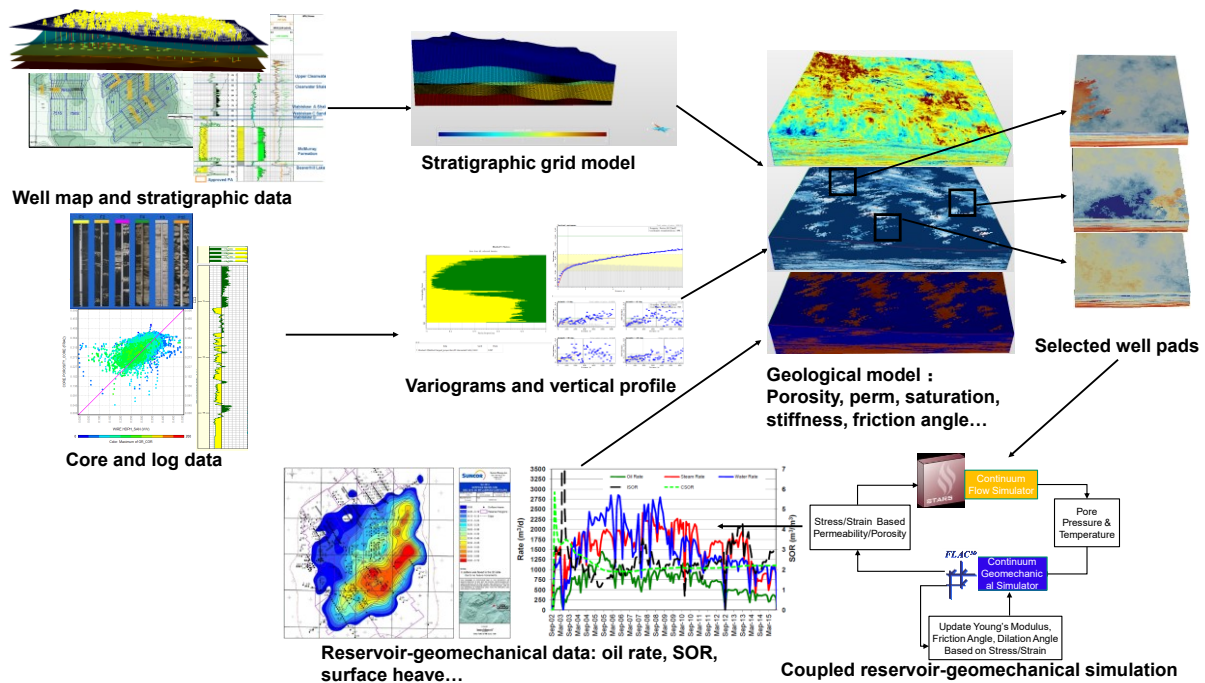
Figure 5-1.   Integrated geological modeling workflow with coupled reservoir-geomechanics simulation.

5.1.2   Data Audit and Stratigraphic Grid Model Generation

The Suncor MacKay River project is chosen because it is well-established with a long and successful production history providing extensive data resources for geological modeling. The horizontal wells are located in the McMurray Formation at a depth of 98-145 m, which falls in the category of shallow Athabasca oil sands where geomechanics assessments have become an AER application requirement. The MacKay River project is Suncor's first operated SAGD facility located 60 km NW of Fort McMurray (Figure 5-2). The current approved bitumen production rate is 11600 m^3/day (73 kb/d) and 112 wells pairs have been added according to the 2015 Suncor MacKay River project AER report.
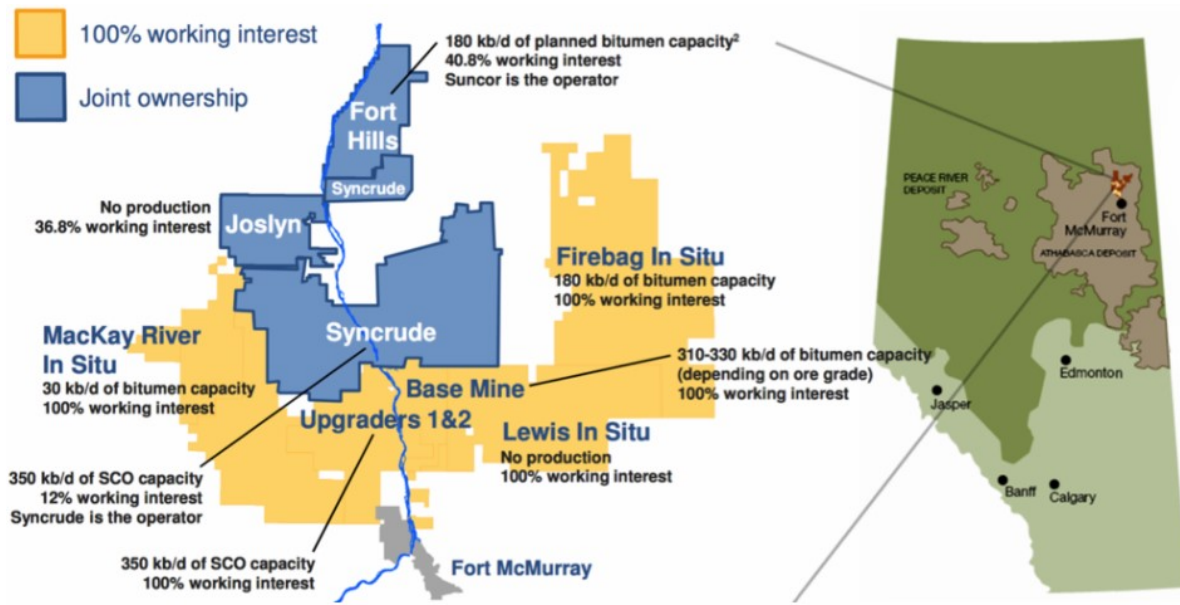
Figure 5-2.   Location of Suncor MacKay River SAGD project (From Oil Sands Magazine 2017).

The stratigraphic, log and core data are extracted from geoSCOUT (© geoLOGIC), which is a visualization, analysis and forecasting suite with an extensive library of energy data. The well pads and subsurface patterns are shown in Figure 5-3a. The area of interest can be found in geoSCOUT near the cross-section of T93 and Range 12 (Figure 5-3b). Among the 1561 wells available, 585 wells have the location and elevation of formation tops to generate stratigraphic horizons; 183 wells have core data, e.g. oil/water saturation, porosity and absolute permeability; 112 wells have Log ASCII Standard (LAS) files including high-resolution Gamma Ray, neutron/density porosity, resistivity, spontaneous potential and bulk density.

a) Well trajectories and subsurface patterns   b) Well pads in geoSCOUT
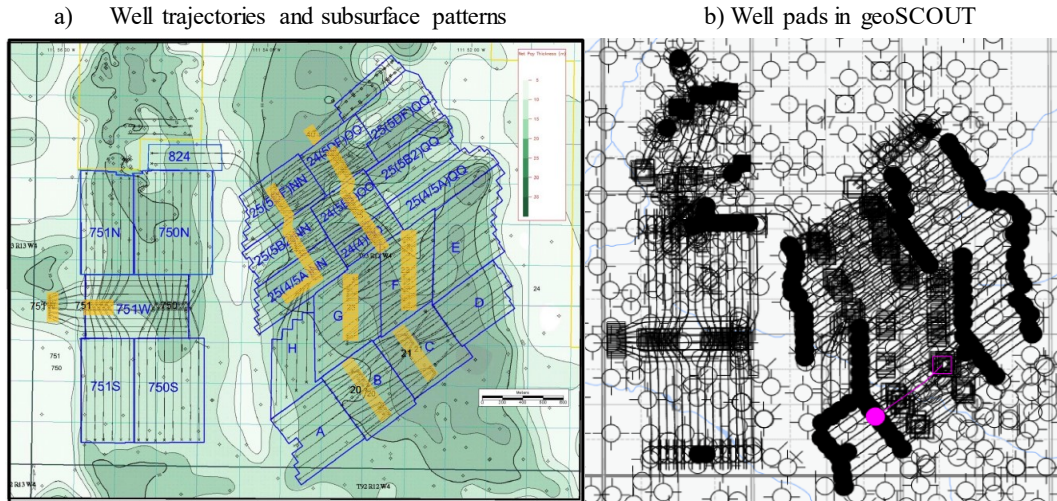
Figure 5-3.   Well trajectories and subsurface patterns (Alberta Energy Regulator 2015) and corresponding well pads in geoSCOUT where the log data is extracted.

The SKUA GOCAD (© Paradigm) is a commercial geological modeling platform, combining geophysics interpretation, reservoir modeling and flow simulation in a unified work process. Inputting the LAS files, the formation tops for each vertical well can be identified as the well markers. They are used to determine the stratigraphic horizons: Till, Clearwater, Wabiskaw, McMurray and Devonian Formation from top to bottom (Figure 5-4).
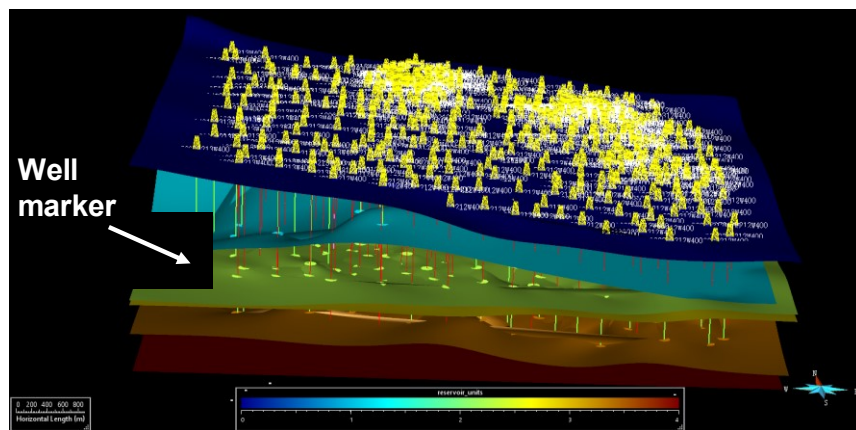
Figure 5-4. Well marker and stratigraphic horizons for Till, Clearwater, Wabiskaw, McMurray and Devonian Formations (top to bottom).

Given current computational power, a geologic model of 1-10 million cells is recommended. Therefore, the length of cell is set to 50 m. The thickness of cell varies at different formations (Table 5-1). In McMurray and Wabiskaw Formation, the average cell thickness is 1 m as it is the major pay zone with highly heterogeneous oil sands mixed with shale bedding planes. For Clearwater Formation, the average grid thickness is 1.5 m because it is the caprock for geomechanics assessment. The entire stratigraphic grid model (Figure 5-5) has 4.6 million grids.

Table 5-1 Number of layers and layer thickness in the gridded model.

Formation	Number of layers	Average layer thickness
Till	13	10
Clearwater	81	1.5
Wabiskaw	27	1.0
McMurray	66	1.0
Devonian	7	9.0
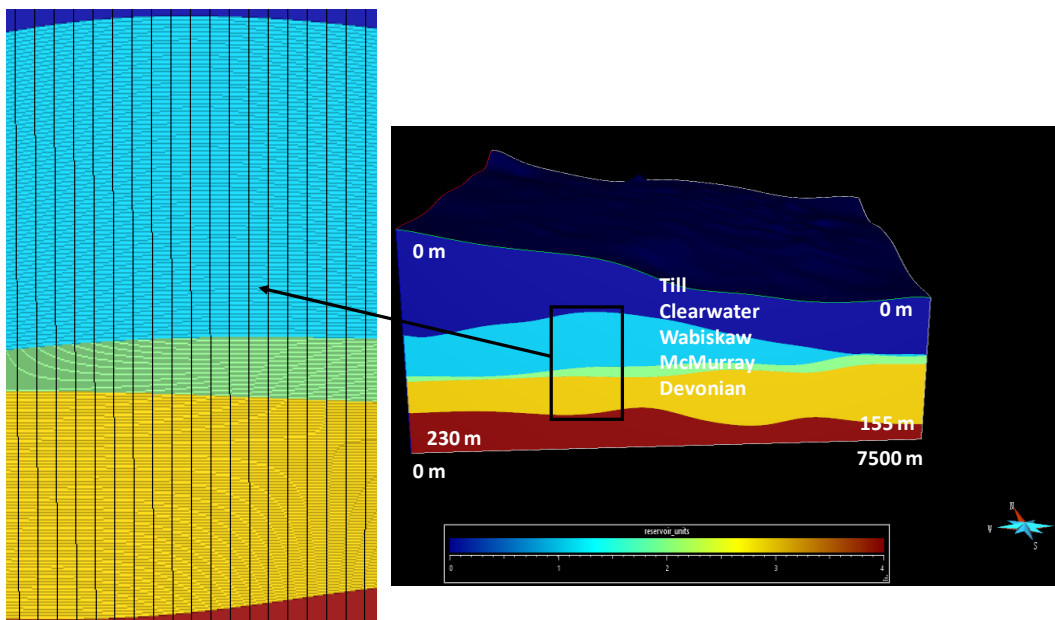
Figure 5-5.   Framework model of the MacKay River oil sands area.

5.1.3 Data Analysis

The reservoir, geomechanical properties and in-situ stress conditions are required to have a full mechanical earth model. The determination of these properties requires specific workflows from the data available. The following subsections demonstrate the applied workflows for data analysis of each individual property for the generation of geological models for coupled simulation.

5.1.3.1 Facies, Porosity and Saturation

The Gamma Ray (GR) log is a continuous measurement of the natural radioactivity from the formations, which is used to characterize the lithology (facies) of rock or sediment in a borehole or drill hole. As isotopes concentrate in clays, the measurement of GR log (API unit) is directly related to V_{sh}. The shale layers in the GR log can be identified by cutoff lines at user-defined intervals depending on reservoir types. The details of current shale discrimination methods can be found in Bartetzko et al. (2012). Here, 75° API is selected as the cutoff between sand and shale facies according to EUB/AGS Earth Sciences Report (Alberta Energy and Utilities Board 2006-06). The resolution of GR is usually at a 25 cm scale which is finer than the cell thickness, so upscaling is required to determine the facies of each cell by the largest proportion discriminated by the shale cutoff. The histograms of the sand and shale after upscaling are close to the original results determined by GR (Figure 5-6). The McMurray Formation is sand dominant (79.4%); the Wabiskaw Formation (23.3%) has 10% more sand facies than Clearwater Formation (13.9%).
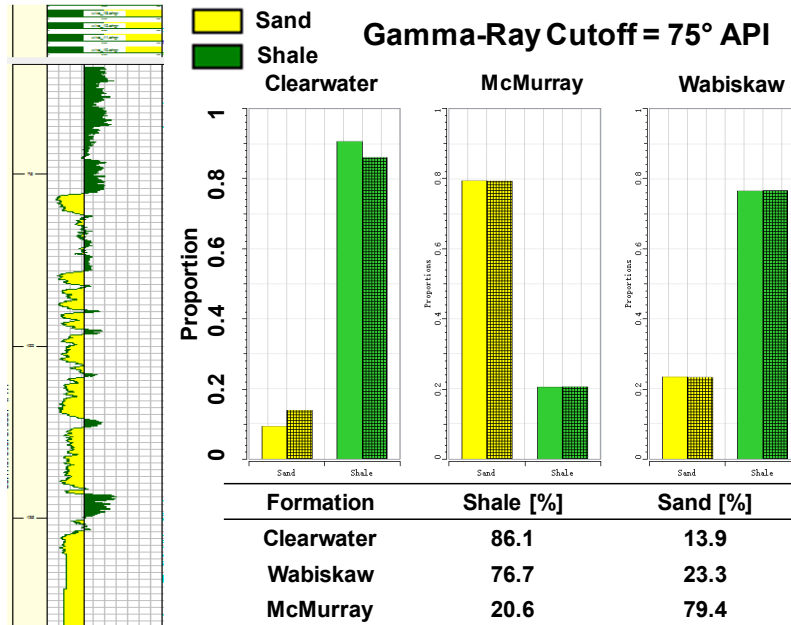
Figure 5-6. Histograms of the sand and shale at the Clearwater, Wabiskaw and McMurray Formations of the gridded model (blocked bar) and original results from GR log (color bar).

Formation	Shale [%]	Sand [%]
Clearwater	86.1	13.9
Wabiskaw	76.7	23.3
McMurray	20.6	79.4

The vertical proportion for sand and shale are calculated for all 112 wells and plotted in Figure 5-7. At the depth of 60-120 m, low permeability shales dominate the Clearwater and Wabiskaw Formation as the caprock of the reservoir. Overlain by the caprock, the McMurray Formation is the major pay zone of the Athabasca oil sands.
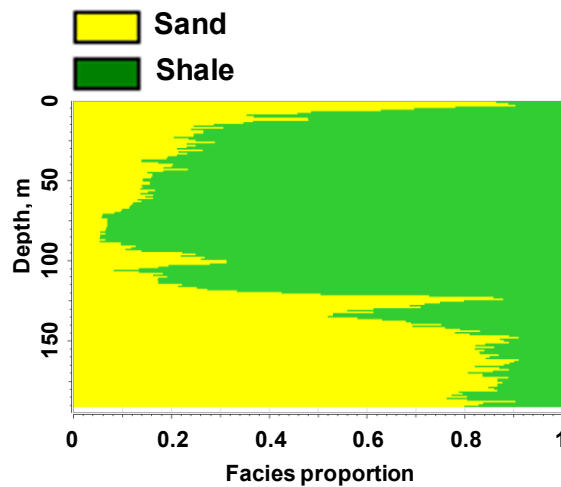
Figure 5-7. Vertical proportion curves for sand and shale.

142

In computing porosity from core and log data, depth and cross plots of the core data versus various porosity log data (density porosity, neutron porosity and sonic derived porosity) are used to determine which porosity log has the strongest correlation with the core porosity measurements. The density log is usually the best option for porosity estimates except for caved holes and lithologies with heavy minerals (Patchett and Coalson 1979). For the MacKay River oil sand area, it is in close agreement with the core density (Figure 5-8) in both depth and cross-plots against core data as analyzed in Geolog (© Paradigm). Therefore, the density porosity is used for porosity estimates here. The histograms of porosity for the Clearwater, Wabiskaw and McMurray Formations are shown in Figure 5-9, where the average porosity is 0.26, 0.28 and 0.31, respectively.
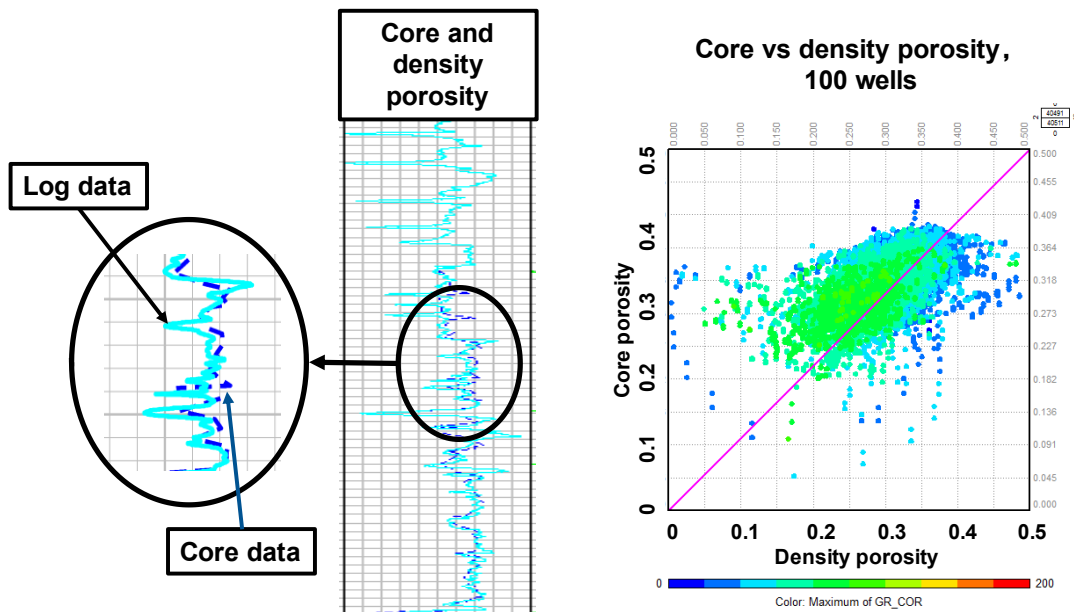
Figure 5-8.   Density porosity log compared to core porosity.
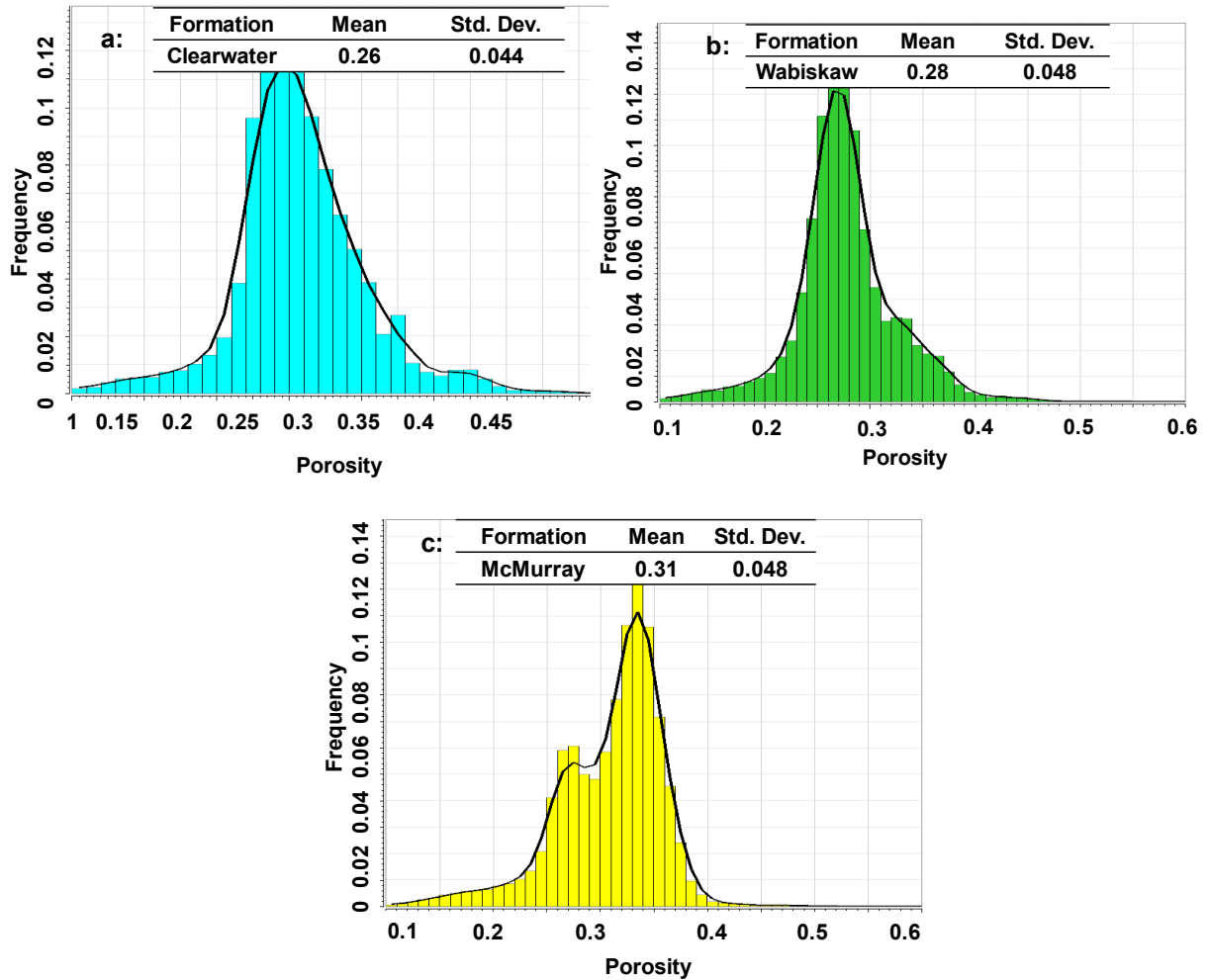
Figure 5-9.   Porosity histograms for the a) Clearwater, b) Wabiskaw and c) McMurray Formations.

Accurate determination of water saturation (S_w) is important for geological modeling and many methods, e.g. log evaluation, saturation-height function from capillary pressure, core evaluation and artificial neural network models, are available (Al-bulushi et al. 2009). Resistivity logs, e.g. induction logs, laterologs and micro resistivity logs, are widely used for oil and water saturation determination as required by government regulations. The details of the workflows for the determination of water and oil saturation are not discussed here as they are highly dependent on

the data available and reservoir types. For the MacKay River oil sand area, the resistivity from the array induction log (AIT) is used for the computation of water and oil saturation.

5.1.3.2 High-resolution Electrofacies

High-resolution electrofacies are applied to characterize the small variations in the reservoir reflected by different log interpretations. The classification of electrofacies is conducted through the cluster analysis to identify clusters with similar characteristics of log response. Cluster analyses with/without subjective judgments are available to determine electrofacies (Lee et al. 2002), e.g. nearest neighbor, k-means clustering and unsupervised artificial neuron network (Correia and Schiozer 2016).

For the MacKay River oil sand area, five clusters can be identified in the cross-plot of density and GR (Figure 5-10). Electrofacies 1 corresponds to the low permeability facies with low clay content, such as limestone and dolomite with a high density (2400 kg/m^3), low GR (10-50) and porosity (0.1-0.2). Electrofacies 2 represents the clay-rich shale, resulting in the highest GR (>88), medium to high density (2100-2380 kg/m^3) and low to medium porosity (0.2-0.3). Electrofacies 3 is close to the IHS. The log interpretation is between the oil sand and shale facies: medium GR (53-88), medium density (2000-2250 kg/m^3) and medium porosity (0.25-0.35). Electrofacies 4 is the oil-rich sand facies with interlocked structure, with the low Gamma Ray (10-53), low density (2000-2250 kg/m^3) and high porosity (0.3-0.4). Electrofacies 5 represents loose sand with extra pore space compared to interlocked oil sands, leading to a lower density (1850-2000 kg/m^3) and higher porosity (0.4-0.5).
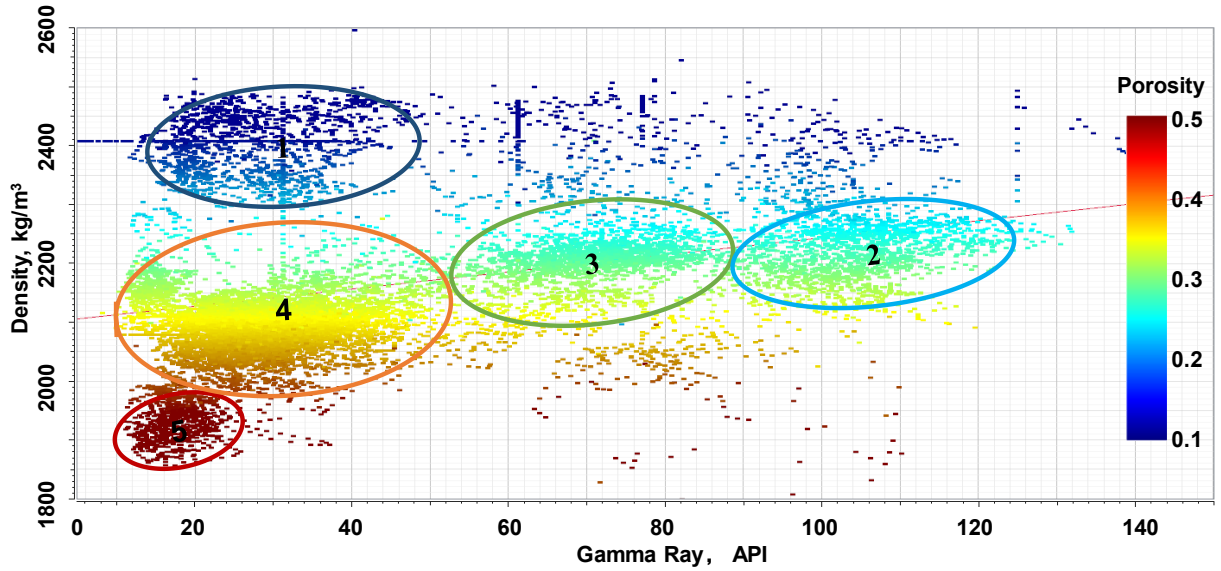
Figure 5-10.   Clusters observed in cross-plots of density vs. GR. The color scale shows the porosity calculated based on density for all of the intervals.

Following the definition of electrofacies 1 to 5, the histograms in the Clearwater, Wabiskaw and McMurray Formations are illustrated in Figure 5-11. Most of the limestone and dolomite are located in the Clearwater and Wabiskaw Formations. The IHS facies occupies 22% in Wabiskaw and 28% in McMurray Formation, which draws increasing attention due to its complex flow and geomechanical response. The Clearwater Formation is dominated by low porosity and permeability shale facies (70%) and limestone/dolomite (15%), which serves as the caprock. The McMurray Formation has nearly 60% oil sand and 30% IHS indicating the rich pay zone.
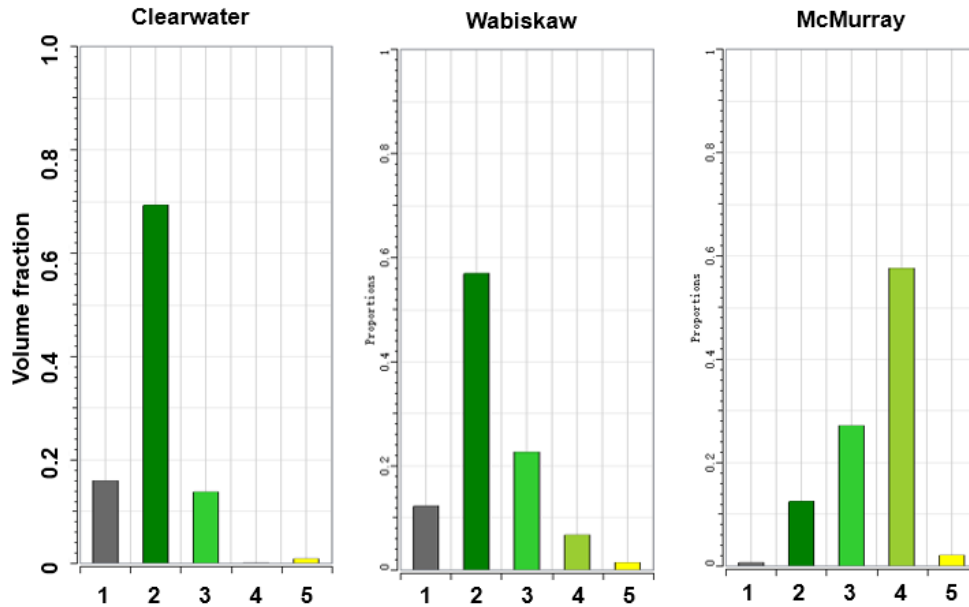
Figure 5-11. Volume fraction of electrofacies in the Clearwater, Wabiskaw and McMurray Formations. 1: Limestone and Dolomite; 2: Shale; 3: IHS; 4: Oil sand; 5: Loose sand.

Although electrofacies help to refine the characterization of the reservoir, it also adds difficulties in determining the appropriate flow and geomechanical properties for different facies because they are not well-defined rock types like sand or shale. Given the current development and understanding of coupled reservoir-geomechanics simulation, a complex geological model with electrofacies is not used here but is useful for reservoir characterization and helps understand the geology of the area of interest.

5.1.4   Generation of Mechanical Earth Model

The log and core data only provide information near the borehole, but the MacKay River oil sand reservoir is highly heterogeneous according to seismic inversion case studies (Bellman et al. 2012). The spatial variability of the reservoir and geomechanical properties can be quantified by variograms. Variogram models are fit to the data for the generation of the distributions of facies and petrophysical properties for the Clearwater, Wabiskaw and McMurray Formations.

147

5.1.4.1 Facies

The experimental variograms of facies in the McMurray Formation are calculated from the facies at cells along the wellbore by GR log. Variogram models are fit to the experimental variograms, e.g. vertical variogram model is shown in Figure 5-12. For the Clearwater and Wabiskaw Formation, the experimental variograms and variogram models are processed with the same workflow. With the generated variogram models and histograms (Figure 5-6), the facies model of the Clearwater, Wabiskaw and McMurray Formations in MacKay River oil sand area (Figure 5-13) is created by sequential indicator simulation (SIS). The Till and Devonian Formations are neglected in the facies model and petrophysical model because of insufficient GR log. The impact of heterogeneity in these two formations on the reservoir performance is not as important as the Clearwater, Wabiskaw and McMurray Formations.
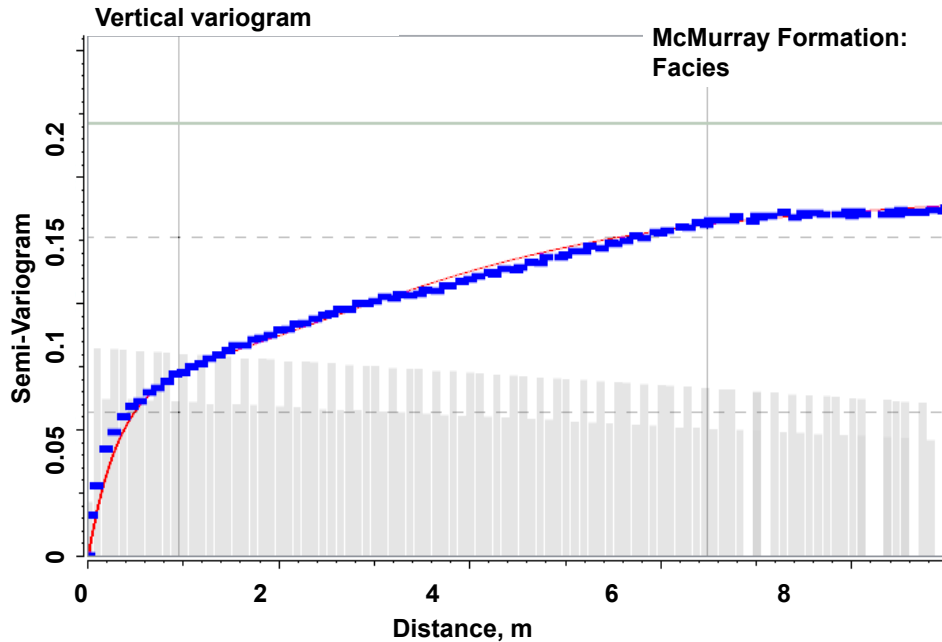
Figure 5-12.   Vertical variogram model fitted to the experimental variogram for facies in the McMurray Formation.
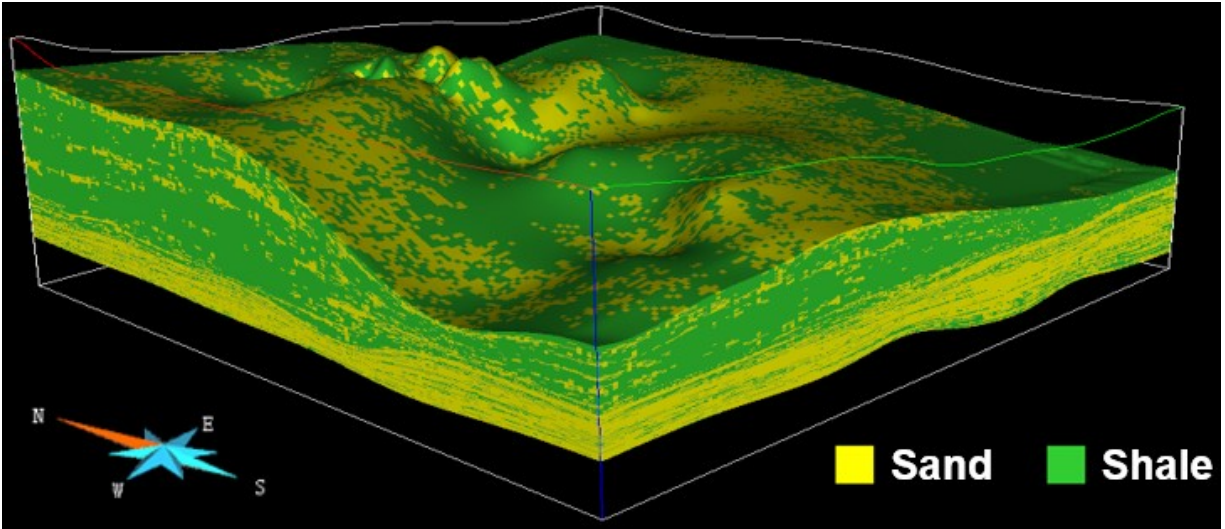
Figure 5-13.   The facies model for the Clearwater, Wabiskaw and McMurray Formations.

5.1.4.2 Porosity

The histograms of porosity are computed from the corrected density porosity log in Figure 5-14. The experimental variograms of corrected density porosity are calculated for sand and shale (Figure 5-15). Sequential Gaussian simulation (SGS) is used to generate the distributions of porosity for the Clearwater, Wabiskaw and McMurray Formation in Figure 5-16. The porosity model is well correlated with the facies model showing high porosity in the McMurray Formation and low porosity in the Clearwater and Wabiskaw Formations.
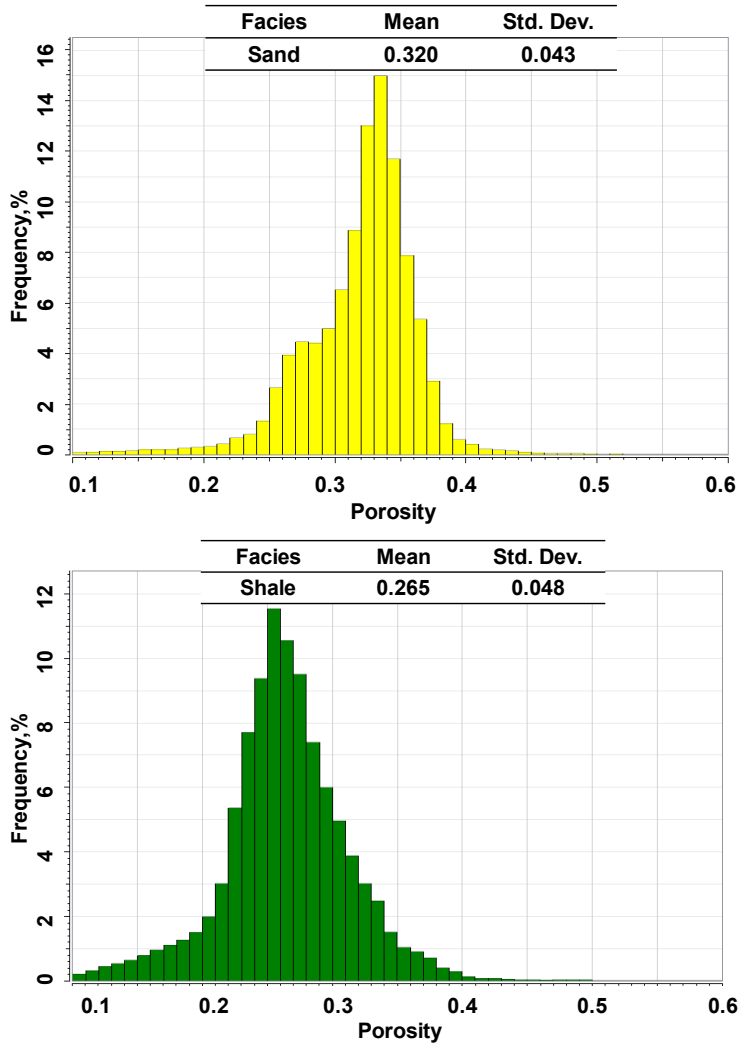
Figure 5-14.   Histograms of porosity for sand (yellow) and shale (green) facies for sand and shale cells from density porosity measured by well log data.
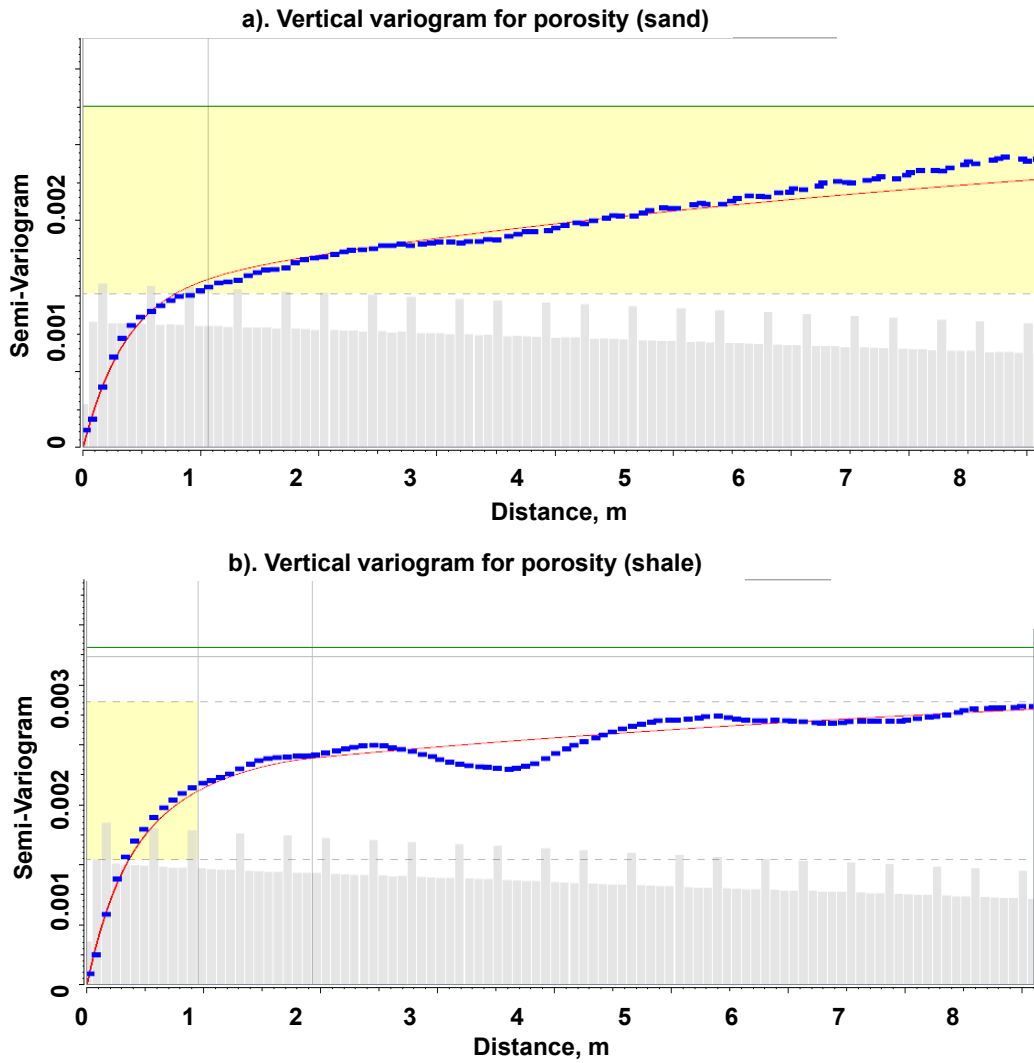
Figure 5-15.   Vertical variogram models for porosity in sand and shale fitted to experimental variograms.
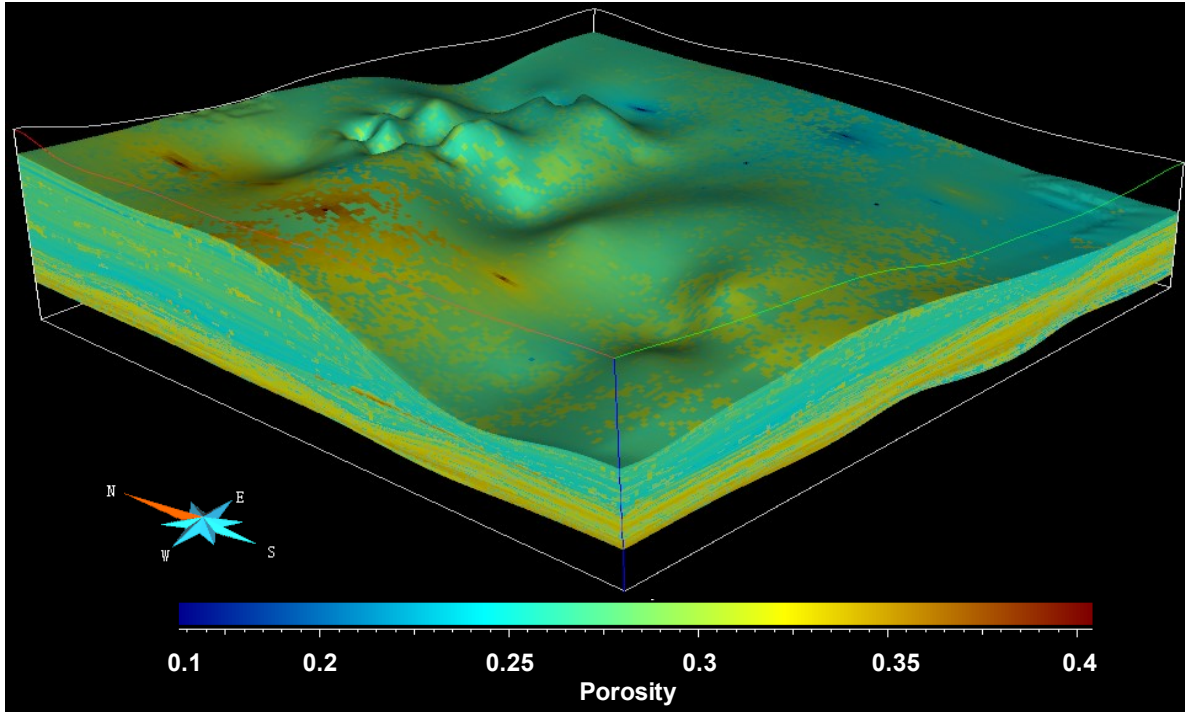
Figure 5-16. The porosity distribution for the Clearwater, Wabiskaw and McMurray Formations.

5.1.4.3 Permeability

Core data is the starting point for calculations of permeability in field evaluations. The cross-plots of core permeability versus porosity is usually used to determine the correlation of permeability from porosity. The correlations for oil sands permeability in the literature are applied due to the lack of core permeability data to generate a trustworthy correlation. For sand, the vertical permeability uses correlation proposed by Deutsch (2010) for the McMurray Formation.

$$log_{10}(K_{zz}) = a_0 + a_1\phi + a_2(1 - e^{-3\phi/\phi_c}) ,$$

Equation 5-1

where a_0 is -2, a_1 is 3.67, a_2 is 4.151 and ϕ_c is 0.31 here.

At the geological cell scale (0.5 - 1.0 m in vertical, 10 m to 50 m in horizontal), laboratory tests on permeability are not available, so minimodelling (Deutsch 2010) is used to determine the ratio

of vertical and horizontal permeability. For horizontal permeability ranges from 200 mD to 2000 mD, the vertical permeability can be assumed 0.2 to 0.8 of the vertical permeability for sand depending on the V_{sh} of cells, e.g. 0.5 here.

For shale facies, the correlation follows the form to Kozeny-Carman equation as:

$$K_{zz} = (\frac{\Phi}{0.26})^{15} .$$
<div align="right">Equation 5-2</div>

For shale with low permeability, the vertical permeability can be assumed 0.1 to 0.25 of the horizontal permeability, e.g. 0.25 here.

Based on the porosity model, the distribution of vertical permeability for the Clearwater, Wabiskaw and McMurray Formations is computed from the correlations in Equation 5-1 and 5-2 (Figure 5-17).
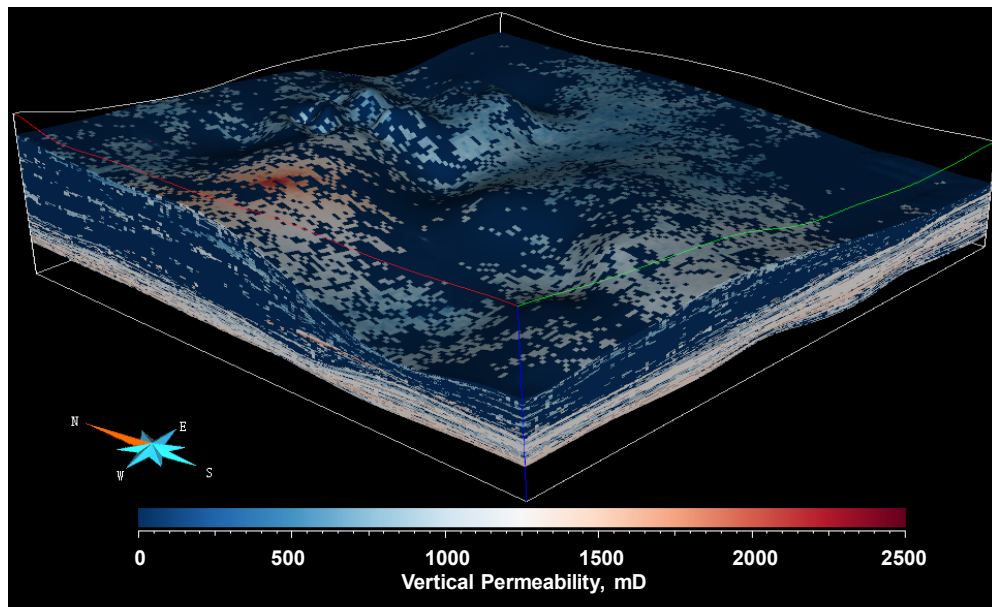
Figure 5-17. The distribution of vertical permeability for the Clearwater, Wabiskaw and McMurray Formations.

5.1.4.4 Saturation and Bulk Density

Water saturation is generated from the saturation core data and resistivity logs. No gas cap has been reported for the MacKay River project, so the gas saturation is 0. The oil saturation is calculated as:

$$S_o = 1 - S_w - S_g \, .$$
<div align="right">Equation 5-3</div>

The Till and Devonian Formations are assumed fully saturated with water.

The bulk density for each cell is required as it determines the stress and strain behavior during the coupled simulation process. The distribution of bulk density follows the same workflow as porosity: 1) calculate histograms and variograms; 2) SGS simulation. The bulk density for the Till and Devonian Formations is calculated as:

$$\rho_b = \rho_s(1 - \phi) + \phi(S_o\rho_o + S_w\rho_w + S_g\rho_g) \, ,$$
<div align="right">Equation 5-4</div>

where $\rho_o = 900 \; kg/m^3$, $\rho_w = 1000 \; kg/m^3$ and $\rho_g = 10 \; kg/m^3$.

5.1.4.5 Temperature, Pore pressure and Effective Stress

The temperature and pore pressure are the key parameters that are transferred between the sequentially coupled reservoir and geomechanical simulations. The temperature is estimated via the measurement of surface temperature and the temperature gradient in the reservoir:

$$T = T_o + \Delta T \times Z \, ,$$
<div align="right">Equation 5-5</div>

where T_o is the temperature at the surface, ΔT is the temperature gradient and Z is the depth of the center of each cell.

The incremental pore pressure is estimated by the pore fluid for each cell:

$$dP = (S_o\rho_o + S_w\rho_w + S_g\rho_g) \times 9.806 \times dZ .$$ Equation 5-6

The incremental vertical stress is calculated via the bulk density:

$$d\sigma_z = \rho_b \times g \times dZ ,$$ Equation 5-7

where g is the gravity gradient and dZ is the thickness of each cell. The pore pressure and vertical stress are calculated by the summation of the incremental pore pressure and vertical stress over depth.

The in-situ stress is anisotropic due to the variation of tectonic forces. Figure 5-18 presents the stress map of Alberta showing that the maximum horizontal compressional stress (σ_{Hmax}) is SW to NE, which is perpendicular to the edge of the Rocky Mountains and Alberta Basin. The X-axis of Pad C is the maximum principal stress direction along the horizontal well pairs (Figure 5-3). As the MacKay River oil sand area is shallow, the vertical total stress (σ_v) is between the minimum and maximum horizontal stress (σ_{Hmin}) and σ_{Hmax}. K_o ($\sigma_{Hmin}/\sigma_{Hmax}$) is assumed to be 0.6; while S_o (σ_{Hmax}/σ_v) is 1.1 (Chalaturnyk and Li 2004). σ_x and σ_y can be calculated from:

$$\sigma_x = (\sigma_z - P) \times S_o + P ,$$ Equation 5-8

$$\sigma_y = (\sigma_x - P) \times K_o + P .$$ Equation 5-9
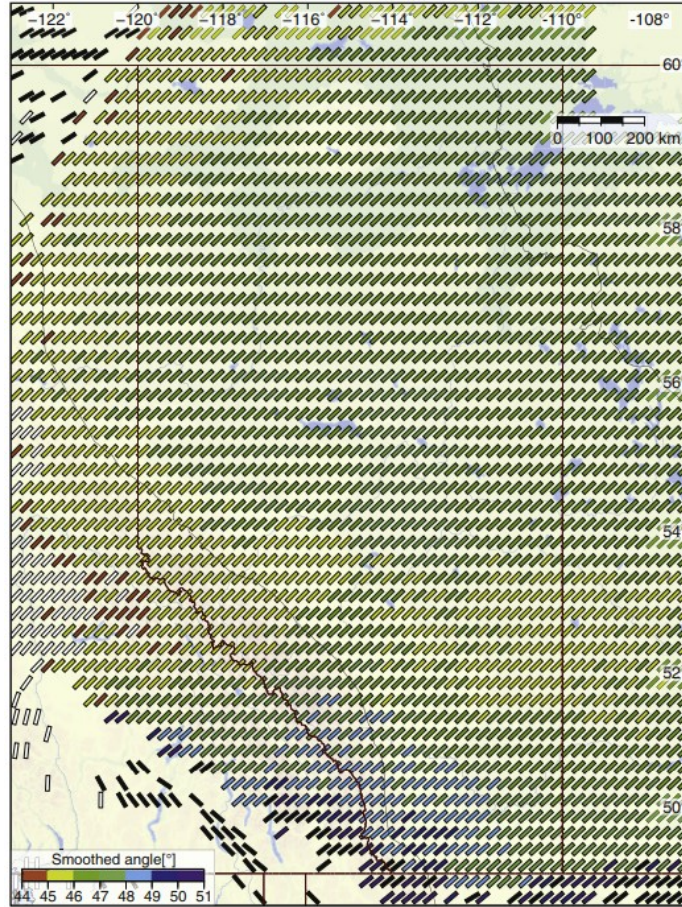
Figure 5-18.   The directions of major principal stress in Alberta (Retrived from Reiter K. et al. 2014).

The effective stress is calculated as the average total stress minus the pore pressure:

$$\sigma' = \frac{(\sigma_x + \sigma_y + \sigma_z)}{3} - P \ ,$$
                                                                                                Equation 5-10

The reservoir properties and in-situ conditions generated for the geological model of the MacKay

River oil sands area are summarized in Table 5-2.

Table 5-2 Reservoir properties and in-situ conditions for the mechanical earth model of the MacKay River oil sand area.

Formation	Till	Clearwater	Wabiskaw	McMurray	Devonian
Facies	N/A	Sand		Shale	N/A
Porosity	0.3	0.28-0.36		0.24-0.29	0.3
Permeability X&Y, md	2	1565-4252		5.2-7.7	50
Permeability Z, md	2	782-2126		1.3-1.9	50
Bulk Density, kg/m³	1840	2139-2216		2269-2320	2365
Oil Saturation	0	0.76-0.84		0.09-0.11	0
Water Saturation	1	0.16-0.24		0.89-0.91	1
Temperature, °C	3.1-4.3	5.1-7.0		4.4-7.0	7.1-8.3
Pressure, MPa	49-490	223-867		203-867	915-1358
σ_x, MPa	94-943	1649-3331		1061-3330	3425-4558
σ_y, MPa	74-737	1084-2211		824-2210	2284-3103
σ_z, MPa	90-902	1570-3107		1014-3106	3197-4267
σ', MPa	37-371	1290-2016		500-2015	2054-2618

5.1.4.6 Geomechanical Properties

The required geomechanical properties are dependent on the constitutive models used for geomechanical simulation. The Mohr-Coulomb model is used for the Till and Devonian Formations to avoid non-linearity in geomechanical simulations (Table 5-3). For the Clearwater, Wabiskaw and McMurray Formations, the strain-softening M-C model is used to mimic the progressive failure of oil sands and shale obtained by experimental results (Chalaturnyk 1996). The Young's modulus of oil sands is strongly related to the confining stress (Figure 2-10). Chalaturnyk (1996) proposed the equation below to estimate Young's modulus of oil sands:

$$E = 343\sigma'^{0.875} ,$$

<div align="right">Equation 5-11</div>

The bulk and shear modulus can be estimated via:

$$K = E / 3(1 - 2v) ,$$

<div align="right">Equation 5-12</div>

$$G = E / 2(1 + v) .$$

<div align="right">Equation 5-13</div>

The friction and dilation angle of sand are fixed before failure and decrease after plastic deformations occur. The post-peak friction and dilation angles follow the correlations generated by Li and Chalaturnyk (2005) as a function of plastic shear strain for Alberta oil sands (Table 5-4).

For shale, a correlation is fit to the experimental data by Zadeh and Chalaturnyk (2015) in the Clearwater shale:

$$E = 58.4\sigma' ,$$ Equation 5-14

The geomechanical properties for the different formations are summarized in Table 5-3.

Table 5-3 Geomechanical properties for the MacKay River oil sand area mechanical earth model.

Formation	Till	Clearwater	Wabiskaw	McMurray	Devonian
Facies	N/A	Sand		Shale	N/A
Constitutive Model	M-C	Strain-softening		Strain-softening	M-C
Young's modulus (E), MPa	250	253-633		60-240	6800
Poisson' ratio (ν)	0.33	0.33		0.3	0.145
Bulk modulus (K), MPa	245	249-621		50-201	3192
Shear modulus (G), MPa	94	95-238		23-93	2969
Friction Angle, °	30	51.3		30.5	55
Dilation Angle, °	15	24.5		15.0	20
Cohesion, MPa	0.3	0		0.14	33.3
Tension, MPa	0.2	0		0.1	1.4
Biot's number	1	1		1	1
Thermal expansion coefficient, 10^{-6} 1/°C	1	20		10	10

Table 5-4 Strain-softening table for sand and shale facies.

Plastic shear strain	0	0.01	0.02	0.03	0.04	0.05	0.06	0.07	0.08	0.09	0.1
Friction angle (sand), °	51.3	49.5	47.7	45.9	44.1	42.3	40.5	38.7	36.9	35.1	33.3
Dilation angle (sand), °	24.5	23.1	21.7	20.3	19.0	17.6	16.2	14.8	13.4	12.0	10.6
Friction angle (shale), °	30.5	29.5	28.5	27.5	26.5	25.5	24.5	23.5	22.5	21.5	20.5
Dilation angle (shale), °	15	14	13	12	11	10	9	8	7	6	5
Cohesion (shale), kPa	140	126	112	98	84	70	56	42	28	14	0
Tension (shale), kPa	100	90	80	70	60	50	40	30	20	10	0

5.2 Coupled Reservoir-geomechanics Simulation

The coupled reservoir-geomechanics simulation is used as the last step of the geological modeling workflow to calibrate the MEM model with the production data and field observations available. Running coupled simulation on the geological model of the entire area with multiple SAGD pads pilot is possible with current computing power. Simulations of a single well pad are usually analyzed for predictions of reservoir performance and geomechanical response.

5.2.1 Sequentially Coupled Reservoir-geomechanics Simulation

For the SAGD process associated with significant temperature and pressure change, it has been widely accepted that considering the interactions of flow and deformation response help to achieve a more complete understanding and accurate prediction of the SAGD process. Sequentially coupled thermal-flow-geomechanical simulations are applied here to improve the predictions of SAGD performance in deformable oil sand reservoirs. The development of coupled reservoir-geomechanics simulation for thermal recovery methods in Alberta oil sands is presented in Section 2.2.2. The advantages of sequentially coupling technique compared to other coupling techniques were discussed in Section 2.2.1.

The strain-softening M-C model is used in FLAC3D to model the elastic and plastic deformations for each grid at each coupling step under drained condition. It has been confirmed to be a reasonable assumption as demonstrated by Li et al. (2004) that the excess pore pressure is immediately drained away in or near the steam chamber. The user-defined permeability update functions for different facies, e.g. sand and shale, give the flexibility to model the significant increase of permeability for only a small amount of plastic deformations as shown by Touhidi-Baghini (1996) in Figure 2-13. The permeability models used to quantify the impact of deformations are explained in Section 4. Figure 5-21 shows the relationship between permeability

160

model 1 (Equation 4-8) and 2 (Equation 4-9) up to 10% volume dilation. The updated permeability is normalized by the original permeability. For permeability model 1, $a = 1$, $C_e = 1$ and $C_p = 42$. It corresponds to observations in Touhidi-Baghini (1998), the permeability change is negligible during contraction and elastic dilation. The sharp change in permeability during shear dilation is well represented by permeability model 1. For permeability model 2, $b = 1$ and $C_\Phi = 14.56$ as calibrated by Li and Chalaturnyk (2006) for vertical cores.

The permeability of the deformed porous media reaches the cap value when most of the preferred flow path is generated by shear failures (Figure 2-13). Thus, a low and high cut-off for the updated permeability should be specified to make the predicted permeability reasonable in coupled simulations. Here, permeability model 2 is used as the use of permeability model 1 at the field scale needs further investigation on the scaling laws from lab results to field parameters.
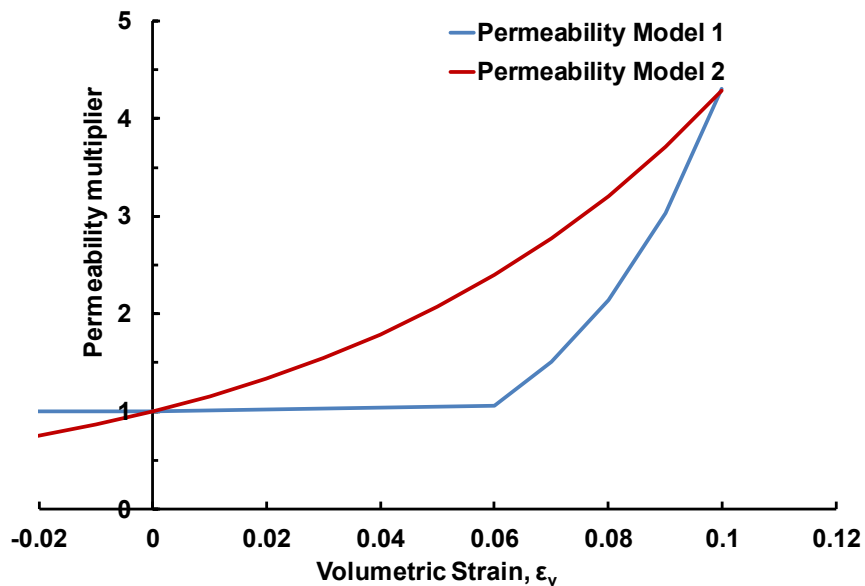
Figure 5-19.   Permeability updating models 1 and 2 from the calculated volumetric strain from geomechanical models. Model 1 updates permeability based on porosity and plastic shear strain. Model 2 updates permeability based on volumetric strain.

5.2.2 Description of Selected Well Pad

Pad C in Figure 5-3-a is selected as it is in phase 1 and has plenty of field data available since 2002.

The surface heave of the MacKay River project is provided in the 2017 AER report (Figure 5-20).

The large surface heave (70 cm) in Pad C increases the importance of geomechanical assessment.
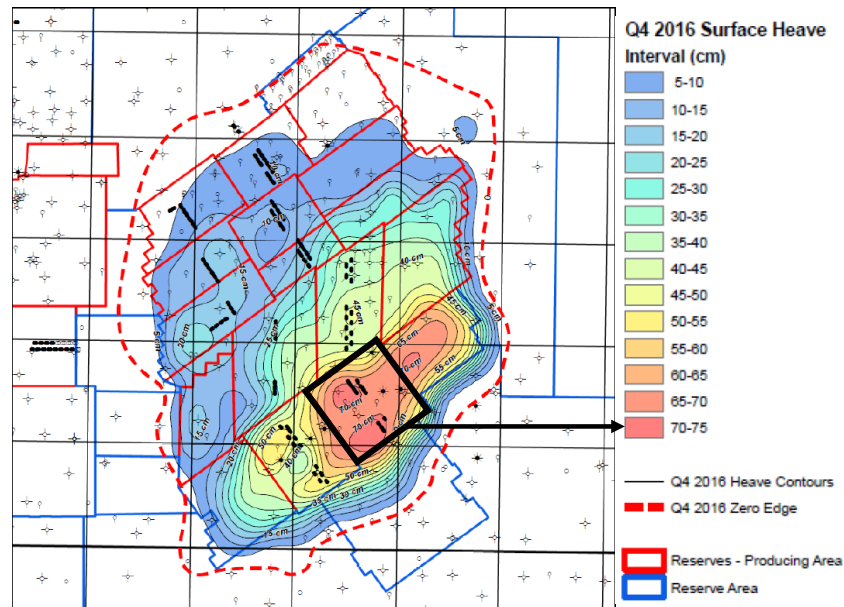
Figure 5-22.   The surface heave of MacKay River project. The pad C has the highest surface heave as pointed out (Adopted from 2017 MacKay River project AER report).

Pad C of the MacKay River oil sands area is cut from the MEM model generated in Section 5.1. The length of the cell is refined to 5 m so that the aspect ratio is maintained smaller than 2.5. In FLAC3D, the relative error monotonically increases with aspect ratios (Abbasi et al. 2013). For 3D models, the error caused by a deformed mesh compared to the ideal mesh is within 5% when the aspect ratio is smaller than 3.

The geomechanical model is 1000 m by 1000 m by 200 m (Figure 5-21a). From top to bottom, the geomechanical model consists of the Till, Clearwater, Wabiskaw, McMurray and Devonian

Formations. The Till Formation is the overburden, Clearwater Formation is the Caprock and Devonian Formation is the underburden where the flow is negligible in these nearly impermeable formations. Therefore, they are only included in the geomechanical model during the coupled reservoir-geomechanics simulation to make sure the stress and strain boundaries are correct for the embedded reservoir model. The Wabiskaw and Mcmurray Formations are included in the reservoir and geomechanical model because they are the zones of interest where the interactions of flow and deformation response dominate the overall performance of the SAGD process. The bottom and side boundaries of the geomechanical model are fixed, while the top boundary is free of stress.
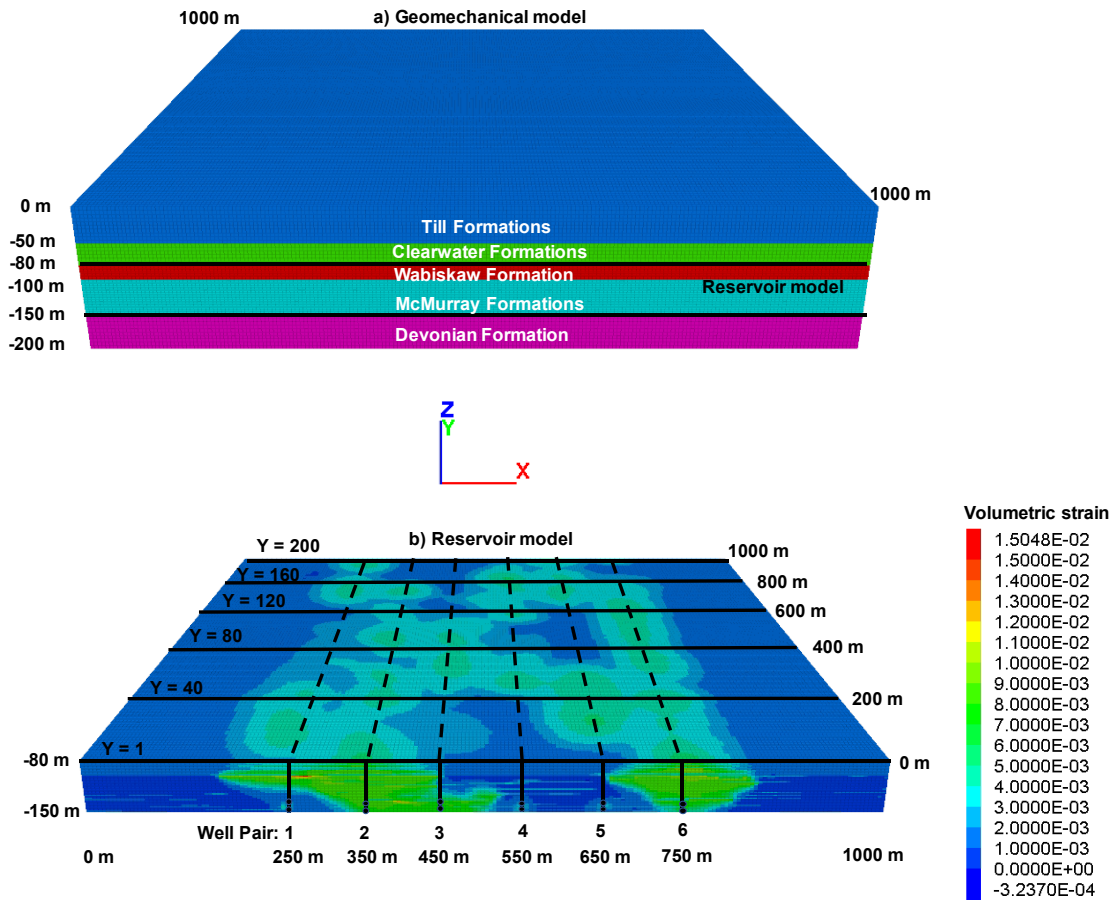
Figure 5-21.   a) Geomechanical and b) reservoir model of Pad C. The reservoir model only contains the Wabiskaw and McMurray Formation.

The well spacing of the horizontal wells is 100m. A total of 6 well pairs are operating at an injection pressure and temperature of 1283 kPa and 191 °C. The volume change of the reservoir (Figure 5-21b) shows the locations of well pairs and corresponding heterogeneous steam chambers at day 3860 in the coupled simulation. 6 XZ cross-sections (Y = 1, 40, 80, 120, 160 and 200) are selected to further investigate the impact of heterogeneity on the interactions of steam chamber propagation and permeability changes caused by deformation. The permeability distribution of the XZ cross-sections (Figure 5-22) shows that the shale barriers are continuous at the top of the reservoir (Wabiskaw Formation) and vary more in the McMurray Formation. The XY cross-sections (Figure 5-23) illustrate the trajectories of the horizontal injectors (Z=32) and producers (Z=35) through the low permeability shale layers. In the next section, sequentially coupled reservoir-geomechanics simulation of the SAGD process is conducted on this heterogeneous geological model of Pad C.
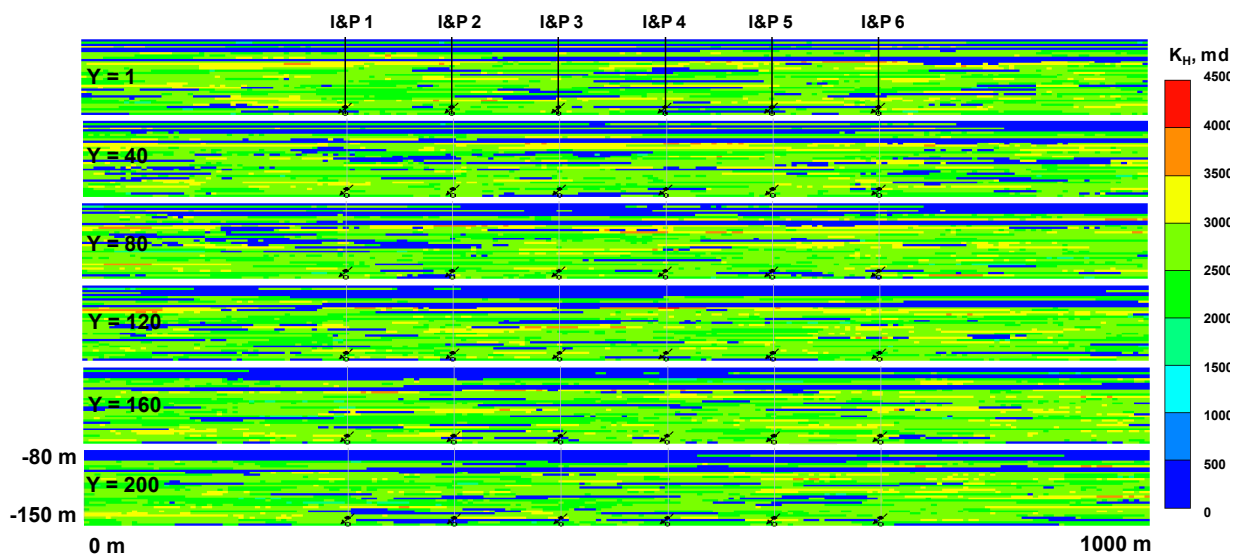
Figure 5-22.   Permeability distribution at XZ cross-sections of Pad C (Y=1, 40, 80 ,120, 160 and 200).
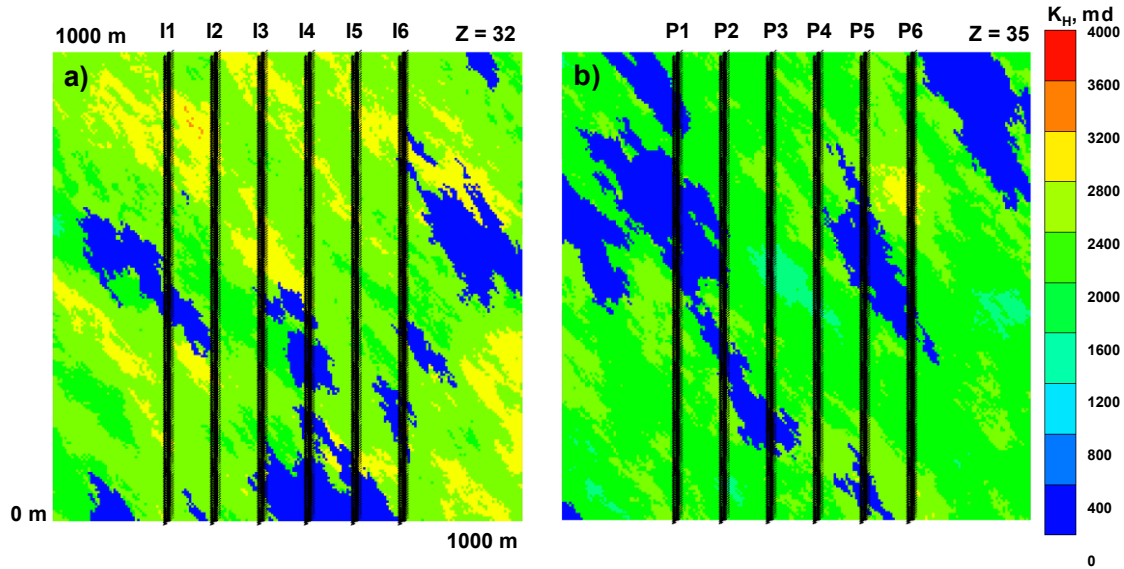
Figure 5-23. Permeability distribution at XY cross-sections of Pad C in the depth of horizontal injectors at Z=32 and producers at Z=35.

5.3 Effect of Deformations on Reservoir-geomechanics Response

The injectors open from the first day of the simulation for preheating of the cold bitumen near the wellbore and the producers open on Day 150 for production of mobilized bitumen. The uncoupled and sequentially coupled cases are compared based on the elastic and plastic deformations during SAGD. Before the production stage (day 150), the reservoir and geomechanical simulation are coupled every 30 days to compensate for the sharp changes in effective stress due to steam injection. During the production stage, when the process becomes stable, the coupling step is set to 100 days.

5.3.1 Interactions Between Deformation and Flow Response

The steam chamber and deformation of the reservoir for Pad C are illustrated in Figure 5-24. The steam chamber is highly non-uniform because the shale barriers hinder the propagation of steam. Even along the horizontal well in the Y direction, the steam chamber is not continuous. The

165

injection of hot steam drops the effective stress leading to the dilation of porous media and notable

vertical displacements at the top of the reservoir (Figure 5-24).
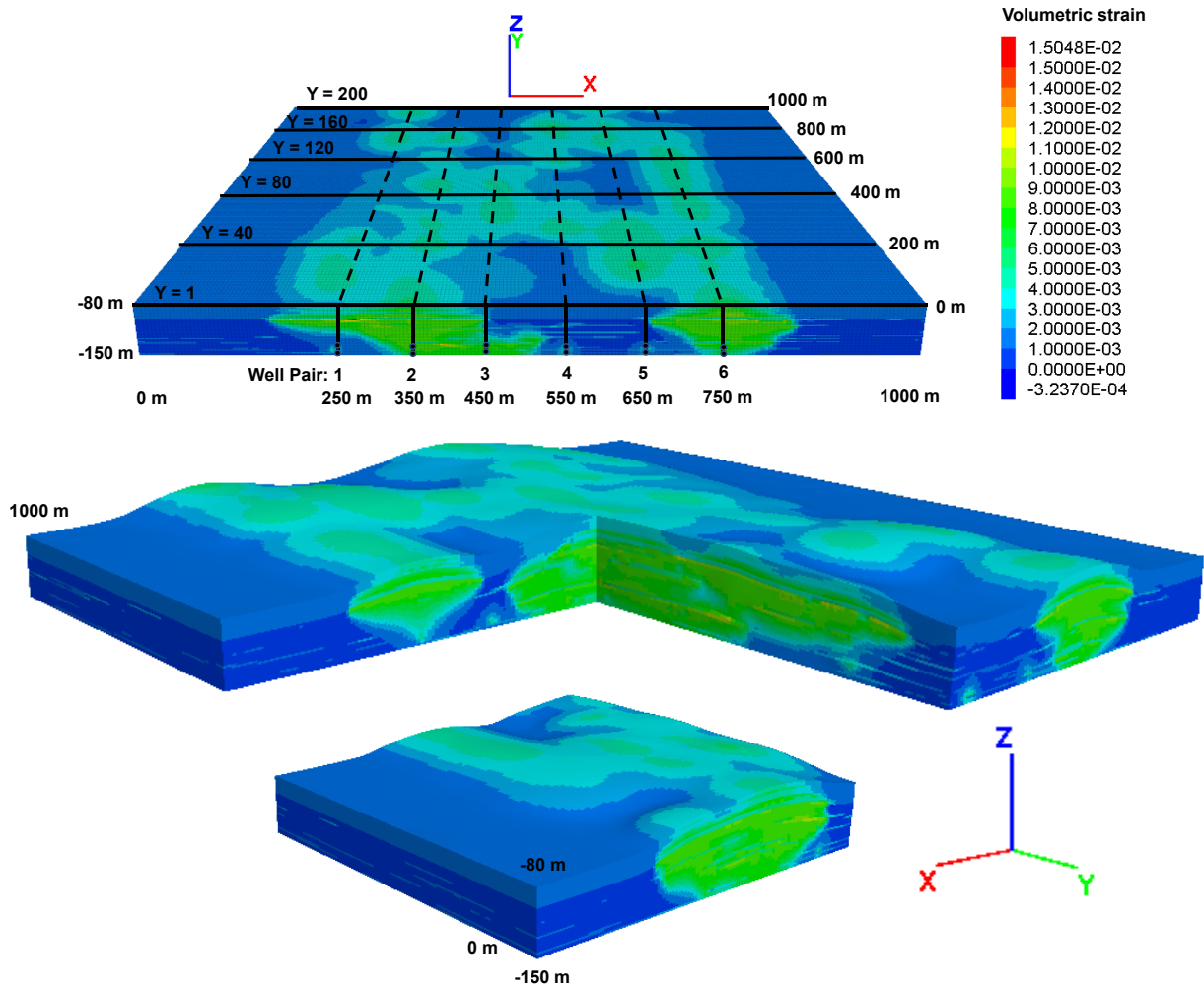
Figure 5-24. The volumetric strain profile at day 3860 showing the SAGD chamber and deformations of the reservoir for sequentially coupled reservoir-geomechanics simulation.

166

The permeability contrast between sand (1565-4252 mD) and shale facies (5-7 mD), has a large impact on steam chamber development during SAGD as illustrated by the temperature profiles in the first XZ cross-section (Y = 1) in Figure 5-25. For well pairs 1, 4 and 5 where the injector is located in the low permeability shale, hot steam cannot be efficiently injected to mobilize the cold bitumen. For well pair 6, where connected shale barriers exist in the middle of the reservoir, two disconnected steam chambers develop. The formation of the upper chamber may have two reasons: 1) horizontal crossflow in the Y direction; 2) plastic deformations create high permeability flow paths vertically and allow the steam to channel through the horizontal shale barrier. The deformation of the shale barriers further complicates the predictions of reservoir performance by conventional reservoir simulation.

In the sequentially coupled reservoir-geomechanics simulation, permeability is updated in each coupling step. The permeability profiles at corresponding coupling time steps show that it is significantly enhanced with the steam chamber (Figure 5-26). The increase in the absolute permeability enhances the oil production rate and propagation speed of the steam chamber and causes the large discrepancy between the coupled and uncoupled simulation (Figure 5-27). For the XZ cross-section (Y=120), the steam chambers in well pairs 2, 3 and 4 coalesce in the coupled simulation. No chamber is built up for well pair 1 in section Y=120 as the injector is in the low permeability shale; while the steam chamber is observed above well pair 1 for the coupled simulation due to the increase of steam propagation speed in the created flow path by shear failures. The decrease in effective stress and the thermal expansions are the main reasons for the induced shear failures in the weaker shale cells. In the coupled simulation, the geomechanical simulation can correctly model this phenomenon and update the flow response in the reservoir simulation.

Therefore, the chamber is slowly built up in well pair 1 and connected to the nearby steam chamber nearby in the XZ cross-section (Y = 120).
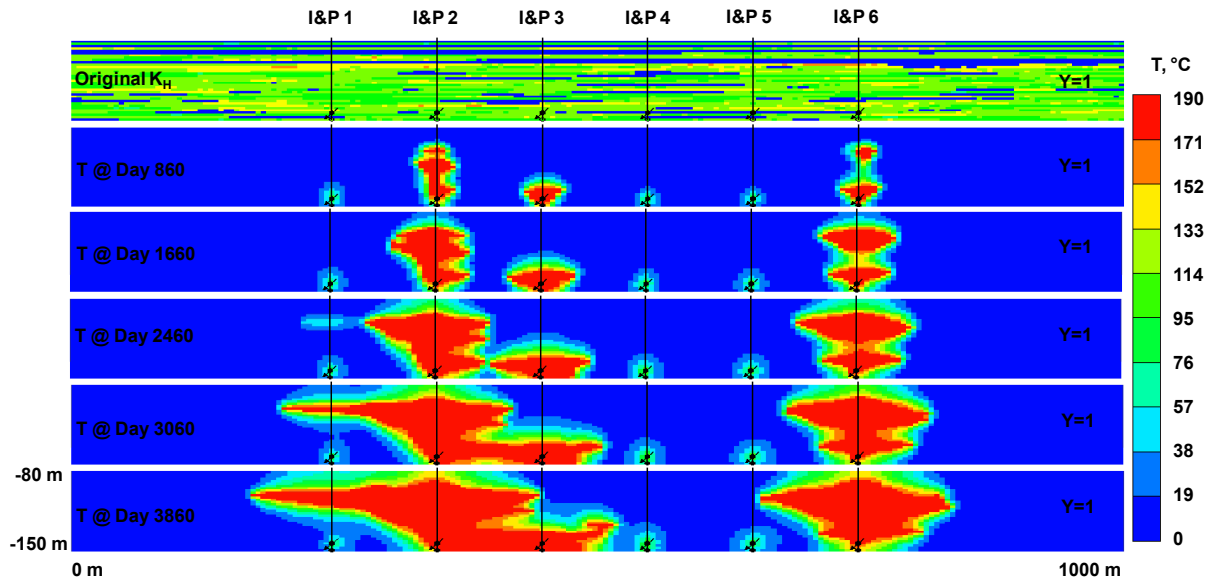
Figure 5-25.   The temperature profile at day 860, 1660, 2460, 3060 and 3860 showing the growth of the steam chamber in the first cross-section of the sequentially coupled reservoir-geomechanics simulation.
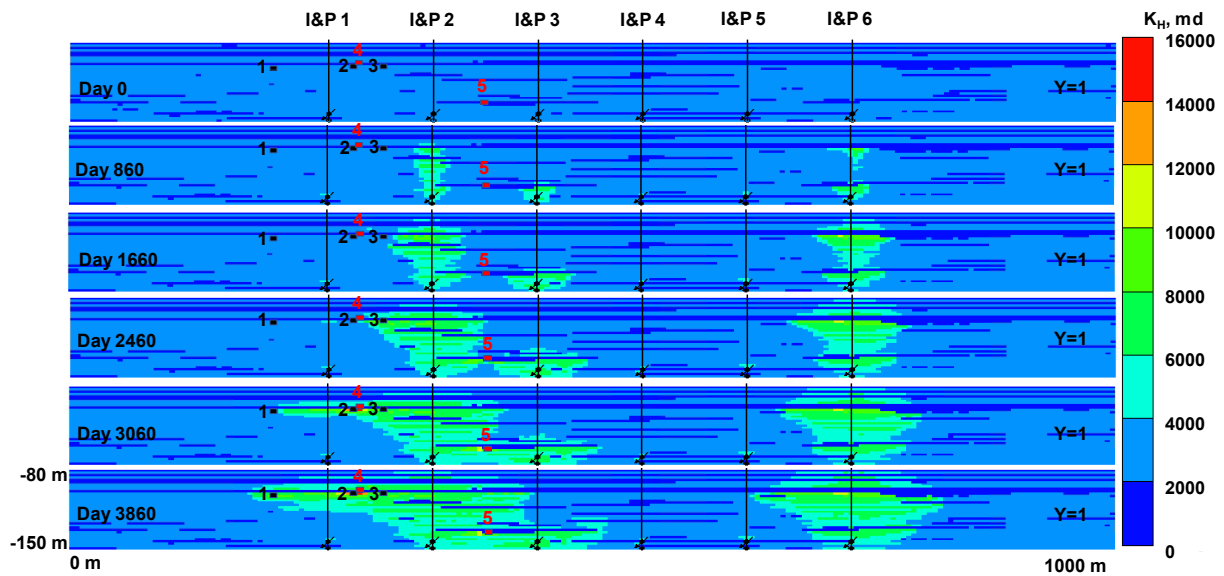
Figure 5-26.   The horizontal permeability (K_H) profiles at day 0, 860, 1660, 2460, 3060 and 3860 showing the change of absolute permeability due to the growth of the steam chamber in the first cross-section of the sequentially coupled reservoir-geomechanics simulation.
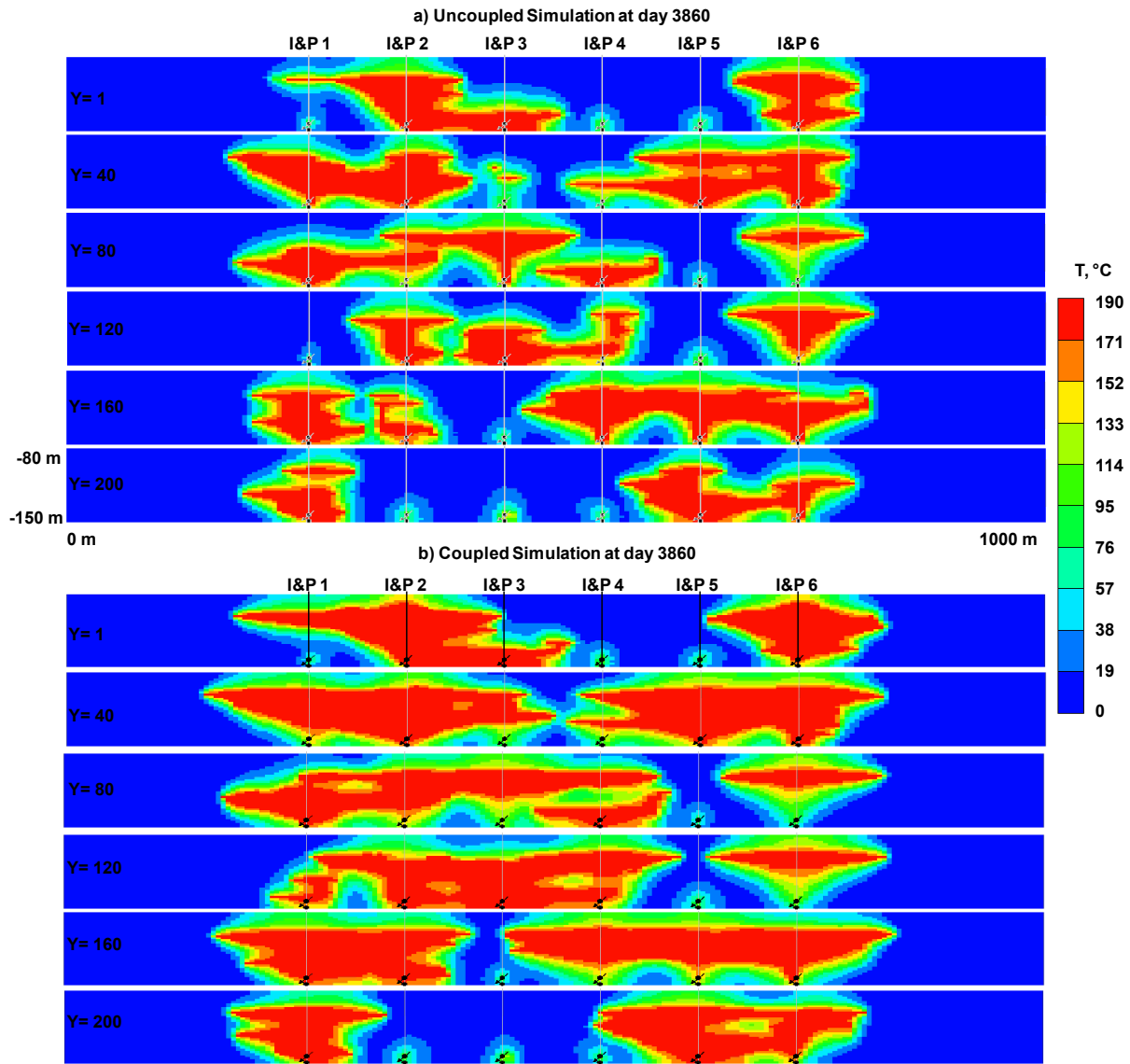
Figure 5-27. The temperature profile at day 3860 showing the difference of the steam chamber for different cross-sections (1, 40, 80, 120, 160 and 200) of a) uncoupled and b) sequentially coupled reservoir-geomechanics simulation..

Figure 5-28 shows the volumetric change of the XZ cross-section (Y = 1). The maximum volumetric plastic strain is 1.5% and the average volumetric strain in the steam chamber is 1%. Even this small amount of volume change in the reservoir leads to 60% increase in oil recovery

compared to uncoupled simulation on day 3860 (Figure 5-29). The recovery of the coupled simulation is closer to the production data provided in the AER report, indicating the importance of correct modeling of deformation response for SAGD processes.
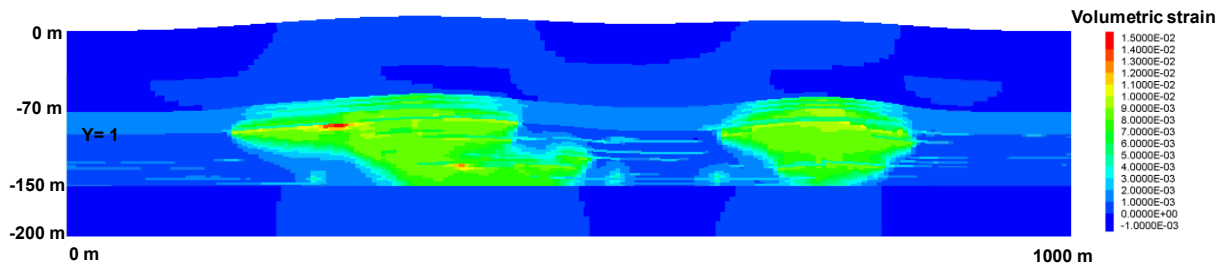
Figure 5-28. The volumetric change of XZ cross-sections (Y=1) at the last coupling step (day 3860).
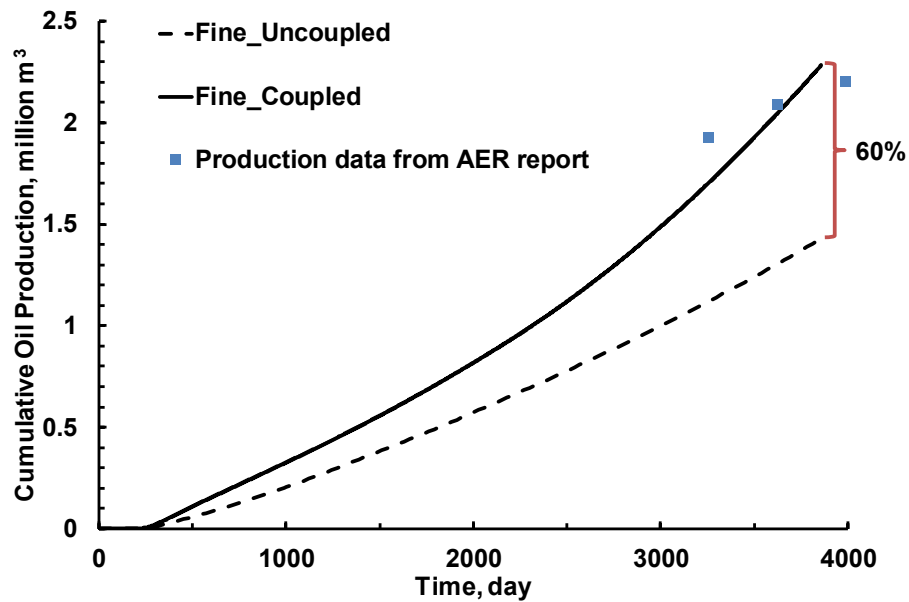
Figure 5-29. The cumulative oil production of coupled, uncoupled simulation compared to production data from Alberta Energy Regulator 2017. Cumulative oil production is calibrated to standard conditions.

5.3.2 Stress-Paths in Coupled Reservoir-geomechanics Simulation

The impact of stress-paths on SAGD has been extensively studied by Chalaturnyk and Li (2004) in the one-way coupled 2D reservoir and geomechanical simulations. The simulation results demonstrated the importance of geomechanics in SAGD at different depth of reservoir and injection pressure. They recommend more realistic coupled reservoir-geomechanics simulations for further investigations. Here, the impact of geomechanics on the Pad C of MacKay River oil sand area is analyzed based on the stress-paths in the sequentially coupled reservoir-geomechanics simulation.

Based on the coupled simulation, shear failures are not significant in the reservoir as the injection pressure is kept low (1283 kPa) to prevent caprock integrity issues. In the region where continuous shale barriers are embedded in oil sands, the plastic shear strain is around 0.3% to 0.8%. Five zones with plastic deformations are selected for the investigation of stress-paths in SAGD (Figure 5-26). Zone 1, 2 and 3 are in a sand layer below a continuous shale layer. Zone 4 and 5 are weaker and softer shale cells at different depths of the reservoir. Effective stress paths follow two predominant paths: 1). Pore pressure increase at the preheating period; 2) Thermal expansion during the production stage (Chalaturnyk and Li 2004). Due to the continuous injection and development of the steam chamber, pore pressure increase, and thermal expansion occur simultaneously throughout SAGD forming a curved stress-path as a combination of these two stress paths (Figure 2-6).

By analyzing the temperature and pressure front, it is possible to distinguish the predominant mechanism for stress changes at different periods of production and areas of the reservoir. In Figure 5-26, it can be observed the major steam chamber is developed by well pair 2 and sequentially bypasses zone 3, 2 and 1. The temperature and pressure profiles (Figure 5-30) show

that the propagation of the pressure front is faster than temperature front. The pressure front 1 sweeps zone 1, 2 and 3 at the same time during the injection stage (0-150 days). The first predominant stress-path (increase in pore pressure) occurs when the pressure front sweeps the reservoir. The pressure front 2 (200 kPa) pushes the steam chamber sequentially bypassing zone 3, 2 and 1. Following pressure front 2, the temperature front reaches zone 1, 2 and 3 with the development of the high-temperature steam chamber. The propagation speed of pressure front 2 is slower compared to pressure front 1, which varies from day 2000 to day 3000 depending on the distance from the steam chamber.
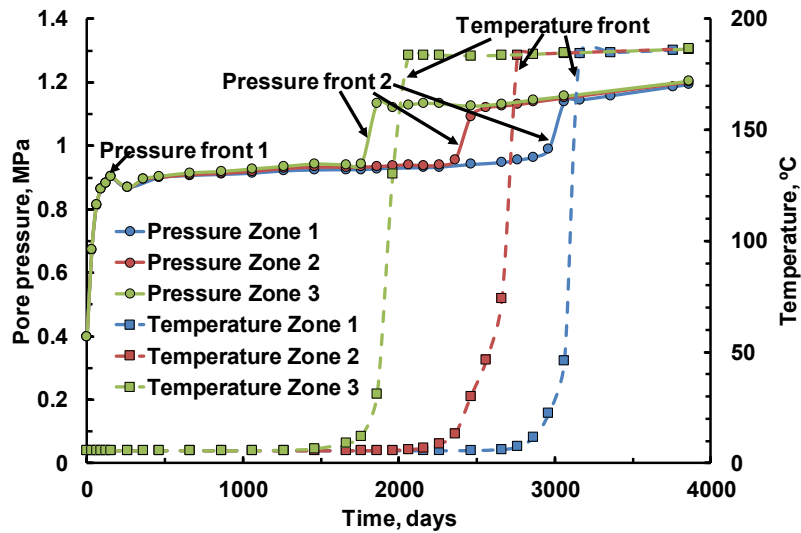
Figure 5-30.   Temperature and pressure fronts at sand cell 1, 2 and 3.

The initial stress states are anisotropic with $\sigma_{Hmax} > \sigma_v > \sigma_{Hmin}$ as the MacKay River oil sand area is shallow. The initial stress states of zone 1, 2 and 3 fall on the same Ko line ($\sigma_3/\sigma_1 = 0.6$). The stress-paths for the sand cell 1, 2 and 3 are plotted in the p'-q space (Figure 5-31).
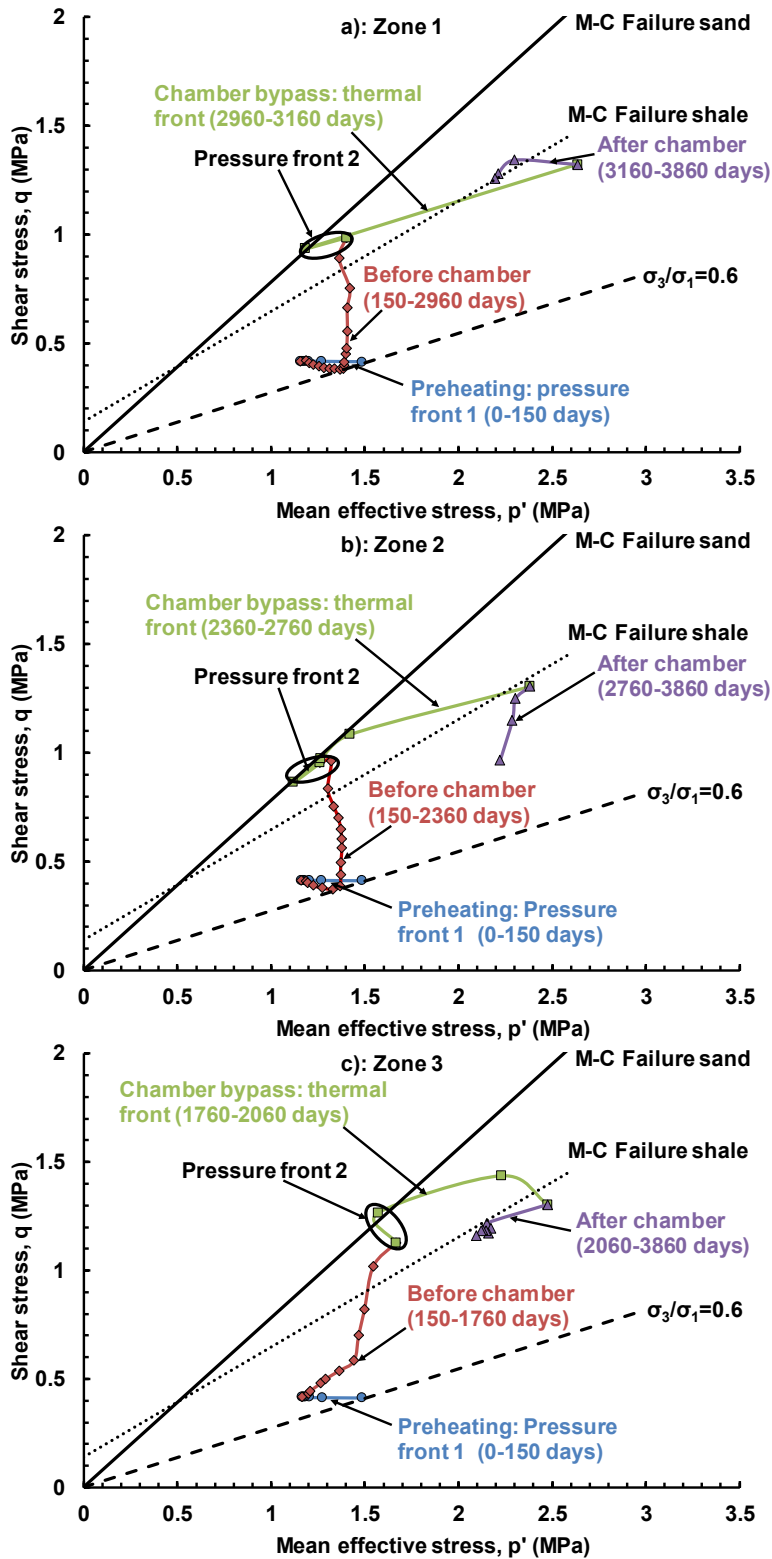
Figure 5-31.   Stress-paths at the sand cell 1, 2 and 3 during SAGD process.

Depending on the operation period and the relative location of zones, e.g. in or away from the steam chamber, the stress-paths for sand cells are divided into four parts:

1) During the preheating period from 0 to 150 days, the stress-paths move left because the increase in pore pressure lowers the mean effective stress. This leads to an increase in pore volume which causes an increase in porosity and permeability. The deformation caused by pore pressure increase is elastic in the preheating period.

2) After the first pressure front, the pressure and temperature are almost constant before the second pressure front. The first half of the stress-path (red) in Figure 5-31 shifts right because the thermal expansion of porous media causes similar increases in vertical and horizontal total stress. Thus, the mean effective stress increases while the change in shear stress is negligible. When the chamber approaches zone 1, 2 and 3, the orientation of steam chamber development is nearly horizontal. Therefore, thermal expansion leads to a significant increase in horizontal total stress, which drives the stress-paths upward.

3) The third part of the stress path (green) reflects the influence of the temperature front and associated pressure front on the stress-paths when bypassing zone 1, 2 and 3. Pressure front 2 arrives before the thermal front, which causes a decrease in mean effective stress. The stress-path moves to the left and impinges on the Mohr-Coulomb failure envelope for sand. This is the time step when shear failures are triggered. When the thermal front bypasses the zone, the thermal expansion causes a dramatic increase in horizontal stress, leading to increases in mean effective stress and shear stress. Shear failures usually lead to dilation of oil sands, alter the pore structure and create new preferred flow paths for mobile bitumen.

4) The last part of the stress-path is usually associated with the removal of the induced thermal stress increase after the steam chamber passes the investigated zone. With the gradual decrease in

horizontal total stress caused by thermal expansion, the stress-paths move to the left and bottom as the purple curve shows.

Plastic deformations also exist in the shale cells. The pressure and temperature profiles of zone 4 and 5 are illustrated in Figure 5-32. The first pressure front arrives instantly after the steam injection. The pressure front in zone 5 is 300 kPa higher compared to zone 4 as it is deeper. As a result, the second pressure front is negligible for zone 5 as the pressure is already close to the injection pressure. For zone 4, the second pressure front merges with the steam chamber thermal front.
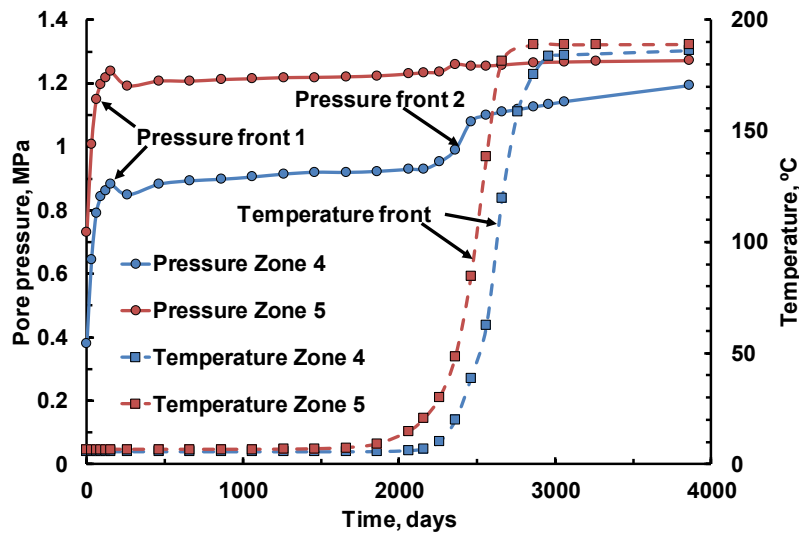
Figure 5-32.   Temperature and pressure profiles t shale cells 4 and 5.

The stress-paths for shale are significantly different compared to sand (Figure 5-33). The stress-paths during the preheating period are similar, where stress-paths move left due to the increase of pore pressure. When the steam chamber approaches, the stress-path moves left towards the Mohr-Coulomb failure envelope of shale. Mean effective stress decreases because the thermal expansion

coefficient of shale is just half of the sand so the horizontal total stress in shale zone actually decreases as zone 4 and 5 are surrounded by sand. After the shear failures occur in the shale zone, the shear stress decreases rather than an increase in sand. The main reason is that the increase of maximum horizontal stress (horizontal in Figure 5-26) is smaller than the minimum horizontal stress (normal to the XZ plane in Figure 5-26). Therefore, the shear stress decreases with the increase in the mean effective stress.
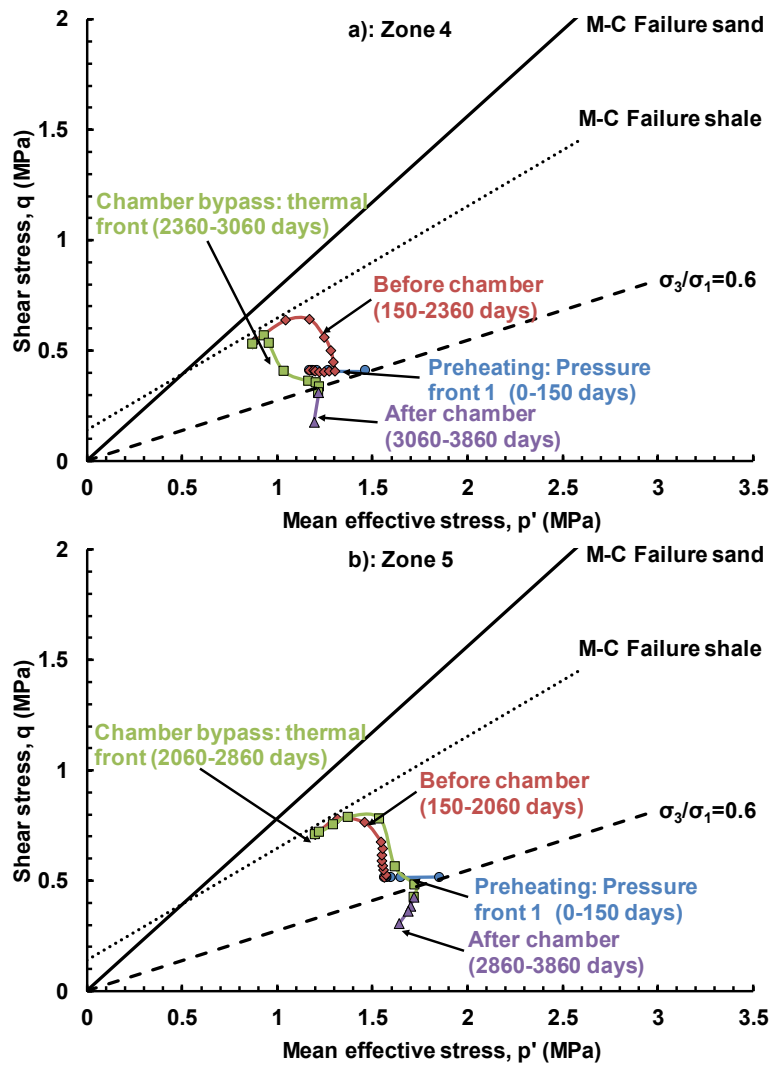
Figure 5-33.   Stress-paths at zone 4 and 5 during SAGD process.

Azad (2012) concluded that zones closer to the bottom and top of the reservoir are most likely to reach the failure envelope based on the coupled simulations of homogeneous models. In sequentially coupled simulation on the heterogeneous geological models, plastic deformations also happen in the IHS zone. For these critical zones where interactions between flow and deformation are important, stress-paths should be investigated for the purpose of reservoir design and monitoring.

5.4   Summary

SAGD performance is greatly affected by plastic deformation because porosity and permeability are strong functions of plastic shear strain. The mechanical earth model of the MacKay River oil sand area is generated for further investigation of the deformation response of SAGD using sequentially coupled reservoir-geomechanics simulation. Oil production and steam chamber growth are significantly enhanced by deformations and failures compared to uncoupled simulation. The first pressure front instantly sweeps the entire reservoir. The thermal front is usually pushed by a second pressure front when the steam chamber passes. As a consequence, the complicated stress-paths of sequentially coupled simulation can be divided into four parts depending on the predominant stress path and relative positions between the steam chamber and the investigated zone. Plastic deformations are observed at the heterogeneous region mixed with sand and shale. The stress-paths for the shale cells are different compared to the adjacent sand cell because of the different degrees of thermal expansion. Elastic and plastic deformations have to be carefully assessed to obtain accurate predictions of the geomechanical response and induced changes in production performance in SAGD, which a successful upscaling technique should be able to reproduce at a coarser scale.

CHAPTER 6:   LOCAL NUMERICAL UPSCALING OF ELASTIC PROPERTIES

This chapter focuses on the extensions of Khajeh's 2D upscaling technique to fully 3D orthotropic materials with improved local numerical tests adopting the concept of six linearly independent loading schemes from Zohdi and Wriggers (2008) originally designed to estimate the anisotropic elastic response caused by microscopic heterogeneity at REV scale. Improved estimation of effective shear modulus is obtained through local shear tests rather than estimation from Young's modulus and Poisson's ratio, as in Khajeh's method. The local numerical testing regimes demonstrate the capability in dealing with complex spatial variability and anisotropic deformations in heterogeneous reservoirs. The non-symmetry of the upscaled compliance matrix is found to be more pronounced for inclined heterolithic stratification (IHS) than a layered system. E-upscale successfully minimizes the potential error in the prediction of global compression and shear response compared to the arithmetic (Voigt), geometric and harmonic (Reuss) averages. The application of the proposed upscaling methodology in the coupled reservoir-geomechanics simulation of the SAGD process demonstrates its potential to significantly reduce the computational efforts in coupled simulation while honoring the deformation response of the reservoir.

6.1   Methodology

6.1.1   Theoretical Background

The upscaled elastic compliance matrix for each coarse (upscaled) geomechanical cell is calculated based on Hooke's law. The stress-strain relationship of an anisotropic linear elastic material can be expressed as:

$$\begin{bmatrix} \varepsilon_{xx} \\ \varepsilon_{yy} \\ \varepsilon_{zz} \\ \varepsilon_{yz} \\ \varepsilon_{xz} \\ \varepsilon_{xy} \end{bmatrix} = \begin{bmatrix} S_{11} & S_{12} & S_{13} & S_{14} & S_{15} & S_{16} \\ S_{21} & S_{22} & S_{23} & S_{24} & S_{25} & S_{26} \\ S_{31} & S_{32} & S_{33} & S_{34} & S_{35} & S_{36} \\ S_{41} & S_{42} & S_{43} & S_{44} & S_{45} & S_{46} \\ S_{51} & S_{52} & S_{53} & S_{54} & S_{55} & S_{56} \\ S_{61} & S_{62} & S_{63} & S_{64} & S_{65} & S_{66} \end{bmatrix} \begin{bmatrix} \sigma_{xx} \\ \sigma_{yy} \\ \sigma_{zz} \\ \sigma_{yz} \\ \sigma_{xz} \\ \sigma_{xy} \end{bmatrix} , \qquad \text{Equation 6-1}$$

where ε_{ij} is the strain tensor, σ_{kl} is the stress tensor and S_{ij} is Voigt's notation of elastic compliance tensor. In the six independent local numerical tests on a coarse or upscaled cell, each loading scheme leads to 6 independent equations when applied to Equation 6-1. A total of 36 equations are sufficient to compute the 36 independent constants in the compliance matrix. Solving 36 equations for each coarse geomechanical cell is computationally expensive at the reservoir scale. Consequently, the assumption of orthotropy is adopted for the purpose of computational efficiency in a Cartesian coordinate system, where 36 constants in the compliance matrix reduce to 9:

$$\begin{bmatrix} \varepsilon_{xx} \\ \varepsilon_{yy} \\ \varepsilon_{zz} \\ \varepsilon_{yz} \\ \varepsilon_{xz} \\ \varepsilon_{xy} \end{bmatrix} = \begin{bmatrix} S_{11} & S_{12} & S_{13} & 0 & 0 & 0 \\ S_{21} & S_{22} & S_{23} & 0 & 0 & 0 \\ S_{31} & S_{32} & S_{33} & 0 & 0 & 0 \\ 0 & 0 & 0 & S_{44} & 0 & 0 \\ 0 & 0 & 0 & 0 & S_{55} & 0 \\ 0 & 0 & 0 & 0 & 0 & S_{66} \end{bmatrix} \begin{bmatrix} \sigma_{xx} \\ \sigma_{yy} \\ \sigma_{zz} \\ \sigma_{yz} \\ \sigma_{xz} \\ \sigma_{xy} \end{bmatrix} . \qquad \text{Equation 6-2}$$

Including the elastic properties in the compliance matrix, the strain-stress relationships result in Equation 6-3.

$$\begin{bmatrix} \varepsilon_{xx} \\ \varepsilon_{yy} \\ \varepsilon_{zz} \\ \varepsilon_{yz} \\ \varepsilon_{xz} \\ \varepsilon_{xy} \end{bmatrix} = \begin{bmatrix} 1/E_x & -v_{yx}/E_y & -v_{zx}/E_z & 0 & 0 & 0 \\ -v_{xy}/E_x & 1/E_y & -v_{zy}/E_z & 0 & 0 & 0 \\ -v_{xz}/E_x & -v_{yz}/E_y & 1/E_z & 0 & 0 & 0 \\ 0 & 0 & 0 & 1/2G_{yz} & 0 & 0 \\ 0 & 0 & 0 & 0 & 1/2G_{xz} & 0 \\ 0 & 0 & 0 & 0 & 0 & 1/2G_{xy} \end{bmatrix} \begin{bmatrix} \sigma_{xx} \\ \sigma_{yy} \\ \sigma_{zz} \\ \sigma_{yz} \\ \sigma_{xz} \\ \sigma_{xy} \end{bmatrix} , \qquad \text{Equation 6-3}$$

where E_i is Young's modulus in i direction; v_{ij} is the Poisson's ratio characterizing lateral strain in j when stress is in i; G_{ij} is the shear modulus in plane ij.

The normal and shear strain of the heterogeneous upscaled geomechanical cell can be written as functions of elastic properties and applied stress:

$$\varepsilon_{xx} = (1/E_x)\sigma_{xx} - (v_{yx}/E_y)\sigma_{yy} - (v_{zx}/E_z)\sigma_{zz} ,$$
<div align="right">Equation 6-4</div>

$$\varepsilon_{yy} = -(v_{xy}/E_x)\sigma_{xx} + (1/E_y)\sigma_{yy} - (v_{zy}/E_z)\sigma_{zz} ,$$
<div align="right">Equation 6-5</div>

$$\varepsilon_{zz} = -(v_{xz}/E_x)\sigma_{xx} - (v_{yz}/E_y)\sigma_{yy} + (1/E_z)\sigma_{zz} ,$$
<div align="right">Equation 6-6</div>

$$\varepsilon_{yz} = \sigma_{yz}/2G_{yz} ,$$
<div align="right">Equation 6-7</div>

$$\varepsilon_{xz} = \sigma_{xz}/2G_{xz} , \text{ and}$$
<div align="right">Equation 6-8</div>

$$\varepsilon_{xy} = \sigma_{xy}/2G_{xy} .$$
<div align="right">Equation 6-9</div>

For each numerical testing regime, Equations 6-4 through 6-9 are simplified with a user-defined stress boundary $\hat{\sigma}$. The average normal and shear strains of the upscaled geomechanical cells can be computed from the fine-scale results of each local test. Thus, the corresponding upscaled elastic properties leading to identical local stress-strain behavior are obtained. The details of the 6 independent local testing regimes and the algorithm for E-upscale are discussed in the following section.

6.1.2 Local Numerical Testing Regimes

The local numerical testing regimes are set up for each upscaled geomechanical cell which consists of fine-scale geological cells with heterogeneous elastic properties. Figure 6-1 illustrates the overall workflow for the local numerical test procedure. During production and/or injection operations the reservoir stress changes due to pressure and temperature fluctuations. These changes result in variations in the stress boundary conditions for the upscaled geomechanical cell (Figure 6-1a) and lead to complex deformations of each fine-scale geological cell (Figure 6-1b). The

effective strain tensors for the upscaled cell (Figure 6-1c) can be computed from the displacements of fine-scale models at the face boundary (Figure 6-1b). The upscaled compliance matrix (Figure 6-1d) is solved in a series of local numerical tests given the applied stress tensors and corresponding effective strain tensors.

a) Fine model-Original state

E_1 G_1 v_1 E_2 G_2 v_2
E_3 G_3 v_3 E_4 G_4 v_4

b) Fine model-After deformation

E-upscale

E-upscale

d) Upscaled model-Original state   ion

E^* G^* v^*
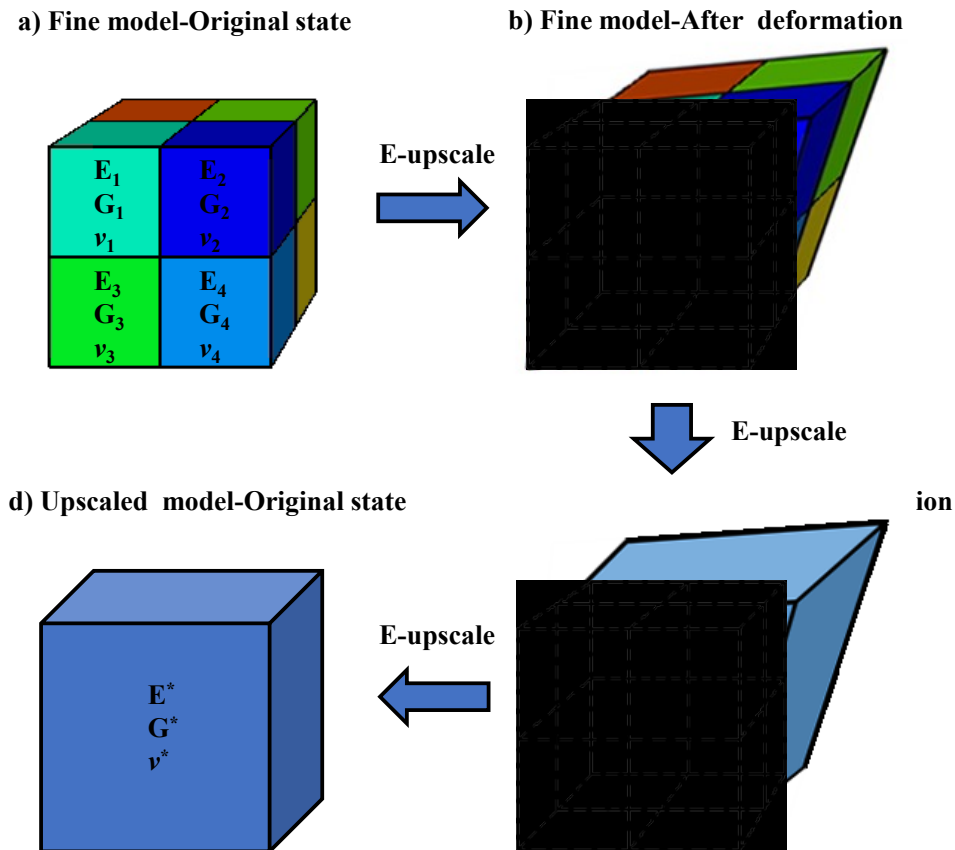
E-upscale

Figure 6-1. Schematic of E-upscale for upscaling a fine-scale 2 by 2 by 2 model. The deformed upscaled model should represent the strain tensors of the fine-model under the given stress boundary for the fine-scale model (from b to c).

The E-upscale algorithm is demonstrated on a 5 by 5 by 5 upscaled region (Figure 6-2c) extracted from a geological model developed for the MacKay River oil sand area of northeastern Alberta

(Figure 6-2a). Each cell has unique geomechanical properties modeled by sequential Gaussian simulation. The sand cells have larger Young's modulus, Poisson's ratio and shear modulus than shale cell (Table 6-1). The orthotropic model in FLAC^{3D} (© 2012 Itasca Consulting Group, Inc) is used as the constitutive model for geomechanical simulation. The boundary conditions of the 6 independent testing regimes are illustrated in Figure 6-3. For the first test, a constant stress of 0.1 MPa is applied normal to the YZ plane of the upscaled cell. The other faces are free of confinement. The stress boundary can be expressed as:

$$\hat{\sigma} = \begin{bmatrix} \sigma_{xx} \\ 0 \\ 0 \\ 0 \\ 0 \\ 0 \end{bmatrix} = \begin{bmatrix} 0.1\ MPa \\ 0 \\ 0 \\ 0 \\ 0 \\ 0 \end{bmatrix},$$
Equation 6-10

Substituting Equation 6-10 into Equation 6-3, Equation 6-4, 6-5 and 6-6 can be rearranged to solve for E_x, v_{xy} and v_{xz}:

$$E_x = \sigma_{xx}/\varepsilon_{xx},$$
Equation 6-11

$$v_{xy} = -\varepsilon_{yy}/\varepsilon_{xx}, \text{ and}$$
Equation 6-12

$$v_{xz} = -\varepsilon_{zz}/\varepsilon_{xx}.$$
Equation 6-13

The effective strains ε_{xx}, ε_{yy} and ε_{zz} of the upscaled block are calculated from the average strain increment on the YZ plane after the simulation reaches the criteria to stop, which is set as the equilibrium state (unbalanced stress/applied stress<10^{-5}).

For the second and third tests, constant stress boundaries σ_{yy} and σ_{zz} are applied (Figure 6-3b and 6-3c). With $\sigma_{yy} = 0.1\ MPa$ as the stress tensor for the second compression test, the corresponding Young's modulus and Poisson's ratio can be computed via Equations 6-14, 6-15 and 6-16:

$$E_y = \sigma_{yy}/\varepsilon_{yy} \,,$$

Equation 6-14

$$v_{yx} = -\varepsilon_{xx}/\varepsilon_{yy} \,, \text{ and}$$

Equation 6-15

$$v_{yz} = -\varepsilon_{zz}/\varepsilon_{yy} \,.$$

Equation 6-16
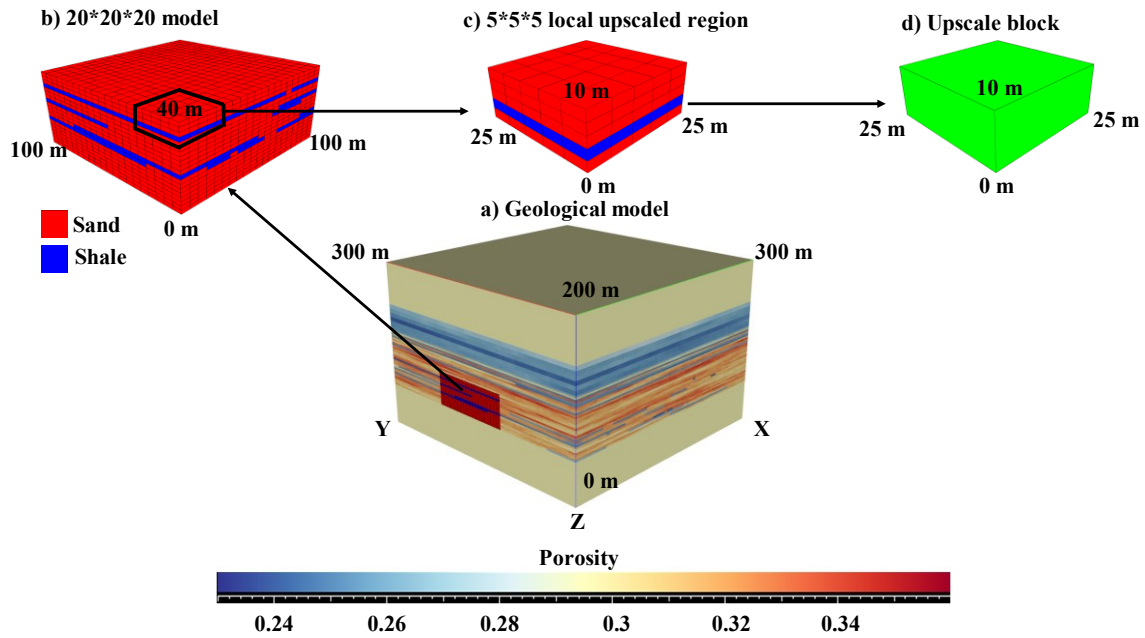
Figure 6-2. E-upscale algorithm for a 5*5*5 upscaling region (c) in a 20*20*20 sand-shale sequence model (b). The 20*20*20 model (Model 1) is extracted from a geological model generated for the MacKay River oil sand area of northeastern Alberta (a). The effective elastic properties for the upscaled block (d) is generated by E-upscale reproducing the stress-strain behavior of the 5*5*5 upscaling region with 6 independent testing regimes.

The stress tensor for the third compression test is $\sigma_{zz} = 0.1 \, MPa$. Equations 6-17, 6-18 and 6-19 express the determination of E_z, v_{zx} and v_{zy}:

$$E_z = \sigma_{zz}/\varepsilon_{zz} \,,$$

Equation 6-17

$$v_{zx} = -\varepsilon_{xx}/\varepsilon_{zz} \,, \text{ and}$$

Equation 6-18

$$v_{zy} = -\varepsilon_{yy}/\varepsilon_{zz} .$$
Equation 6-19
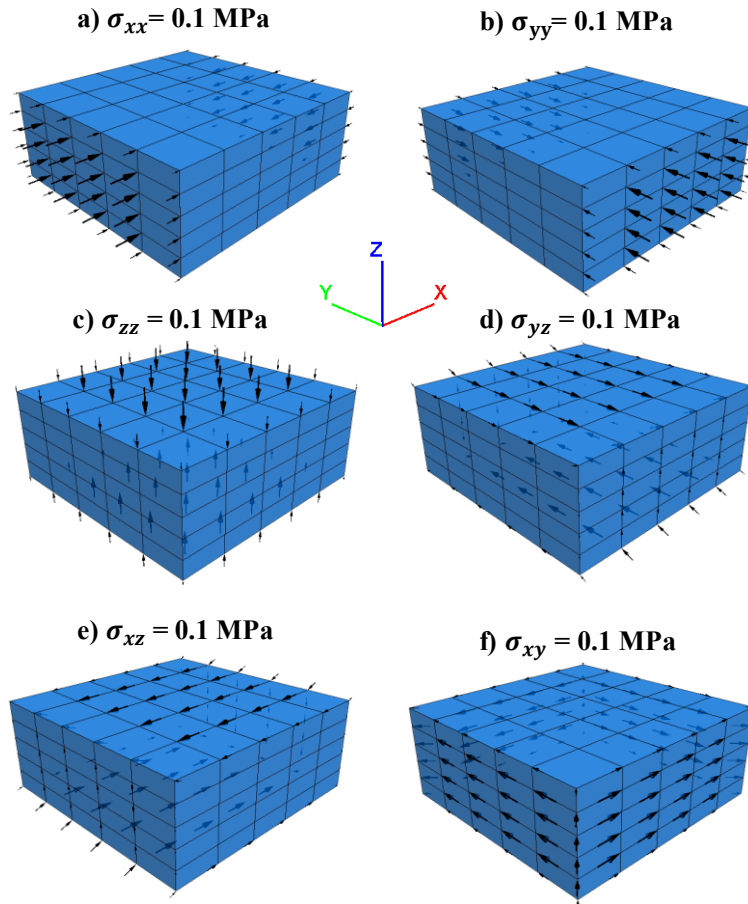
Figure 6-3. Stress boundaries for 3 compression and 3 shear tests for calculation of the effective elastic properties.

The upscaled shear modulus is calculated with simple shear tests in each axis direction (Figure 6-3d, 3e and 3f) for each upscaled region. For the first shear test (Figure 6-3d), the stress tensor is:

$$\hat{\sigma} = \begin{bmatrix} 0 \\ 0 \\ 0 \\ \sigma_{yz} \\ 0 \\ 0 \end{bmatrix} = \begin{bmatrix} 0 \\ 0 \\ 0 \\ 0.1\ MPa \\ 0 \\ 0 \end{bmatrix} .$$
Equation 6-20

The shear strains are calculated from the average shear displacements of the fine cells at the boundaries where shear stresses are applied. The shear moduli G_{yz}, G_{xz} and G_{xy} are calculated from Equations 6-7, 6-8 and 6-9.

The total simulation time for the 6 local tests on the 5 by 5 by 5 region is less than 2 seconds. The local testing regimes can be extended to inelastic behavior if allowing more simulation time. For elasto-plastic behavior, the anisotropic tangent elastic modulus for the upscaled block can be obtained with the same boundary conditions with different compression stress. To determine the effective failure envelope of the upscaled region, the original stress boundaries (Figure 6-3) are adjusted to smooth plane loading with incremental strains. When the stress-strain curve of the upscaled block reaches the peak, the failure envelope in the loading direction can be computed via the designated failure theory, e.g. Mohr-Coulomb failure criterion. The required simulation time steps for the local tests are strongly dependent on the inelastic behavior and the applied strain rate. The focus of this research, however, is upscaling of elastic behavior; therefore, the criteria used to end the local numerical simulation is set to unbalanced stress smaller than 10^{-5} of the applied stress to minimize simulation time so that E-upscale can be applied to a reservoir scale problem.

6.1.3 Reservoir Scale Algorithm

An automated algorithm is required for the E-upscale workflow to upscale all necessary regions in a large-scale reservoir geomechanical simulation model. The algorithm is coded in C++ with data transformation and automation of the local numerical tests applied sequentially for each selected upscaled region. The detailed procedure for E-upscale is explained below.

Step 1: E-upscale generates the local testing module for the selected upscaled region of the fine-scale geological model. The number of fine cells in each upscaled coarse block can be customized

in X, Y and Z making it possible to optimize the upscaling ratio for different areas of the reservoir, e.g. finer mesh near wells and coarser mesh for under/side-burden of the reservoir.

Step 2: Six local tests are performed sequentially with the necessary stress boundaries (Figure 6-3) at user-defined stress levels or an incremental strain boundary. The displacements of each fine cell in the non-uniformly deformed body (Figure 6-1b) are computed and recorded at the boundary of the upscaled block (Figure 6-1c).

Step 3: The effective strain tensors of the upscaled coarse block are calculated as the average of the fine cells at the stress boundary.

Step 4: The upscaled anisotropic elastic properties for each coarse block are calculated based on the given stress boundaries and corresponding strain tensors obtained in Step 3.

Step 5: The outputs of upscaled elastic properties are organized in an ASCII format file compatible with most geological modeling software.

The upscaling ratio is defined as the number of geological cells that are merged into the coarse geomechanical cell. For the 5 by 5 by 5 upscaled region (Figure 6-1c), the upscaling ratio is 125:1. To further improve the efficiency of E-upscale in full-field geological models, the upscaled regions can be split into parallel groups and the numerical tests run simultaneously on different processors.

6.2   Numerical Validation of E-upscale

6.2.1   Model Description

A field-scale geological model is built for the Alberta MacKay River oil sand area in SKUA GOCAD (© Paradigm). Well log and core data are extracted from geoSCOUT (© geoLOGIC

SYSTEMS). The geological model has five formations, designated Till, Clearwater, Wabiskaw, McMurray and Devonian, which are arranged from shallow to deep, respectively. A series of numerical geomechanical tests with different boundary conditions are conducted for the 20*20*20 cell model (Model 1) extracted from the reservoir (Figure 6-2b). The geomechanical elastic properties for sand and shale within this model are provided in Table 6-1. The input elastic properties are assumed isotropic, but it will be shown that anisotropic effective elastic properties are caused by sub-grid scale heterogeneity of the upscaled region.

The shale layers in Model 1 are almost horizontal. Through intensive geological studies of the Alberta oil sands, Thomas et al. (1987) demonstrated the importance of inclined heterolithic stratification (IHS) lithosomes. Consequently, a second model (Model 2) is generated where the shale layers are inclined at 30° (Figure 6-4) to demonstrate the difference between a transverse isotropic system (Model 1) and a fully orthotropic system (Model 2).

Table 6-1 Geomechanical properties for Model 1.

	Sand	Shale
Density, g/cm^3	2150-2198	2277-2297
Young's modulus, MPa	515-632	199-239
Poisson' ratio	0.35	0.25
Shear modulus, MPa	191-234	80-95
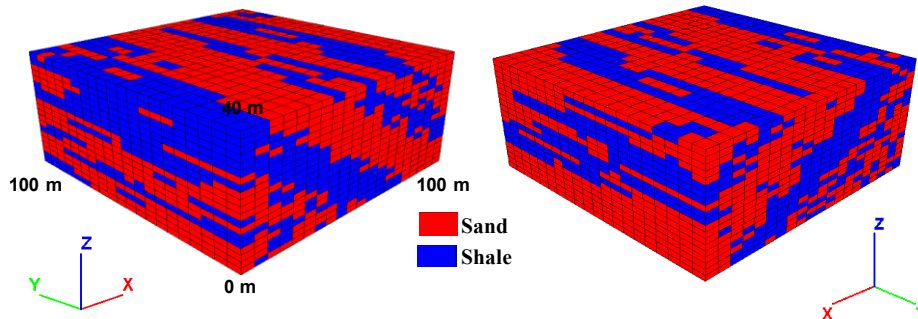
Figure 6-4. The synthetic 20*20*20 IHS model (Model 2) with 30°inclined shale layers (two views).

6.2.2   Traditional Analytical Bounds of Elastic Modulus

To model the effective elastic properties of a heterogeneous coarse region consisting of two lithologies, e.g. sand and shale, the elastic properties, the volume fraction and spatial correlation of each facies are required. At the REV scale, microscopic heterogeneities are difficult to measure. Thus, Voigt and Reuss bounds (Equation 6-21) are powerful tools to estimate the upper and lower limits of the effective elastic modulus following a power law average of the sand and shale facies.

$$\bar{M} = V_s M_s^\omega + V_{sh} M_{sh}^\omega \ , \hspace{4cm} \text{Equation 6-21}$$

where $\bar{M}$ is the effective modulus of the heterogeneous material, which are bulk and shear modulus by definition, M_s and M_{sh} are the modulus of sand and shale, V_s and V_{sh} are the volume fraction of sand and shale and ω is a constant determined by the geometry of facies and stress/strain distribution and ranges from -1 to 1.

Voigt assumed a uniform strain field parallel to the displacement field leading to $\omega = 1$. The Voigt bound $(\overline{M_V})$ of bulk and shear modulus is analogous to the arithmetic average. With a uniform stress field assumed perpendicular to applied traction, the Reuss bound $(\overline{M_R})$ results in $\omega = -1$, which is the harmonic average. Hill (1951) suggested that effective modulus is usually between the two limits. The Voigt-Reuss-Hill (VRH) bound is the arithmetic average of the Voigt and Reuss bounds:

$$\overline{M_{VRH}} = (\overline{M_V} + \overline{M_R})/2 \ . \hspace{4cm} \text{Equation 6-22}$$

The geometric average is an intermediate power-law average between arithmetic and harmonic averages often used in the upscaling of reservoir properties without apparent geological features. Subsurface reservoirs usually have complex depositional environments for different formations. However, the Voigt, Reuss, VRH bound and geometric average assume isotropic elastic response

within the upscaled block. It will be shown subsequently that this is not entirely appropriate for conditions where the upscaled block is highly heterogeneous.

6.2.3   Anisotropic E-upscaled Properties

The proposed E-upscale methodology is designed to reproduce the anisotropic elastic response of an upscaled block under various boundary conditions. Following the algorithm of E-upscale, each 5*5*5 cell region in Model 1 and 2 is upscaled into a single cell resulting in 8000 fine-scale cells in each model being upscaled to 64 coarse cells in the upscaled model. The sand-shale heterogeneity within each coarse cell, measured by V_{sh}, is used as a metric to characterize the development of anisotropic elastic properties in the upscaled model. For both Model 1 and 2, Figure 6-5 illustrates how the development of anisotropy evolves as V_{sh} varies within the coarse cells. For each model, notable anisotropic behavior initiates at V_{sh} less than 10% and becomes increasingly anisotropic with increasing V_{sh}. The upscaled elastic properties for horizontal shale layers, Model 1, becomes transversely isotropic (Figures 6-5a, 6-5b and 6-5c) consistent with the work of Backus (1962) and the inclined shale layers of Model 2 produce fully orthotropic elastic properties (Figures 6-5d, 6-5e and 6-5f).
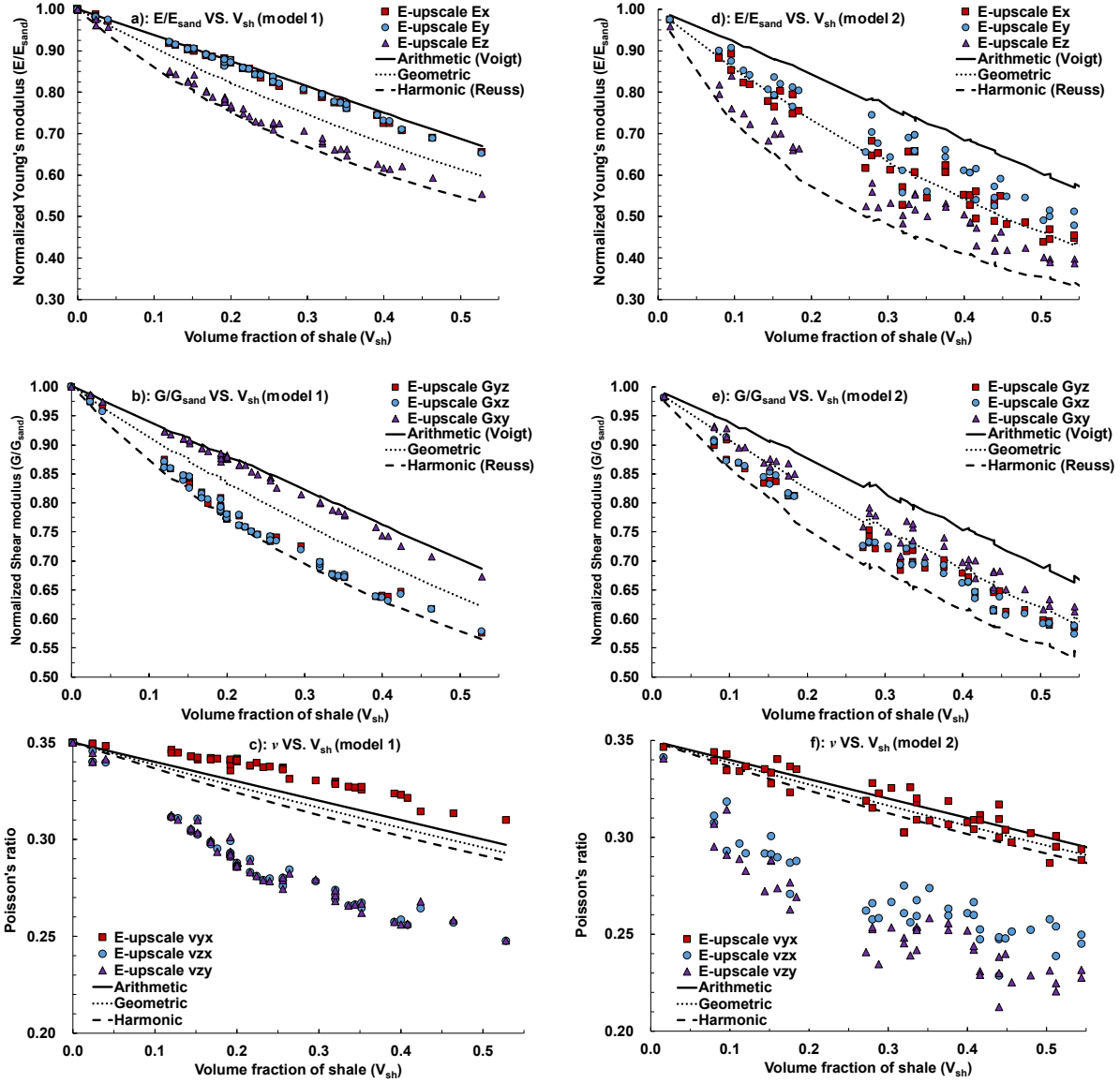
Figure 6-5. The anisotropic upscaled elastic properties for each coarse grid in Model 1 and 2 ranked by V$_{sh}$. The Young's and shear modulus are normalized by the sand's modulus under the same effective mean stress (at the same depth of the depositional body). The arithmetic, geometric and harmonic averages are plotted as solid, dot and dash, respectively.

For Model 1, the arithmetic average (Voigt bound) and harmonic average (Reuss bound) are observed as rigorous upper and lower bounds on E-upscaled Young's and shear modulus. E_x and E_y are close to the Voigt bound as the numerical testing regime for E-upscale (loading is parallel with shale layers) is similar to Voigt's iso-strain model. E_z is closer to the Reuss bound as the

compression direction is perpendicular to the shale layers as in Reuss's iso-stress model (Figure 6-5a). The Voigt bound is a good estimate of G_{xy} while the Reuss bound is close to G_{yz} and G_{xz} (Figure 6-5b). The shear modulus is larger when shear stress is parallel with the shale layers. Poisson's ratio (v_{yx}), which characterizes the change of strain in Y when the loading is in X, is higher than the arithmetic average; while v_{zy} and v_{zx} are much lower than the harmonic average (Figure 6-5c). For consistency, the arithmetic, geometric and harmonic averages for Poisson's ratio are computed, even though strictly, the Voigt and Reuss bounds only apply for modulus calculations. The high sensitivity of Poisson's ratio to heterogeneity supports the importance of the proposed E-upscale workflow in order to obtain an accurate estimation of upscaled Poisson's ratio.

The arithmetic and harmonic averages also work as a rigorous upper and lower bound on Young's and shear modulus in Model 2. However, they cannot provide an appropriate estimate of upscaled elastic properties as the shale configurations in each upscaled cell become more complex. Because of the 30° shale layer inclination along X, upscaled E_x becomes smaller than E_y. The upscaled Poisson's ratio for Model 2 is not constrained by the arithmetic and harmonic averages and Figure 6f illustrates the development of three clear clusters of anisotropy.

6.2.4 Non-Symmetry of Upscaled Compliance Matrix

For each fine grid, symmetric strain tensors are assumed if under symmetric stress tensors; therefore, the compliance matrix should be symmetric according to Hooke's law. In upscaling problems, the strain tensors are not guaranteed symmetric due to heterogeneities at the coarse scale, even under symmetric stress tensors. As a consequence, symmetry may not hold for the upscaled compliance matrix when there are lithological trends that deviate from perfect layering. Rijpsma

and Zijl (1998) provided derivations showing that the thermodynamic foundations of elasticity theory are not violated with a non-symmetric upscaled compliance matrix.

The symmetry ratio is defined to further investigate the relationship between symmetry of compliance matrix and the geometry of shale configurations:

$$R_{ij} = S_{ij}/S_{ji} \, , \hspace{4cm} \text{Equation 6-23}$$

where S_{ij} is the auxiliary compliance tensor. The symmetry ratio S_{12}/S_{21}, S_{13}/S_{31} and S_{23}/S_{32} of each coarse cell in Model 1 and 2 are illustrated in Figure 6-6a and 6-6b, respectively. For Model 1, S_{12}/S_{21} remains symmetric (unity) for all upscaled blocks (Grid ID's) because the shale layers are nearly symmetric in the horizontal direction or XY plane. For S_{13}/S_{31} and S_{23}/S_{32} however, the deviation from symmetry in the XZ and YZ planes results in the ratios varying from unity. With a substantial departure from planar symmetry in Model 2 as the shale layers start to incline, the compliance matrix becomes more non-symmetric, as shown by the scatter in symmetry ratios (Figure 6-6b). The skewness of the auxiliary compliance tensor is strongly related to the symmetry of the depositional body. The previous upscaling method including Backus's averaging method cannot correctly capture the non-symmetry of the upscaled compliance matrix which may lead to inaccurate predictions of upscaled elastic properties for highly heterogeneous systems similar to Model 2.
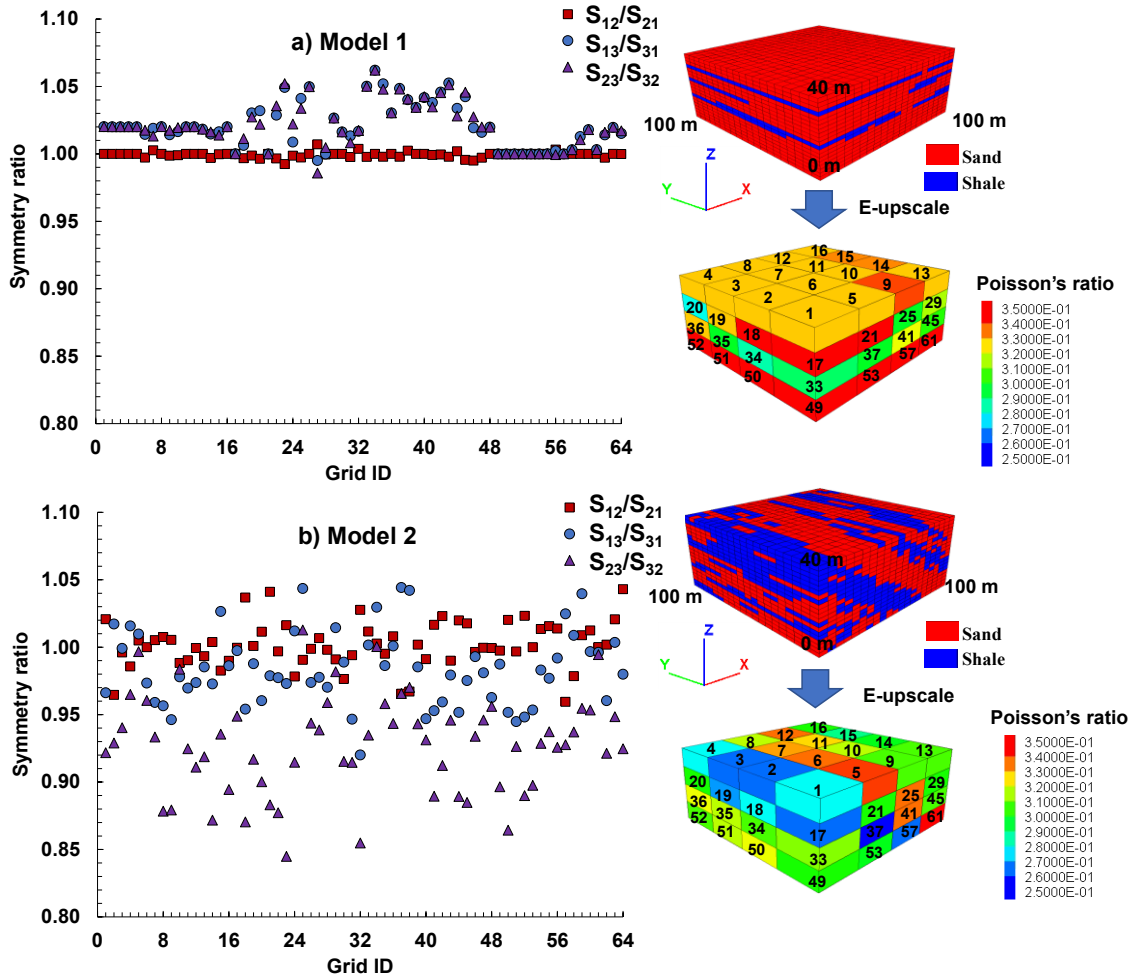
Figure 6-6. The symmetry ratio of the upscaled compliance matrix for the coarse-scale grids in Model 1 and 2. The skewness of the compliance matrix for Model 2 is significantly larger than Model 1 due to the inclined shale layers.

6.2.5   Validation of Global Model Response

The successful application of a local upscaling technique should also demonstrate its ability to match or reproduce the global geomechanical response of the fine-scale model. In this study, this implies that under the same loading conditions, the 64-cell upscaled model should, within an acceptable error, provide the same geomechanical response as the 8000-cell fine-scale model. For the three compression and three shear testing regimes shown in Figure 4, the following sections

compare the axial stress and volumetric strain for Models 1 and 2 for both the fine-scale and corresponding upscaled geometries.

6.2.5.1 Global Compression Response

For Model 1, three uniaxial compression tests in X, Y and Z are conducted on the fine-scale (8,000 cells) and the upscaled (64 cells) coarse model by applying a constant displacement rate of 10^{-4} m/step on each X, Y and Z boundary (Figures 6-3a, 6-3b and 6-3c). Figure 6-7 shows the results from the numerical Z-direction compression test on Model 1. The Z-direction is chosen to demonstrate the difference in stress-strain behavior between the different upscaling methods because it is perpendicular to the plane of symmetry in Model 1. E-upscaled coarse model predictions are able to match the axial stress and volumetric strain results from the fine-scale model (Figure 6-7a and 6-7b). The harmonic average coarse model also performs well for axial stress prediction because the numerical experimental setup is analogous to the Reuss iso-stress model. Predictions of volumetric strain (Figure 6-7b) are less consistent because the Reuss bound is not strictly valid for Poisson's ratio.
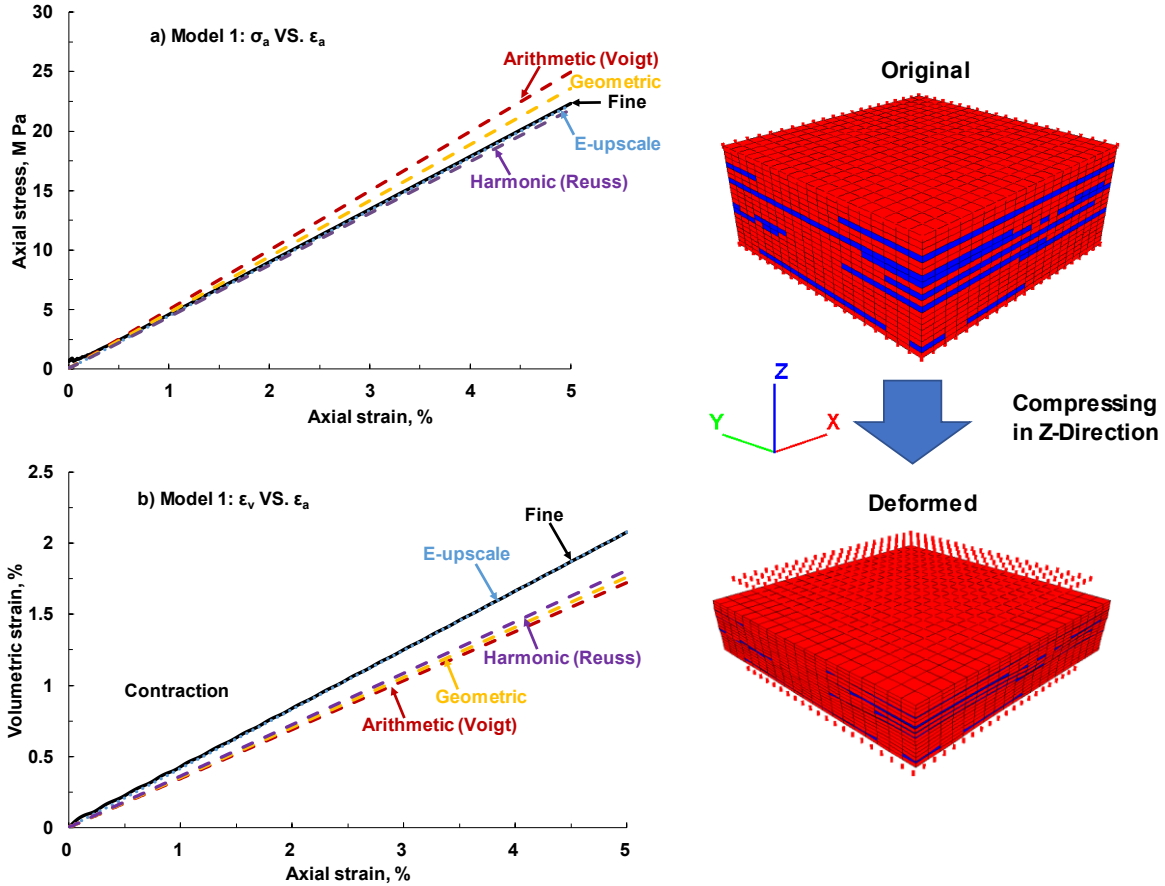
Figure 6-7. The axial stress (a) and volumetric strain (b) versus axial strain for vertical compression of Model 1.

As shown in Figure 6-8a, the Voigt (arithmetic) upscaling approach nearly matched the fine-scale response for compression loading in Model 1 for the X and Y directions. These results by the Voigt bound approach are expected since the configuration of the numerical experimental setup is identical to Voigt's iso-strain model; however, for loading in the Z direction, the mismatch error exceeds 10%. For all directions of loading, the E-upscale model matches the axial stress response of the fine-scale model to less than 1%. It is expected that the ability of the E-upscale model to match the global model behavior depends on the finite difference discretization scheme. A sensitivity analysis of the upscaling ratio should be conducted to validate global model responses of small-scale models prior to applying E-upscale to full-field simulation models. For other loading

configurations, the performance of the other homogenization techniques is poor and highly dependent on the direction of loading (Figure 6-8a and 6-8b) providing additional evidence of the applicability of E-upscale to provide anisotropic elastic properties.

For Model 2, uniaxial compression tests in the X and Z direction have been chosen to assess upscaling methods when inclined shale layers produce non-uniform deformations. In this case, arithmetic and harmonic averaging are unable to replicate the axial stress behavior (Figure 6-9a and 6-9c) because the geometry of the model violates the assumed boundary conditions for the Voigt or Reuss over-simplified model. For these geological settings, E-upscale provides the best estimation of upscaled elastic properties and predictions of axial stress and volumetric strain. Fine-scale volumetric strain can only be approximated by the E-upscaled model (Figure 6-9d) as the Voigt and Reuss bounds do not apply for Poisson's ratio. Again, for these loading assumptions, E-upscale is able to provide anisotropic elastic properties in highly heterogeneous models with inclined lithologies.
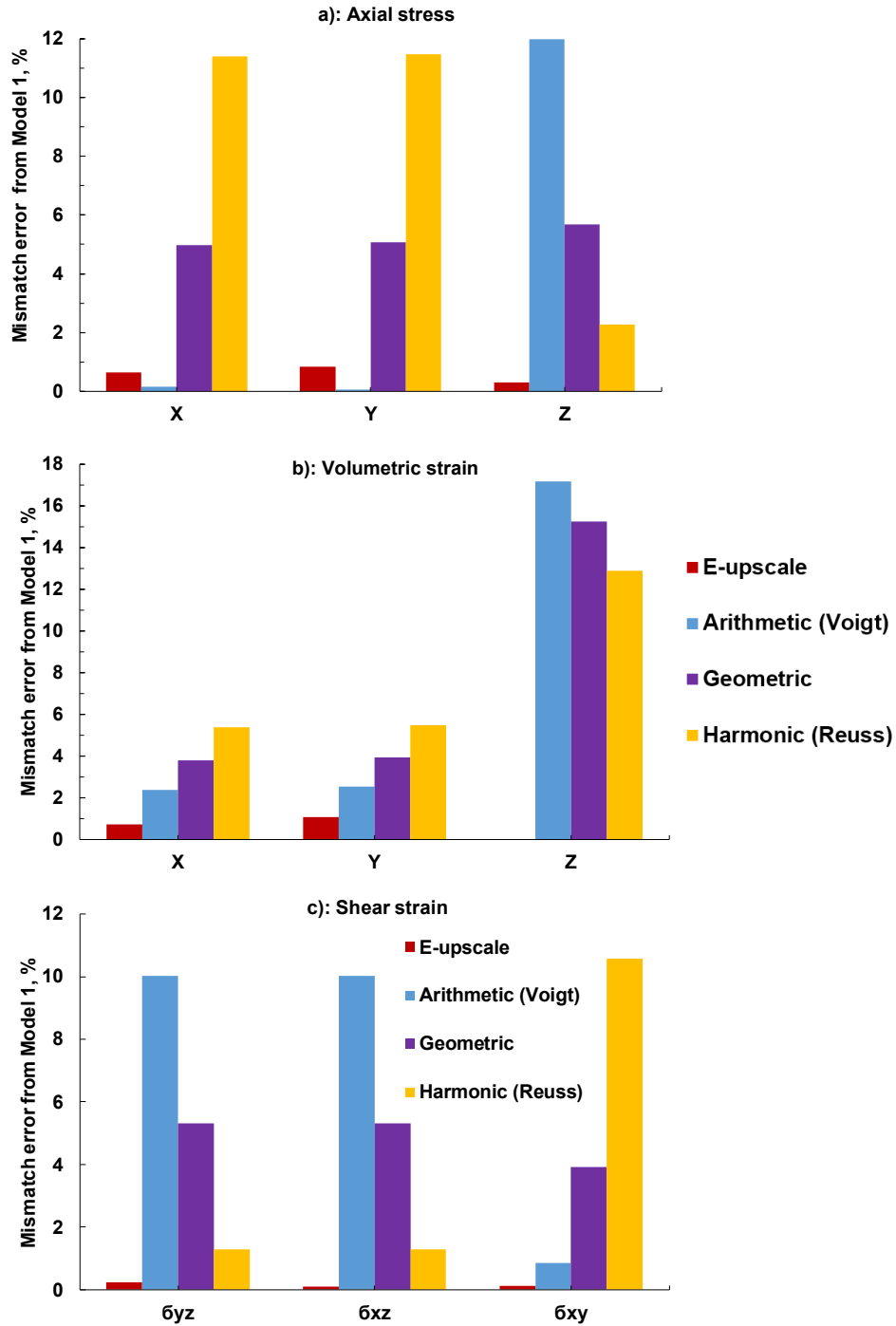
Figure 6-8. The mismatch error of axial stress (a) and volumetric strain (b) for upscaled models with E-upscaled, arithmetic, geometric and harmonic average elastic properties from Model 1 in global compression response. The mismatch error of shear strain (c) for upscaled models from Model 1 in the global shear response. The horizontal axis corresponds to the boundary conditions in the global tests. X represents global compression test in X (Figure 6-3a). σ_{xy} represents global shear tests (Figure 6-3f).

197
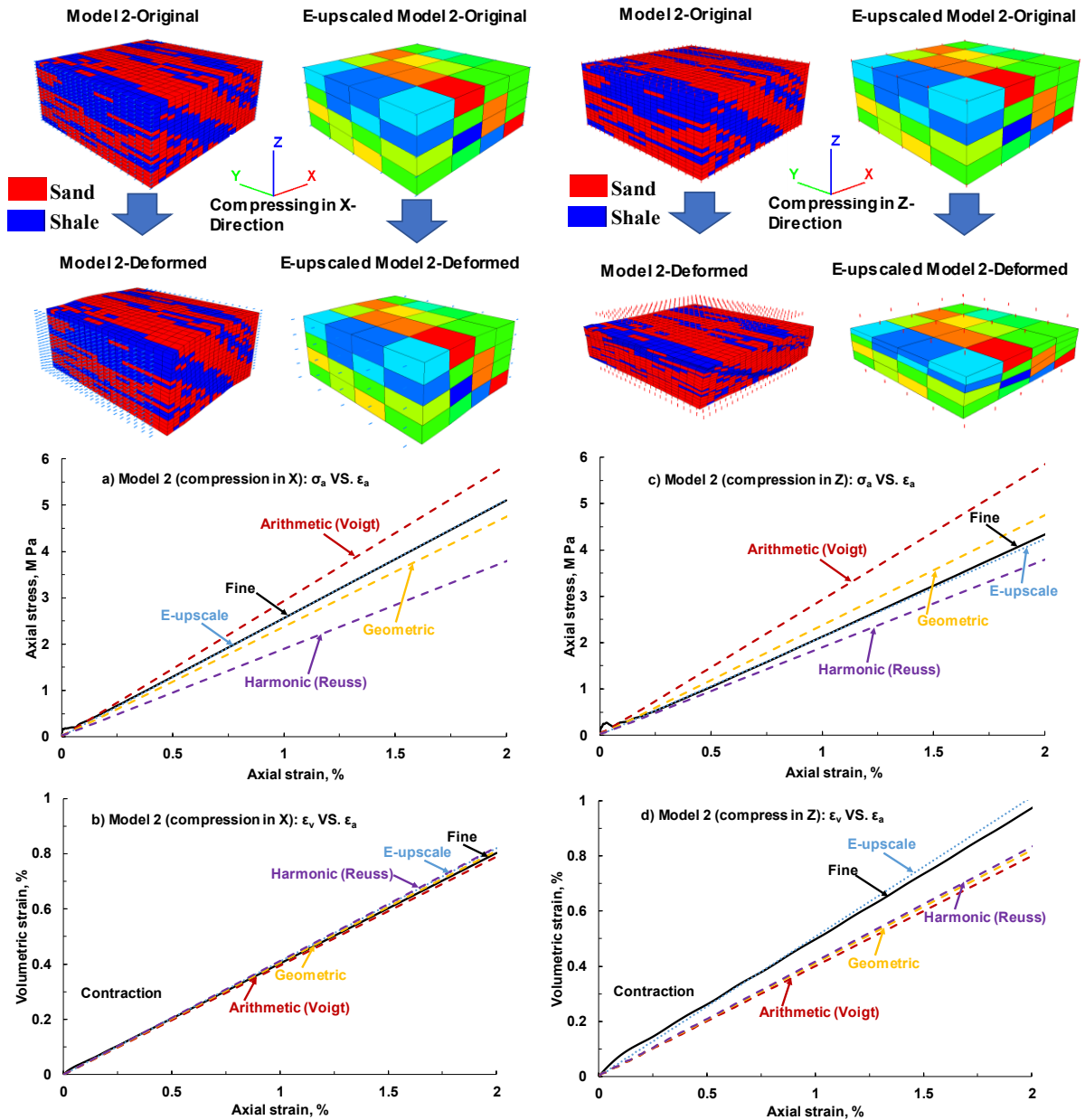
Figure 6-9. The axial stress (a, c) and volumetric strain (b, d) vs. axial strain for Model 2 with different upscaling methods and a constant displacement rate in X and Z.

6.2.5.2 Global Shear Response

The E-upscale methodology is validated for global model response in axis-parallel shear tests with the stress boundaries shown in Figures 6-3d, 6-3e and 6-3f but with 10 MPa shear stress to show

larger deformations for comparison. E-upscale is able to replicate the results of the fine-scale model with an average error of less than 0.2% (Figure 6-8c). Significantly larger errors, in some cases as high as 10%, occur when using the three other upscaling techniques. Sub-grid scale heterogeneity results in an anisotropic deformation response of the model under shear stress loading boundary conditions that cannot be captured using arithmetic, geometric or harmonic upscaling. The inclined shale layers present in Model 2 result in even greater non-uniform deformations (Figure 6-10). For an upscaling ratio of 125:1, the E-upscaled model can capture the shape of the deformed model for three different shear stress boundaries. The mismatch error in shear strain for E-upscale is approximately 1%, whereas for the arithmetic (Voigt) and harmonic (Reuss) averages, mismatch errors are 5 to 10 times larger due to oversimplified uniform strain/stress assumptions.
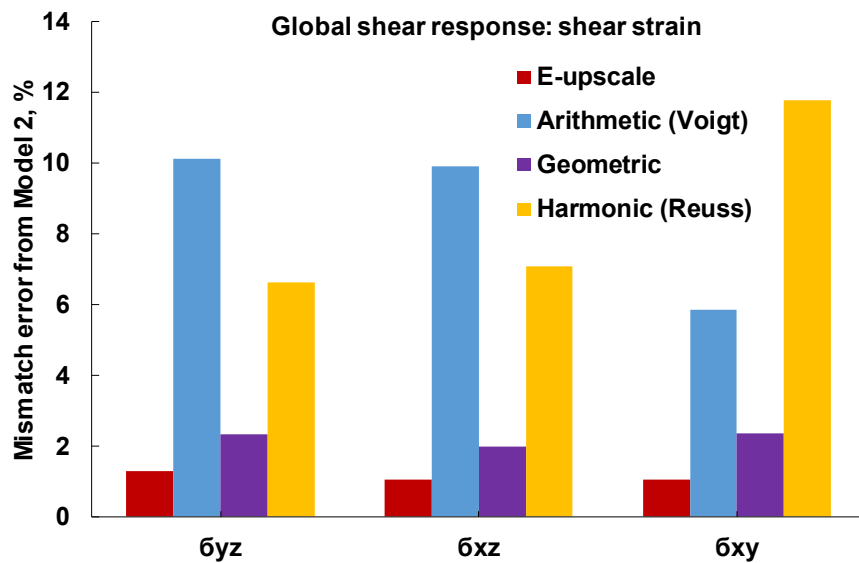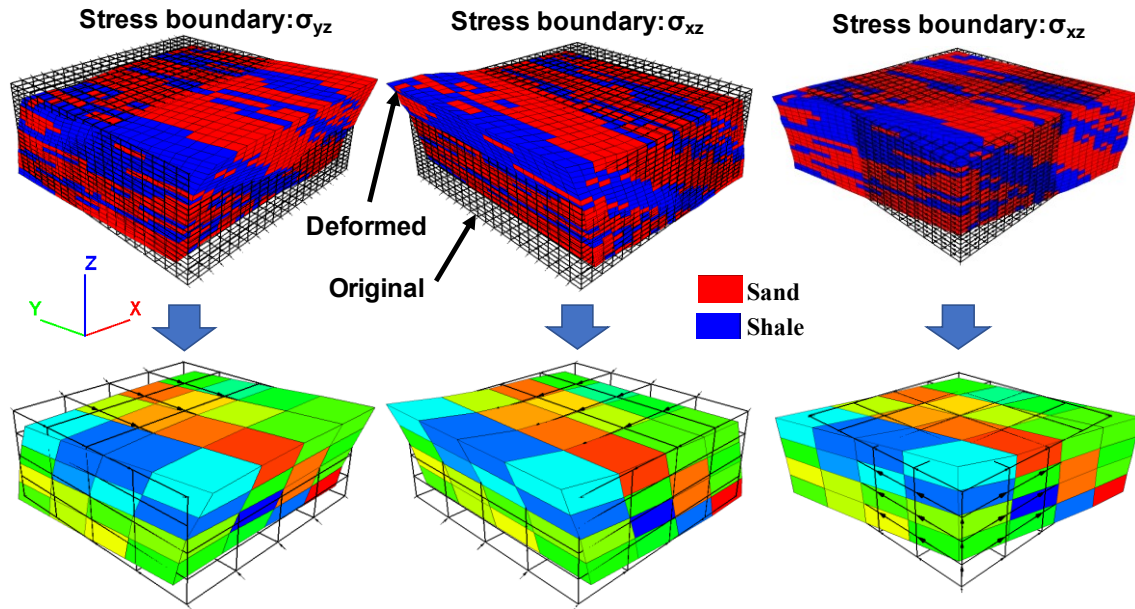
Figure 6-10. The mismatch error in global shear response for upscaled models with E-upscaled, arithmetic, geometric and harmonic average elastic properties from Model 2.

6.3 E-upscale Applied to Coupled Reservoir-geomechanics SAGD Simulation

As shown in Section 6.2.5, upscaled models using E-upscale can capture the geomechanical behavior of a fine-scale model under both compression and shear stress loading conditions. To assess the computational efficiency gained in adopting E-upscale, it is applied to a field-scale

coupled reservoir-geomechanics SAGD simulation. The interactions of geomechanical and flow response are widely accepted to have a significant impact on reservoir performance and caprock integrity in SAGD projects. The increase of pore pressure and thermal expansion associated with steam chamber development in heterogeneous oil sands reservoirs can lead to complex deformations. Laboratory experiments show that volumetric strain changes due to these deformations alter porosity, absolute permeability and relative permeability (Touhidi-Baghini 1998, Oldakowski 1994). Field observations of SAGD projects also provide evidence that high porosity and high permeability zones ahead of steam chambers allow hot fluids to flow into colder regions of the reservoir (Birrell 2001, Ito et al. 2000 and Collins 2007). Numerical simulations for these scenarios have typically adopted uncoupled or coupled reservoir geomechanical modeling approaches. Geomechanical modeling requirements impose different constraints than reservoir modeling and typically leads to larger upscaling ratios to improve computational efficiency. This process is only effective if the upscaled model can honor the behavior of the fine-scale geocellular model.

6.3.1   Fine-Scale Reservoir-Geomechanics Simulation

A fine-scale coupled reservoir-geomechanics simulation is generated based on the geological model (Figure 6-2a) of the MacKay River oil sand area. The Wabiskaw and McMurray Formations are the zones of interest for the reservoir and geomechanical models. The Till, Clearwater and Devonian Formations are only included in the geomechanical model as the over and under-burden for the reservoir (Figure 6-11a). The geomechanical and reservoir properties for the fine-scale reservoir-geomechanics simulation are summarized in Table 6-2. A steam injection pressure of 1283 kPa with a corresponding steam injection temperature of 191°C is chosen for the simulation (MacKay River project AER report 2017). Figure 6-11b shows the location of XZ cross-sections

within the model that are used to illustrate model heterogeneity and modeling results. The initial

horizontal permeability distribution (Figure 6-12) for the fine-scale model in XZ cross-sections 1,

20, 40 and 60 highlights the degree of heterogeneity within the model.
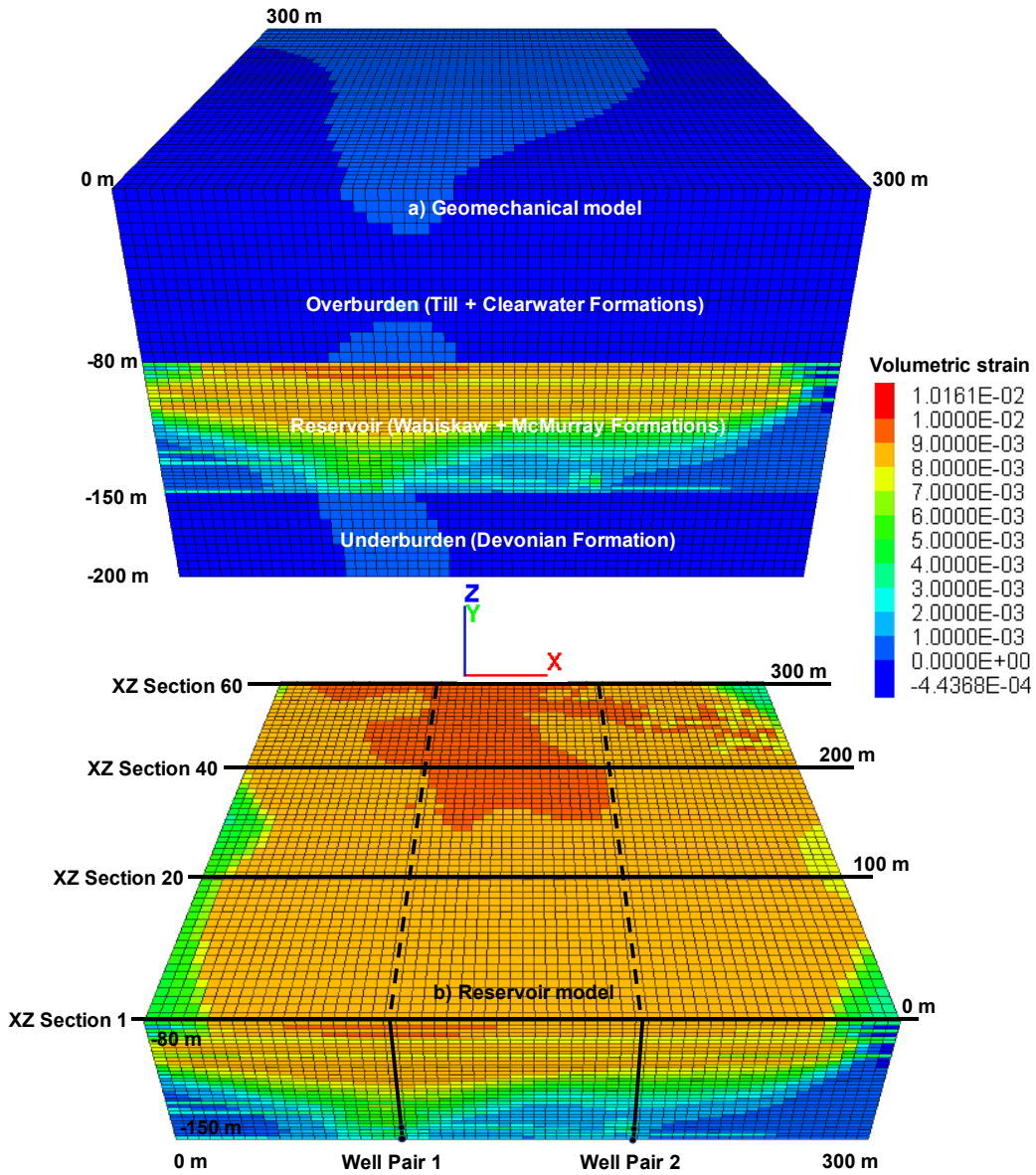
Figure 6-11. Schematic of the geomechanical (a) and reservoir (b) model for coupled simulation. The volume change of the reservoir at day 4760 is selected to highlight the location of steam chambers and corresponding XZ sections. The reservoir model is part of the geomechanical model which also includes the over and under-burden.
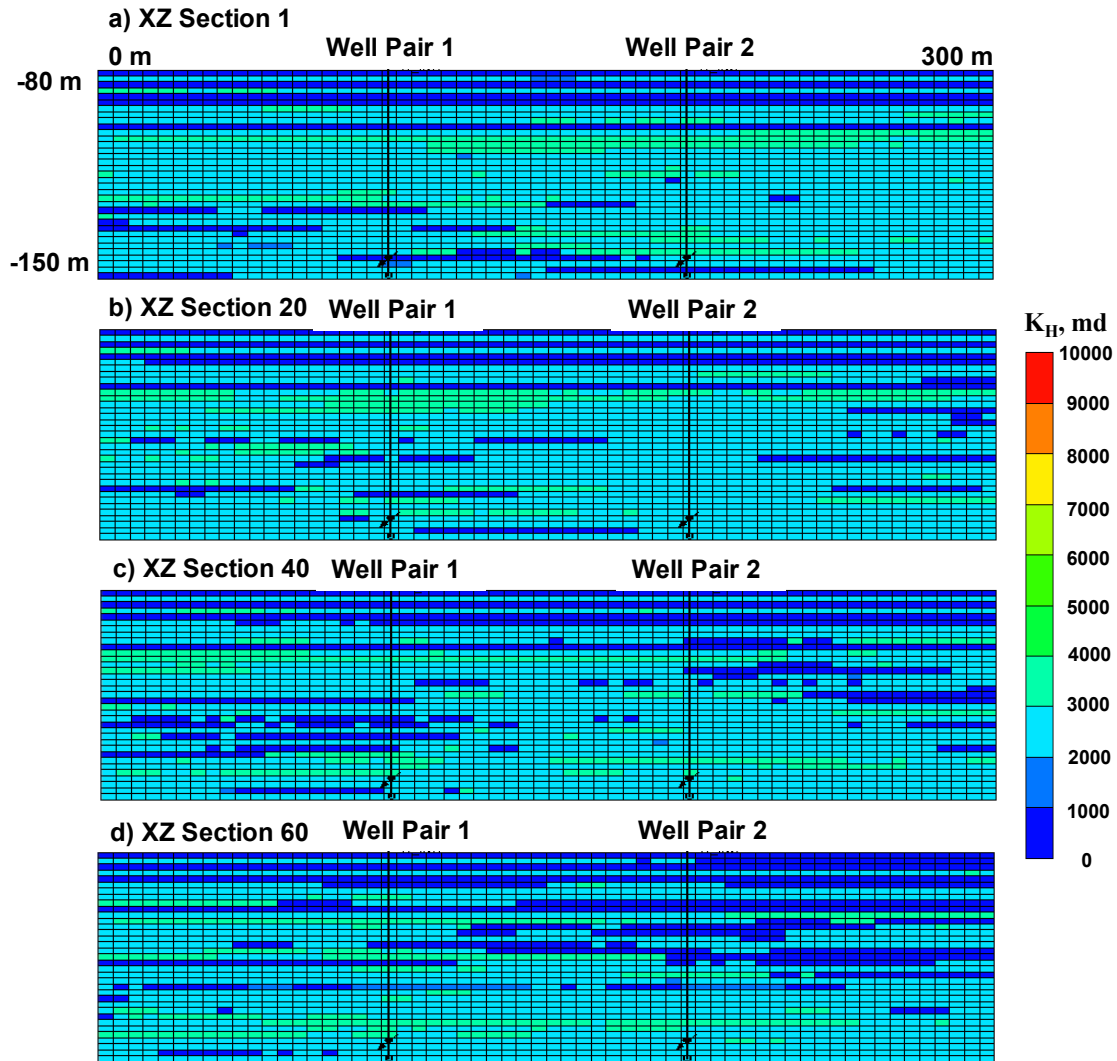
Figure 6-12. Initial horizontal permeability fields for XZ Section 1, 20, 40 and 60 before steam injection.

Table 6-2 Geomechanical properties for Model 2.

	Sand	Shale
Density, g/cm^3	2152-2207	2276-2310
Young's modulus, MPa	392-531	83-117
Poisson' ratio	0.35	0.25
Shear modulus, MPa	131-177	50-70

For the simulation, a preheating period is modeled where steam is circulated within the injection and production wells until Day 150. Steam is then injected in the upper well and fluids are

produced from the lower well, under steam trap control (MacKay River project AER report 2017). For the preheating period, absolute permeability is updated every 30 days until Day 150. For the production period, the sequential coupling between the reservoir and geomechanical processes occurs every 100 days until Day 4760 which is the end of the simulation. The absolute permeability is updated based on a correlation generated for the McMurray Formation oil sands at low confining stresses [27], which is a simplified form of Tortike and Farouq's correlation (Tortike and Farouq 1991) incorporating volumetric strain into the changes of absolute permeability:

$$k_i^n = a k_i^o \exp(b\varepsilon_{vol}), \text{ when } c < k_i^n < d \ ;$$

$$k_i^n = \text{c}, \text{when } k_i^n \le \text{c} \ ; \ k_i^n = \text{d}, \text{when } k_i^n \ge \text{d} \ , \hspace{3cm} \text{Equation 6-24}$$

where k_i^n is the updated permeability, i represents the direction of permeability (X, Y and Z) and n is the number of coupling steps. Constants a and b are tuned to fit laboratory and field data. Constants c and d are the upper and lower bounds of the updated permeability to avoid spurious calculated permeability. Table 6-3 provides the sand and shale tuning parameters and the upper and lower boundaries for the permeability updating function.

The simulations predict the evolution of deformations within the reservoir and surrounding formations as the fluid pressures and temperatures change during steam chamber development. For XZ cross-section 20, Figure 6-13 illustrates the growth of the steam chamber and the temperature field at days 1060, 1760, 3060 and 4760. For the same time periods, reservoir geomechanical coupled processes occurring during the development of the steam chambers impart significant changes to the horizontal permeability (Figure 6-14) and these changes exert significant influence on the geometry of steam chamber development. These results demonstrate that flow and geomechanical response closely interact in the SAGD and it is critical that upscaling

workflows adopt for these types of coupled simulations honor the geomechanical response of fine-scale models.
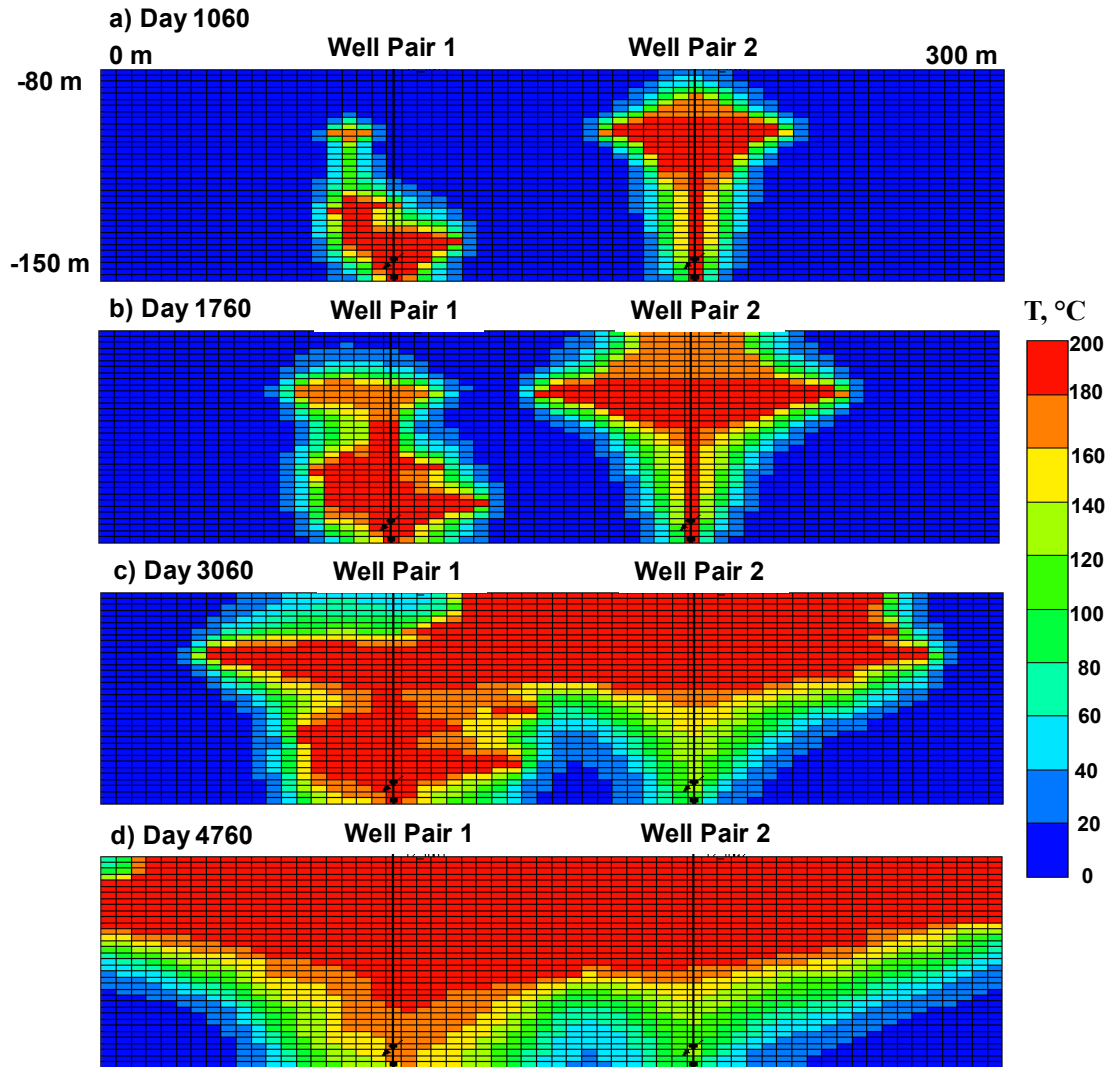
Figure 6-13. Steam chamber XZ Section 20 at day 1060, 1760, 3060 and 4760 during SAGD.
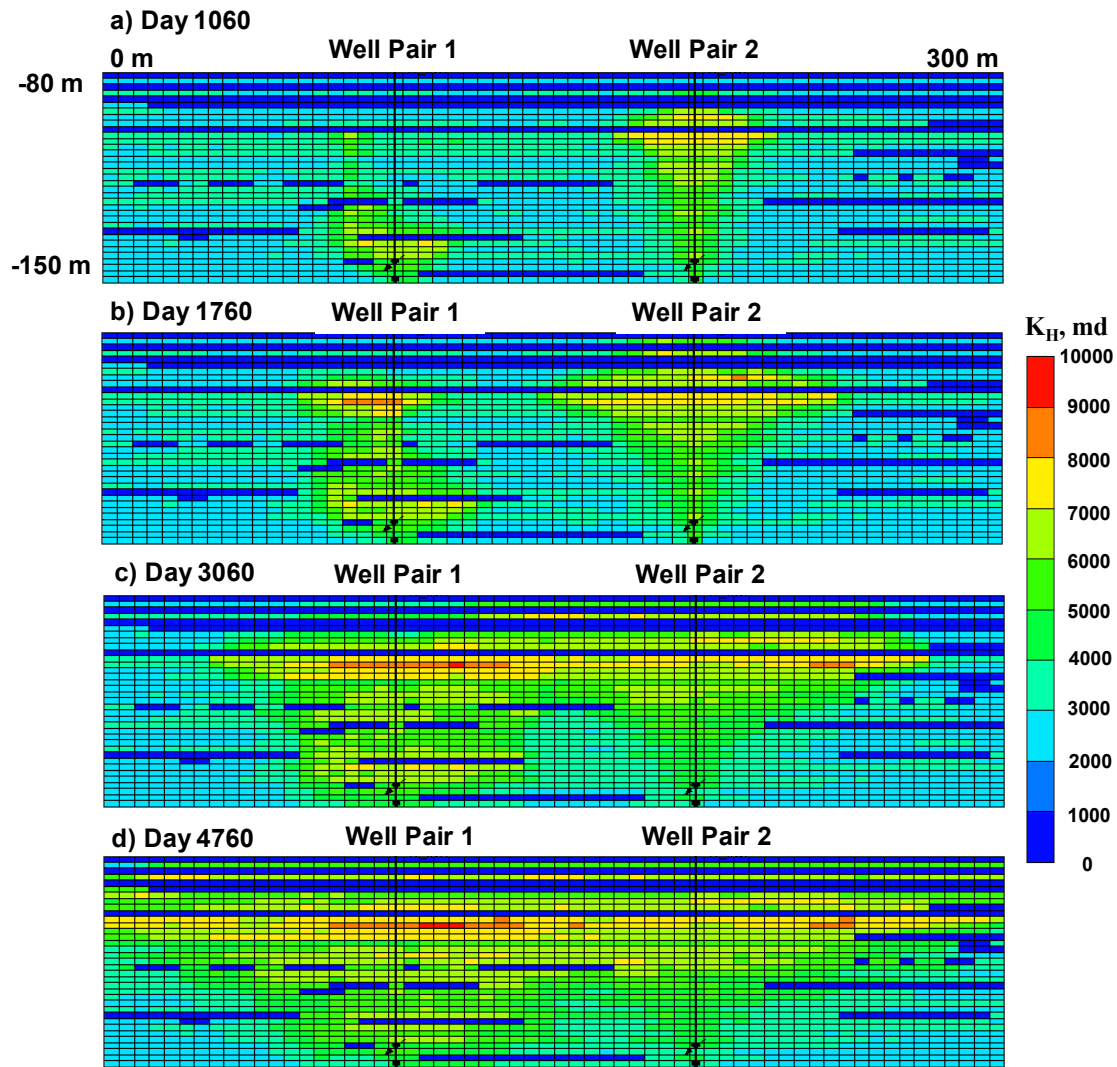
Figure 6-14. Horizontal permeability field for XZ Section 20 at day 1060, 1760, 3060 and 4760 showing the impact of steam chamber propagation on absolute permeability in SAGD.

Table 6-3 Geomechanical and reservoir properties for coupled simulation.

Formation	Till	Clearwater Wabiskaw	McMurray	Devonian
Facies	N/A	Sand	Shale	N/A
Bulk density, kg/m^3	1840	2143.8-2207.0	2274.47-2317.58	2365
Young's modulus, MPa	50	253.4-633.0	60-240.4	3000
Poisson' ratio	0.25	0.35	0.25	0.145
Shear modulus, MPa	20	93.9-234.5	24-96.2	1310
SXX, MPa	94.3-943.3	1648.9-3329.3	1062.6-3314.9	3425.6-4555.8
SYY, MPa	73.7-737.4	1083.9-2210.1	824.7-2201.9	2284.3-3102.0
SZZ, MPa	90.2-902.2	1570.2-3105.4	1015.0-3092.3	3197.3-4265.0
Porosity	0.3	0.288-0.351	0.243-0.287	0.3
Permeability X&Y, md	2	1690.2-3843.9	5.2-7.7	50
Permeability Z, md	2	845.1-1922.0	1.3-1.9	50
Oil saturation	0	0.768-0.831	0.092-0.113	0
Temperature, °C	3.1-4.3	5.1-6.2	4.4-5.3	7.1-8.3
Pressure, MPa	49.0-490.3	222.9-867.2	203.4-866.3	914.8-1357.5
Thermal expansion coefficient, 10^{-6} 1/°C	1	20	10	10

The steam chamber gradually propagates in the reservoir and deformations occur due to changes in pressure and temperature. The temperature profiles for cross-section 20 are selected to show the propagation of the steam chamber at selected coupling steps which are day 1060, 1760, 3060 and 4760 in Figure 6-8. The horizontal permeability is significantly affected by the steam chamber propagation as demonstrated by Figure 6-9. As a result of the absolute permeability change, chamber propagation speed inevitably changes. Thus, the geomechanical response, such as volumetric strain and surface heave, is going to be affected. The detailed reservoir performance and geomechanical response for this fine-scale reservoir-geomechanics simulation of SAGD are demonstrated in the following section and compared with the upscaled model by E-upscale and traditional averaging methods.

Table 6-4 Scale, shape factor, upper and lower boundary for permeability updating function.

	Sand	Shale
Scale factor for updated permeability, a	1	1
Shape factor for updated permeability b	100	500
Upper boundary of Permeability, c	100	0.1
Lower boundary of Permeability, d	25000	100

6.3.2 Flow-based Permeability Upscaling

To facilitate the application of E-upscale to field-scale modeling problems, the workflow is implemented in an in-house reservoir-geomechanics simulation platform (Deisman et al. 2018). Weighted volume averages are used for porosity and saturation upscaling as they are not directional dependent. The upscaled permeability tensor is calculated by the pressure-field solution method through the conservation of mass from the fine-scale to the coarse grid. Upscaling of permeability has been extensively investigated as it is one of the key factors in flow response, according to Darcy's law:

$$u = -\frac{k}{\mu}\nabla P ,$$
<div align="right">Equation 6-25</div>

where u, k, μ and ∇P are the flux vector, permeability tensor, viscosity and pore pressure gradient, respectively.

The effective permeability of the coarse block can be obtained by integration of flow over the volume of the upscaled region:

$$\int_V u dV = -k_{eff} \int_V \nabla P dV ,$$
<div align="right">Equation 6-26</div>

where V is the volume of the upscaled cell and k_{eff} is the effective permeability tensor. The total flux (Q) in the upscaled region (left side of Equation 6-26) is calculated by the summation of flux at all permeable boundaries:

$$Q = \int_V u dV .$$ Equation 6-27

The pressure changes in the coarse block are solved from divergence theorem of the upscaled region:

$$\nabla P = \int_V \nabla P dV = \oint_S P n dS ,$$ Equation 6-28

where n is the outward unit normal to the pressure boundary and S is the area of the face boundary.

A steady-state flow boundary is assumed in the local flow tests in X, Y and Z. Thus, the effective permeability k_{eff} in the direction i is calculated by:

$$k_{eff}^i = -Q^i / \nabla P^i .$$ Equation 6-29

6.3.3   E-upscale in Coupled Reservoir-geomechanics Simulation

Due to depositional processes, the vertical range of spatial correlation is usually shorter compared to horizontal, e.g. thin shale layers in the oil sand reservoir. The longer horizontal range of continuity in shale bedding planes allows for larger upscaling ratios horizontally without over-mixing of sand and shale facies. For the upscaled model 6*6*1, the horizontal upscaling ratio is fixed to 6 while keeping the vertical grid size. E-upscale, arithmetic, geometric and harmonic averages are used for the upscaling of elastic properties. Flow-based upscaling is performed for all models leading to the same initial permeability fields.

The cumulative oil production (COP) for fine-scale and upscaled cases are illustrated in Figure 6-15. The E-upscaled model has the most accurate oil recovery prediction compared to the fine-scale response. The arithmetic (Voigt) and harmonic (Reuss) bounds of effective elastic properties lead to variations in predicted oil recovery from the fine-scale model due to the complex stress state that occurs during the SAGD process. As the intermediate average between Voigt and Reuss bound,

209

the geometric average has a slightly better prediction in terms of oil recovery as it provides a more accurate deformation response for the upscaled model.
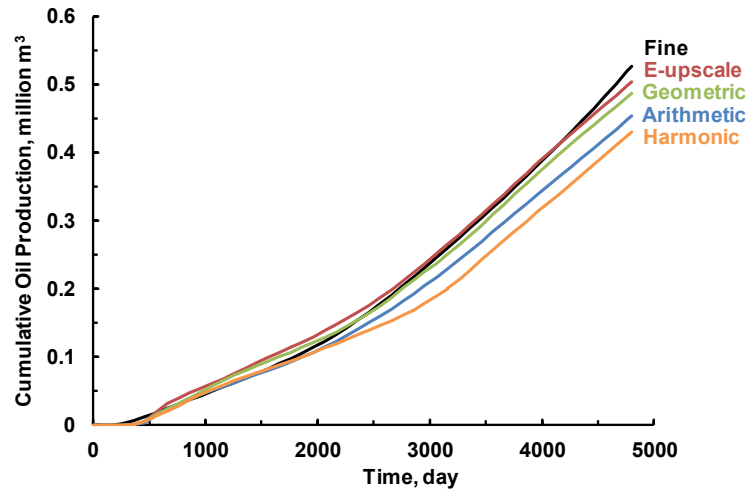
Figure 6-15.   Cumulative oil production vs. time for the fine and upscaled model (6*6*1) with E-upscale, arithmetic, geometric and harmonic upscaling for elastic properties and flow-based upscaling for permeability.

Surface heave is commonly monitored in SAGD operations to avoid potential caprock integrity issues. While all upscaled models do not replicate the predicted surface heave from the fine-scale model, the E-upscaled model is the most accurate prediction of magnitude and shape of surface heave (Figure 6-16). The displacement field shows that vertical displacements dominate the reservoir deformations (Figure 6-17). The side view of the vertical displacement contour for XZ Section 60 also demonstrates the improved prediction of E-upscale. The deformation and permeability change of the reservoir is closely related to the steam chamber propagation of the reservoir. Therefore, E-upscale does improve the overall prediction of upscaled coupled simulation.

The reduction of computational time is significant for the fine-scale coupled simulation. Figure 6-18 illustrates the strong dependence of simulation time on the number of model cells. The

simulation time using the E-upscale workflow is 0.75 hours compared to 15.4 hours for the fine-scale model. Creating the upscaled model is within 1 hour with the help of the generated parallel programs.
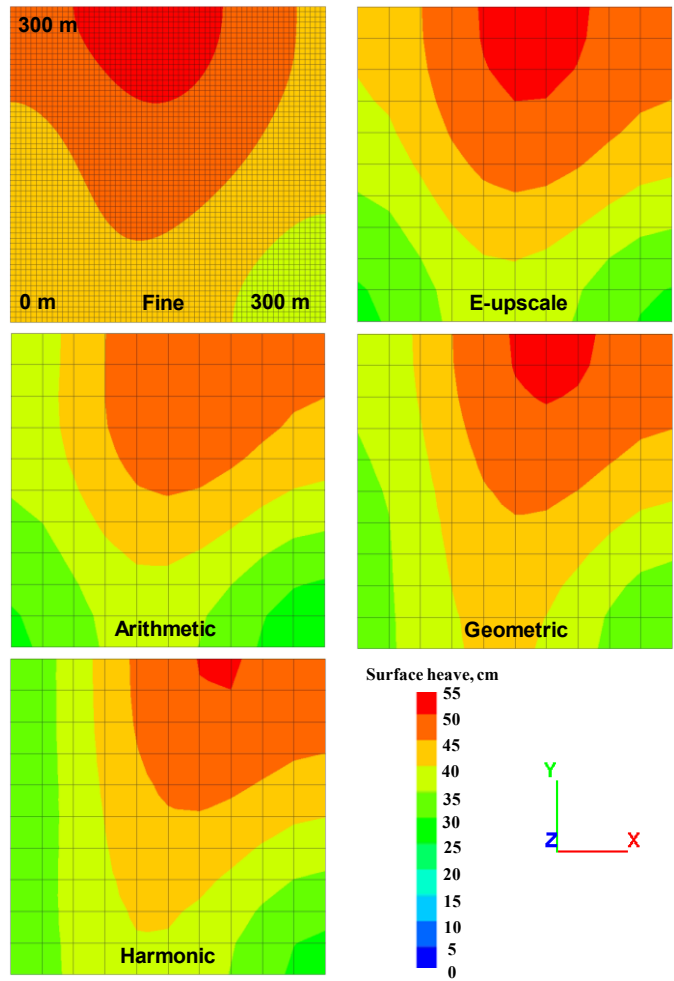
Figure 6-16.   Surface heave (@ 0 m depth) at the end of the simulation (Day 4760) for fine-scale, E-upscaled, arithmetic, geometric and harmonic averaged models.
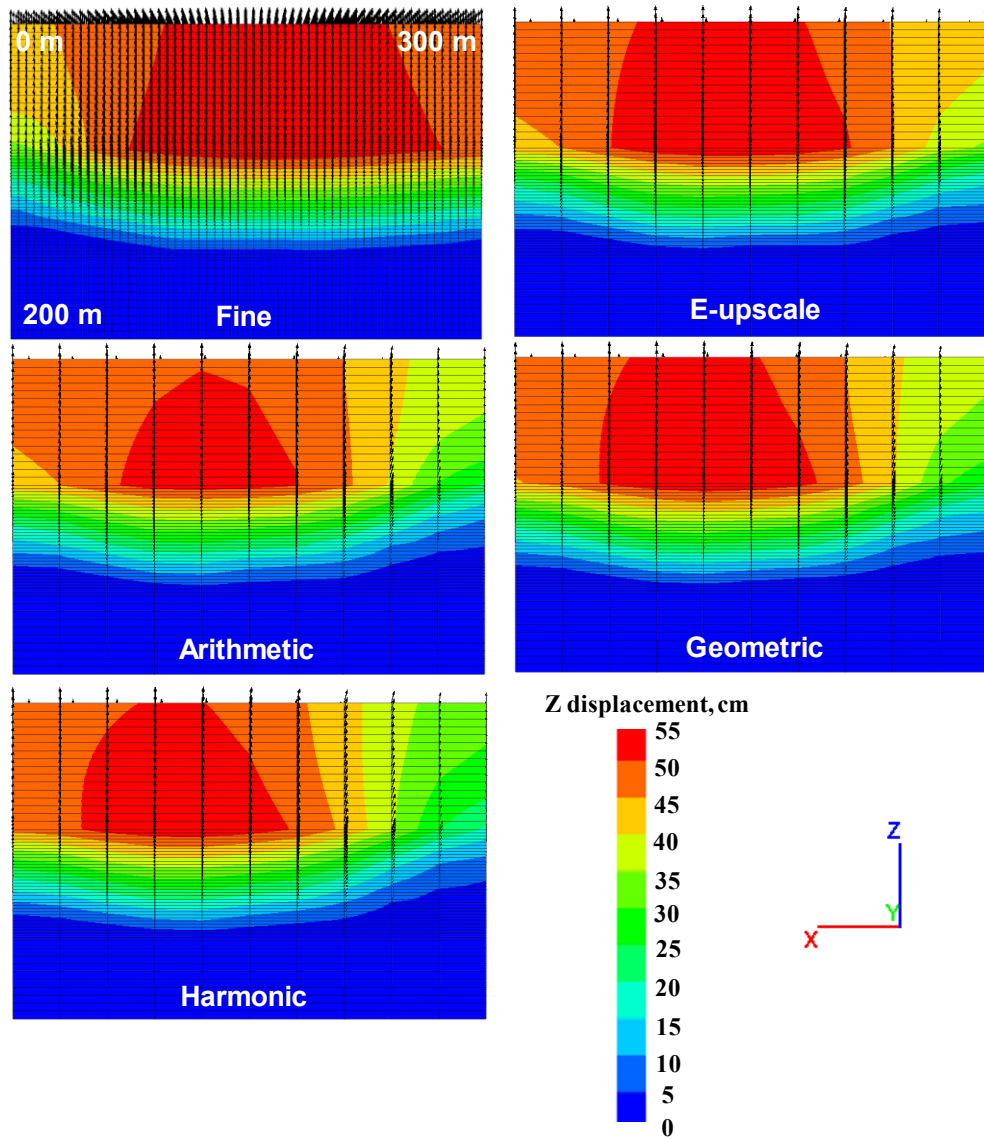
Figure 6-17.   Vertical displacement field at the end of the simulation (Day 4760) for fine scale, E-upscaled, arithmetic, geometric and harmonic models at XZ Section 60.
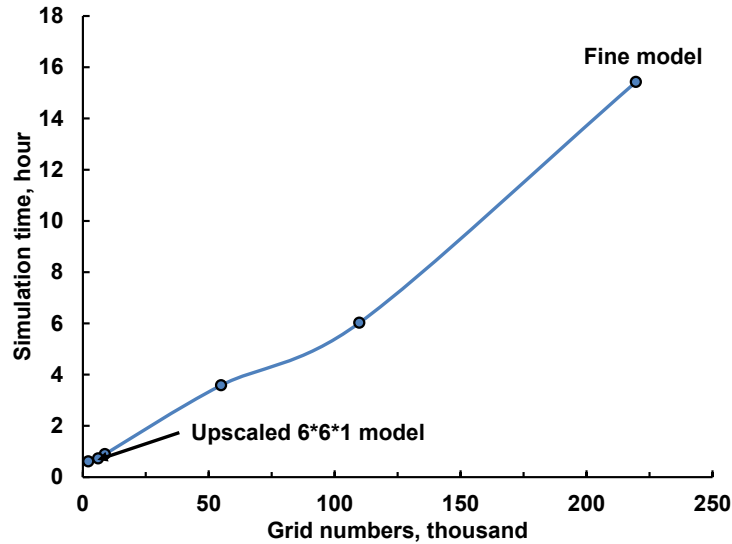
Figure 6-18.   Simulation time for fine-scale and upscaled coupled simulations.

6.4   Summary and Conclusions

A local numerical upscaling technique, E-upscale, is developed to estimate the effective elastic geomechanical properties for heterogeneous continua. For each upscaled cell, the anisotropic Young's modulus, Poisson's ratio and shear modulus are solved to replicate the local strain tensors of the fine-scale model under three compression and three shear stress boundaries in a parallel program. The global compression and shear response are validated for two different sand-shale sequence systems: 1) Model 1 with horizontal shale bedding planes (transverse isotropic); 2) Model 2 with 30° inclined shale layers (fully orthotropic). Successful application of E-upscale in reservoir-scale coupled SAGD simulation demonstrates that E-upscale can significantly improve the prediction of surface heave, subsurface displacements and oil production when integrated with flow-based permeability upscaling.

213

The anisotropic E-upscaled elastic properties are solved with different numerical testing regimes to reproduce the anisotropic geomechanical response caused by sub-grid scale heterogeneities. The orthotropic assumption of the compliance matrix may not be applicable for reservoirs with massive discontinuities (faulting and fractures), where further investigation is required to confirm whether the anisotropic compliance matrix with 21 or 36 constants can deal with upscaling problems in heterogeneous discontinua. E-upscale can help to better accommodate the complex interactions of flow and deformations in reservoir processes. When significant inelastic behavior is involved, additional simulation time steps are required for the local tests to determine the effective geomechanical properties which can capture the effective/dynamic modulus of elasto-plastic behavior.

As flow parameters are strongly related to deformation response, it is recommended that E-upscale be applied in recovery processes involved with significant pressure and temperature change, e.g. SAGD. The improved predictions of E-upscaled model can enable a larger upscaling ratio for full-field geological models while maintaining the accuracy of coupled simulation. The reliable surface and subsurface deformations associated with production performance provided by the E-upscaled model for full-field pilots can provide valuable predictions to make an improved resource recovery plan. When plastic deformations occur in the reservoir, E-upscale alone cannot compute the upscale plastic properties which control the failure criteria. Therefore, a local numerical technique is introduced in Chapter 7 for upscaling of plastic properties.

CHAPTER 7: LOCAL NUMERICAL PLASTIC UPSCALING TECHNIQUE AND VALIDATION IN FULL-FIELD RESERVOIR-GEOMECHANICS SIMULATION

The importance of geomechanical simulation is well documented for projects associated with significant pressure and temperature changes, such as SAGD) or hydraulic fracturing. Deformations and failure zones in reservoirs will impact fluid flow, caprock integrity, and well integrity. However, geological modeling cell sizes are typically at the centimeter scale in order to incorporate geological features resulting in models with millions of cells that are computationally expensive for current reservoir-geomechanics simulations. One option to overcome these computational challenges is to properly upscale geomechanical properties and simulate at a larger scale with fewer cells. While many current upscaling techniques normally assume isotropic elastic deformation and failure criteria for each upscaled cell, anisotropic deformation and failure response caused by sub-grid heterogeneity are significant complicating factors for heterogeneous continua.

The local and global non-uniform deformations of highly heterogeneous systems can be well reproduced by the non-symmetric upscaled compliance matrix obtained by local numerical compression and shear tests in Chapter 6. With the elevated pressure or temperature in oil/gas recoveries, the in-situ stress state may impinge upon the failure envelope leading to elasto-plastic response and plastic deformations (Chalaturnyk and Li, 2004). The lithological heterogeneities lead to different failure modes at the same stress boundaries due to strain localization (Desrues and Viggiani 2004). For upscaled cells with non-symmetric heterogeneities, changes in principal stress direction, e.g. thermal expansion, also result in altered failure modes. The complexity of lithological heterogeneities and stress-state change in hydrocarbon recoveries, such as thermal

recovery in oil sands and hydraulic fracturing in shale gas, make anisotropic failure criteria necessary to capture the anisotropic failure mechanism for each upscaled cell.

Here, the numerical testing regimes for elastic local upscaling (Zhang et al., 2019) are extended to anisotropic failure criteria. Incremental strain boundaries are applied in three orthotropic axes of the upscaled cell during local numerical triaxial tests. The anisotropic upscaled plastic properties are solved from the preferred failure theory for different rock types in an efficient and robust algorithm, this is termed P-upscale.

P-upscale is integrated with the deformation-based E-upscale and flow-based permeability upscaling technique for applications in the reservoir-geomechanics simulation of the fine-scale geological model of Pad C in the MacKay River oil sand area. This chapter focuses on the methodology of P-upscaling and workflows of application in full-field mechanical earth models.

7.1   Methodology for P-upscale

7.1.1   Theoretical Background and Testing Regimes

The Mohr-Coulomb (M-C) failure criterion is used to determine shear strength properties defined by friction angle ϕ' and cohesion c'. In terms of principal stresses, the M-C failure criterion is:

$$\sigma'_1 - \sigma'_3 = (\sigma'_1 + \sigma'_3) \, sin \, \phi' + 2c' \, cos \, \phi', \qquad \text{Equation 7-1}$$

where σ'_1 and σ'_3 are the maximum and minimum principal effective stresses.

The local numerical triaxial tests are set up for each upscaled cell; each upscaled cell is composed of many heterogeneous fine-scale cells that are at the scale of the geological features deemed important to geomechanical simulation. To obtain an effective failure envelope for each orthogonal axis i, two smooth plates are compressed with fixed displacement rate (ε_a boundary) in the x, y, and z-directions (Figure 7-1a, 7-1c, and 7-1e). The numerical triaxial tests with different confining

216

stress (σ_3^1 and σ_3^2) are simulated until reaching the peak stress (σ_1^1 and σ_1^2) to compute the anisotropic linear M-C failure envelopes.
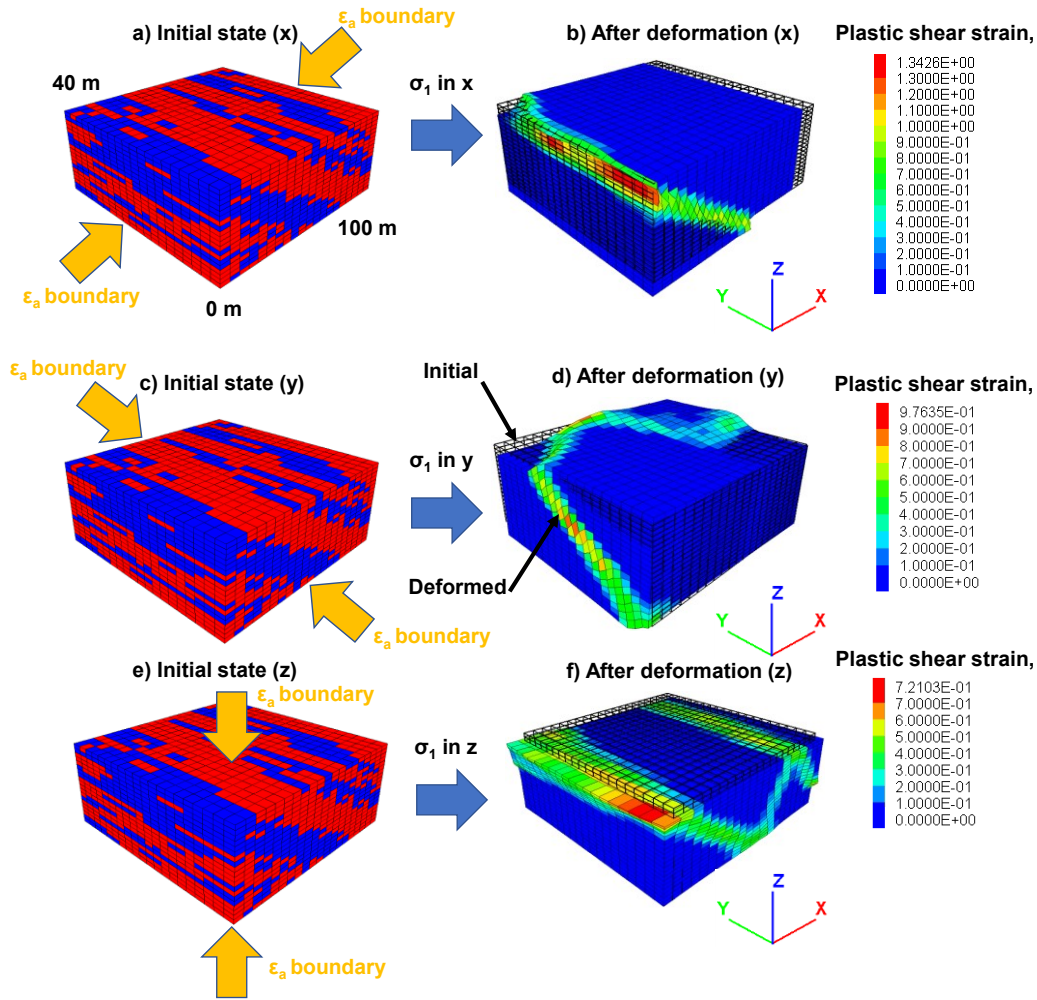
Figure 7-1   Initial condition of an upscaled cell in x, y and z directions (a, c and e). Deformed upscaled cell with different failure modes after local triaxial tests (b, d, and f). Blue cells represent shale with lower strength compared to sand cells (red). The confining stress is applied in others faces other than the strain boundaries.

Usually, σ_3^1 and σ_3^2 are selected as the initial minimum and maximum principal stress before deformation unless the upscaled cell is in isotropic stress states. The M-C failure criteria for the triaxial tests in the i direction with confining stresses σ_3^1 and σ_3^2 are:

217

$$\sigma_{i1}^1 - \sigma_{i3}^1 = (\sigma_{i1}^1 + \sigma_{i3}^1) \sin \phi_i + 2c_i \cos \phi_i , \qquad\qquad \text{Equation 7-2}$$

$$\sigma_{i1}^2 - \sigma_{i3}^2 = (\sigma_{i1}^2 + \sigma_{i3}^2) \sin \phi_i + 2c_i \cos \phi_i , \qquad\qquad \text{Equation 7-3}$$

where σ_{i1}^2 and σ_{i1}^1 are the peak stress in load direction i for the local triaxial tests under confining stress σ_{i3}^2 and σ_{i3}^1, respectively.

Substituting Equation 7-2 into 7-3, the upscaled friction angle (ϕ_i) is calculated as:

$$\phi_i = \sin^{-1} \frac{(\sigma_{i1}^2 - \sigma_{i1}^1) - (\sigma_{i3}^2 - \sigma_{i3}^1)}{(\sigma_{i1}^2 - \sigma_{i1}^1) + (\sigma_{i3}^2 - \sigma_{i3}^1)} , \qquad\qquad \text{Equation 7-4}$$

The cohesion in each orthogonal axis (c_i) can be calculated by:

$$c_i = \frac{(\sigma_{i1}^2 - \sigma_{i3}^2) - (\sigma_{i1}^2 + \sigma_{i3}^2) \sin \phi_i}{2 \cos \phi_i} , \qquad\qquad \text{Equation 7-5}$$

Following the two stress paths (triaxial conditions with confining stress of σ_3^1 and σ_3^2) in three orthogonal axes (x, y, and z), three independent M-C failure envelopes are inverted from the six local triaxial tests.

7.1.2 Implementation of P-upscale in IHS system

An inclined heterolithic strata (IHS) system composed of 30° inclined shale layers embedded in sand (Figure 1a) is selected to demonstrate the implementation of P-upscale because anisotropic failure is expected and critical for reservoir performance. Local numerical triaxial tests with incremental strain boundaries are conducted in x, y, and z-directions (Figure 1a, 1c, and 1e). During the numerical triaxial tests, the stress state of the upscaled cell follows the stress paths 1, 2, and 3 (Figure 2) and stops at different peak states for x, y, and z.
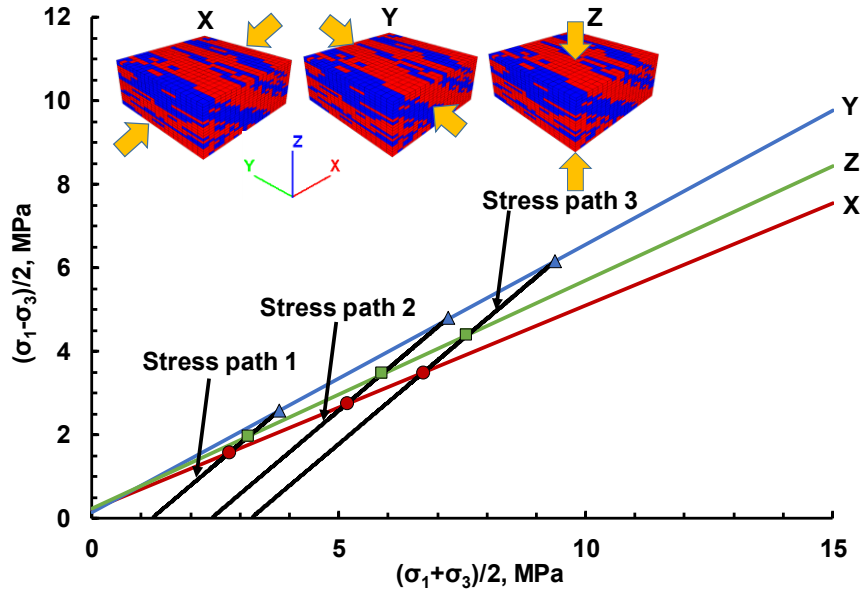
Figure 7-2   Mohr-Coulomb failure envelopes in X, Y, and Z-directions for numerical triaxial compression tests with three different confining stresses (stress paths 1, 2 and 3).

The three confining stresses are the initial stress magnitude in X (3.2 MPa), in Y (2.4 MPa) and half of the stress magnitude in Y (1.2 MPa). After triaxial compression tests in X, Y and Z, the upscaled regions (Figure 7-1b, 1d and 1f) demonstrate different modes of failure caused by the strain localization in the weaker shale cell and nearby sand cell. The stress-strain behavior is strongly related to the failure modes in the local triaxial compression tests as shown in Figure 7-1. As the failure planes are across the stronger sand cells when compressing in Y (Figure 7-1d), the peak stress is significantly higher than compressing in X when failure planes are localized in the weaker shale cell (Figure 7-1b).
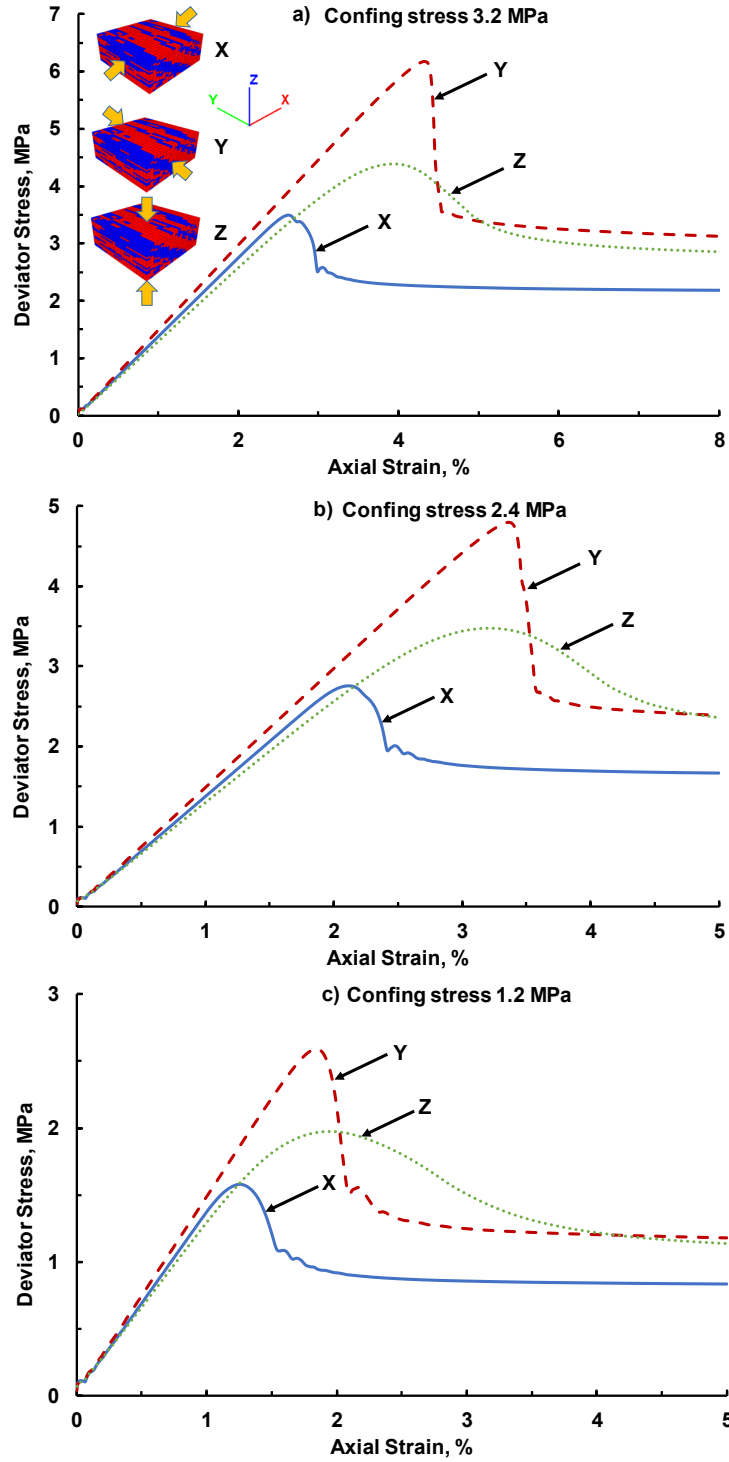
Figure 7-3   Stress-strain behavior of IHS model for numerical triaxial compression tests in X, Y, and Z-directions with three different confining stresses (stress paths 1, 2 and 3).

The stiffnesses of the IHS model in the X, Y and Z direction are also significantly affected by the inclined shale bedding planes as shown by the slope of stress-strain curve before the peak (Figure 7-3). The stiffness of the model is strongly correlated to the shear strength for this sand-shale sequence model as shown by triaxial compression tests in X and Y. However, the vertical stiffness is smaller than the horizontal stiffness even when the shear strength in the Z direction is significantly higher than X direction. The effective Poisson's ratio can be determined by the plot of the volumetric strain versus the axial strain in Figure 7-4. The steeper slope before peak reflects smaller Poisson's ratio in the Z direction.

The effective M-C failure envelopes in the X, Y and Z direction are determined by the peak points of the triaxial tests with three confining stresses in Figure 7-2. The M-C failure envelope in the x-direction is the lowest as the shear plastic strain concentrates among the weaker shale cells (Figure 7-1b). When compressed in the y-direction, the shear planes propagate through the stronger sand cells leading to the highest M-C failure envelope (Figure 1d). The resulting ϕ_y is 10° higher than ϕ_x due to the embedded 30° inclined shale bedding planes as listed in Table 7-1.

Table 7-1 Upscaled Plastic Properties at X, Y and Z direction.

	Friction Angle, °	Cohesion, kPa
Sand	51.3	0
Shale	30.5	140
X	30.8	116
Y	41.0	66
Z	35.0	98

The 30° inclined shale bedding planes has led to a significant anisotropic impact on elastic response and failure modes. Thus, P-upscale is recommended to generate the anisotropic M-C

failure criteria to fully capture the non-uniform deformation and failure of high heterogeneous region with a significant change of principal stress magnitude and direction, e.g. SAGD process.
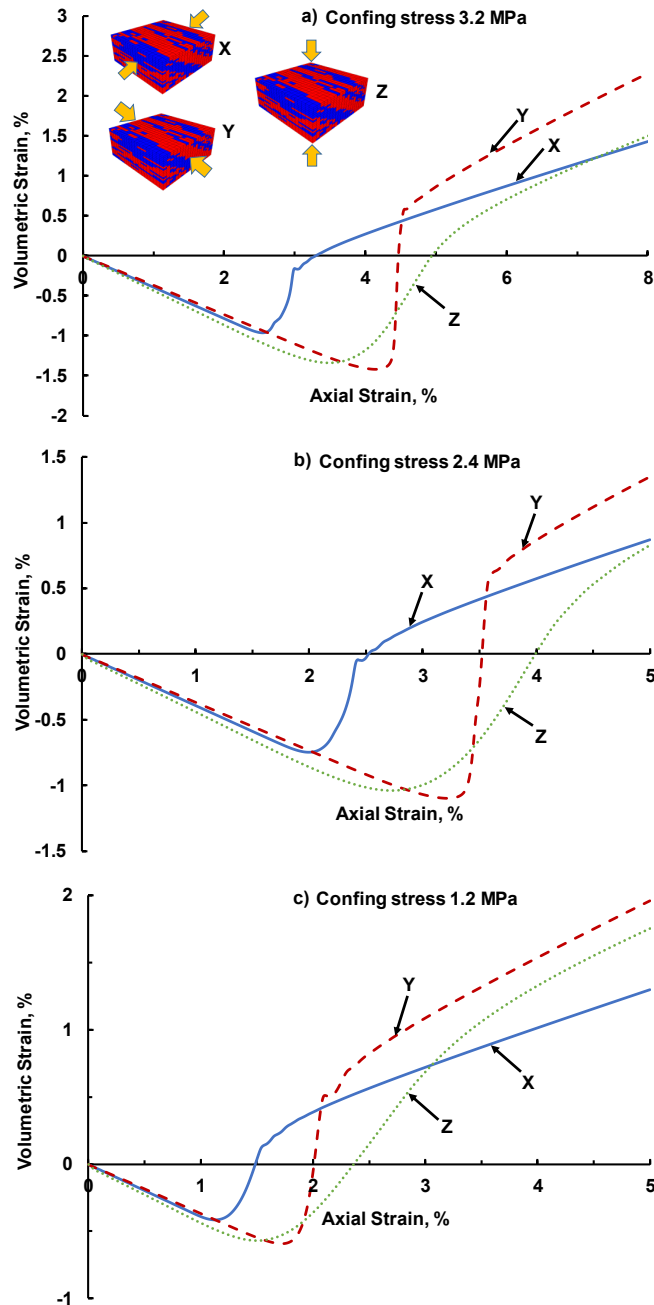
Figure 7-4   Volumetric strain versus axial strain of IHS model for numerical triaxial compression tests in X, Y, and Z-directions with three different confining stresses (stress paths 1, 2 and 3).

7.1.3   Reservoir-scale Algorithm

The axial displacement required to fail a given depositional body is fixed under a certain load direction. If accuracy is the priority, the loading rate of the incremental strain boundary should be small enough to capture the peak point and minimize the numerical error. However, the required computational time is nearly linear to the simulation time steps. Therefore, the loading rate should be optimized when applying P-upscale in a large-scale reservoir-geomechanics model.

Sensitivity analyses are conducted for selected upscaled cells (with different upscaling ratio) in a large-scale reservoir-geomechanics simulation model to determine the most appropriate loading rate for each orthogonal axis. Here, the loading rate in the benchmark model is going to be selected to minimize the numerical error. Figure 7-5 illustrates the change of deviation from the benchmark model versus the required simulation time for a single local numerical test. The "Gold Zone" is defined for the loading rate which meets the allowance for simulation time and maintains the acceptable numerical error. The proposed P-upscale manages to upscale the 8000-cell highly heterogeneous IHS model into a single cell within a 5% error in less than 180 seconds. If the upscaled cell is discretized by 5 by 5 by 5 cells as demonstrated in E-upscale, the simulation time for P-upscale is maintained within 3 seconds. The computational efficiency of the P-upscale method enables its application in large-scale models with millions of cells if an optimum loading rate can be selected through sensitivity analyses.

The reservoir scale algorithm of P-scale is summarized as:

Step 1: The local numerical testing programs for the selected upscaled geomechanical cells of the fine-scale geological model are generated automatically with customized upscaled ratios in X, Y and Z direction, e.g. finer mesh near wells and highly heterogeneous areas.

Step 2: Adopting the original maximum and minimum principal stress as the two confining stress, local numerical triaxial tests are conducted for the selected upscaled cell under various displacement rates for sensitivity analysis.

Step 3: The optimum displacement rates are chosen for X, Y and Z directions based on the allowance for simulation time and error for the upscaled cells with different upscaling ratios.

Step 4: The local numerical triaxial tests with the optimized incremental strain boundaries (step 3) are conducted sequentially in X, Y, and Z direction for all of the upscaled cells. The stress tensors of the upscaled cells are recorded when the loaded cells reach peak stress.

Step 5: The anisotropic effective friction angle and cohesion for the upscaled cells are computed by Equation 7-4 and 7-5 and organized in an ASCII format file.
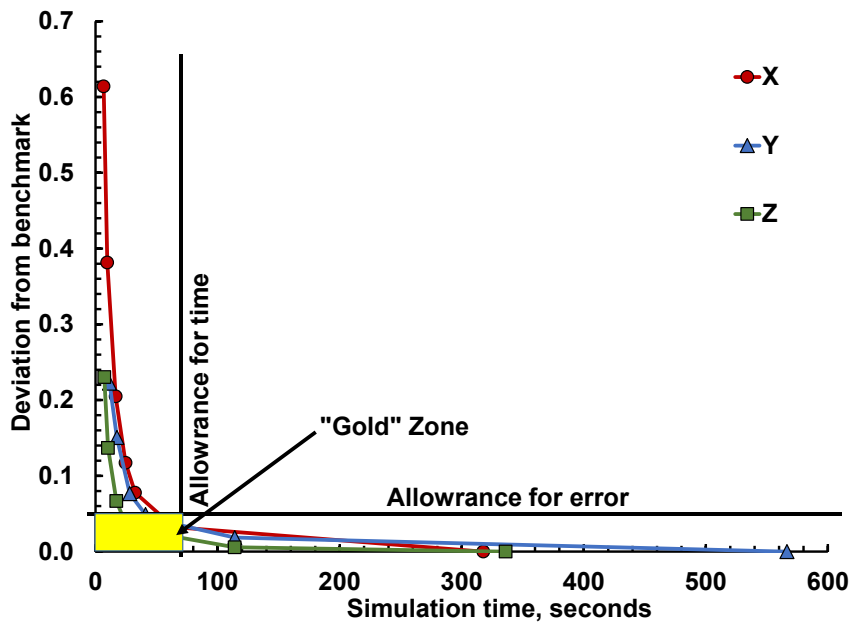
Figure 7-5   Sensitivity analysis of P-upscale with various loading rates in local numerical triaxial tests showing the deviation from the benchmark model. The allowance bars of time and error should be optimized for cases with different upscaling ratio and accuracy requirement.

7.1.4   Anisotropic Failure Criterion for Upscaled Heterogeneous Material

The sub-grid heterogeneity in the upscaled cell leads to anisotropic failure criteria and stress-strain behavior as demonstrated in section 7.1.2 for the IHS model. Following the P-upscale algorithm, anisotropic upscaled plastic properties, e.g. friction angle and cohesion, are obtained from the local triaxial tests at different confining stress. Although inherent anisotropy has been recognized to have a remarkable influence on the shear strength and failure modes as explained in section 3.7, a widely accepted anisotropic failure criterion has yet to be established and applied in most geomechanical simulators (Gao et al. 2010).

In FLAC3D, the ubiquitous-joint model is an anisotropic plasticity constitutive model that includes weak planes of specific orientation embedded in a Mohr-Coulomb solid. The bilinear strain-hardening/softening ubiquitous-joint model allows the representation of material hardening and softening behavior for the matrix and weak plane based on assigned plastic properties as functions of plastic shear and tensile strain. However, the thickness, spacing and stiffness of the weak plane are not considered in the ubiquitous-joint model. Thus, detailed and complicated calibration of material response is required to avoid misleading simulation results due to the over-simplified geometric setting (Sainsbury B. and Sainsbury D. 2017). The calibrated ubiquitous-joint model has shown successful applications in 2D anisotropic open pit slope failure and 3D anisotropic deformation in the underground excavation, which provides an alternative way to utilize the anisotropic upscaled failure criteria than developing a custom-built anisotropic plastic constitutive model in FLAC3D. However, the efficiency of the calibrated ubiquitous-joint model in reservoir-scale upscaling of geological model is yet to be determined in future research.

7.1.5 Integration of Local Numerical Upscaling and Geostatistical Parameterization

To further improve the efficiency of P-upscale, the local numerical test is not necessary to be performed for each upscaled cell. P-upscale is only performed at highly heterogeneous coarse cells, while geostatistical parameterization is used to characterize the equivalent plastic properties. The generalized algorithm of the integration is presented in Figure 7-6. For the SAGD process in the MacKay River oil sand area, horizontal stress changes induced by thermal expansion is confirmed to be the major changes of principal stress. Therefore, the characterized plastic properties can at least be used as an initial estimate for the upscaled cell. In Chapter 3, ϕ and c was found to be close to the corresponding weighted harmonic average (Figure 3-19 and 21). The dilation angle has a linear relationship with V_{sh}, so the weighted arithmetic average is a reasonable initial estimate for ψ.

Using the initial estimate of the upscaled plastic properties, upscaled coupled simulation is then conducted and compared with the fine-scale simulation results. If the results are acceptable, the initial estimate is retained for the upscaled plastic properties; otherwise, the reservoir-scale P-upscale algorithm is performed for the selected upscaled cell under the stress boundaries determined by the global upscaled simulation. From P-upscale, the correlation between the upscaled plastic properties and critical quantification parameters (V_{sh} & range ratio) is generated for the selected upscaled cell. With the calculated V_{sh} and range ratio, the new upscaled plastic properties are obtained from the updated correlation for the other regions. Upscaled coupled simulation is performed again and compared with the fine-scale simulation, which is another cycle of the loop in Figure 7-6. If the results still deviate from the fine-scale simulation, more upscaled cells are selected for P-upscale instead of estimation from correlation. The selection of the upscaled

cell is closely related to the heterogeneity level and its importance in the reservoir and geomechanical simulation.

The loop in Figure 7-6 will be terminated after the user-defined criteria are matched. The criteria can be the error of the cumulative oil production, steam oil ratio, surface heave, volumetric strain or other parameters used to describe the reservoir and geomechanical response in upscaled simulation compared to the fine-scale simulation. After determining the upscaled peak plastic properties, the corresponding strain-softening table needs to be adjusted accordingly.
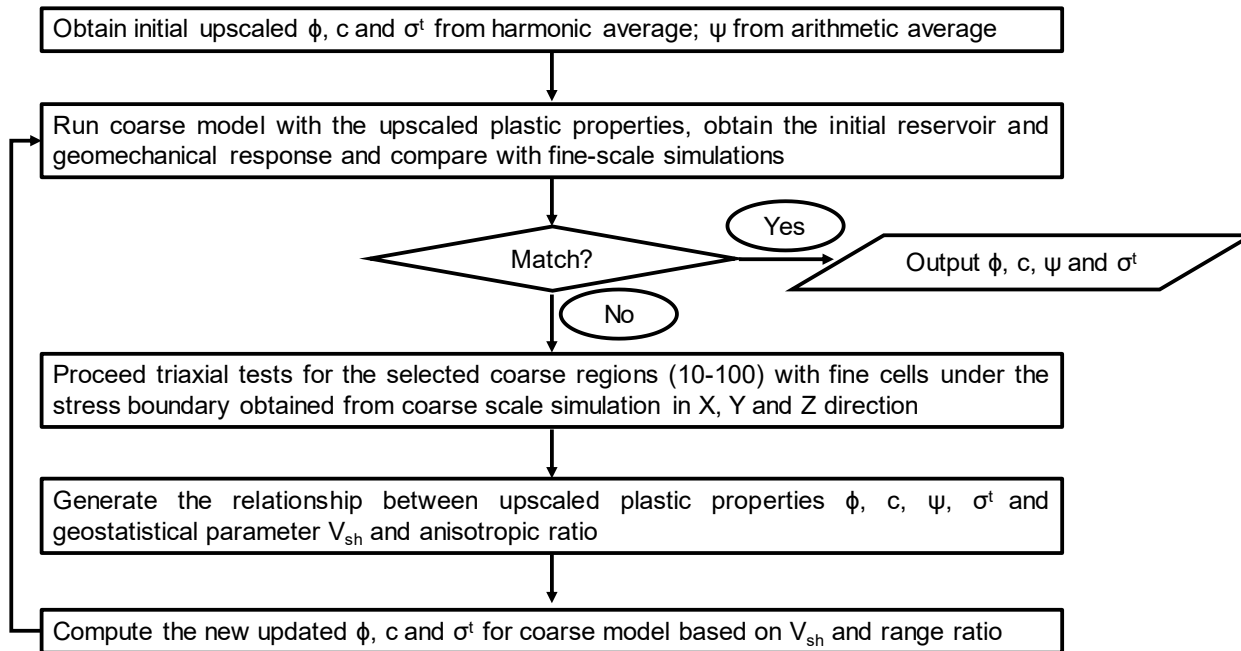
Figure 7-6.   Flow chart for application of P-upscale in the reservoir-scale model.

The schematic in Figure 7-7 helps to understand and highlights the advantage of the integration of E-upscale, P-upscale, flow-based permeability upscaling and geostatistical parameterization in the full-field geological model. The confining stresses in P-upscale are determined by three steps in coarse-scale simulation: 1) initial stress state, 2) the steam chamber reaches the upscaled cell and

3) after the steam chamber passes the upscaled cell. P-upscale is accurate in determining the upscaled plastic properties and consider the anisotropic failure and deformation response caused by sub-grid heterogeneity. However, the computational efficiency of geostatistical characterization is far better than P-upscale as no local numerical geomechanical simulations are required to be run for upscaled cells. The optimization of load rate in local numerical tests and parallel simulation will significantly improve the computational efficiency of P-upscale but the integrated technique can still save substantial simulation time without sacrificing accuracy with current computation power if following the flow chart in Figure 7-6.

Fast: hours for a few million-cell model
Local Elastic & Permeability upscaling (E, v and k)

Fast: minutes for a few million-cells model
Heterogeneity Parameterization for each coarse block (V_{sh} and R_a)

×10-100

Local plastic upscaling

Correlation between Heterogeneity Level and Upscaled Plastic Properties

- Time consuming: Need to load until peak for P-upscale) > E-upscale (Equilibrium);
- Efficiency: 1. Optimized loading rate (less steps until peak); 2. Parallel programs.

Figure 7-7.   Schematic showing the reason that heterogeneity parameterization and local numerical upscaling technique should be integrated into geocelluar models with millions of cells.

7.2   Determination of Optimum Upscaling Ratio

For regions with high permeability contrast, the sub-grid heterogeneity is recommended to be retained for the upscaled cell to fully capture its dominant effect on the flow response (Durlofsky 1991). A homogenized cell can mimic the macroscopic geomechanical response but cannot

reproduce the complex failures modes caused by sub-grid heterogeneity. The effective permeability is strongly related to the failure paths as demonstrated in Chapter 4. Therefore, the upscaling ratio should be selected carefully based on the level of heterogeneity to balance the efficiency and accuracy in terms of both geomechanical response and reservoir performance.

7.2.1   Level of Heterogeneity

The level of heterogeneity for flow and geomechanical properties usually varies in different formations. Taking the Alberta oil sands as an example, a large permeability contrast is expected at the boundary of the Clearwater and McMurray Formations. In the Clearwater Formation, the shale is usually continuous as the caprock. In upper McMurray Formation, massive IHS lead to high contrast in permeability and geomechanical properties. Regardless of the upscaling technique, coarsening the mesh inevitably averages the sub-grid scale heterogeneities. Therefore, high upscaling ratios are only recommended for regions with low heterogeneity to retain the fine-scale heterogeneities in the upscaled model.

The Dykstra-Parsons (1950) coefficient is widely used in the petroleum industry to measure the permeability variability in the reservoir. It is a dimensionless number with the assumption that permeability data are drawn from a log-normal distribution from high to low values:

$$R_{DP}^k = \frac{k_{50} - k_{84.1}}{k_{50}}, \qquad\qquad\qquad \text{Equation 7-6}$$

where k_{50} is the median permeability and $k_{84.1}$ is the permeability at 84.1% probability.

Here, the Dykstra-Parsons coefficient is extended to estimate the level of heterogeneity in the geomechanical properties. The Young's modulus (E) is selected as a representative:

$$R_{DP}^E = \frac{E_{50} - E_{84.1}}{E_{50}}. \qquad\qquad\qquad \text{Equation 7-7}$$

It should be noted that E only represents the stiffness of the reservoir, which controls the elastic deformation response under stress changes. If plastic deformations dominate, the friction angle (φ) should be used instead for cohesionless oil sands:

$$R_{DP}^{\phi} = \frac{\phi_{50} - \phi_{84.1}}{\phi_{50}} \ . \qquad\qquad\qquad \text{Equation 7-8}$$

The level of heterogeneity in the flow and geomechanical properties can be quickly estimated by Equation 7-6, 7-7 and 7-8. R_{DP}^{k}, R_{DP}^{E} and R_{DP}^{ϕ} are all dimensionless numbers from 0 to 1. For the homogeneous region, the extended Dykstra-Parson coefficients are 0. For upscaled cells with low extended Dykstra-Parson coefficients, it is safe to upscale the region into a single coarse block with proposed technique. When they are approaching 1 for the upscaled cell, it is recommended to retain the sub-scale heterogeneities due to high contrast in the flow and geomechanical properties.

Due to the sedimentation process, the variations of lithologies are large in vertical compared to horizontal, which leads to larger contrast in permeability and geomechanical vertically. Therefore, estimation of heterogeneity level is required when combining different layers of high heterogeneous reservoir. The 61 layers of the geological models created for the Pad C of MacKay River oil sand area are upscaled into 20 layers based on the level of heterogeneity as demonstrated in Table 7-2. It can be observed that R_{DP}^{k} is close to 1 when the neighboring layer has significant higher or lower permeability. Therefore, combing the layers which have close to unity R_{DP}^{k} leads to larger errors, and it is recommended to retain the original permeability contrast for these layers.

The extended Dykstra-Parson coefficients for Young's modulus and friction angle are also recommended to be used if the geomechanical properties are highly heterogeneous. Here, they are not used as the lithology heterogeneity is the main cause of geomechanical heterogeneity, which has already been reflected by the significant difference in permeability for sand and shale.

Table 7-2 Level of heterogeneity and upscaling based on R_{DP}^k.

Formation	Original Layer	Upscaled Layer	k_{50} (at the layer)	k_{50} (at the upscaled layer)	Deviation from k_{50}	R_{DP}^k
Till	1	1	2.0	2.0	0.00	0.00
Till	2	1	2.0	2.0	0.00	0.00
Till	3	1	2.0	2.0	0.00	0.00
Till	4	1	2.0	2.0	0.00	0.00
Till	5	1	2.0	2.0	0.00	0.00
Till	6	1	2.0	2.0	0.00	0.00
Till	7	1	2.0	2.0	0.00	0.00
Till	8	1	2.0	2.0	0.00	0.00
Till	9	1	2.0	2.0	0.00	0.00
Till	10	1	2.0	2.0	0.00	0.00
Clearwater	11	2	7.7	7.6	1.14	0.00
Clearwater	12	2	7.7	7.6	1.14	0.00
Clearwater	13	2	7.6	7.6	0.03	0.00
Clearwater	14	2	7.5	7.6	-1.44	0.00
Clearwater	15	2	7.4	7.6	-2.90	0.00
Clearwater	16	2	7.3	7.6	-4.33	0.00
Wabiskaw	17	3	6.3	6.3	0.61	0.00
Wabiskaw	18	3	6.3	6.3	0.02	0.00
Wabiskaw	19	3	6.2	6.3	-0.53	0.00
Wabiskaw	20	3	6.2	6.3	-1.11	0.00
Wabiskaw	21	3	6.2	6.3	-1.70	0.00
Wabiskaw	22	4	2175.3	2175.3	0.00	1.00
Wabiskaw	23	5	2491.9	2491.9	0.00	0.09
Wabiskaw	24	6	2725.0	2725.0	0.00	0.09
Wabiskaw	25	7	6.0	6.0	0.27	0.00
Wabiskaw	26	7	6.0	6.0	-0.33	0.00
McMurray	27	8	2897.8	2951.4	-1.82	1.00
McMurray	28	8	2988.0	2951.4	1.24	0.15
McMurray	29	9	2748.8	2780.2	-1.13	0.10
McMurray	30	9	2824.2	2780.2	1.58	0.11
McMurray	31	10	2451.4	2467.7	-0.66	0.12
McMurray	32	10	2418.9	2467.7	-1.97	0.16
McMurray	33	10	2533.1	2467.7	2.65	0.13
McMurray	34	10	2452.6	2467.7	-0.61	1.00
McMurray	35	11	2700.0	2702.5	-0.09	0.24
McMurray	36	11	2742.3	2702.5	1.47	1.00
McMurray	37	11	2675.5	2702.5	-1.00	0.13
McMurray	38	11	2697.5	2702.5	-0.19	0.14
McMurray	39	12	2379.8	2379.8	0.00	1.00
McMurray	40	13	2495.4	2557.8	-2.44	0.13
McMurray	41	13	2608.9	2557.8	2.00	0.12
McMurray	42	14	2432.4	2432.4	0.00	0.10
McMurray	43	15	2680.7	2696.7	-0.59	0.19
McMurray	44	15	2708.5	2696.7	0.44	0.11
McMurray	45	16	2483.0	2483.0	0.00	0.13
McMurray	46	17	2676.5	2714.8	-1.41	0.11
McMurray	47	17	2745.8	2714.8	1.14	0.09
McMurray	48	17	2725.2	2714.8	0.38	0.14
McMurray	49	18	2510.2	2552.6	-1.66	1.00
McMurray	50	18	2595.2	2552.6	1.67	0.13
McMurray	51	19	2345.5	2345.5	0.00	1.00
Devonian	52	20	50.0	50.0	0.00	0.00
Devonian	53	20	50.0	50.0	0.00	0.00
Devonian	54	20	50.0	50.0	0.00	0.00
Devonian	55	20	50.0	50.0	0.00	0.00
Devonian	56	20	50.0	50.0	0.00	0.00
Devonian	57	20	50.0	50.0	0.00	0.00
Devonian	58	20	50.0	50.0	0.00	0.00
Devonian	59	20	50.0	50.0	0.00	0.00
Devonian	60	20	50.0	50.0	0.00	0.00
Devonian	61	20	50.0	50.0	0.00	0.00

7.2.2 Upscaling Ratios at Different Regions and Orientations

The optimum upscaling ratio is not only determined by the level of heterogeneity but also dependent on the area of interest in the flow and geomechanical model. The overburden, underburden and regions away from the well pairs usually serve as a "jacket zone" to provide more accurate flow and geomechanical boundaries. The upscaling ratio can be set high for these regions especially when they are not highly heterogeneous. For the regions near the well pairs, the upscaling ratio should be minimized unless it is extremely homogeneous as demonstrated in the case study in Section 7.3.

As the level of heterogeneity of the Till, Clearwater and Devonian Formations are 0, it is safe to homogenize the 10 layers of the Till (blue), 6 layers of the Clearwater (teal) and 10 layers of the Devonian Formations (red) into 3 layers vertically as shown in Figure 7-8. The well pairs are located 50 cells (250 m) from the side boundaries. Thus, the left 40 and right 40 cells are upscaled moderately by 2 horizontally.

The variogram model matched for MacKay River oil sand area is:

$$\gamma(h) = 0.514 sph_{\substack{a_v=1.17 \\ a_{hmin}=100 \\ a_{hmax}=298}} + 0.486 sph_{\substack{a_v=13.14 \\ a_{hmin}=2888 \\ a_{hmin}=5127}}, \qquad \text{Equation 7-9}$$

The maximum horizontal size of the upscaled cell should be smaller than the minimum horizontal range to prevent over averaging. The side and top view of the upscaled case 1 are illustrated and compared with the original geological model in Figure 7-8 and 7-9. The horizontal upscaling ratio along the horizontal well pairs in Y-axis is 5; while the cell size in X-axis is kept the same to retain the heterogeneity between the well pairs. The maximum upscaled cell size in the horizontal

direction is 25 m, which is less than a quarter of the minimum horizontal range (101 m). After the customized upscaling ratios, the total cell numbers drop from 2.4 million to 0.24 million cells.
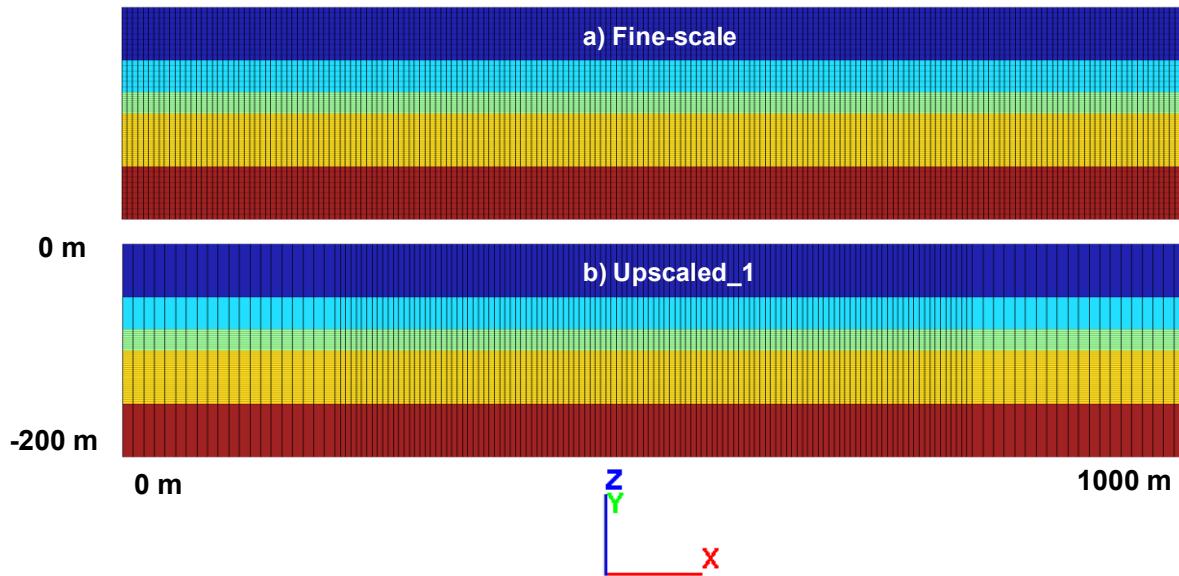
Figure 7-8.   Side view of the (a) fine-scale and (b) upscaled case 1 of the geological model.
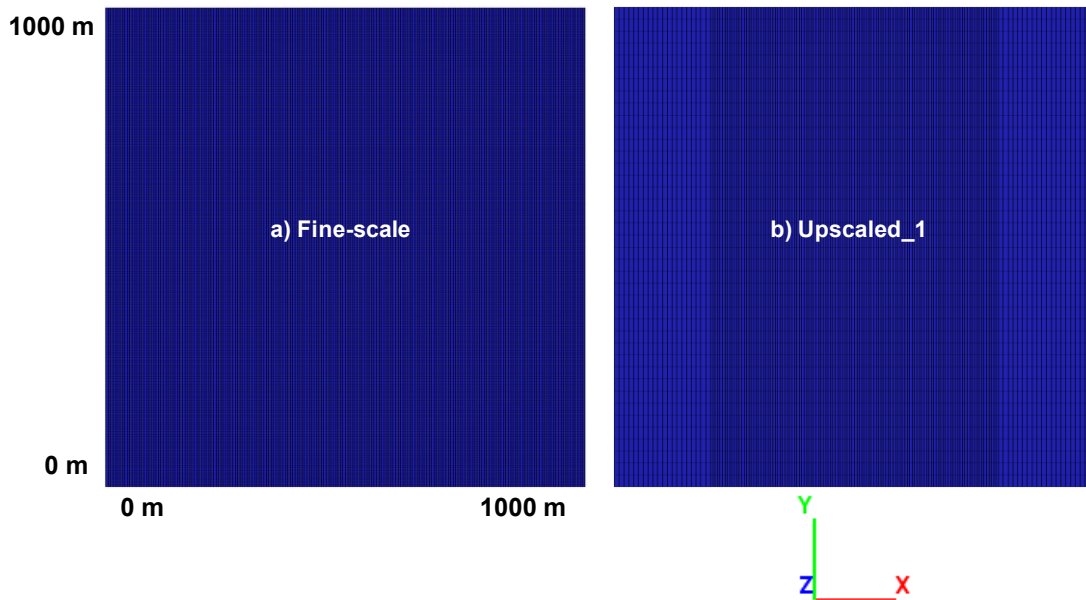
Figure 7-9   Top view of the (a) fine-scale and (b) upscaled case 1 of the geological model.

7.3 Case Studies of Integrated Reservoir-Geomechanics Upscaling Technique in Coupled Simulations of SAGD Processes

The proposed upscaling techniques are applied to generate the corresponding upscaled flow and geomechanical properties for the upscale models. The cumulative oil production, steam chamber shape, volumetric strain and surface heave are compared to demonstrate the effect of proper upscaling ratio and techniques to reduce computational time while retain the accuracy of coupled simulations.

7.3.1 Impact of Upscaling Ratios

To investigate the impact of upscaling ratios in different orientations and formations, six upscaled models are generated (Table 7-3). The geology and coupled simulation results of the fine-scale model are explained in Chapter 5. The initial permeability distributions for the selected three layers are illustrated in Figure 7-10, 7-11 and 7-12 representing the bottom, middle and top of the reservoir, respectively. The bottom and middle layers belong to the Middle and Lower McMurray Formations, which are the major pay zones. The top of the reservoir belongs to the Wabiskaw Formation where shale bedding planes are widely distributed (Figure 7-12).

Table 7-3 Upscaling ratios for the upscaled cases from 1 to 6.

Case	Axis	Till	Clearwater	Wabiskaw	McMurray	Devonian
1	X		1-40: 2; 41-160: 1; 161-200: 2			
	Y		1-200: 5			
	Z	10	6	1	1	10
2	X		1-40: 2; 41-160: 1; 161-200: 2			
	Y		1-200: 10			
	Z	10	6	1	1	10
3	X		1-200: 2			
	Y		1-200: 5			
	Z	10	6	1	1	10
4	X		1-200: 2			
	Y		1-200: 10			
	Z	10	6	1	1	10
5	X		1-40: 2; 41-160: 1; 161-200: 2			
	Y		1-200: 5			
	Z	10	6	2	2	10
6	X		5			
	Y		5			
	Z		1			

Table 7-4 Grid number and simulation time for fine and upscaled cases.

Case	Grid number, 10^3	Simulation time, hour
Fine	2440	318.7
Upscale_1	243.2	20.1
Upscale_2	121.6	9.9
Upscale_3	152.0	14.1
Upscale_4	76.0	5.2
Upscale_5	140.8	9.0
Upscale_6	97.6	5.0
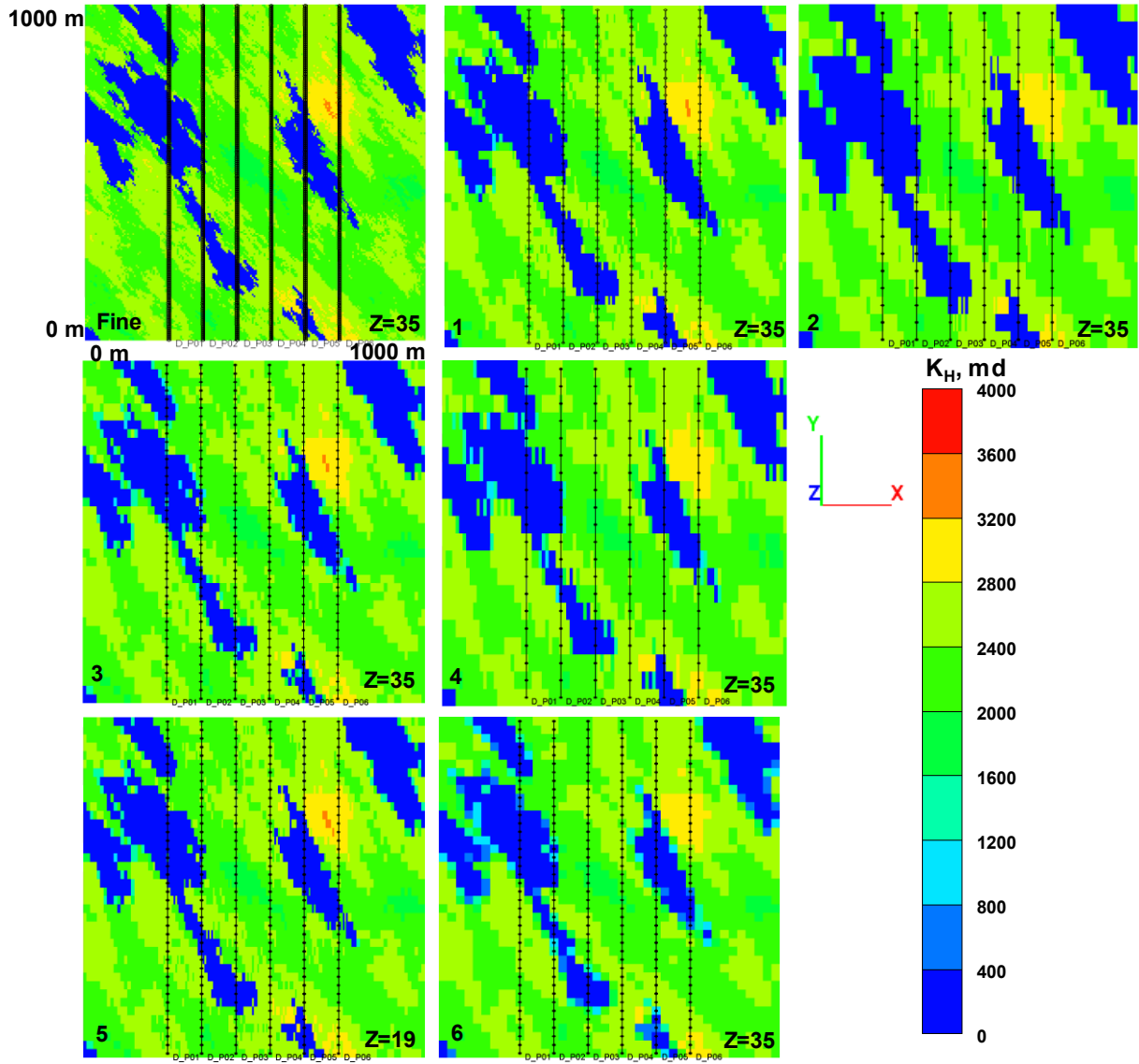
Figure 7-10   Permeability profiles at initial condition for XY cross-section at the bottom of reservoir. Fine representes the fine-scale model. Upscaled case 1, 2, 3, 4, 5 and 6 are labled at the left bottom of each realization. Z=35 represents the 35th layer of the reservoir model which is the bottom of the McMurray Formation . For case 5, Z=19 because the upscaling ratio is 2 in the vertical direction.
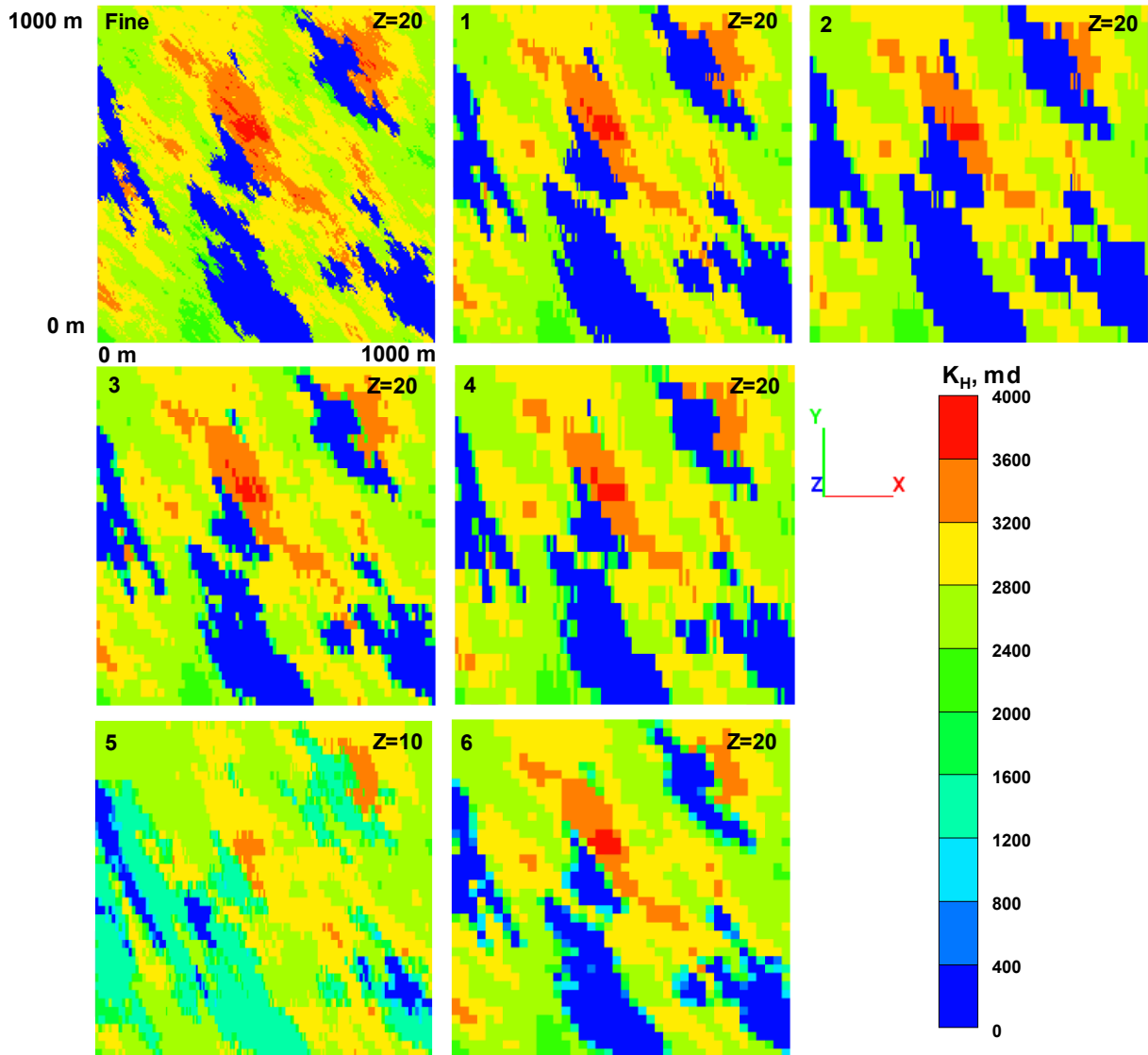
Figure 7-11   Permeability profiles at initial condition for XY cross-section at the middle of the reservoir. Fine representes the fine-scale model. Z=20 represents the 20th layer of the reservoir model which locates in the middle of the McMurray Formation. For case 5, Z=10 because the upscaling ratio is 2 in the vertical direction.

237
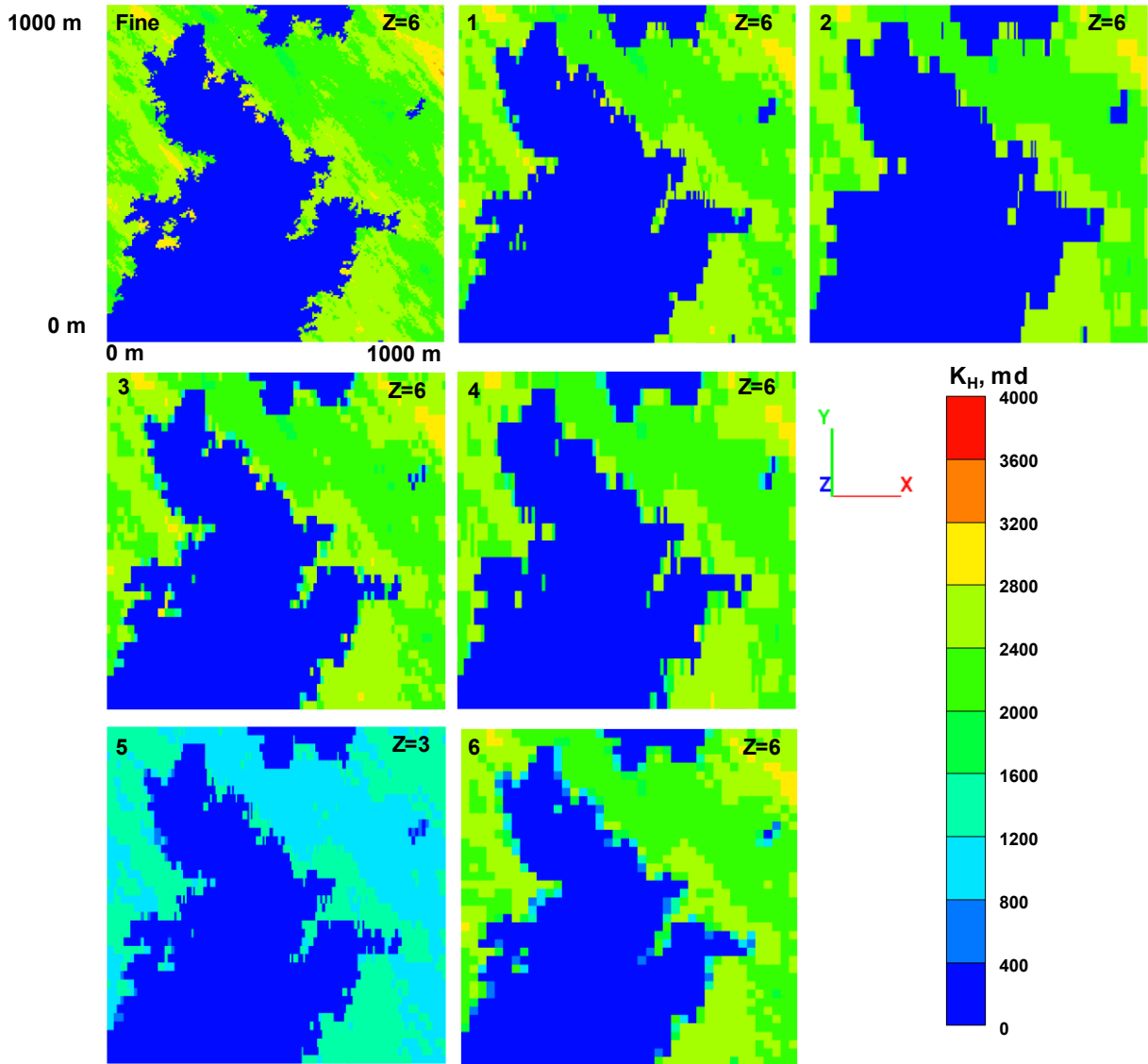
Figure 7-12   Permeability profiles at initial condition for XY cross-section at the top of reservoir. Fine representes the fine-scale model. Z=6 represents the 6th layer of the reservoir model which locates in the middle of the Wabiskaw Formation. For case 5, Z=3 because the upscaling ratio is 2 in the vertical direction.

Case 1 is explained in section 7.2.2 as the upscaled case with suggested upscaling ratios. The upscaled permeability is calculated by the flow-based upscaling technique established in Section 6.3.2. The shale configurations are well reproduced visually except for some smoothing effect in the Y direction (Figure 7-10, 7-11 and 7-12). For case 2, the upscaling ratio in the Y direction is

increased from 5 to 10, which further upscale the permeability along the horizontal wells. For case 3, the grids near the well pairs are not retained but upscaled with a ratio of 2. From case 3 to 4, the upscaling ratio in the Y-axis increases from 5 to 10. Case 5 is the coarser version of case 1 in the vertical direction with an upscaling ratio of 2 for the Wabiskaw and McMurray Formations, e.g. layer 3 of case 5 is the combination of layers 5 and 6 in case 1. Case 6 is the case with a constant upscaling ratio of 5 horizontally. For the Till, Clearwater and McMurray Formations, the resolution of case 6 is retained. The grid number and computational time for the coupled simulations of fine-scale and upscaled cases are provided in Table 7-4.

The cumulative oil production (COP) for the fine-scale and upscaled cases in coupled simulations are illustrated in Figure 7-13. Although the upscaling techniques are the same, the customized upscaling ratios still lead to large COP differences. For case 1 and 2, the COP is almost identical to the fine-scale results, while the simulation time drops from 318.7 hours to 20.1 (case 1) and 9.9 hours (case 2). With the help of the parallel computation and integrated upscaling workflow, the time required for the upscaling process is within 2 hours for the fine-scale model with 2.44 million cells. When increasing the upscaling ratio along the horizontal well from 5 (case 1) to 10 (case 2), the additional error of COP is negligible. For case 3 and 4, a notable decrease of production (5%) is observed when the upscaling ratio is increased to 2 in X-axis (perpendicular to the horizontal wells) at the well pair region. When the upscaling ratio is increased to 5 (case 6), the COP just becomes half of the fine-scale coupled simulation results. The comparisons among the upscaled cases from 1 to 6 indicate that the accuracy of coupled upscaling simulations is more sensitive to upscaling perpendicular to horizontal wells than along them. It is closely related to the steam chamber propagation in the heterogeneous reservoir.
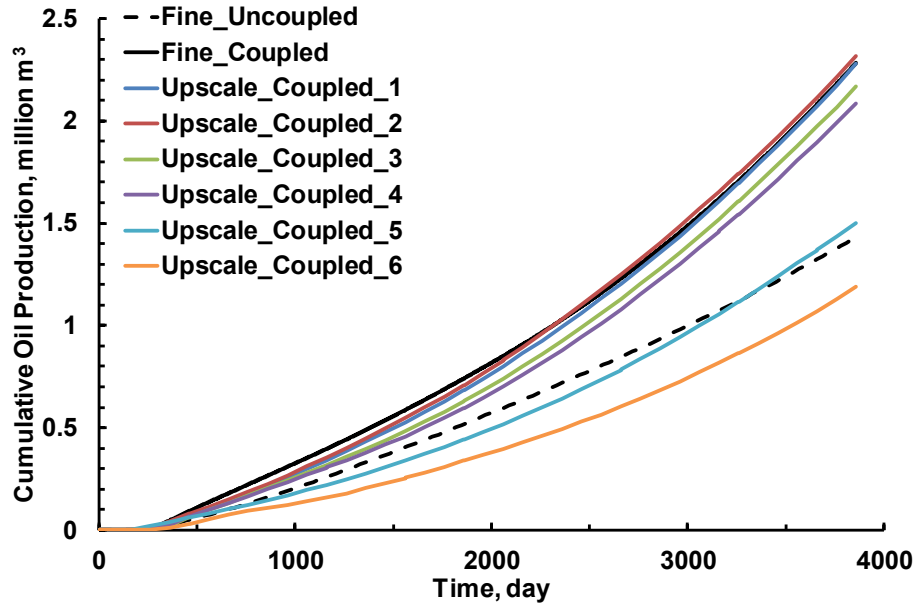
Figure 7-13   Cumulative oil production for the fine-scale and upscaled cases (1, 2, 3, 4, 5 and 6) in Pad C

The temperature profiles at the end of the simulation (day 3860) illustrate the XY cross-sections of steam chambers at the corresponding bottom, middle and top layer of the reservoir in Figure 7-14, 7-15 and 7-16. The steam chambers are more continuous in the Y-axis because of the continuous steam injection along the horizontal wells. Therefore, upscaling along the horizontal well direction will lead to less error caused by over-averaging the heterogeneities in the reservoir. For case 6, the constant upscaling ratio (5 by 5) over-averages the permeability contrast, which leads to erroneous predictions of the development of steam chambers in the heterogeneous reservoir. The simulation time for case 6 is 5 hours which is close to case 4 with a customized upscaling ratio. The improvement of COP and steam chamber shapes are substantial, which demonstrates the importance of choosing the optimum upscaling ratio.
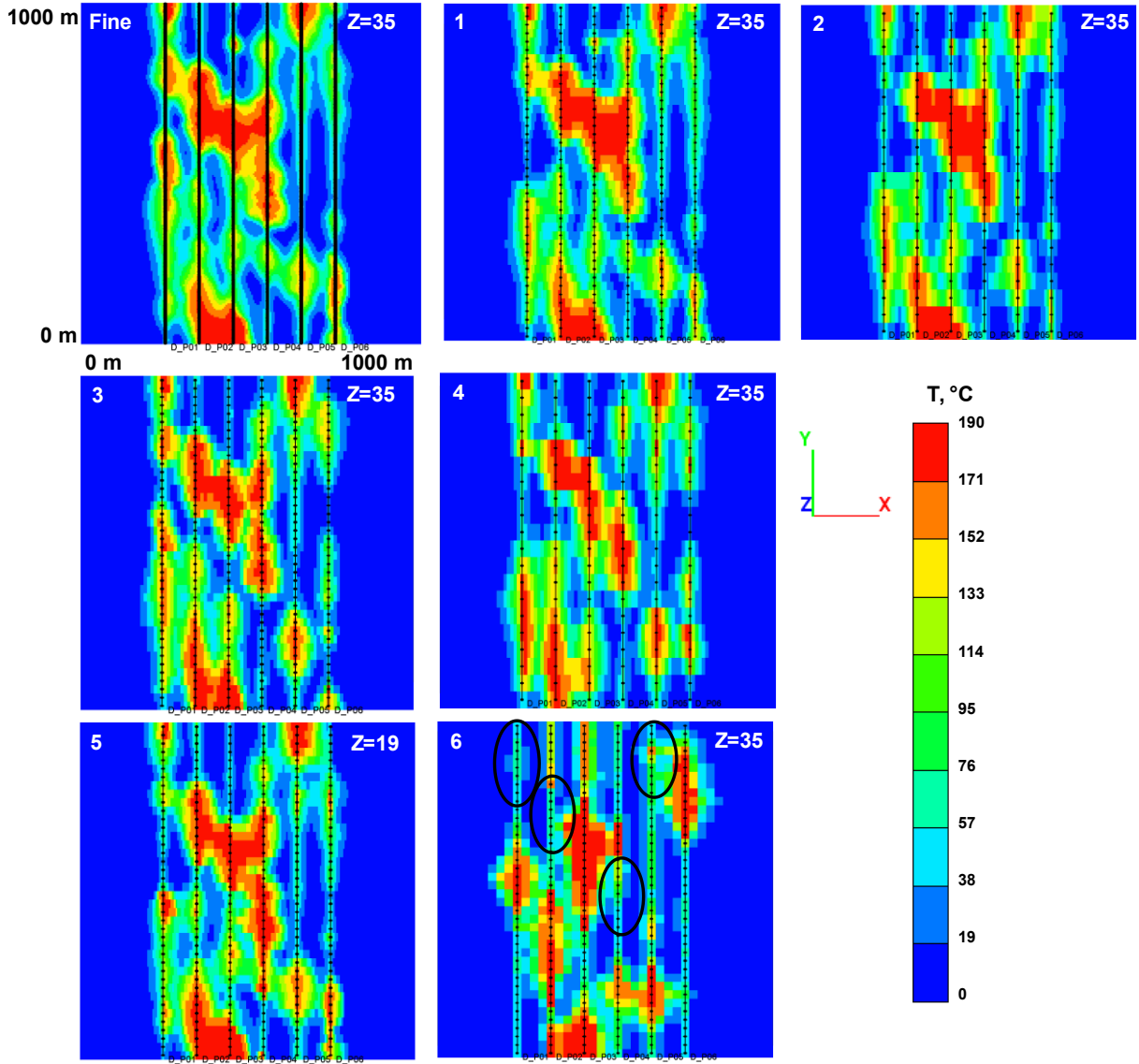
Figure 7-14   Temperature profiles at day 3860 for XY cross-section at the bottom of the McMurray Formation. Fine representes the fine-scale model. Z=35 represents the 35th layer of the reservoir model which locates in the middle of the Wabiskaw Formation. For case 5, Z=19 because the upscaling ratio is 2 in the vertical direction.
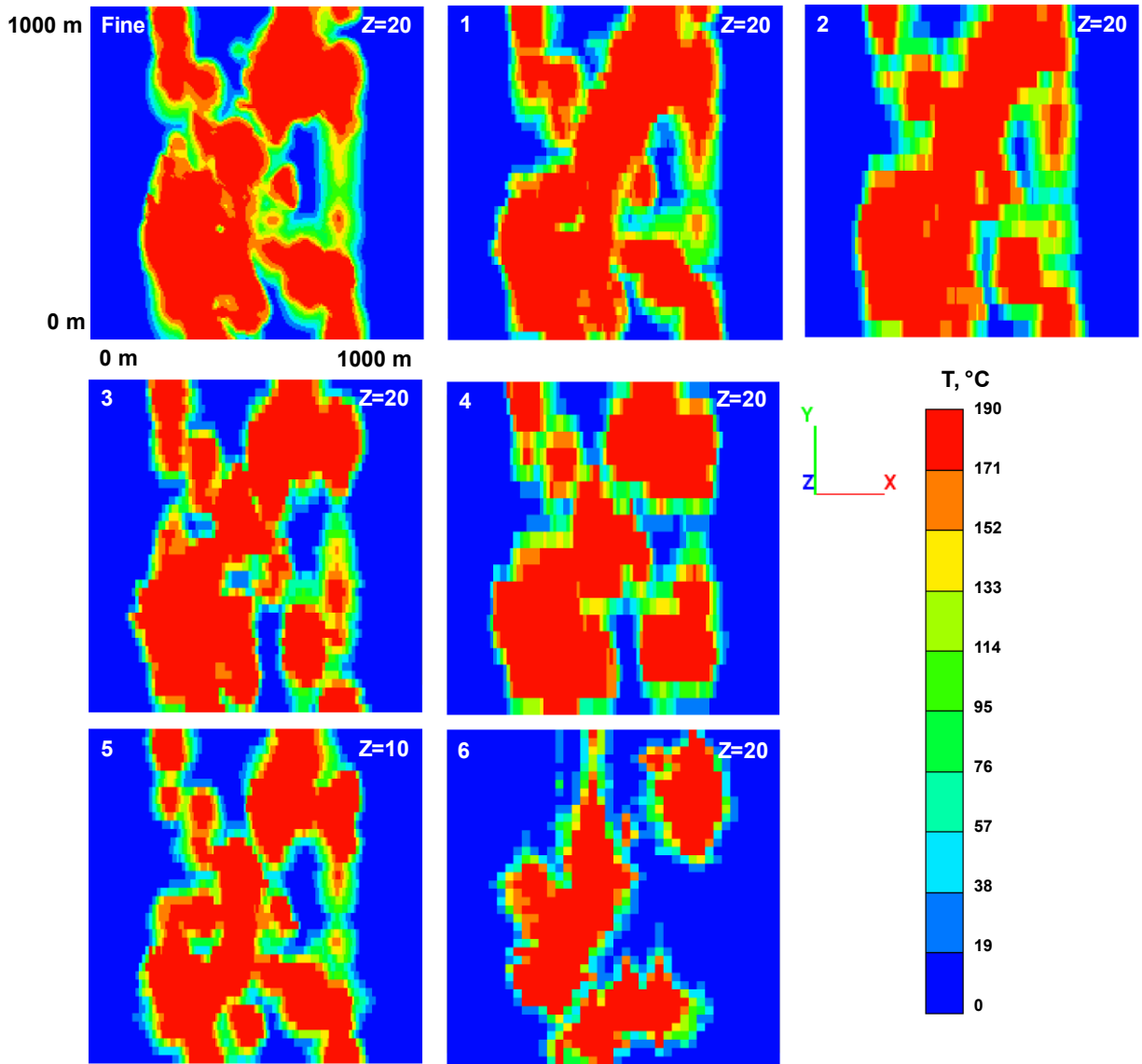
Figure 7-15   Temperature profiles at day 3860 for XY cross-section at the middle of reservoir. Fine representes the fine-scale model. Z=20 represents the 20th layer of the reservoir model which locates in the middle of the Wabiskaw Formation. For case 5, Z=10 because the upscaling ratio is 2 in the vertical direction.
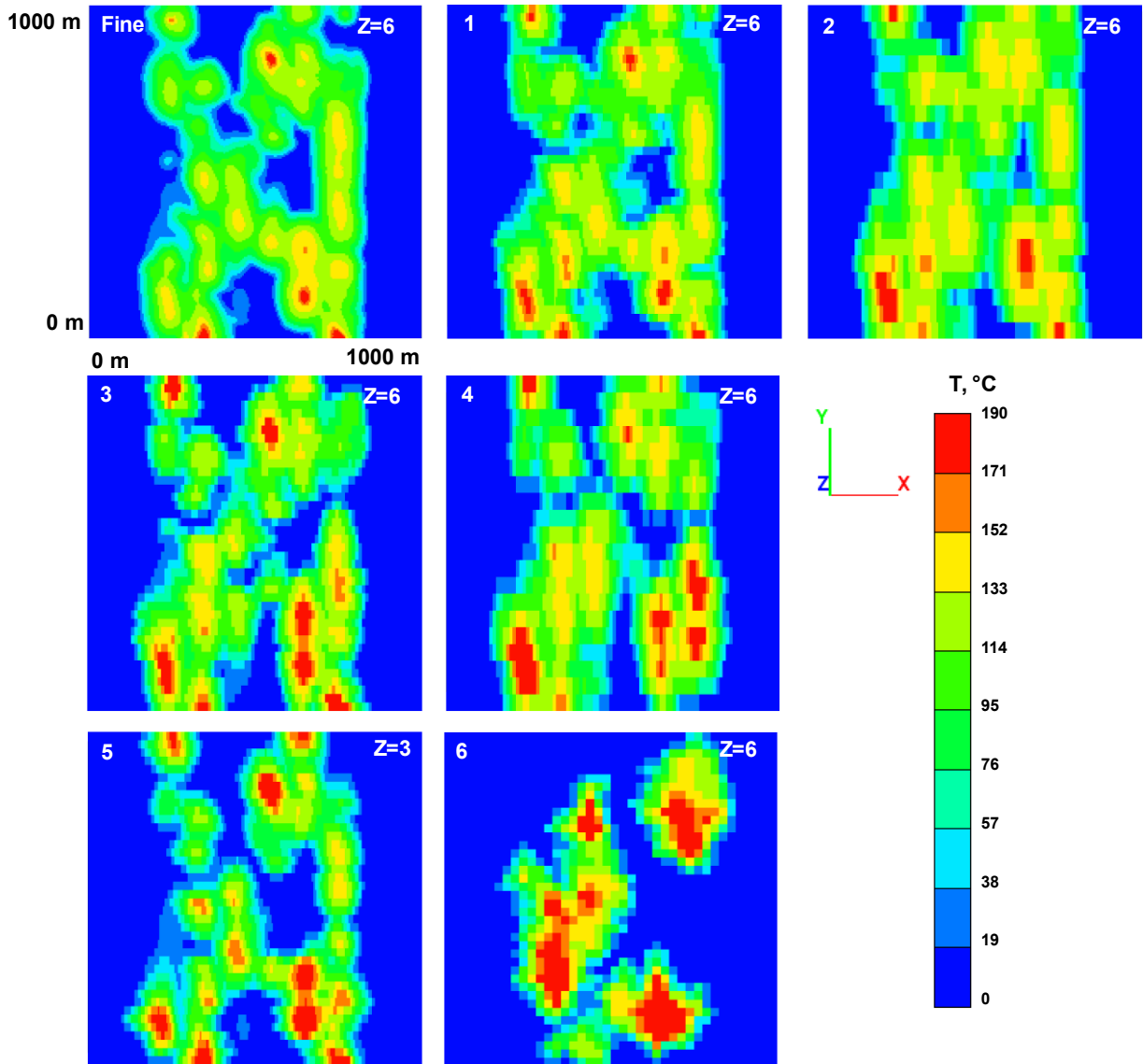
Figure 7-16   Temperature profiles at day 3860 for XY cross-section at the top of reservoir. Fine representes the fine-scale model. Z=6 represents the 6th layer of the reservoir model which locates in the middle of the Wabiskaw Formation. For case 5, Z=3 because the upscaling ratio is 2 in the vertical direction.

For case 5, the thickness of the upscaled cells increases from 2 m to 4 m in the Wabiskaw and

McMurray Formations, leading to the smooth-out of the heterogeneities vertically. In Figure 7-14,

the difference between the fine-scale and case 5 is not pronounced at the bottom of the steam

chamber. When the chamber slowly develops to the top of the reservoir, the over-averaging

vertically leads to the shrinkage of the steam chamber (Figure 7-15 and 7-16). The temperature profiles at the first XZ cross-section (Figure 7-17) confirm the smaller steam chamber at middle and top of the reservoir. Thus, reduced cumulative production of oil is expected for case 5 (Figure 7-13).

For case 3 and 4 with an upscaling ratio of 2 near the well pairs, the steam chambers for well pair 5 and 6 are not consistent with the fine-scale results. Although the flow-based upscaling technique is performed for permeability, the upscaled cases cannot fully capture the flow response of the fine-scale case at highly heterogeneous regions between the well pairs. Therefore, upscaling in the direction perpendicular to the horizontal wells should be treated carefully for highly heterogeneous regions between the well pairs in SAGD process.
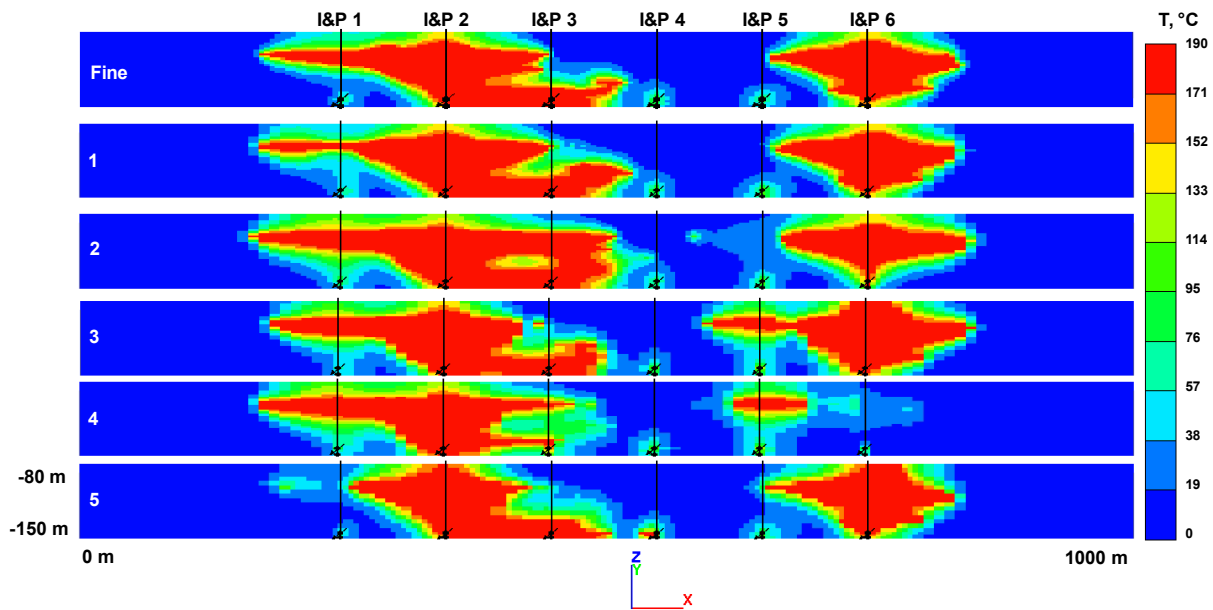
Figure 7-17   Temperature profiles at day 3860 for the first XZ cross-section (Y=1) for the fine-scale and upscaled cases.

The deformations in the reservoir cause significant changes in SAGD performance (Section 5.3.1). The permeability changes are closely correlated to the volumetric strain as shown in Figure 5-21. To analyze the impact of upscaling ratios on geomechanical response and induced permeability changes, the volumetric strain profiles in the first XZ cross-section are plotted in Figure 7-18. The developed steam chambers have significant higher volumetric strain due to the decrease of effective stress and thermal expansion during the SAGD process. The highest volumetric strain is around 1.5% locating at the interface of the Wabiskaw and McMurray Formations. Case 1 well reproduces the volume expansion of the steam chamber for different well pairs; while different degrees of deviations can be observed for the other upscaled cases (Figure 7-18).
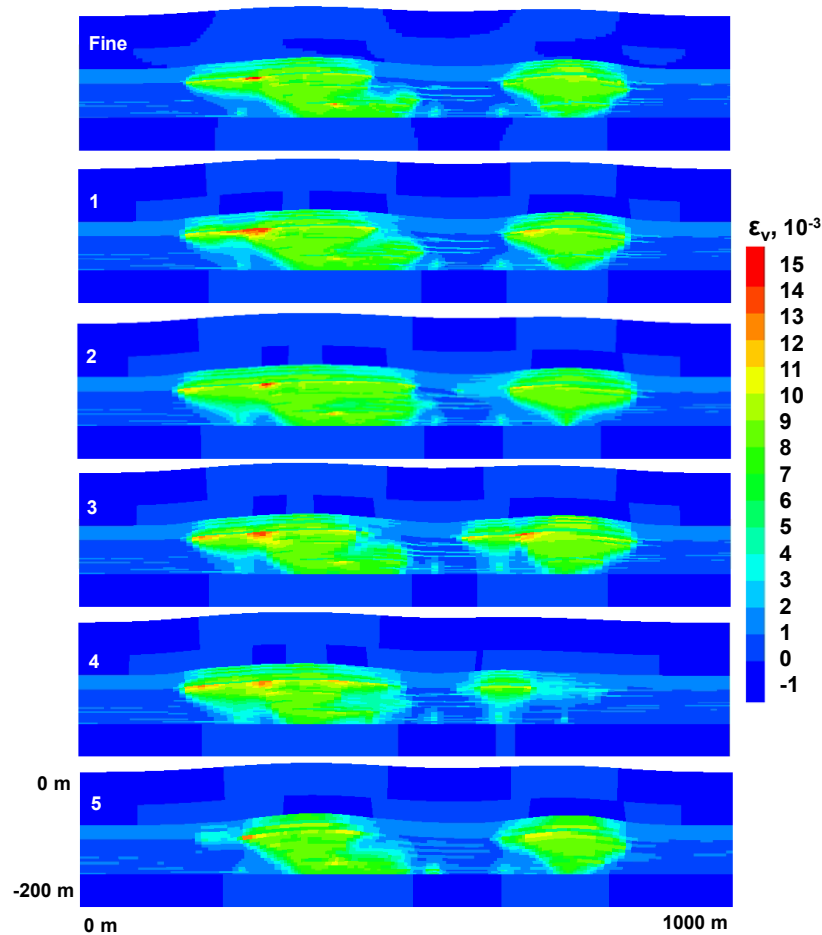
Figure 7-18   Volumetric strain profiles at day 3860 for the first XZ cross-section for fine-scale and upscaled cases.

The ground surface is lifted by associated pore volume expansion in the developed steam chamber. The surface heave is widely used to monitor the SAGD process. The coupled reservoir-geomechanics simulations provide the surface heave profile at the ground surface (Figure 7-19). The magnitude and shape of the surface heave for case 1 are the closest to the fine-scale results. The maximum surface heave is just 1 cm higher which is acceptable compared to the massive save of computational time. For case 2 and 4 with upscaling ratio of 10, the magnitude of surface heave is overestimated. For case 6, the surface heave is lower because the upscaling in vertical leads to underestimations of the volume expansion in the smaller steam chamber (Figure 7-18).
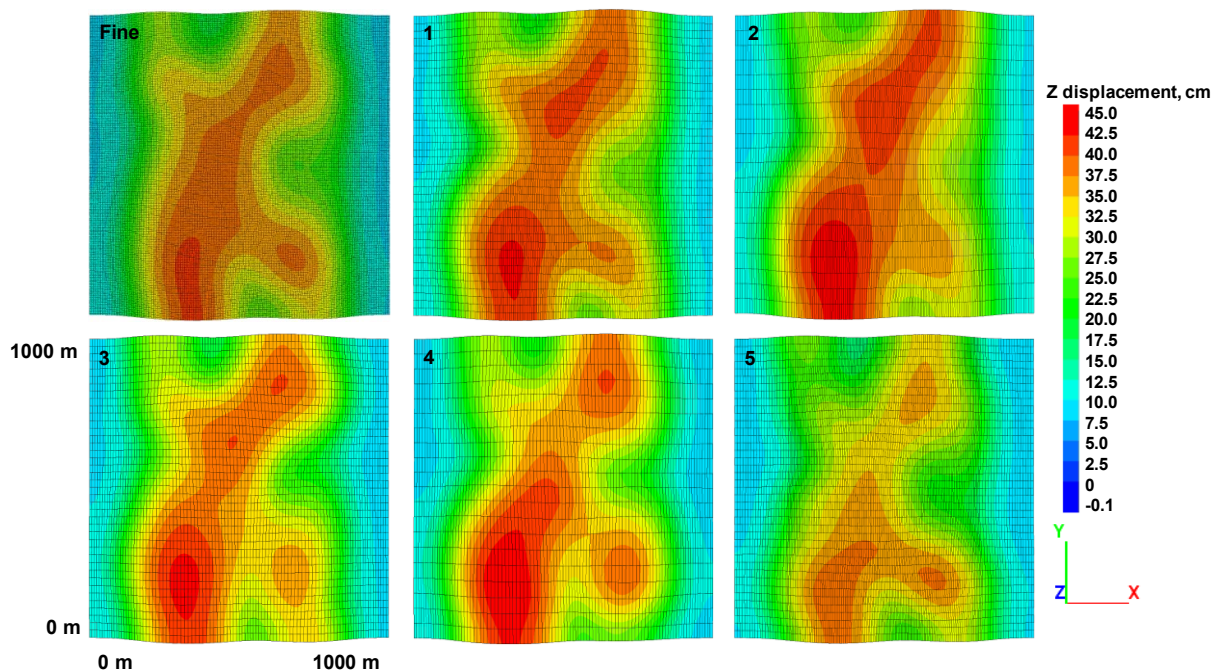
Figure 7-19   Vertical displacements pat day 3860 for XY cross-section at the ground surface in fine scale and upscaled cases.

To summarize, selecting the optimum upscaling ratio in different locations and formations is crucial for the accuracy of the upscaled coupled simulation. For the Alberta oil sands, the McMurray Formation is the major pay zone which needs high resolution to retain the heterogeneity. The Wabiskaw Formations overlays McMurray Formation with widely spread of IHS giving complex interactions of flow and geomechanical response. Due to the sedimentation process, the vertical ranges of variogram are usually in the meter scale, which is close to the thickness of the geological model. The upscaling ratio in vertical direction should be determined carefully by the estimation of the level of heterogeneity to determine the optimum combination of layers with contrast of permeability and geomechanical properties (Table 7-2). In horizontal direction, the upscaling ratios can be a few times higher along the horizontal wells than the direction perpendicular to well pairs in the SAGD process. To provide a realistic flow boundary, the scale of reservoir model is usually larger than the well pairs region. Therefore, the upscaling ratio can be higher for the "jacket zone" away from the horizontal well pairs like case 1. For the geomechanical model, the overburden (Clearwater and Till Formations) and underburden (Devonian Formations) of the reservoir allow coarser mesh unless the caprock integrity is one of the main interests.

7.3.2   Importance of Correct Upscaling Technique

Two additional cases are considered to demonstrate the importance of the correct upscaling techniques. Upscaled case 7 and 8 are compared with case 3 because the same upscaling ratio of 2 is applied in Y-axis (perpendicular to horizontal wells). The upscaling ratios of case 7 and 8 are 2 which is smaller than case 3 with an upscaling ratio of 5. If the same upscaling techniques are used, case 7 and 8 should lead to better accuracy due to finer mesh.

Here, different upscaling techniques are used for case 3, 7 and 8 as listed in Table 7-3. Both case 7 and 8 use geometric averaging for upscaled permeability. For elastic and plastic geomechanical properties, case 7 uses arithmetic average while case 8 applies geometric average.

Table 7-5 Upscaling techniques for case 3, 7 and 8.

Case	Permeability	Elastic Properties	Plastic Properties
Upscale_3	Flow-based	E-upscale	P-upscale
Upscale_7	Geometric average	Arithmetic average	Arithmetic average
Upscale_8	Geometric average	Geometric average	Geometric average

The upscaled permeability fields at the top (Z=6) and middle (Z=20) of the reservoir are illustrated in Figure 7-20 and 7-21. Although the upscaled permeability distribution of case 7 and 8 are in finer mesh than case 3, the COP prediction of case 3 is closer to the fine-scale results (Figure 7-22). The prediction of the steam chamber of case 7 and 8 is not as good as case 3 which applies the integrated reservoir-geomechanics upscaling technique.

Discrepancies can be observed between case 7 and 8 (black circles in Figure 7-20 and 7-21) with the same upscaled permeabilities but different upscaled elastic and plastic properties. The difference of the geomechanical upscaling techniques leads to deviations of deformation prediction for each coupling step, which affects the prediction of the updated permeability from the volumetric strain.
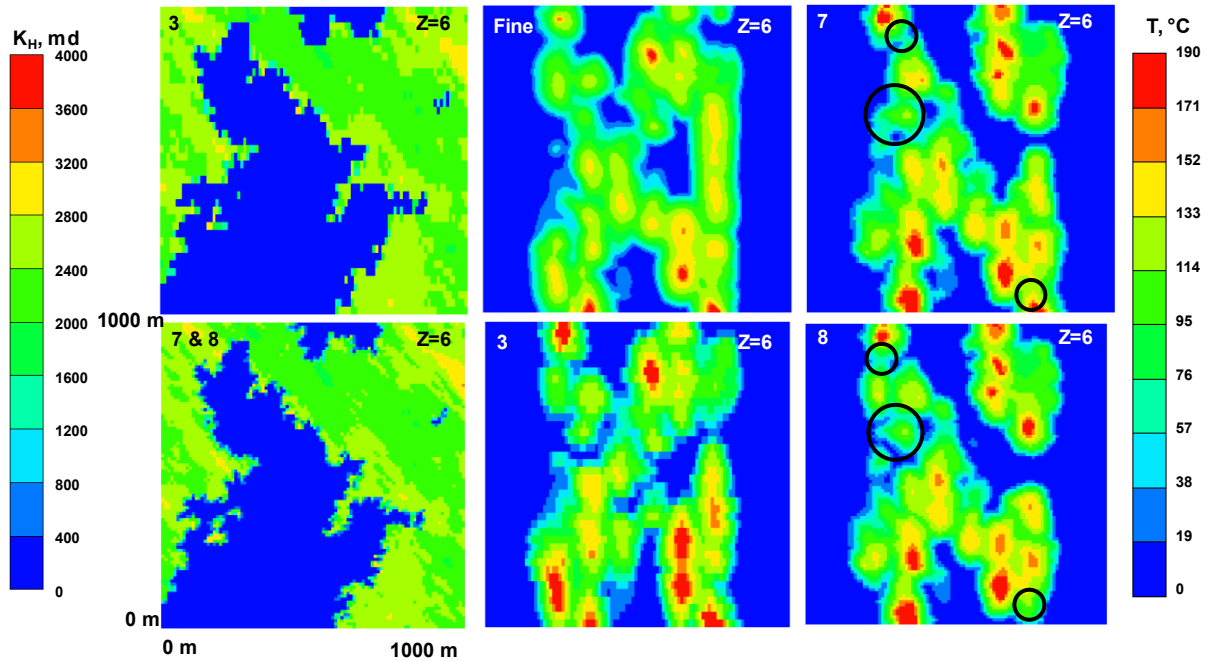
Figure 7-20　Permeability and temperature profiles at day 3860 at the top (Z=6) of reservoir showing the impact of upscaling techniques on steam chamber prediction.
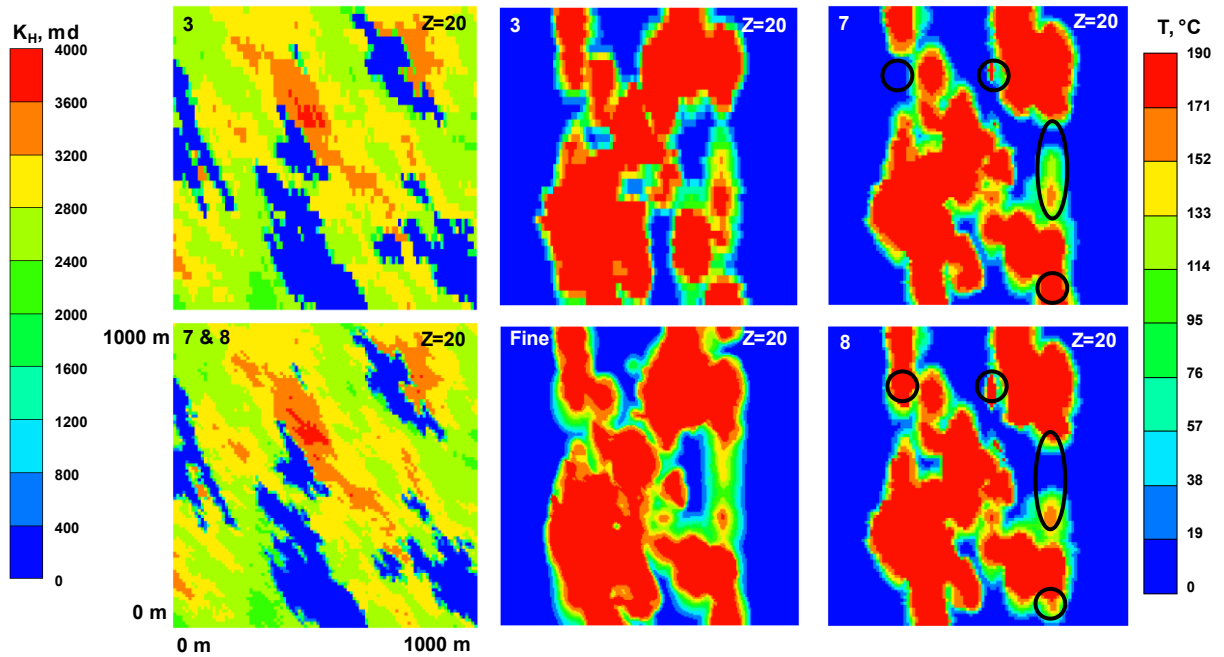
Figure 7-21　Permeability and temperature profiles at day 3860 at the middle (Z=20) of reservoir showing the impact of upscaling techniques on steam chamber prediction.
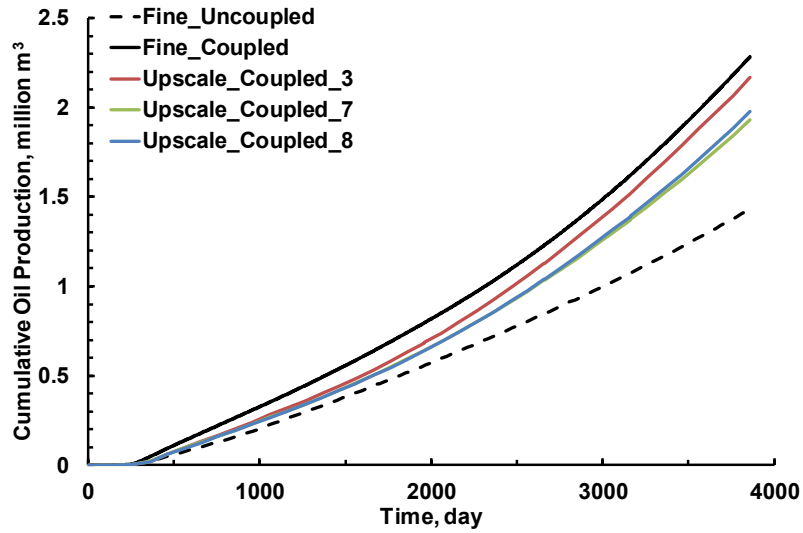
Figure 7-22   Cumulative oil production for the fine-scale and upscaled cases (3, 7 and 8) in Pad C.

Surface heave is used to demonstrate the geomechanical response of case 3, 7 and 8 (Figure 7-23). The magnitude and shape of the surface heave for case 3 is closer to case 7 and 8 even with a larger upscaling ratio, which demonstrates the importance of correct upscaling of the reservoir and geomechanical properties. The error in deformations further affects the predictions of steam chamber development because of the complex interactions of flow and geomechanical response.
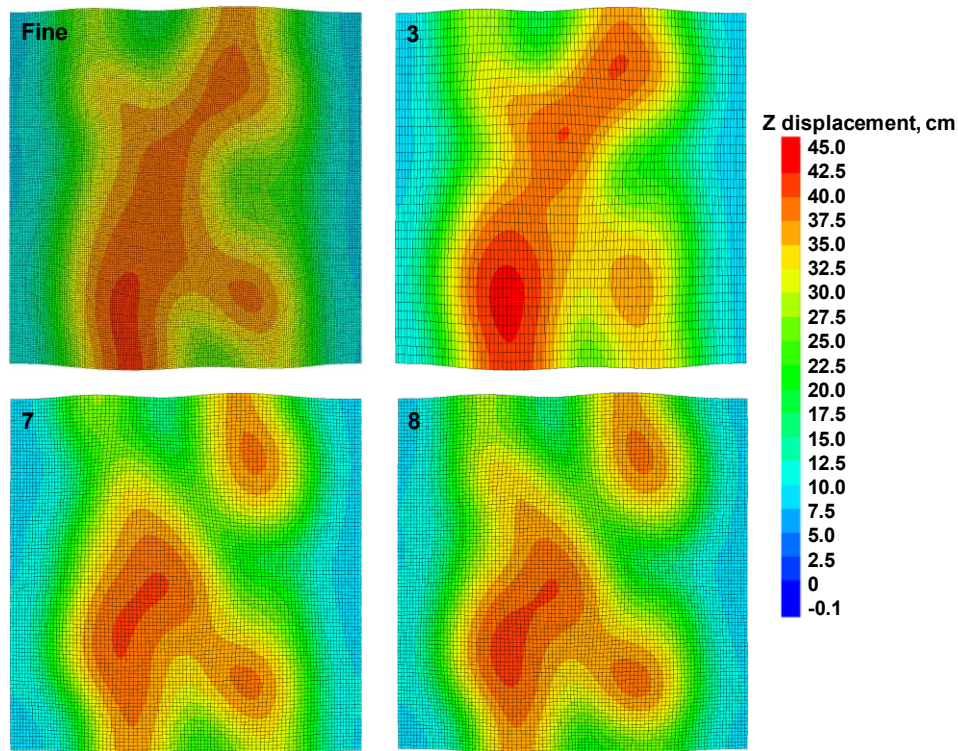
Figure 7-23   Vertical displacement at groud surface (day 3860) for fine and upscaled cases (3, 7 and 8).

7.4   Summary

The P-upscale technique is developed to consider the anisotropic failure criteria caused by sub-grid heterogeneity. With appropriate sensitivity analyses on the loading rate for local numerical triaxial shear tests and integration with geostatistical characterization, P-upscale can be efficiently applied in the full-field geological model following the proposed reservoir-scale algorithm. Together with the flow-based upscaling method for permeability and deformation-based upscaling technique for elastic geomechanical properties in Chapter 6, P-upscale can significantly improve the computation efficiency of the coupled reservoir geomechanical simulation more than 20 times while retaining the accuracy in COP, steam chamber development, volumetric strain and surface heave prediction.

The upscaling ratio in different regions and formations should be selected carefully along different directions to balance efficiency and accuracy. The level of heterogeneity can be assessed to determine the optimum upscaling ratio in the vertical direction to prevent over-averaging. Upscaling along the horizontal wells leads to is more recommended than upscaling between the horizontal wells according to our case studies. During the upscaling process, selecting the most appropriate upscaling ratios and applying the correct upscaling techniques can significantly improve the computational efficiency of the time-consuming coupled reservoir-geomechanics simulation while retaining the accuracy to provide reliable predictions in both reservoir and geomechanical response in the reservoir.

CHAPTER 8:   CONCLUDING REMARKS

8.1   Summary

This research focussed on exploring the effect of geological heterogeneity on the geomechanical response and reservoir performance of the SAGD process. An integrated reservoir-geomechanics upscaling technique is proposed based on the flow and deformation behavior at the sub-grid scale and applied in reservoir-geomechanics simulations of SAGD in the MacKay River oil sand area.

To represent the heterogeneities of oil sands or IHS at the sub-grid scale, spatially correlated sand-shale realizations are generated by SIS with various histograms and variograms. The failure modes and effective geomechanical properties are found to be closely related to the volume fraction, spatial ranges and inclination angles between shale bedding planes and major principal stress direction from numerical compression tests. The development of failure planes is determined by strain localization. Shear failures first initiate in the weaker shale cells and then gradually propagate to the nearby sand cells even before the macroscopic peak. The highly non-linear elasto-plastic behavior before the peak is caused by the local shear failures in the weaker shale bedding planes of IHS. Therefore, the tangent modulus for oil sands can be even lower than the shale stiffness when approaching peak due to local shear failures. The geomechanical properties, such as stiffness, cohesion, peak and residual friction angle, dilation angle, are all found to be well correlated with the V_{sh} in heterogeneous oil sands. For effective plastic properties at the sub-grid scale, the relationship between the strength parameter (friction angle and cohesion) and V_{sh} are close to the weighted harmonic average. The effective dilation angle is close to the weighted arithmetic average for the heterogeneous oil sands as a binary mixture of sand and shale.

The failure modes are found to be well correlated with variogram ranges in the numerical compression tests. Large horizontal ranges lead to continuous shear planes across the entire sample.

Zone failures are dominant in realizations with sparse short shale bedding planes. Shear failures in the thicker shale layers trigger coalesced failures in the surrounding sand cells, resulting in lower stiffness close to peak and shear strength for oil sands with large vertical ranges. The range ratio, defined as the ratio of the dimensionless horizontal and vertical range, is used to parameterize the impact of spatial variability on the strength parameters (friction angle and cohesion) of IHS.

The shale bedding planes are not always horizontal and can have a large dip in IHS zones. Together with the rotation of the major principal stress direction changes during SAGD, the anisotropic impact should be considered carefully on the geomechanical response of IHS. The failure modes migrate from line failure across the entire sample to zone failures along the plane of weakness when the angle between principal stress and shale bedding planes increases from 0 to 30°. The peak strength reduces by 50% reduction due to the change in failure modes. Thus, the in-situ stress changes should be considered when upscaling the plastic properties in highly heterogeneous IHS zone.

The permeability changes of heterogeneous oil sands during deformations are strongly related to the failure modes because it determines the tortuosity of the localized high permeability flow channels. If the impact of heterogeneity on the failure modes is not considered carefully, the widely used global average total or plastic shear strain leads to erroneous estimations of the effective permeability. The scale and shape factors should be fit for permeability updating in coupled reservoir-geomechanics simulation at different coarse grids for the highly heterogeneous zones.

Moving from local (REV) scale to global (reservoir) scale, the coupled reservoir-geomechanics simulation is used to investigate the interactions of flow and geomechanical response during SAGD in Chapter 5. The geological model of the MacKay River oil sand area is generated based on log and core data. The sequentially coupled reservoir-geomechanics simulation is applied to

consider the complex interactions of flow and geomechanical response on the SAGD process. Oil production and steam chamber growth are significantly enhanced by the deformation response on permeability compared to uncoupled simulation. Two pressure fronts and one thermal front are found to be closely related to the in-situ stress changes. The first pressure front instantly sweeps the reservoir during the preheating period. The thermal front is usually associated with a second pressure front when the steam chamber passes. The stress-paths can be divided into four parts depending on the major influential mechanism and relative positions between the steam chamber and the investigated zone. Plastic deformations are not only restricted at the boundaries of different formations and can be observed near the shale bedding planes. The stress-paths for the shale cells are different than adjacent sand cells because of the difference in thermal expansions.

A local numerical upscaling technique, termed "E-upscale", is developed to solve the effective elastic geomechanical properties for upscaled models in Chapter 6. For each coarse grid, the compliance matrix of the stress-strain relationship is solved to obtain the anisotropic Young's modulus, Poisson's ratio and shear modulus. The algorithm is automated in a parallel C++ program to speed up the upscaling process. The E-upscaled elastic properties are solved with 3 compression and 3 shear boundary conditions to reproduce the anisotropic geomechanical behavior caused by the sub-grid scale heterogeneities. The correct upscaled anisotropic Poisson's ratio is found to be important in reproducing the recovery process with complex in-situ stress, e.g. SAGD or hydraulic fracturing. A flow-based upscaling technique for permeability is integrated with the deformation-based E-upscale method for geomechanical properties and successfully applied in full-field reservoir-geomechanics simulation.

The local plastic upscaling technique, "P-upscale", is proposed based on Mohr-Coulomb failure theory in Chapter 7. The anisotropic failure criteria caused by sub-grid heterogeneity can be solved

by P-upscale. Given the appropriate sensitivity analysis, the loading rate can be optimized and save numerous simulation time. To further improve the efficiency, P-upscaled is used simultaneously with the heterogeneity parameterization in full-field geological modeling.

The integration of the E-upscale, P-upscale, flow-based permeability upscaling and heterogeneity parameterization are summed up in Section 7.1.5. For reservoirs with different depositional environments, the relationship between geostatistical parameters and upscaled properties should be re-characterized by local numerical testing for different selected regions. The upscaling ratio in different regions and formations should be selected carefully along different axes to balance efficiency and accuracy. The level of heterogeneity in the reservoir should be assessed to determine the optimum upscaling ratio. The optimum upscaling ratio is dependent on the introduced modified Dykstra-Parson coefficients. Upscaling along the horizontal wells leads to smaller deviations in steam chamber development than upscaling between the horizontal wells in the SAGD process. The proposed integrated numerical upscaling technique can significantly improve the computation efficiency of the coupled reservoir geomechanical model while maintaining the accuracy in COP, steam chamber development, volumetric strain and surface heave.

8.2 Contributions

Coupled reservoir-geomechanics simulation is a powerful tool to investigate the deformation response and induced permeability changes in reservoir performance and caprock integrity. However, applications of coupled simulation on a full-field geological model has not yet become a widely used process in reservoir engineering due to computational efficiency. The current understanding of the impact of heterogeneity on the geomechanical response, especially for elasto-plastic behavior and failure modes, is not mature enough to develop an upscaling technique which considers anisotropic elastic and plastic behavior caused by sub-grid scale heterogeneity.

256

1). The main contribution of this work is the integrated reservoir-geomechanics upscaling technique which provides a workflow to transfer a fine-scale full-field geological model to a computational efficient heterogeneous reservoir-geomechanics model. The proposed integrated reservoir-geomechanics upscaling technique can significantly reduce the computational effort of coupled simulation while retaining the anisotropic deformation and flow response for the upscaled block originally consisted of fine grids. The integrated upscaling workflow has been successfully applied in field-scale coupled reservoir-geomechanics SAGD simulation and demonstrated nearly 20 times improvement of computational efficiency.

2). The numerical investigation of the impact of heterogeneity on the failure modes, macroscopic deformation response and induced permeability changes of heterogeneous oil sands mixed with shale bedding planes at the REV scale is another contribution of this work. It provides a systematic numerical study on the heterogeneity consideration and parameterization of heterogeneous oil sands and IHS in terms of deformation and failure response. At the reservoir scale, the sequentially coupled reservoir-geomechanics simulation highlights the geomechanical response and production performance to be matched in the upscaling process.

8.3   Limitations

In our proposed upscaling technique, E-upscale has been modified to consider the impact of anisotropy caused by the sub-grid scale heterogeneity in terms of elastic behavior, and P-upscale is also able to provide the anisotropic upscaled friction angle, cohesion and dilation angle for a highly heterogeneous upscale block. However, the widely used strain-softening model cannot incorporate anisotropic failure criteria. The bilinear strain-softening ubiquitous-joint model might be a good candidate for anisotropic upscaled geomechanical properties; however, it is not possible to include all anisotropic features in the current version of the coupling platform and normal

coupling methods with the isotropic assumption for geomechanical response. Therefore, a major principal stress direction needs to be assumed, e.g. horizontal stress in the SAGD process, to obtain the most probable isotropic upscaled elastic and plastic properties to apply the proposed method.

Another limitation comes from the application of the Mohr-Coulomb failure theory in obtaining the upscaled friction angle and cohesion. If elasto-plastic behavior and strain-softening behavior leads to a nonlinear failure envelope, the linear Mohr-Coulomb failure envelope may not be the best choice. A nonlinear M-C failure criterion may be a good choice, but this will increase CPU time in the upscaling process.

8.4   Future Work

The workflow for the integrated reservoir-geomechanics simulation has been developed and applied in the full-field reservoir-geomechanics model. There are still a number of details that could be further researched to improve the accuracy, applicability and efficiency of the upscaling technique:

1). A new anisotropic constitutive model that incorporates anisotropic plastic behavior is recommended to realize the full potential of applying upscaled anisotropic elastic and plastic properties in coupled simulation.

2). A binary sand-shale sequence realization is used to represent the heterogeneous oil sands and IHS in the heterogeneity parameterization. Although sand and shale bedding planes are the major lithologies in oil sands, it would be interesting to introduce a transition facies, e.g. shaly sand (IHS), to see its influence on the interactions of flow and geomechanical response.

3)The full-field reservoir-geomechanics model tested only contains sand and shale facies. The interactions of flow and geomechanical responses are interesting in a more complex model with

electrofacies representing different clusters of log interpretations. The stress-paths for the intermediate facies between sand and shale and its impact on coupled simulation results would be impactful for reservoir with massive IHS.

4) The equation widely used for absolute permeability changes with deformation is generated with limited experimental results on potentially disturbed cores or outcrops. The structure and heterogeneity inside of the cores are not available to generate numerical models mimicking the pore structure and facies distribution. 3D printed samples with sensors inside and CT scanning technology could be used to reproduce these experiments to further propose a more reliable permeability updating function for coupled reservoir-geomechanics simulation which can be applied in other depositional environments. It is known that deformation and failures also cause changes in relative permeability according to Oldakowski (1994). The investigations of relative permeability change due to deformation response is recommended for future research.

5). Zheng et al. (2018) developed an AI-based workflow for estimating shale barrier configurations from SAGD production histories. Although the workflow has not been fully extended to 3D, it provides insights on transferring the complex geology to simplified but efficient clusters of shale barriers for production predictions. It would be interesting to introduce AI workflow to calibrate the relationship between the deformation response and geostatistical properties for different reservoirs.

REFERENCE

Aarnes, J. 2004. On the Use of a Mixed Multiscale Finite Element Method for Greater Flexibility and Increased Speed or Improved Accuracy in Reservoir Simulation. *Multiscale Model Simulation* 2(3): 421–439.

Agar J.G. 1984. Geotechnical Behavior of oil sands at elevated temperatures and pressures. Ph.D. dissertation, Department of Civil Engineering, University of Alberta, Edmonton, Canada.

Agar, J.G., Morgenstern N.R., and Scott J.D. 1986. Shear Strength and Stress-Strain Behavior of Athabasca Oil Sand at Elevated Temperatures and Pressures. *Canadian Geotechnical Journal* 24: 1–10.

Ainsworth R.B., Stephenson P.M., Johnson D.A. and Seggie R.J. 2000. Predicting Connected Hydrocarbon Volume Uncertainty Ranges: From Static Fault Model to Dynamic Simulator. Paper SPE 64429 presented at the *SPE Asia Pacific Oil and Gas Conference and Exhibition* held in Brisbane, Australia, 16-18 October 2000.

Alberta Energy Regulator 2014. Geological Characterization of the Lower Clearwater Shale in the Athabasca Oil Sands Area, Townships 87-99, Ranges 1-13, West of the Fourth Meridian. *AER/AGS Open File Report* 2014-04.

Alberta Energy Regulator 2016. Reservoir Containment Application Requirements for Steam-Assisted Gravity Drainage Projects in the Shallow Athabasca Oil Sands Area. *AER Directive* 086.

Alberta Energy Regulator 2017. Suncor MacKay River Project 2017 AER Performance Presentation. Reporting Period: September 1, 2016 to August 31, 2017.

Al-Bulushi, N., King P., Blunt M. and Kraaijveld M. 2009. Development of Artificial Neural Network Models for Predicting Water Saturation and Fluid Distribution. *Journal of Petroleum Science and Engineering* 68: 197–208.

Amirian, E., Leung, J. Y., Zanon, S., and Dzurman, P. 2015. Integrated cluster analysis and artificial neural network modeling for steam-assisted gravity drainage performance prediction in heterogeneous reservoirs. *Expert Systems with Applications* 42(2): 723-740.

Azad, A. and Chalaturnyk R. 2011. Numerical Study of SAGD: Geomechanical-Flow Coupling for Athabasca Oil Sands Reservoirs. *Proceedings of the ARMA 45th US Rock Mechanics/Geomechanics Symposium*, 1-14.

Azad, A. 2012. Rapid SAGD Simulation Considering Geomechanics for Closed Loop Reservoir Optimization. Ph.D. dissertation, Department of Civil Engineering, University of Alberta, Edmonton, Canada.

Azad, A., Chalaturnyk R. and Movaghati, S. 2015. Real-Time Reservoir Model Updating in Thermal Recovery: Application of Analytical Proxies and Kalman Filtering. *Journal of Petroleum Science and Engineering* 127: 196–211.

Backus, G. 1962. Long-Wave Elastic Anisotropy Produced by Horizontal Layering. *Journal of Geophysical Research* 67(11): 4427-4440.

Barker, J. and Fayers, F. 1994. Transport Coefficients for Compositional Simulation with Coarse Grids in Heterogeneous Media. *SPE Advanced Technology Series* 2(2): 103-112.

Bartetzko, A., Wessling S., Tesch P., Lautenschläger U., Andonof L., and Broadhead D. 2012. Uncertainty Quantification of Real-Time Pore Pressure Models Caused by Normal Compaction Trendline Setting. Paper presented at the *2012 IADC/SPE Drilling Conference and Exhibition* held in San Diego, California, USA, 6-8 March 2012.

Basu A., Mishra D. and Roychowdhury K. 2013. Rock Failure Modes under Compression, Brazilian and Point Load Tests. *Bulletin of Engineering Geology and the Environment* 72: 457-475.

Bellman, L., Knowles, A., and Pak, R. 2012. McKay Oil Sands 2D Seismic Inversion Case Study. *CSEG RECORDER* 37(3): 32-41.

Berbenni, S., and Capolungo L. 2015. A Mori-Tanaka Homogenization Scheme for Non-Linear Elasto-Viscoplastic Heterogeneous Materials Based on Translated Fields: An Affine Extension. *Comptes Rendus Mecanique* 343: 95-106.

Berryman J. 2011. Mechanics of layered anisotropic poroelastic media with applications to effective stress for fluid permeability. *International Journal of Engineering Science* 49: 122-139.

Birrell G., and Putnam P. 2000. A study of the influence of reservoir architecture on SAGD steam chamber development at the Underground Test Facility, northeastern Alberta, Canada, using a graphical analysis of temperature profiles. Paper presented at the *Canadian International Petroleum Conference*, Calgary, AB, Canada 4-8 June.

Birrell, G. 2001. Heat Transfer Ahead of a SAGD Steam Chamber: A Study of Thermocouple Data from Phase B of the Underground Test Facility (Dover Project). Paper 2001-088 presented at the *Canadian International Petroleum Conference*, Calgary, AB, Canada, 12–14 June.

Budiansky, B. 1965. On the Elastic Moduli of Some Heterogeneous Materials. *Journal of the Mechanic and Physics of Solids* 13(4): 223-227.

Butler, R., McNab, G., and Lo, H. 1981. Theoretical Studies on the Gravity Drainage of Heavy Oil During Steam Heating. *The Canadian Journal of Chemical Engineering* 59: 455-460.

Butler, R. 1985. New Approach to the Modeling of Steam-Assisted Gravity Drainage. *Journal of Canadian Petroleum Technology* 24(3): 42–51.

Butler, R. 1997. Thermal Recovery of Oil and Bitumen. Calgary, Alberta, Canada.

Canada's Oil & Nature Gas Producers 2018. What Are the Oil Sands? Retrieved from https://www.canadasoilsands.ca/en/what-are-the-oil-sands/recovering-the-oil.

Canadian Geographic 2008. Scar sands: Alberta's oil-sands. Retrieved from https://www.canadiangeographic.ca/article/scar-sands-albertas-oil-sands.

Carman, P.C. 1939. Permeability of saturated sands, soils and clays. *The Journal of Agricultural Science* 29(2): 262-273.

Chalaturnyk, R. 1996. Geomechanics of the Steam-Assisted Gravity Drainage Process in Heavy Oil Reservoirs. Ph.D. dissertation, Department of Civil Engineering, University of Alberta, Edmonton, Canada.

Chalaturnyk, R. and Li P. 2004. When Is It Important to Consider Geomechanics in SAGD Operations? *Journal of Canadian Petroleum Technology* 43(4): 53-61.

Chalon F., Mainguy M., Longuemare P. and Lemonnier P. 2004. Upscaling of Elastic Properties for Large Scale Geomechanical Simulations. *International Journal for Numerical and Analytical Methods in Geomechanics* 28: 1105-1119.

Christie, M. and Clifford 1998. Fast Procedure for Upscaling Compositional Simulation. *SPE Journal* 3(3): 272–278.

Collins P., 2007. Geomechanical Effects on the SAGD Process. *SPE Reservoir Evaluation & Engineering* 10(4): 1-3.

Cokar M., Kallos M. and Gates I. 2013. A New Thermogeomechanical Theory for Gravity Drainage in Steam-Assisted Gravity Drainage. *SPE Journal* 18(4): 736-742.

Correia, G. and Schiozer D. 2016. Reservoir Characterization Using Electrofacies Analysis in the Sandstone Reservoir of the Norne Field (Offshore Norway). *Petroleum Geoscience* 22: 165–176.

Couples G., Lewis H., Pickup G., Ma J., Rouainia M., Bicanic N. and Pearce C.J. 2003. Upscaling Fluid-Flow and Geomechanical Properties in Coupled Matrix+Fractures+Fluids Systems. Paper SPE 79696 presented at the *SPE Reservoir Simulation Symposium* held in Houston, Texas, U.S.A, 3-5 February 2003.

Deisman, N., Khajeh, M.M., and Chalaturnyk R.J. 2013. Using Geological Strength Index (GSI) to Model Uncertainty in Rock Mass Properties of Coal for CBM/ECBM Reservoir Geomechanics. *International Journal of Coal Geology* 112: 76–86.

Deisman, N., Juncal A and Chalaturnyk R. 2018. Sequentially coupled reservoir-geomechanics simulation platform in Reservoir Geomechanical Research Group (RGRG) supervised by in University of Alberta.

Desrues, J. and Viggiani, G. 2004, Strain localization in sand: an overview of the experimental results obtained in Grenoble using Stereophotogrammetry. *International Journal for Numerical and Analytical Methods in Geomechanics* 28: 279-321.

Desrumaux, F., Meraghni, F. and Benzeggagh M. 2001. Generalized Mori-Tanaka Scheme to Model Anisotropic Damage Using Numerical Eshelby Tensor. *Journal of Composite Materials* 35(7): 603–624.

Deutsch, C. 1989. Calculating Effective Absolute Permeability in Sandstone/Shale Sequences. *SPE Formation Evaluation* 4(3): 343–348.

Deutsch, C.V. and Journel, A.G., 1998. GSLIB: Geostatistical Software Library and User's Guide, Second edition. New York, Oxford.

Deutsch, C.V. 2006. A Sequential Indicator Simulation Program for Categorical Variables with Point and Block Data: BlockSIS. *Computers and Geosciences* 32 (10): 1669–1681.

Deutsch C. 2010. Estimation of Vertical Permeability in the McMurray Formation. *Journal of Canadian Petroleum Technology* 49(12): 10-18.

Du, J. and Wong, R. 2009. Coupled Geomechanics Reservoir Simulation of UTF Phase A Project Using a Full Permeability Tensor. *Journal of Canadian Petroleum Technology* 48(7): 66-73.

Duncan, J. and Chang, C. 1970. Nonlinear Analysis of Stress and Strains in Soils. *Journal of Soil Mechanics and Foundation Division* 96(5): 1629-1653.

Durlofsky, L. 1991. Numerical Calculation of Equivalent Grid Block Permeability Tensors for Heterogeneous Porous Media. *Water Resources Research* 27(5): 699-708.

Dusseault, M.B. 1977. The geotechnical characteristics of the Athabasca oil sands. Ph.D. Dissertation, Department of Civil Engineering, University of Alberta, Edmonton, Canada.

Dusseault, M.B. and Morgenstern, N.R. 1978. Shear Strength of Athabasca Oil Sands. *Canadian Geotechnical Journal* 15(2): 216-218.

Dusseault M.B. and Morgenstern N.R. 1979. Locked Sands. *Quarterly Journal of Engineering Geology and Hydrogeology* 12(2): 117-131.

Dykstra, H and Parsons, R.L. 1950. The Prediction of Oil Recovery by Water Flood. Secondary Recovery of Oil in the United States, second edition, API, Dallas (1950): 74-160.

Elkateb, T., Chalaturnyk, R., and Robertson, P. 2003. An overview of soil heterogeneity: quantification and implications on geotechnical field problems. *Canadian Geotechnical Journal*: 40(1), 1–15.

Elkateb, T. 2003. Quantification of Soil Heterogeneity. Ph.D. dissertation, University of Alberta, Edmonton, Canada.

Total E&P Canada Ltd 2010. Surface Steam Release of May 18, 2006, Joslyn Creek SAGD Thermal Operation. *ERCB Staff Review and Analysis* February 11, 2010.

EUB/AGS Earth Sciences Report 2006-06. Subsurface Geology of the Athabasca Wabiskaw-McMurray Succession: Lewis-Fort McMurray Area, Northeastern Alberta (NTS 74D/74E).

Fenton, G.A., and Vanmarcke E.H. 1998. Spatial Variation in Liquefaction Risk. *Géotechnique* 48(6): 819–831.

Fjær, E., and Nes O. 2014. The Impact of Heterogeneity on the Anisotropic Strength of an Outcrop Shale. *Rock Mechanics and Rock Engineering* 47: 1603–1611.

Frias, D.G., Murad M.A., and Pereira F. 2004. Stochastic Computational Modeling of Highly Heterogeneous Poroelastic Media with Long-Range Correlations. *International Journal for Numerical and Analytical Methods in Geomechanics* 28: 1–32.

Fung, L., Buchanan L., and Wan R. 1994. Coupled Geomechanical-Thermal Simulation for Deforming Heavy-Oil Reservoirs. *Journal of Canadian Petroleum Technology* 33(4): 22-28.

Gao, Z., Zhao J., and Yao Y. 2010. A Generalized Anisotropic Failure Criterion for Geomaterials. *International Journal of Solids and Structures* 47: 3166–3185.

Garipov, T., Voskov, D. and Tchelepi, H. 2015. Rigorous Coupling of Geomechanics and Thermal-Compositional Flow for SAGD and ES-SAGD Operations. *Paper presented at the SPE Canada Heavy Oil Technical Conference* held in Calgary, Alberta, Canada, 9-11 June 2015.

Garipov, T., Karimi-Fard, M. and Tchelepi, H. 2016. Discrete Fracture Model for Coupled Flow and Geomechanics. *Computational Geosciences* 20(1): 149–160.

Garipov, T., Tomin P., Rin R., Voskov, D. and Tchelepi, H. 2018. Unified Thermo-Compositional-Mechanical Framework for Reservoir Simulation. *Computational Geosciences* 22(4): 1039–1057.

Gerrard, C. 1982. Equivalent Elastic Moduli of a Rock Mass Consisting of Orthorhombic Layers. *International Journal of Rock Mechanics and Mining Science & Geomechanics Abstracts* 19: 9-14.

Gomez-Hernandez, J. and Journel, A. 1994. Stochastic characterization of grid block permeability: *SPE Formation Evaluation* 9(2): 93–99.

Guéry, A., Cormery F., Shao J. and Kondo D. 2007. A Micromechanical Model of Elastoplastic and Damage Behavior of a Cohesive Geomaterial." *International Journal of Solids and Structures* 45: 1406–1429.

Gutierrez, M. and Lewis, R.W. 1998. The Role of Geomechanics in Reservoir Simulation. Paper SPE/ISRM 47932presented at *SPE/ISRM Rock Mechanics in Petroleum Engineering*, 8-10 July 1998, Trondheim, Norway.

Guo P. and Stolle D. 2018. A Physically Meaningful Homogenization Approach to Determine Equivalent Elastic Properties of Layered Soil. *Canadian Geotechnical Journal* 55: 303-311.

Hashin Z. 1962. The Elastic Moduli of Heterogeneous Materials. *Journal of Applied Mechanics* 2: 143-150.

Hashin, Z. and Shtrikman, S. 1962. On some variational principles in anisotropic and nonhomogeneous elasticity. *Journal of the Mechanic and Physics of Solids* 10(4): 335-342.

Hashin, Z. and Shtrikman, S. 1963. A variational approach to the theory of the elastic behavior of multiphase materials. *Journal of the Mechanic and Physics of Solids* 11(2): 127-140.

Hassanpour R., 2009. A Review of McMurray Formation Geology in Athabasca Oil Sands. Paper 201 presented at CCG Annual Report 11, 2009.

Hill R. 1951. The elastic behavior of a crystalline aggregate. *Proceedings of the Physical Society, 65,* 349-354.

Hill, R. 1963. Elastic properties of Reinforced Solids, Some Theoretical Principles. *Journal of the Mechanic and Physics of Solids* 11(4): 281-287.

Hill, R. 1965. Continuum Micro-Mechanics of Elastoplastic Polycrystals. *Journal of the Mechanics and Physics of Solids* 13: 89–101.

Holden, L. and Nielsen, B. F. 2000. Global Upscaling of Permeability in Heterogeneous Reservoirs: the Output Least Squares (OLS) method. *Transport in Porous Media* 40: 115–143.

Huang J. and Griffiths D. 2015. Determining an Appropriate Finite Element Size for Modeling the Strength of Undrained Random Soils. *Computers and Geotechnics* 69: 506-513.

Huet, C. 1990. Application of Variational Concepts to Size Effects in Elastic Heterogeneous Bodies. *Journal of the Mechanic and Physics of Solids* 38(6): 813-841.

Islam, M. and Skalle P. 2013. An Experimental Investigation of Shale Mechanical Properties through Drained and Undrained Test Mechanisms. *Rock Mechanics and Rock Engineering* 46(6): 1391-1413.

Ita J. and Malekzadeh F. 2015. A True Poroelastic Up and Downscaling Scheme for Multi-Scale Coupled Simulation. Paper SPE 173253 presented at the *SPE Reservoir Simulation Symposium* held in Houston, Texas, USA.

Ito, Y., Ichikawa, M., and Hirata, T. 2000. The Growth of the Steam Chamber During the Early Period of the UTF Phase B and Hangingstone Phase I projects. Paper 2000-05 presented at the *Canadian International Petroleum Conference*, Calgary, 4–8 June.

Jaeger J. 1960. Shear Failure of Anisotropic Rocks. *Geological Magazine* 97(1): 65–72.

Lade, P. 1982. Localization Effects in Triaxial Tests on Sand. *IUTAM Conference on Deformation and Failure of Granular Materials*, Delft, 31 Aug- 3 Sep 1982.

Lade, P., Nam, J., and Hong, W. 2008. Shear Banding and Cross-Anisotropic Behavior Observed in Laboratory Sand Tests with Stress Rotation. *Canadian Geotechnical Journal*, 45: 74–84.

Lee, S., Kharghoria A., and Datta-Gupta A. 2002. Electrofacies Characterization and Permeability Predictions in Complex Reservoirs. *SPE Reservoir Evaluation & Engineering* 5(3): 3–6.

Lekhnitskii, S. 1981. Theory of elasticity of an anisotropic body. Moscow: Mir Publishers.

Liakas S., O'Sullivan C. and Saroglou C. 2017. Influence of Heterogeneity on Rock Strength and Stiffness using Discrete Element Method and Parallel Bond Model. *Journal of Rock Mechanics and Geotechnical Engineering* 9:575-584.

Liang W, Yang C, Zhao Y, Dusseault MB, Liu J 2007. Experimental investigation of mechanical properties of bedded salt rock. *International Journal of Rock Mechanics and Mining Sciences* 44(3): 400-411.

Li P., Chalaturnyk R. and Polikar M. 2004. Issues with Reservoir Geomechanical Simulations of the SAGD Process. *Journal of Canadian Petroleum Technology* 43(5): 54-61.

Li, P. and Chalaturnyk R. 2005. Geomechanical Model of Oil Sands. Paper SPE 97949 presented at the *International Thermal Operations and Heavy Oil Symposium* in Calgary, Alberta, Canada, 1-3 Nov 2005.

Li P. and Chalaturnyk R. 2006. Permeability Variations Associated with Shearing and Isotropic Unloading during the SAGD Process. *Journal of Canadian Petroleum Technology* 45(1): 54-61.

Li P., Chalaturnyk R. and Tan T. 2006. Coupled Reservoir Geomechanical Simulations for the SAGD Process. *Journal of Canadian Petroleum Technology* 45(1): 33-40.

Li P. and Chalaturnyk R. 2009. History Match of the UTF Phase A Project with Coupled Reservoir Geomechanical Simulation. *Journal of Canadian Petroleum Technology*, *48*(1), 29–35.

Li. P 2006. Numerical Simulation of the SAGD Process Coupled with Geomechanical Behavior Ph.D. dissertation, Department of Civil Engineering, University of Alberta.

Li S., Deutsch C., Si J. 2012. Ranking Geostatistical Reservoir Models with Modified Connected Hydrocarbon Volume. Paper presented at *Ninth International Geostatistics Congress*, Oslo, Norway June 11-15, 2012.

Li, Weixin, Rezakhani R., Jin C., Zhou X. and Cusatis G. 2017. A Multiscale Framework for the Simulation of the Anisotropic Mechanical Behavior of Shale. *International Journal for Numerical and Analytical Methods in Geomechanics* 41(14): 1494-1522.

Lin H., Cao P. and Wang Y. 2013. Numerical Simulation of a Layered Rock under Triaxial Compression. *International Journal of Rock Mechanics and Mining Sciences* 60: 12-18.

Ma, Z., Leung, J. Y., Zanon, S., and Dzurman, P. 2015. Practical implementation of knowledge-based approaches for steam-assisted gravity drainage production analysis. *Expert Systems with Applications* 42(21): 7326-7343.

Mackenzie J.K. 1950. The Elastic Constants of a Solid Containing Spherical Holes. *Proceedings of the Royal Society London*, 63(1): 2-11.

Manica M.A, Gens A., Vaunat J. and Ruiz D 2018. Nonlocal plasticity modeling of strain localization in stiff clays. *Computers and Geotechnics* 103: 138-150.

Martinius, A.W., Fustic, M., Garner, D.L., Jablonski, B.V.J., Strobl, R.S., MacEachern, J.A., and Dashtgard, S.E. (2017). Reservoir characterization and multiscale heterogeneity modeling of inclined heterolithic strata for bitumen-production forecasting, McMurray Formation, Corner, Alberta, Canada. *Marine and Petroleum Geology*, 82: 336–361.

McLamore, R., Gray, K.E., 1967. The mechanical behavior of transversely isotropic sedimentary rocks. *Journal of Engineering for Industry* 89(1): 62-73.

Mori, T., and Tanaka K. 1973. Average Stress in Matrix and Average Elastic Energy of Materials with Misfitting Inclusions. *Acta Metallurgica* 21(5): 571–574.

Morte, M., and Hascakir B. 2016. Estimation of Pseudo-Relative Permeability Curves through an Analytical Approach for Steam Assisted Gravity Drainage (SAGD) and Solvent Aided-Steam Assisted Gravity Drainage. *Journal of Unconventional Oil and Gas Resources* 16: 45–52.

Natural Resources Canada 2017. Energy Sources and Distribution, Oil Resources. Retrieved from *http://www.nrcan.gc.ca/energy/oil-sands/18085*.

Natural Resources Canada 2018. Fundamentals of Non-Aqueous Extraction of Oil Sands. Retrieved from *https://www.nrcan.gc.ca/science-and-data/funding-partnerships/funding-opportunities/current-investments/fundamentals-non-aqueous-extraction-oilsands/16124*.

Nielsen, B. and Tveito, A. 1998. An Upscaling Method for One-Phase Flow in Heterogeneous Reservoirs. A Weighted Output Least Squares (WOLS) Approach. *Computational Geosciences* 2: 93–123.

Jensen J. and Currie I. 1990. A New Method for Estimating the Dykstra-Parsons Coefficient to Characterize Reservoir Heterogeneity. *SPE Reservoir Engineering* 5(3): 369-374.

Khajeh, M., Chalaturnyk R. and Boisvert J. 2011. Impact of Heterogeneous Geomechanical Properties on Coupled Geomechanical-Flow Simulation of SAGD. Paper presented at the 2011 *SPE Reservoir Characterization and Simulation Conference and Exhibition* held in Abu Dhabi, UAE, 9-11 October 2011.

Khajeh M., Chalaturnyk R. and Boisvert J. 2012. A Numerical Local Upscaling Approach for Elastic Rock Mechanical Properties: Dealing with Heterogeneity. Paper presented at 46th U.S. *Rock Mechanics/Geomechanics Symposium*, 24-27 June 2012, Chicago, Illinois

Khajeh, M. 2013. Heterogeneity Consideration and Upscaling of Elastic Properties in Coupled Geomechanical Flow Simulation of SAGD. Ph.D. dissertation, University of Alberta, Edmonton, Canada.

Kim J., Tchelepi H.A., and Juanes R., 2011. Stability, Accuracy, and Efficiency of Sequential Methods for Coupled Flow and Geomechanics. *Computer Methods in Applied Mechanics and Engineering* 200 (23-24): 2094-2116.

Kosar, K.M. 1989. Geotechnical Properties of Oil Sands and Related Strata. Ph.D. dissertation, University of Alberta, Edmonton, Canada.

Kozlova, A., Li, Z.,Watanabe, J., Zhou, S., Bratvedt, K., Lee, S. 2016. A Real-Field Multiscale Black-Oil Reservoir Simulator. *SPE Journal* 21: 2049–2061.

Steven Fick 2008. Scar Sands: Alberta's Oil Sand.

Oldakowski K., 1994. Stress Induced Permeability Changes of Athabasca Oil Sands. Master thesis, Department of Civil Engineering, University of Alberta, Edmonton, Canada.

Olson, J.E., Yaich E. and Holder J 2009. Permeability changes due to shear dilatancy in uncemented sands. Paper ARMA09-157 presented at the *43rd US Rock Mechanics and 4th U.S.-Canada Mechanics Symposium* held in Asheville NC June 28th-July 1, 2009.

Paul B. 1960. Prediction of Elastic Constants of Multiphase Materials: *Transactions of the Metallurgical Society of AIME* 218: 36-41.

Patchett, J. and Coalson, E. 1979. The Determination of Porosity in Sandstones and Shaly Sandstones, Part One–Quality Control. *The Log Analyst* 20 (6).

Pickup, G., Ringrose, P. Jensen, J. and Sorbie, K. 1994. Permeability Tensors for Sedimentary Structures. *Mathematical Geology* 26(2): 227-250.

Pickup, G., Stephen K., Ma J., Zhang P. and Clark J. 2005. Multi-Stage Upscaling: Selection of Suitable Methods. *Transport Porous Media* 58: 191–216.

Plewes, H.D. 1987. Undrained Strength of Athabasca Oil Sands. MSc thesis, University of Alberta, Edmonton, Canada.

Phillips, J.M., 2011. Sedimentology, Ichnology and Development of a Sub-Regional Depositional and Stratigraphic Framework for the Mcmurray-Wabiskaw Succession in the MacKay River Area, Northeastern Alberta. Master thesis, University of Alberta, Edmonton, Alberta, Canada.

Pyrcz M.J. and Deutsch, C.V., 2014. Geostatistical Reservoir Modeling Second Edition. New York, Oxford.

Reis, J. C. 1992. A Steam-assisted Gravity Drainage Model for Tar Sands: Linear Geometry. *Journal of Canadian Petroleum Technology*, 31(10), 14-20.

Reiter, K., Heidbach O. and Schmitt D. 2014. A Revised Crustal Stress Orientation Database for Canada. *Tectonophysics* 636: 111–124.

Reuss, A. 1929. Berechnung der Fliessgrenzen von Mischkristallen auf Grund der Plastizitätsbedingung Für einkristalle. *Journal of Applied Mathematics and Mechanics* 9: 49–58.

Rijpsma G. and Zijl W. 1998. Upscaling of Hooke's Law for Imperfectly Layered Rocks. *Mathematical Geology* 30(8): 943-969.

Rowe, P. 1962. The Stress-Dilatancy Relation for Static Equilibrium of an Assembly of Particles in Contact. Proceedings of the *Royal Society of Long. Series A, Mathematical and Physical Sciences*, 269(1339): 500-527.

Saeidi O., Rasouli V., Vaneghi R.G., Gholami E. and Torabi S.R. 2014. A Modified Failure Criterion for Transversely Isotropic Rocks. *Geoscience Frontiers* 5(2): 215-225.

Salamon, M. 1968. Elastic Moduli of a Stratified Rock Mass. *Journal of Rock Mechanics and Mining Sciences* 5(6):519-527.

Samieh A. and Wong R. 1997. Deformation of Athabasca Oil Sand at Low Effective Stresses under Varying Boundary Conditions. *Canadian Geotechnical Journal* 34: 985-990.

Scott, J.D., Proskin, S.A. and Adhikary, D.P. 1994. Volume and Permeability Changes Associated with Steam Stimulation in an Oil Sands Reservoir. *Journal of Canadian Petroleum Technology* 33(7): 44-52.

Sainsbury, B., and Sainsbury D. 2017. Practical Use of the Ubiquitous-Joint Constitutive Model for the Simulation of Anisotropic Rock Masses. *Rock Mechanics and Rock Engineering* 50: 1507–1528.

Settari, A. 1988. Modeling of Fracture and Deformation Processes in Oil Sands. Paper No.43 presented at the 4th UNITAR/UNDP Conference on Heavy Crude and Tar Sands, Edmonton, Alberta on August 1988.

Settari, A and Mourits F. 1998. A Coupled Reservoir and Geomechanical Simulation System. *SPE Journal* 40(12): 55–61.

Settari, A. and Walters, D. 2001. Advances in Coupled Geomechanical and Reservoir Modeling with Applications to Reservoir Compaction. *SPE Journal* 6(3): 334–342.

Settari, A., Walters, D., and Behie, G. 2001. Use of Coupled Reservoir and Geomechanical Modeling for Integrated Reservoir Analysis and Management. *Journal of Canadian Petroleum Technology*, 40(12), 55–61.

Settari A., Al-Ruwaili K. and Sen V. 2013. Upscaling of Geomechanics in Heterogeneous Compacting Reservoirs. Paper SPE 163641 presented at the *SPE Reservoir Simulation Symposium* held in The Woodlands, Texas, USA.

Shafie, Z. and Chalaturnyk R. 2015. Geotechnical Characterization of Clearwater Clay Shale and Comparison of the Properties with Other Cretaceous Clay Shales in North America. *Journal of Canadian Petroleum Technology* 54(6): 394–411.

Sharma, J., and Gates, I. 2010. Multiphase Flow at the Edge of a Steam Chamber. *The Canadian Journal of Chemical Engineering*, *88*(3): 312-321.

Shen, W., Shao J., Kondo D. and Gatmiri B. 2012. A Micro-Macro Model for Clayey Rocks with a Plastic Compressible Porous Matrix. *International Journal of Plasticity* 36: 64–85.

Shen, W., Kondo D., Dormieux L. and Shao J. 2013. A Closed-Form Three Scale Model for Ductile Rocks with a Plastically Compressible Porous Matrix. *Mechanics of Materials* 59: 73–86.

Gurpreet S., Leung W., and Wheeler M. Multiscale Methods for Model Order Reduction of Non-Linear Multiphase Flow Problems. *Computational Geosciences* 23: 305–323.

Tang, C., Liu H. and Lee P. 2000. Numerical Studies of the Influence of Microstructure on Rock Failure in Uniaxial Compression-Part I: Effect of Heterogeneity. *Internal Journal of Rock Mechanics and Mining Sciences* 37(2000): 555-569.

Thomas R., Smith D., Wood J., Visser J., Calverley-Range E. and Koster E. 1987. Inclined Heterolithic Stratification-Terminology, Description, Interpretation and Significance. *Sedimentary Geology* 53: 123-179.

Tien Y., Kuo M. and Juang C. 2006. An Experimental Investigation of the Failure Mechanism of Simulated Transversely Isotropic Rocks. *International Journal of Rock Mechanics and Mining Sciences* 43(8): 1163-1181.

Tortike W.S. 1991. Numerical simulation of thermal multiphase fluid flow in an elastoplastic deforming oil reservoir. Ph.D. thesis. Department of Mining and Petroleum Engineering, University of Alberta.

Tortike W. and Farouq. A. 1993. Reservoir Simulatio Integrated with Geomechanics. *Journal of Canadian Petroleum Technology* 32(5): 28-37.

Touhidi-Baghini A., 1998. Absolute Permeability of McMurray Formation Oil Sands at Low Confining Stresses. Ph.D. dissertation, Department of Civil Engineering, University of Alberta.

Tran, D., Settari A., and Nghiem L. 2004. New Sequentially coupling Between a Reservoir Simulator and a Geomechanics Module. *SPE Journal* 9(3): 362–369.

Tran D., Nghiem L., and Buchanan L., 2005. An Overview of Sequentially coupling Between Geomechanical Deformation and Reservoir Flow. Paper SPE 97879 presented at the *2005 SPE International Thermal Operations and Heavy Oil Symposium* held in Calgary, Alberta, Canada.

Tziallas G., Saroglou H. and Tsiambaos G 2013. Determination of Mechanical Properties of Flysch Using Laboratory Methods. *Engineering Geology* 166:81-89.

Vergara M., Kudella P. and Triantafyllidis T. 2015. Large Scale Tests on Jointed and Bedded Rocks Under Multi-Stage Triaxial Compression and Direct Shear. *Rock Mechanics and Rock Engineering* 48(1):75-92.

Vermeer P.A. and Borst R. de 1984. Non-Associated Plasticity for Soils, Concrete and Rock. *Heron* 29(3): 1–64.

Voigt, W. 1907. Bestimmung der Elastizitätskonstanten von Eisenglanz. *Annalen der Physik* 24: 129-140.

Wang, C., and Leung, J. 2015. Characterizing the effects of lean zones and shale distribution in steam-assisted-gravity-drainage recovery performance. *SPE Reservoir Evaluation & Engineering* 18: 329-345.

White J., Borja R. and Fredrich J. 2006. Calculating the effective permeability of sandstone with multiscale lattice Boltzmann/finite element simulations. *Acta Geotechnica* 1(4): 195-209.

Willis M. 2013. Upscaling Anisotropic Geomechanical Properties Using Backus Averaging and Petrophysical Clusters in the Vaca Muerta Formation. Master Thesis, Department of Petroleum Engineering, Colorado School of Mines, USA.

Wong R. 1999. Mobilized Strength Components of Athabasca Oil Sand in Triaxial Compression. *Canadian Geotechnical Journal* 36(4): 718-735.

Yang D., Moridis G.J. and Blasingame T.A. 2013. Numerical Upscaling of Coupled Flow and Geomechanics in Highly Heterogeneous Porous Media. Paper presented at the *Unconventional Resources Technology Conference* held in Denver, Colorado, USA, 12-14 August 2013.

Yang, G., and Butler, R. 1992. Effects of Reservoir Heterogeneities on Heavy Oil Recovery by Steam-Assisted Gravity Drainage. *Journal of Canadian Petroleum Technology*, 31(8): 37-43.

Yang, T.H., Tham L.G., Tang C.A., Liang Z.Z. and Tsui Y. 2004. Influence of Heterogeneity of Mechanical Properties on Hydraulic Fracturing in Permeable Rocks. *Rock Mechanics and Rock Engineering* 37(4): 251–275.

Yin, S., Dusseault, M.B. and Rothenburg, L. 2009. Thermal Reservoir Modeling in Petroleum Geomechanics. *International Journal for Numerical and Analytical Methods in Geomechanics*. 33: 449-485.

Zadeh, N. S., and Chalaturnyk, R., 2015. Geotechnical Characterization of Clearwater Clay Shale and Comparison of the Properties with Other Cretaceous Clay Shales in North America. *Journal of Canadian Petroleum Technology:* 54(6):394-411.

Zeng, T., Shao J. and Xu W. A Micromechanical Model for the Elastic-Plastic Behavior of Porous Rocks. *Computers and Geotechnics* 70: 130–137.

Zhang, P., Pickup G., Monfared H. and Christie M. 2008. Flow Upscaling in Highly Heterogeneous Reservoirs. *Geological Society, London, Special Publications* 309: 135–144.

Zhang, B. and Okuno, R. 2015. Modeling of Capacitance Flow Behavior in EOS Compositional Simulation. *Journal of Petroleum Science and Engineering* 131: 96–113.

Zhang H. and Fu Z. 2010. Coupling Upscaling Finitely Element Method for Consolidation Analysis of Heterogeneous Saturated Porous Media. *Advances in Water Resources* 33: 34-47.

Zhang B., Deisman N., Khajeh M., Chalaturnyk R. and Boisvert J. 2019. Numerical Local Upscaling of Elastic Geomechanical Properties for Heterogeneous Continua. *Petroleum Geoscience*: petgeo2018-159

Zhu, Q., Zhao L. and Shao. J. 2016. Analytical and Numerical Analysis of Frictional Damage in Quasi Brittle Materials. *Journal of the Mechanics and Physics of Solids* 92: 137–163.

Zheng, J., Leung J., Sawatzky R. and Alvarez J.M. 2018. An AI-Based Workflow for Estimating Shale Barrier Configurations from SAGD Production Histories. *Neural Computing and Applications* 9: 1–25.

Zijl W., Hendriks M. and Hart M. 2002. Numerical Homogenization of the Rigidity Tensor in Hooke's Law Using the Node-Based Finite Element Method. *Mathematical Geology*, 34(3):291-322.

Zohdi, T., and Wriggers P. 2008. *An introduction to computational micromechanics*. 2nd Edition published by Springer.